UNIVERSITAT DE BARCELONA

Enhanced Optical Response in Arrays of Multifunctional Plasmonic Nanostructures

Javier Rodríguez Álvarez

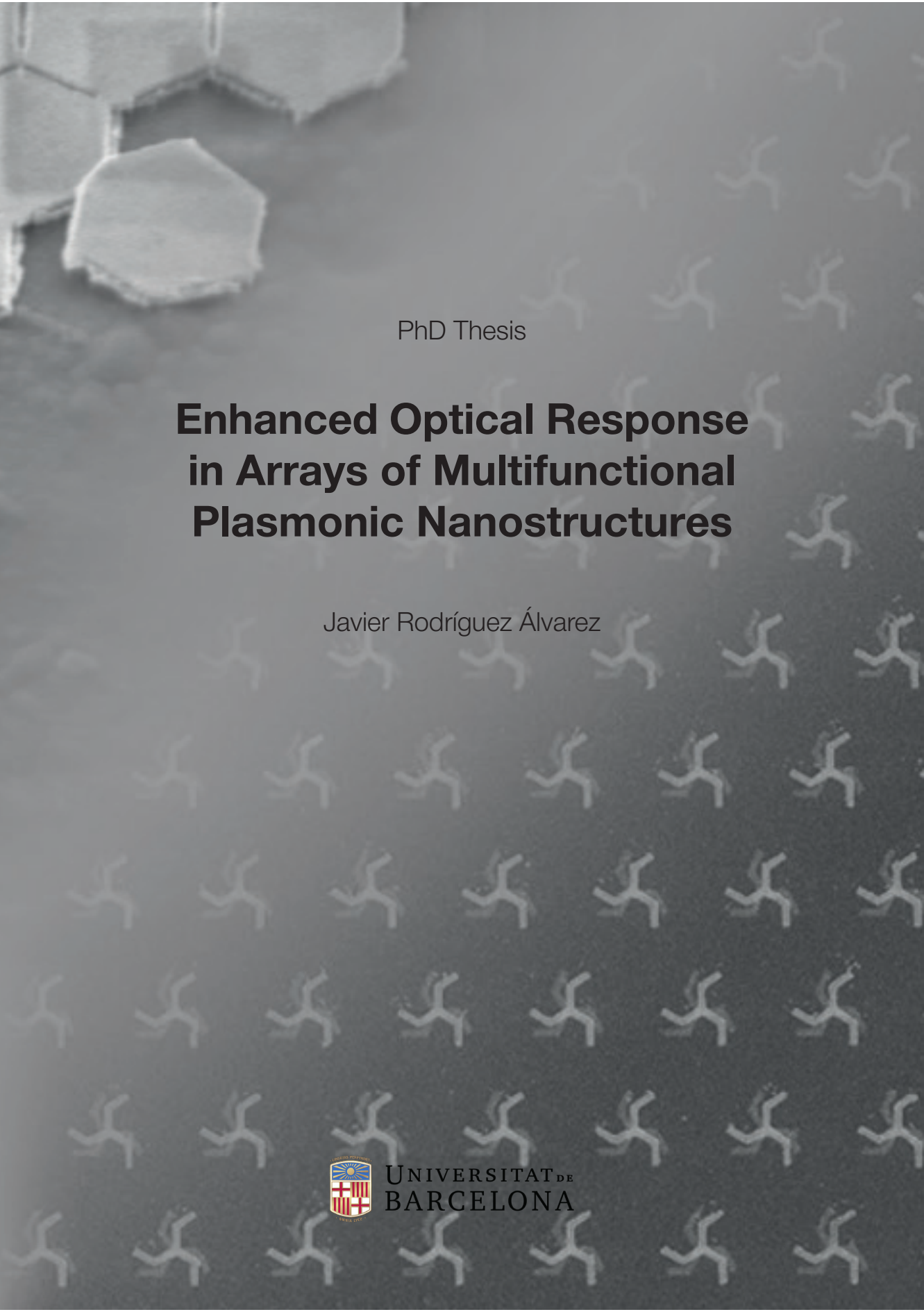

PhD Thesis

Enhanced Optical Response in Arrays of Multifunctional Plasmonic Nanostructures

Javier Rodríguez Álvarez

UNIVERSITAT DE BARCELONA

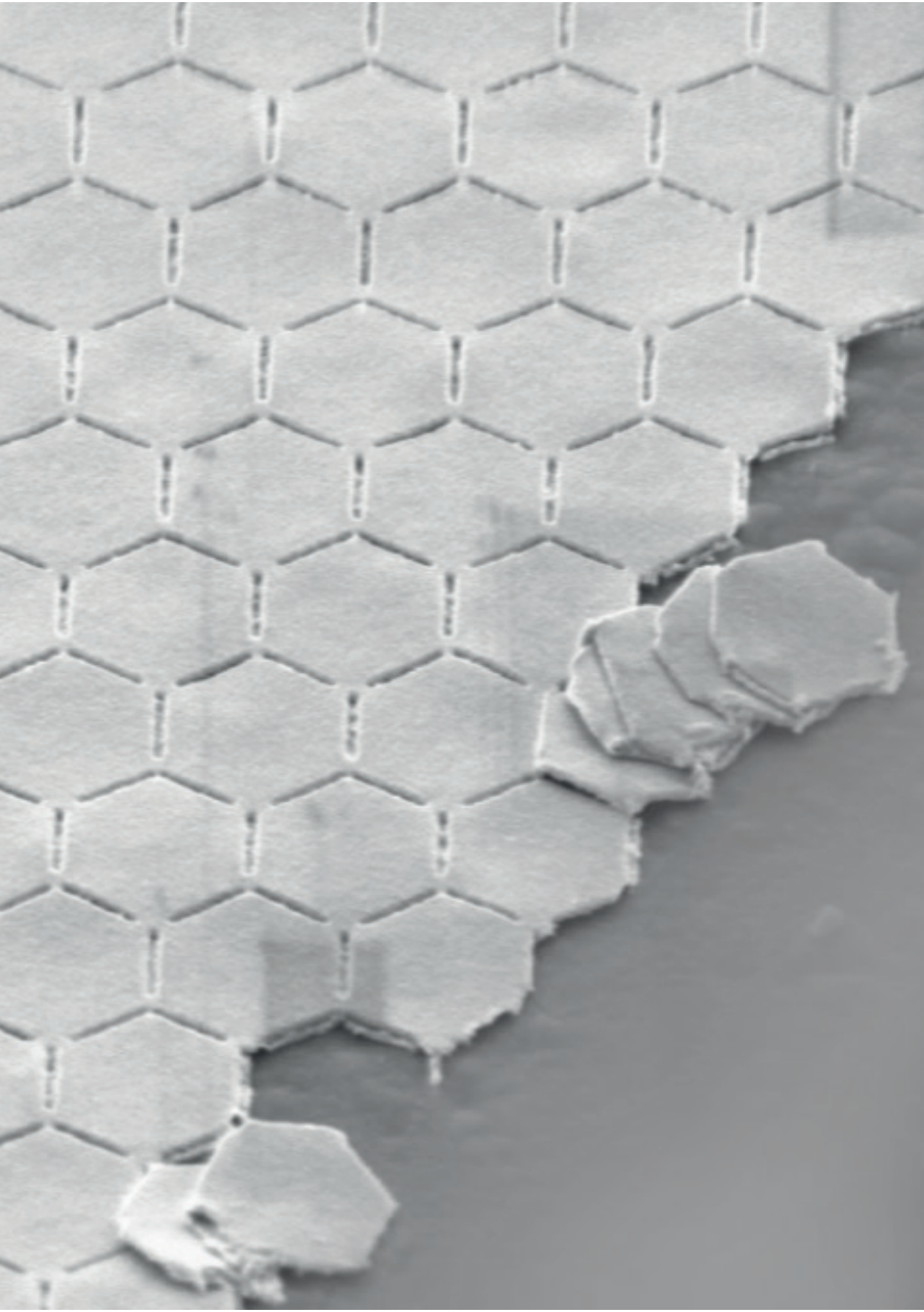

Enhanced Optical Response in Arrays of Multifunctional Plasmonic Nanostructures

Memòria presentada per optar al grau de doctor per la Universitat de Barcelona

Programa de doctorat en Nanociències

Autor: Javier Rodríguez Álvarez

Directors: Arantxa Fraile Rodríguez
Amílcar Labarta

Tutora: Arantxa Fraile Rodríguez

Departament de Física de la Matèria Condensada
Institut de Nanociència i Nanotecnologia de la Universitat de Barcelona (IN2UB)
Grup de Nanomaterials Magnètics

UNIVERSITAT DE BARCELONA

Javier Rodríguez Álvarez
Enhanced Optical Response in Arrays of Multifunctional Plasmonic Nanostructures
Programa de doctorat en Nanociències, 9 de Gener del 2025
Supervisors: Arantxa Fraile Rodríguez i Amílcar Labarta

Memòria presentada per optar al grau de doctor per la
Universitat de Barcelona
Grup de Nanomaterials Magnètics
Institut de Nanociència i Nanotecnologia de la Universitat de Barcelona (IN2UB)
Departament de Física de la Matèria Condensada
Martí i Franqués, 1
08028, Barcelona

Abstract

This thesis is devoted to the study of two plasmonic nanostructures that present a 3-fold symmetry, namely, inverted honeycomb lattices of bars and twisted stacks of triskelion nanostructures. These systems are particularly interesting due to the inherent geometric frustration originated by the mismatch between dipolar excitations, and the odd parity associated with the 3-fold symmetry. The combination of FDTD simulations with the fabrication and subsequent far-field and near-field optical characterization of such structures allows for a multifaceted description of the system. In this thesis, a remarkable agreement between experiments and simulation is achieved, demonstrating the effectiveness of this combined approach in elucidating the response of plasmonic systems.

This thesis begins with a fundamental overview of the field, laying the groundwork for the essential concepts necessary for understanding the main findings presented in subsequent sections. These results are discussed in detail through the publications derived from this research. Furthermore, simulation methodologies, nanofabrication techniques, and characterization methods are introduced, as they form the core of the research presented herein.

Publications I and II are devoted to the study of inverted honeycomb plasmonic lattices. Here we prove the potential of such structures as refractive index sensors, taking advantage of the sharp SLR and the well-defined spectral dependence with the refractive index. The general sensing capabilities of this SLR can easily be expanded due to the out-of-plane electric field of hot spots spanning hundreds of nanometers away from the structure surface, providing a huge potential sensing volume. From a fundamental point of view, we have successfully characterized the plasmonic response of this system through state-of-the-art EELS experiments and FDTD simulations. By using EELS, both bright and dark modes can be detected. In particular, we present the first observation of resonances with an anti-ferroelectric arrangement of the dipolar excitations of the slits in the honeycomb lattice that occur with such spatial periodicity so that their unit cell has twice the

area of the honeycomb lattice. The samples presented in this part have been fabricated by EBL and specially dedicated FIB milling using Au ions to avoid contamination of the sample.

Publications III and IV focus on the study of two stacked triskelia nanostructures, and their response as a function of the geometry of the structure, in particular, the twist angle between them. The triskelion motif is characterized by its 3-fold symmetry and inherent two-dimensional chirality in 2D. This system holds two coupled plasmonic resonances tunable by controlling the angle between both triskelia. We have demonstrated that a simple bonding-antibonding model is insufficient to fully elucidate the behavior of these two resonances. Instead, we have observed a continuous evolution of the excited modes as a function of the angle between the elements. Further insight into the combination of such resonances with SLR is proposed. The fabrication of this structure by successive EBL over large areas and high degree of alignment are also detailed.

Keywords: Plasmonic lattice, Surface lattice resonance, Plasmonic sensor, Plasmonic coupling, Circular dichroism, Electron beam lithography, FTIR.

Resum en català

Aquesta tesi està dedicada a l'estudi de dues nanostructures plasmòniques que presenten una simetria trigonal, xarxes de panal d'abella d'escletxes i apilaments de nanostructures en forma de triskelió. Aquests sistemes són particularment interessants a causa de la seva inherent frustració geomètrica, originada pel fet que les excitacions dipolars no es poden acomodar correctament a un sistema amb simetria trigonal. La combinació de simulacions FDTD amb la fabricació i posterior caracterització d'aquestes estructures permet una descripció completa del sistema. En aquesta tesi s'aconsegueix un notable acord entre experiments i simulacions, demostrant l'èxit de la combinació de tècniques a l'hora de comprendre la resposta dels sistemes plasmònics.

Aquest treball comença amb una introducció bàsica al camp d'estudi, establint els conceptes fonamentals necessaris per tal de comprendre els principals resultats d'aquesta tesi. Aquests resultats s'exposen detalladament a les publicacions que se'n deriven. Addicionalment, es resumeixen les principals les tècniques de simulació, nanofabricació i caracterització utilitzades, ja que són l'eix vertebrador de la recerca presentada en aquesta tesi.

Les publicacions I i II es dediquen a l'estudi de xarxes plasmòniques de panal d'abella invertit. En aquest cas, es demostra el seu potencial com a sensors d'índex de refracció, aprofitant la forta ressonància SLR i la seva dependència espectral amb l'índex de refracció del medi. Les capacitats generals de detecció d'aquest SLR es poden ampliar fàcilment gràcies a la generació de zones de concentració del camp elèctric fora del pla, que abasten centenars de nanòmetres fora de l'estructura, proporcionant un enorme potencial volum de detecció. Des d'un punt de vista fonamental, hem caracteritzat amb èxit la resposta plasmònica d'aquest sistema mitjançant mesures experimentals d'EELS i simulacions FDTD. Mitjançant EELS, es poden detectar tant modes brillants com foscos. Concretament, presentem la primera observació de ressonàncies originades per una disposició antiferroelèctrica d'excitacions dipolars a les escletxes que formen la xarxa de panal d'abella, que es produeixen amb una periodicitat espacial tal que la seva cèl·la unitat té el doble

d'àrea que la de la xarxa original. Les mostres presentades en aquesta part s'han fabricat amb EBL i un fresat FIB específic amb ions d'or per evitar la contaminació de la mostra.

Les publicaciones III i IV es centren en l'estudi de dues nanostructures amb forma de triskelió apilades i de la seva resposta en funció de la geometria de l'estructura, concretament, en funció l'angle de rotació entre elles. El triskelió es caracteritza per presentar una simetria trigonal, però també per ser quiral en 2D. Aquest sistema presenta dues ressonàncies plasmòniques acoblades que es poden modular controlant l'angle entre ambdós triskelionss. Hem demostrat que un simple model de "bonding-antibonding" no pot explicar amb èxit el comportament d'aquestes dues ressonàncies, sinó que es produeix un canvi continu en els modes excitats a mesura que canvia l'angle entre els elements. També es proposa un anàlisi més profund sobre la combinació d'aquestes ressonàncies amb les SLR. Es detalla, a més, la fabricació d'aquesta estructura mitjançant processos de EBL consecutius sobre una àrea gran i amb un alt grau d'alineament.

Titol de la tesi: Resposta òptica millorada en xarxes de nanoestructures plasmòniques multifuncionals

Paraules clau: Xarxa plasmònca, Ressonància de xarxa en superfície, Sensor plasmònic, Acoblament plasmònic, Dicroisme circular, Litografia per feix d'electrons, FTIR.

Resumen en castellano

Esta tesis está dedicada al estudio de dos nanoestructuras plasmónicas que presentan una simetría trigonal, redes de panal de abeja de rendijas y apilamientos de nanoestructuras en forma de triskel. Estos sistemas son particularmente interesantes debido a su inherente frustración geométrica, originada por el hecho de que las excitaciones dipolares no pueden acomodarse correctamente a un sistema con simetría trigonal. La combinación de simulaciones FDTD con la fabricación y posterior caracterización de estas estructuras permite una completa descripción del sistema. En esta tesis se logra un notable acuerdo entre experimentos y simulaciones, demostrando el éxito de la combinación de técnicas a la hora de comprender la respuesta de los sistemas plasmónicos.

Este trabajo comienza con una introducción básica al campo de estudio, estableciendo los conceptos fundamentales necesarios para comprender los principales resultados de esta tesis. Estos resultados se exponen detalladamente en las publicaciones que se derivan de ella. Adicionalmente, se resumen las principales técnicas de simulación, nanofabricación y caracterización utilizadas, ya que son el eje vertebrador de la investigación presentada en esta tesis.

Las publicaciones I y II se dedican al estudio de redes plasmónicas de panal de abeja invertido. En este caso, se demuestra su potencial como sensores de índice de refracción, aprovechando la fuerte resonancia SLR y su dependencia espectral con el índice de refracción del medio. Las capacidades generales de detección de este SLR pueden ampliarse fácilmente gracias a la generación de zonas de concentración del campo eléctrico fuera del plano. Éstas abarcan cientos de nanómetros fuera de la estructura, proporcionando un enorme potencial volumen de detección. Desde un punto de vista fundamental, hemos caracterizado con éxito la respuesta plasmónica de este sistema mediante medidas experimentales de EELS y simulaciones FDTD. Mediante EELS, se pueden detectar tanto modos brillantes como oscuros. Concretamente, presentamos la primera observación de resonancias originadas por una disposición antiferroeléctrica de excitaciones dipolares

en las rendijas que forman la red de panal de abeja, que se producen con una periodicidad espacial tal que su célula unidad tiene el doble de área que la de la red original. Las muestras presentadas en esta parte se han fabricado con EBL y un fresado FIB específico con iones de oro para evitar la contaminación de la muestra.

Las publicaciones III y IV se centran en el estudio de dos nanoestructuras con forma de triskel apiladas y de su respuesta en función de la geometría de la estructura, concretamente, en función del ángulo de rotación entre ellas. El triskel se caracteriza por presentar una simetría trigonal, pero también por ser quiral en 2D. Este sistema presenta dos resonancias plasmónicas acopladas que se pueden modular controlando el ángulo entre ambos triskeles. Hemos demostrado que un modelo simple de "bonding-antibonding" no puede explicar con éxito el comportamiento de estas dos resonancias, sino que se produce un cambio continuo en los modos excitados a medida que cambia el ángulo entre los elementos. También se propone un análisis más profundo sobre la combinación de estas resonancias con las SLR. Se detalla además la fabricación de esta estructura mediante procesos de EBL consecutivos sobre un área grande y con un alto grado de alineamiento.

Palabras clave: Red plasmónica, Resonancia de red en superfície, Sensor plasmónico Acoplamiento plasmónico, Dicroismo circular, Litografía por haz de electrones, FTIR.

Acknowledgements

Ninguna tesis doctoral estaria completa sin citar apropiadamente las referencias en las que se fundamenta su investigacion. De igual manera, creo que es esencial reconocer el apoyo y la inspiración de todas las personas que, de una forma u otra, han hecho posible que cinco años de esfuerzo, aprendizaje y dedicación lleguen a buen puerto.

En primer lugar, quiero expresar mi más sincero agradecimiento a Arantxa y a Amílcar por las largas discusiones sobre física, por su confianza y por su enorme dedicación. Gracias por transmitirme vuestro entusiasmo, por demostrarme que el rigor no está reñido con la pasión y por estar siempre al pie del cañón, con una palabra de ánimo, con un consejo o con un montón de ideas que, aunque a veces me han complicado la vida, siempre han contribuido a que hoy pueda ser un mejor científico. También quiero agradecer su apoyo al resto de miembros del grupo, en especial con todo lo relacionado con la docencia, a través de la cual he tenido la suerte de interactuar con muchos de ellos. Mención especial para Xavi por haber estado en tantas reuniones, pese a todas las obligaciones con el departamento.

Moltes gràcies també a en Francesc i en Xevi per permetre'm descobrir el món de la nanofabricació i per tractar-me sempre com un més. També vull agrair a tots els membres del grup de NANONEMS la seva ajuda i la seva càlida acollida, especialment venint de fora. En especial, estic profundament agraït a l'Albert Guerrero, per tot el que m'ha hagut de suportar a la sala blanca. Ha estat un plaer poder aprendre de tu, i t'agraeixo de tot cor la teva contagiosa dedicació i entrega.

También quiero agradecerle a Antonio todas las horas y horas que ha pasado discutiendo sobre plasmónica, presencialmente y por teléfono. Por ayudarme con las simulaciones, acojerme en congresos y en visitas a Madrid, por ponerme en contacto con colegas, por invitarme a cenar en su querido Colmenar, pero, sobre todo por su excepcional valor humano.

I also want to express my sincere gratitude to Joan and Christian, and to the

whole LXN group at PSI. I fondly remember the discussions during lunch at OASE, the barbecues, the fondue, and the adventurous visit to the tunnels. But especially for the long hours in the clean room and the genuine interest for a simple visiting PhD student.

I am also grateful to the numerous collaborators throughout these 5 years, Juan Carlos Idrobo, Damiano Giubertoni, Agustín Mihi, Pau Molet, Alvaro Blanco, Carlos Pecharromán and Tariq Jawhari.

Sergio, m'ha encantat poder fer aquest camí amb tu, des de la carrera gairebé fins al final del doctorat, qui sap si algun dia tornarem a la UB. Jasper, Íñigo, junto con Sergio me habeis dado un refugio en la facultad, siempre dispuestos a un cafelito o unas bravas. Muchas gracias por estar siempre ahí. I am also extremely thankful for the people of office 4.11, I would have never dreamed of a better place to call home in this faculty. Thank you Robert, Laia, Marc, and also Yuri and Blanca. Gràcies també a tu, Mariona, pel teu incansable optimisme. Va ser una sort haver pogut coincidir amb tu. También me acuerdo de vosotros Dani y Carol, nos metimos en esto desde el máster y diría que, al final, ha salido bastante bien.

Tampoco puedo olvidarme de todos mis amigos del Prat. Algunos hace decadas que me conocéis, otros mucho menos, pero os aseguro que esto no hubiera sido posible sin vosotros. ¡Qué bueno es tener gente que te ponga en tu sitio cuando hace falta!

A toda mi familia, mil gracias. A padres y abuelos, que siempre me han animado a hacer lo que más me apasionara y que siempre me han enseñado, con su ejemplo, a esforzarme de verdad por las cosas que valen la pena, en el trabajo y en la vida. Gracias porque siempre habéis estado ahí para recogerme cuando he caído y porque nunca habéis dejado de confiar en mí.

Per últim estàs tu, Maria. Gràcies per ser el meu pilar en els moments bons i els dolents, per ser sempre al meu equip. Sento que una gran part de tot això també és teu. No podria tenir una companya millor en aquest viatge.

De corazón, muchas gracias.

Contents

List of Figures 1

List of Acronyms 3

List of Publications 5

Motivation and Objectives 7

I Introduction 13

1 General introduction 15

2 Optical properties of metals 19
2.1 Overview of classical electromagnetism 19
2.2 The free electron gas: Drude model 22
2.3 Optical response of the free electron gas 25

3 Surface plasmon polaritons 27

4 Localized surface plasmons 31
4.1 The quasi-static approximation 31
4.2 Beyond the quasi-static approximation: Mie theory 35
4.3 Coupled localized surface plasmon resonances 38
4.4 Surface lattice resonances 42
4.4.1 Experimental considerations 46
4.5 Chiral plasmonics 48
4.5.1 A first approach to chiral plasmonics: the Born-Kuhn model 49
4.5.2 Chiral response in coupled nanostructures and near-field chirality 54

5 Finite-difference time-domain simulations 57

5.1 Working principle 58
5.2 Simulation elements 60
5.2.1 Sources 60
5.2.2 Boundary conditions 62
5.2.3 Meshing 64
5.2.4 Material parameters 65
5.2.5 Monitors 66

6 Nanofabrication and characterization techniques 69
6.1 Nanofabrication overview 69
6.2 Material choice 70
6.3 Electron beam lithography 70
6.4 Focused ion beam 75
6.5 Characterization techniques 77
6.5.1 Fourier-transform infrared spectroscopy 78
6.5.2 Electron energy loss spectroscopy 79

II Inverted Honeycomb Plasmonic Lattices 83
Introduction 85
Publication I 87
Publication II 101

III Chiral Plasmonic Nanostructures 117
Introduction 119
Publication III 121
Publication IV 134

Discussion 146

Conclusions 149

Bibliography 153

List of Figures

2.1 Dielectric function of the free electron gas 24
2.2 Volume plasmons 26

3.1 Surface plasmon polaritons 29

4.1 Quasi-static polarizability of a sphere 33
4.2 Charge and electric field for LSP in small nanoparticles 36
4.3 LSP spectral shift as a function of particle size 38
4.4 LSP spectral dependence on the shape of nanoparticles 39
4.5 Hybridization model 40
4.6 LSP coupling 41
4.7 SLR and dipole sum 45
4.8 Experimental requirements for SLR 47
4.9 Refractive index asymmetry on SLR 47
4.10 Scheme of the Born-Kuhn model 50
4.11 Plasmonic realization of the Born-Kuhn model 51
4.12 ORD and CD 53
4.13 Plasmonic coupling as a source chiroptical activity 54
4.14 Optical chirality 56

5.1 Electric and magnetic fields in a Yee cell 59
5.2 Sources in FDTD Lumerical 62

6.1 EBL process positive resist 72
6.2 EBL process negative resist 73
6.3 Exposed volume in EBL 74
6.4 FIB structures 76
6.5 FTIR working principle 79

6.6 Overview of near-field characterization techniques 80
6.7 Scheme of EELS and CL equipment 81
6.8 EELS mapping 82

List of Acronyms

BC Boundary conditions.

CD Circular dichroism.

CL Cathodoluminiscence.

CP Circularly polarized.

EBL Electron beam lithography.

EDX Energy-dispersive X-ray.

EELS Electron energy loss spectroscopy.

FDTD Finite-difference time-domain.

FIB Focused ion beam.

FTIR Fourier transform infrared.

HAADF High angle annular dark field.

HSQ Hydrogen silsesquioxane.

IR Infra-red.

LCP Left-handed circularly polarized light.

LP Linearly polarized.

LSP Localized surface plasmon.

NIR Near infra-red.

OC Optical chirality.

ORD Optical rotatory dispersion.

PBC Periodic boundary conditions.

PML Perfectly matched layers.

PMMA Poly(methyl methacrylate).

RCP Right-handed circularly polarized light.

RIU Refractive index units.

SEM Scanning electron microscope.

SLR Surface lattice resonance.

SPP Surface plasmon polariton.

TE Transversal electric.

TEM Transmission electron microscope.

TFSF Total-field scattered-field.

TM Transversal magnetic.

UV Ultraviolet.

List of Publications

I. J. Rodríguez-Álvarez, L. Gnoatto, M. Martínez-Castells, A. Guerrero, X. Borrisé, A. Fraile Rodríguez, X. Batlle, A. Labarta. An inverted honeycomb plasmonic lattice as an efficient refractive index sensor. *Nanomaterials*, (2021) 11(5), 1217.

II. J. Rodríguez-Álvarez, A. Labarta, J. C. Idrobo, R. Dell'Anna, A. Cian, D. Giubertoni, X. Borrisé, A. Guerrero, F. Perez-Murano, A. Fraile Rodríguez, and X. Batlle. Imaging of antiferroelectric dark modes in an inverted plasmonic lattice. *ACS Nano*, (2023) 17(9), 8123-8132.

III. J. Rodríguez-Álvarez, A. García-Martín, A. Fraile Rodríguez, X. Batlle, and A. Labarta. Tunable circular dichroism through absorption in coupled optical modes of twisted triskelia nanostructures. *Scientific Reports*, (2022) 12(1), 26.

IV. J. Rodríguez-Álvarez, J. Vila-Comamala, C. David, A. García-Martín, A. Guerrero, X. Borrisé, F. Pérez-Murano, A. Blanco, C. Pecharromán, X. Batlle, A. Fraile Rodríguez and A. Labarta. *Submitted to Nanophotonics*, (2025).

Additional publications not directly related with this thesis:

V. I. Valmianski, A. Fraile Rodríguez, J. Rodríguez-Álvarez, M. García del Muro, C. Wolowiec, F. Kronast, J. G. Ramírez, I. K. Schuller, A. Labarta, and X. Batlle. Driving magnetic domains at the nanoscale by interfacial strain-induced proximity. *Nanoscale*, (2021) 13(9), 4985-4994.

VI. C. Moya, M. Escoda-Torroella, J. Rodríguez-Álvarez, A. I. Figueroa, I. García, I. Batalla Ferrer-Vidal, A. Gallo-Cordova, M. Puerto Morales, L. Aballe, A. Fraile Rodríguez, A. Labarta, and X. Batlle. Unveiling the crystal and magnetic texture of iron oxide nanoflowers. *Nanoscale*, (2024) 16, 1942-1951.

Motivation and Objectives

Plasmonic nanostructures exhibit an exceptional capacity to interact with visible light , albeit operating at higher frequencies [1]. The potential implications of this unprecedented level of control over visible light have sparked the interest of the nanophotonics community during the last decades [2, 3, 4, 5, 6]. The significance of plasmonic nanosystems extends beyond their fundamental properties, encompassing out-of-equilibrium phenomena that facilitate the generation of hot carriers near metal-insulator interfaces [7], symmetry-breaking effects associated with frequency up-conversion [8], and chirality [9], among others. The potential applications of plasmonic nanostructures are diverse and far reaching. These include, but are not limited to enhanced catalysis [10, 11, 12], perfect absorbers [13, 14], plasmonic lasing [15, 16, 17], energy harvesting [18, 19], or to improve the sensitivity of spectroscopies, reaching single molecule detection levels [20, 21].

This thesis focuses on the study of two key systems among the wide range of subtopics within plasmonics: 2D arrays of planar nanoelements and 3D chiral stacks of plasmonic nanostructures. These systems demonstrate enhanced plasmonic responses through various interactions between localized modes, including long-range collective excitations and strong near-field coupling between adjacent structures. Such interactions manifest in remarkable phenomena, such as narrow resonances, dark mode excitation, and pronounced circular dichroism, thereby expanding the potential for manipulating light-matter interactions at the nanoscale [22, 23, 24].

A paradigmatic example of such complex interactions is the generation of SLR. In ordered arrays of plasmonic nanostructures, it is feasible to generate an in-phase excitation of the LSP in each individual nanostructure [25]. This phenomenon is intimately related to both the geometry of the plasmonic resonator and the array configuration. Consequently, SLR offer additional degrees of freedom for fine-tuning the system's response, which has garnered significant attention within the scientific community due to the characteristically intense and narrow spectral profiles of the plasmonic resonances. The unique properties of SLR have far-reaching applications,

to name a few: SLR can be used in color generation, with a resonant wavelength that can be tuned by changing the periodicity of the array [26, 27], embedding the plasmonic array in an active medium can lead to an enhanced lasing behavior with a controlled directionality [28, 29, 30], and the strong spectral dependence on the surrounding media of SLR can be used as the sensing mechanism of a new generation of plasmonic sensors [31, 32, 33, 34]. This thesis delves into the study of coupled plasmonic elements and the emergent phenomena that arise from this interaction. Many simple designs and lattice geometries were previously explored using nanodots [35, 36], bars [37], or different lattice geometries [38, 39]. Within this context, earlier research by our group highlighted the significance of simple elements positioned in close proximity and organized into arrays with triangular symmetry, specifically in the arrangement of hexagonal and honeycomb lattices [40, 41].

A primary aim of this thesis is to investigate the role of geometric frustration in shaping the plasmonic response of a system. This phenomenon, well-established in fields such as magnetism [42], arises when structural symmetries hinder low-energy dipolar modes, thereby promoting the emergence of more complex system excitations. In plasmonic nanostructures exhibiting 3-fold symmetry, a mismatch can occur between the harmonic excitation of electric dipoles, which possess even parity, and the underlying geometry, resulting in the suppression of simple dipolar modes in favor of higher-order excitations. To investigate this phenomenon, this thesis focuses on the response of plasmonic lattices with 3-fold symmetry and individual nanostructures inherently possessing such geometry.

Subsequent investigations demonstrated an increase in the sensing capabilities of such structures when an inverted nanostructure is considered, due to the strong out-of-plane hot spots generated [43, 44, 45]. For this reason, the response of plasmonic lattices has been extensively studied through theoretical modeling [46, 47] and FDTD simulations [35, 46, 48]. Experimental work based on the the fabrication of samples by EBL [36, 37, 49, 50], FIB milling [51] and nanoimprinting lithography [52, 53], and a far-field characterization by FTIR spectroscopy [36, 41, 43, 50] have also been extensively performed. In this thesis, two primary inverted honeycomb lattices were investigated: Si_3N_4 membranes and a metal-insulator-metal configuration. The comparative analysis of these substrate configurations

elucidates the complex interplay between the plasmonic nanostructures and their supporting media. This research contributes to a more comprehensive understanding of substrate-mediated effects on plasmonic phenomena, with potential implications for the design and optimization of plasmonic devices for various applications. These findings highlight the critical role of the substrate in either enhancing or suppressing specific lattice resonances, thereby significantly modulating the overall plasmonic response of the system.

The second main topic of this work deals with plasmonic nanosystems exhibiting chiroptical responses, a phenomenon of increasing importance in the field of nanophotonics [54, 23]. Chirality, defined as the geometric property of an object that cannot be superimposed on its mirror image, plays a crucial role in the interaction between these nanostructures and CP light [55]. The two mirror images of a chiral object, known as enantiomers, respond differently to LCP and RCP light due to the inherent chirality of CP electromagnetic radiation [56]. The significance of chiral plasmonic systems stems from the fundamental role of chirality in biological molecules such as enzymes, DNA, and proteins [57]. These systems serve as versatile platforms for enhancing and manipulating chiroptical phenomena [23].

The flexibility of plasmonic metasurfaces allows for diverse strategies to generate chiroptical responses, including the fabrication of helical nanostructures [58, 59], the assembly of nanoparticles in chiral configurations [60, 61], or the stacking of planar structures to create 3D chiral geometries [62, 63, 64]. These approaches leverage the unique properties of plasmonic materials to create strong, localized electromagnetic fields that can amplify chiroptical effects and enable precise analysis of chiral asymmetry, potentially down to the single-molecule level.

The study of near-field coupling of plasmonic resonances provides a valuable framework for examining and elucidating the phenomena of plasmonic chirality. Our approach is based on the vertical stacking of planar nanostructures with sub-100 nm separations. This 3D configuration facilitates interaction with CP light due to the relative rotational orientation between the elements within the stack. The geometry of the system and its differential response to RCP and LCP light is investigated. While similar systems have been previously examined within the framework of the Born-Kuhn model [65], which considers the role of de-phased excitation in stacked elements by

CP light, this thesis proposes an alternative approach. Our concept focuses on the excitation of coupled resonances in stacked nanostructures, enabled by the sub-wavelength separation between elements. This configuration allows for near-field coupling, a phenomenon not accounted for in the traditional Born-Kuhn model. The small inter-element distance, significantly less than half the incident wavelength, facilitates strong electromagnetic interactions between the plasmonic components. Previous research on planar chiral structures has predominantly focused on two-dimensional (2D) chiral nanostructures, with gammadions being a prominent example. Extensive studies have been conducted on arrays of gammadions operating in the visible and NIR regimes [66, 67, 68]. The chiroptical activity observed in these planar nanostructures is attributed to the symmetry-breaking effect induced by the substrate, as 2D structures are inherently incapable of exhibiting CD due to reciprocity constraints [69]. To overcome this limitation and ensure the 3D nature of the system, researchers have employed stacked nanostructures as an effective strategy [62, 63, 64, 70]. While stacked gammadions have been explored in the literature, their optical responses were typically observed in lower-energy regions of the electromagnetic spectrum, primarily due to their larger dimensions [71, 72, 73]. In this thesis, we present a novel approach utilizing state-of-the-art equipment to fabricate stacked nanostructures through successive EBL processes. This methodology has enabled us to achieve precise alignment with misalignment errors below 50 nm over relatively large areas (approximately 1x1 mm^2). The resulting samples were characterized using FTIR spectroscopy with CP light, revealing a strong chiroptical response in both the visible and NIR spectral ranges.

This comprehensive work aspires to serve as an introduction to the field of plasmonics, providing an in-depth understanding of the current state of the art and elucidating the key features of several relevant techniques central to this field of research. The compilation of peer-reviewed articles and the accompanying manuscript draft summarize the main findings of this thesis.

In order to do so, the main objectives of this thesis are:

1. Investigate innovative designs of plasmonic nanostructures exploiting interactions between localized surface plasmons and surface lattice resonances.

2. Fabricate 2D plasmonic lattices, including direct and inverse (trench) networks, with bar-shaped nanoelements of varying gap and pitch, and three-fold symmetry, using EBL- and FIB-based processes.

3. Study and optimize the response of 2D arrays of inverted honeycomb lattices on different substrate configurations and explore their performance for applications in plasmonic-based sensing and spectroscopy.

4. Exploit the role of geometric frustration in shaping the plasmonic response of nanostructures, particularly those with 3-fold symmetry.

5. Develop 3D stacked configurations using advanced EBL-based approaches to create precisely aligned 2D stacks with sub-100 nm separations.

6. Investigate the chiroptical properties of 3D stacked plasmonic nanostructures and their interactions with circularly polarized light, specifically:
   a) Analyze coupled modes and their impact on circular dichroism.
   b) Study effects of geometrical parameters on chiroptical response.
   c) Develop theoretical frameworks for chiroptical responses.

7. Perform simulations of optical far-field spectra and near-field electric field and charge patterns using various excitation sources to assist in interpreting experimental data and identifying promising structural designs.

8. Conduct experimental characterization and analysis of the optical responses of manufactured plasmonic systems in both visible and near-infrared spectral ranges, using a comprehensive methodology combining far-field and near-field techniques with simulations.

These objectives collectively aim to deepen our understanding of complex plasmonic phenomena through innovative design, fabrication, and characterization of 2D and 3D configurations, thereby contributing to the development of next-generation plasmonic devices for sensing and nanoscale light manipulation.

Part I

Introduction

> *Nunca os jactéis de autodidactos, os repito, porque es poco lo que se puede aprender sin auxilio ajeno. No olvidéis, sin embargo, que este poco es importante y que además nadie os lo puede enseñar.*
>
> **— Antonio Machado —**

General introduction

1

The interplay between electromagnetic radiation and matter has long captivated the scientific community, drawing attention from both fundamental and technological perspectives. The invention of the microscope and telescope, and subsequent studies in the late 16th and early 17th centuries by Newton and Huygens, initiated a quest to comprehend the nature of light and its interactions with matter. Throughout the centuries, the progressive advancement of knowledge and technological capabilities has enabled the exploration of even smaller length scales and shorter time spans, and has unveiled a plethora of novel and intricate phenomena, igniting the curiosity of many researchers across the world.

The field of nanophotonics is currently at the forefront of the study of light-matter interaction, although, for a long time, nanophotonics may have seemed like an impossible field to explore. This is because the smallest scale to which a propagating wave can be focused (i.e. confined) is roughly limited to half its wavelength. This limit arises from diffraction-related considerations, given that, to focus light, one must make use of optical elements (e.g., diaphragms and lenses) that will inevitably hinder the ability of those systems to produce a sharp focus. Considering that the visible light has a wavelength between 400 nm and 800 nm, approximately, the prospects of manipulating and studying light-matter interactions at the nanoscale would seem rather limited. Nevertheless, one of the paradigmatic discoveries of nanophotonics is the possibility of subwavelength confinement of electromagnetic fields that exist in the form of evanescent waves in the optical and near-optical regimes. These evanescent electromagnetic fields decay rapidly away from boundaries and interfaces between two materials, thus confining the energy of the electromagnetic radiation to incredibly small volumes, well below the wavelength limit. These strongly, localized "near fields" constitute one of the main interests of nanophotonics and are restricted to the close vicinity of the nanostructure, as opposed to the "far fields" that are radiated outwards and dominate at greater distances.

The possibility of manufacturing structures far smaller than the wavelength of visible light has enabled the exploration of the electric and magnetic fields arising in the nanometer scale surrounding metal-dielectric interfaces, that is in the vicinity of small metallic nanostructures. Perhaps, one of the most defining features of these sub-wavelength field distribution is their coupling with charge oscillations in metallic nanostructures. These coupled resonances are the main goal of plasmonics.

Plasmonics, a field within nanophotonics, is dedicated to investigating the resonances that emerge in metallic nanostructures due to their interactions with radiation having wavelengths comparable or smaller than the characteristic length of the system. This thesis specifically addresses these interactions within the optical and near-infrared regimes. It does so by examining the dynamics of conduction electrons in the metal under the influence of oscillating electric and magnetic fields, as well as the resulting resonances in metallic nanostructures.

The aim of this thesis is to provide a comprehensive and coherent overview of the field of plasmonic nanostructures. From first principles and, through simple approximations, volume plasmons will initially be introduced followed by a brief mention to surface plasmons. Then, localized surface plasmons will be introduced and extensively discussed, due to their relevance to the field and their instrumental role in the work presented in this thesis. Their tunable spectral signature through control of size and shape of the plasmonic elements will be explained, as well as the mechanisms behind the interaction among resonances of neighboring particles. Following this, we will outline the underlying physical principles and characteristics associated with surface lattice resonances in ordered arrays of plasmonic nanoelements, including the emergence of chiral properties, from both theoretical and experimental standpoint.

The concluding section of the introduction focuses on the research methodology utilized in this thesis, comprising Finite-Difference Time-Domain (FDTD) simulations and the fabrication along with experimental characterization of samples. The former are the cornerstone of this thesis, due to their key enabling capabilities to first, pick out the range of promising sample configurations to be explored, thereby substantially lowering the costs of fabrication and experimental characterization, and second, allowing for the

modelling the plasmonic response of the designed systems. The fabrication and experimental characterization of samples are fundamental aspects of nanotechnology research, given the inherent challenges in manufacturing and characterizing nanometer structures.

The subsequent chapters will provide summaries of the publications arising from this thesis, discuss the main conclusions, and conclude with some future perspectives.

Optical properties of metals

2

Prior to an in-depth discussion on plasmonics, it is convenient to summarize the main physical concepts involved in the interaction between metals and electromagnetic waves at optical and near-infrared frequencies. In this section, we will delve into the key concepts derived from Maxwell's equations, particularly focusing on the dielectric function and its relationship with the complex refractive index. We will also present a simple model for the optical response of metals. The concept of volume plasmons will be naturally introduced in this context.

2.1 Overview of classical electromagnetism

The metallic nanostructures studied in this thesis are too large to allow a quantum approach to the problem. Instead, classical electromagnetism has proven to provide an accurate description of plasmonic resonances in metallic nanostructures, while allowing for an intuitive interpretation of the phenomena. In a classical description, Maxwell's equations determine the response of the system:

$$\vec{\nabla} \cdot \vec{D} = \rho_{ext} \tag{2.1}$$

$$\vec{\nabla} \cdot \vec{B} = 0 \tag{2.2}$$

$$\vec{\nabla} \times \vec{E} = -\frac{\partial \vec{B}}{\partial t} \tag{2.3}$$

$$\vec{\nabla} \times \vec{H} = \vec{J}_{ext} + \frac{\partial \vec{D}}{\partial t} \tag{2.4}$$

where $\vec{D}$ is the displacement field, $\vec{E}$ is the electric field, $\vec{H}$ is the magnetic field, and $\vec{B}$ is the magnetic induction. $\vec{J}_{ext}$ and ρ_{ext} are the external current and charge densities, if present, respectively. Here, we do not make the

distinction between free and bounded charges, but we consider internal ($\vec{J}$, ρ) and external ($\vec{J}_{ext}$, ρ_{ext}) quantities so that $\vec{J}_{tot} = \vec{J} + \vec{J}_{ext}$ and $\rho_{tot} = \rho + \rho_{ext}$ (see [74] for a detailed discussion).

Considering the fact that most metals are nonmagnetic at optical and near-infrared frequencies, we can safely neglect the magnetic response of the system. Thus, the following discussion will only consider the effects of the driving field on the polarization $\vec{P}$ of the material. This quantity is related to the rearrangement of the electric dipoles in the metal. Taking into account charge conservation ($\nabla \cdot \vec{J} = -\partial\rho/\partial t$) we can also link the polarization with the charge and current densities

$$\vec{J} = \frac{\partial \vec{P}}{\partial t} \tag{2.5}$$

$$\vec{\nabla} \cdot \vec{P} = -\rho \tag{2.6}$$

Going back to Maxwell's equations, we can now define the displacement field in terms of the polarization vector. $\vec{D}$ can be written as the sum of two contributions. The first one comes from the external field $\vec{E}$, while the second appears due to the response of the material to that external field, that is, the polarization $\vec{P}$. The expression goes as follows

$$\vec{D} = \varepsilon_0 \vec{E} + \vec{P} \tag{2.7}$$

where ε_0 is the electric permittivity of vacuum. Considering the case for linear, isotropic, and nonmagnetic materials we can rewrite Eq. 2.7 as

$$\vec{D} = \varepsilon_0 \varepsilon \vec{E} \tag{2.8}$$

being ε the dielectric constant or relative permittivity of the medium. This expression shows naturally how the details of the material's response to the driving field are contained in the dielectric constant. It can be seen that $\vec{P} = \varepsilon_0(\varepsilon - 1)\vec{E}$. In general, the dielectric constant will depend on the frequency (ω) and on the wave vector ($\vec{K}$). A non-local version in space and time of Eq. 2.8 can be reformulated as

$$\vec{D}(\vec{r}, t) = \varepsilon_0 \int \varepsilon(\vec{r} - \vec{r}', t - t')\vec{E}(\vec{r}', t))dt' d\vec{r}' \tag{2.9}$$

This can be simplified by taking the Fourier transform of Eq. 2.9, turning the

convolutions into products, and thus recovering an equivalent expression in the Fourier space to Eq. 2.8.

$$\vec{D}(\vec{K},\omega) = \varepsilon_0 \varepsilon(\vec{K},\omega)\vec{E}(\vec{K},\omega)) \tag{2.10}$$

It is worth noting that there is a complementary discussion of the optical properties of materials, this time in terms of the electrical conductivity of the material, σ. This quantity is also able to capture the response of the material to an external driving field following $\vec{J} = \sigma\vec{E}$, both in real and Fourier space. It can be seen that both, ε and σ are equivalent descriptions of the response of the material, since one can write $\varepsilon(\vec{K},\omega) = 1 + i\,\sigma(\vec{K},\omega)/\varepsilon_0\omega$. At low frequencies, it is often useful to rely on ε when describing the response of bound charges to an external field, while σ refers to the contributions of free charges to the current flow. However, at optical frequencies, this difference is blurred [75].

In general, we will describe the local response of a material (considering $\vec{K} = 0$) making use of $\varepsilon(\omega) = \varepsilon_1(\omega) + i\,\varepsilon_2(\omega)$ which is a complex-valued function of the angular frequency. At optical frequencies, $\varepsilon(\omega)$ can be experimentally determined by reflectivity measurements because of the relation between the dielectric function of a material and its refractive index. Since $\tilde{n} = \sqrt{\varepsilon}$, for $\mu = 1$, we can define a complex refractive index $\tilde{n}(\omega) = n(\omega) + i\,k(\omega)$, where k, the extinction coefficient, is related to the absorption of electromagnetic waves propagating in a material. It can be directly linked to the absorption coefficient α in Beer-Lambert's law. This law describes the exponential decay of the intensity of an electromagnetic wave traveling through a medium as $I(x) = I_0 e^{-\alpha x}$, where $\alpha(\omega) = 2\omega k(\omega)/c$.

This finally yields the following relations between the real and imaginary parts of both quantities allowing for the experimental determination of $\epsilon(\omega)$:

$$\varepsilon_1 = n^2 - k^2 \tag{2.11}$$

$$\varepsilon_2 = 2nk \tag{2.12}$$

$$n^2 = \frac{\varepsilon_1}{2} - \frac{1}{2}\sqrt{\varepsilon_1^2 + \varepsilon_2^2} \tag{2.13}$$

$$k = \frac{\varepsilon_2}{2n} \tag{2.14}$$

2.2 The free electron gas: Drude model

After describing the interaction of electromagnetic fields with matter, a simple model can be used to explain the mechanism behind such behavior, this is the Drude model, also known as the free electron gas, or plasma model. It was developed by Paul Drude around 1900 to explain the motion of electrons in solids [76, 77]. In this framework, the conduction electrons are modeled as a gas of free, non-interacting particles that relax through collisions with the ionic lattice or with electrons.For many metals, especially noble metals, which are of the highest interest for plasmonic applications, this model holds throughout the IR region until the visible frequencies, where interband transitions limit its validity. Nevertheless, for alkali metals, this model can be applied up to the UV.

Despite the complexity of conduction electrons traveling through a crystal and interacting via electron–electron Coulomb interactions, the system can be effectively modeled as a non-interacting gas. This simplification is validated by a subsequent quantum mechanical approach. In a bulk metal, the lattice imposes a periodic potential with minima located around the positively charged ionic cores. Within this framework, the wavefunction of an electron can be expressed as the product of a plane-wave function and a periodic function that matches the lattice's periodicity, known as a Bloch function [78].

The Schrödinger equation describing the electron motion, can be separated into a stationary part containing the Bloch functions, and a plane-wave function. This separation indicates that the electron motion is primarily determined by the plane-wave function, similar to the behavior of a free electron. The influence of other electrons in the material is accounted for by an effective average potential that represents the collective interaction of all electrons. Since the plane-wave functions span the entire solid, this effective average potential dominates over any individual electron-electron interactions. For the simplest case, the primary distinction between a truly free electron model and this model is the definition of an *effective mass* m^* that differs from the electron's rest mass. In summary, this implies that the motion of electrons in simple metals can be described without explicitly invoking quantum mechanics.

From a classical approximation, the equation of motion of an electron in a crystal under the influence of an oscillating electric field can be written as:

$$m^* \frac{d^2\vec{r}}{dt^2} + m^*\gamma\frac{d\vec{r}}{dt} = -e\vec{E}(\vec{r},t) \tag{2.15}$$

where γ is a damping parameter known as the collision frequency. Typically, γ =100 THz at room temperature.

Assuming an harmonic time dependence of the driving field $\vec{E}(t) = \vec{E}_0 e^{-i\omega t}$, the solution of Eq. 2.15 is

$$\vec{r}(t) = \frac{e}{m^*(\omega^2 + i\gamma\omega)}\vec{E}(t) \tag{2.16}$$

The displacement of the electrons with respect to the positively charged ionic lattice contributes to the macroscopic polarization as $\vec{P} = -ne\vec{E}$. Substituting this polarization into Eq.2.7 we get

$$\vec{D} = \varepsilon_0\left(1 - \frac{\omega_p^2}{\omega^2 - i\,\gamma\omega}\right)\vec{E} \tag{2.17}$$

where $\omega_p^2 = \frac{ne^2}{\varepsilon_0 m^*}$ is the plasma frequency, given by the electron density n, the electron charge e, the electric vacuum permittivity, and the electron effective mass in the material, m^*.

Comparing Eq. 2.17 to Eq. 2.8, the dielectric function under this approximation can be identified as

$$\varepsilon(\omega) = 1 - \frac{\omega_p^2}{\omega^2 - i\,\gamma\omega} \tag{2.18}$$

Where real and imaginary parts of the complex dielectric function $\varepsilon(\omega) = \varepsilon_1(\omega) + i\,\varepsilon_2(\omega)$ are

$$\varepsilon_1(\omega) = 1 - \frac{\omega_p^2}{\gamma^2 + \omega^2} \tag{2.19}$$

$$\varepsilon_2(\omega) = \frac{\omega_p^2}{\gamma\omega(1 + \omega^2/\gamma^2)} \tag{2.20}$$

We will discuss the validity of this model for two different regimes with respect to the collision frequency, limiting ourselves to frequencies $\omega < \omega_p$,

where metals can still be considered so.

For large frequencies, $\omega > \gamma$ (still below ω_p), the damping term in Eq.2.18 is negligible, as a result we are left with the dielectric function of undamped free electrons

$$\varepsilon(\omega) = 1 - \frac{\omega_p^2}{\omega^2} \tag{2.21}$$

In Figure 2.1 we can see that, as the real part of ε approaches 0 (that is, for $\omega \approx \omega_p$), the experimental data for both Au and Ag heavily deviate from the predictions of the Drude model. Note that the dielectric function of noble metals in this frequency range is totally dominated by interband transitions. This deviation is especially relevant considering the use of these metals in plasmonics. Both noble metals present a region of low losses, for which ε_2 is close to zero. Although Ag may a priori be preferable for visible light applications due to the lower ohmic loss and a higher onset of interband transitions [79], Au is favored in the near-infrared region and is chemically more stable (less prone to oxidation), facilitating its use in plasmonic devices.

For small frequencies, $\omega < \gamma$, the damping term is non-negligible. In fact, $\varepsilon_2 >> \varepsilon_1$. This means that, at low frequencies, fields do not propagate through the metals, but rather their amplitude decays exponentially as they penetrate into the metal.

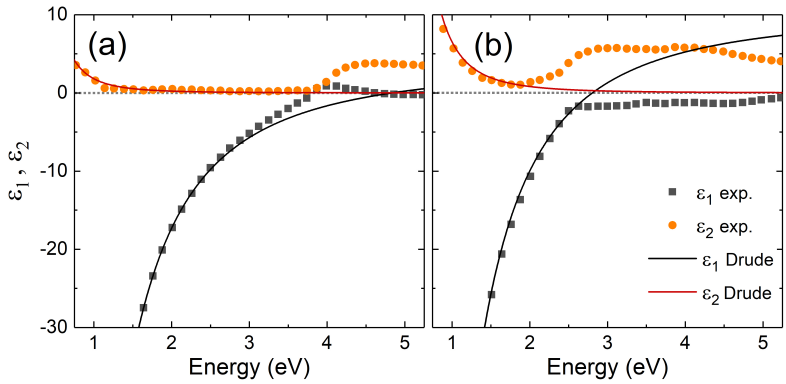

Fig. 2.1: Real and imaginary parts of the dielectric function of the free electron gas (solid line) fitted to experimental values from [80] for (a) Ag and (b) Au. Note that the model has a limited validity at higher frequencies.

2.3 Optical response of the free electron gas

We now turn our attention to the regime above the plasma frequency, $\omega > \omega_p$. Within this frequency region, the free electron model presents a transparency region, and electromagnetic waves can propagate freely through the material.
To accurately describe this phenomenon, we shall find traveling wave solutions to Maxwell equations in these conditions. Hence, in the absence of external charges and currents, Eqs. 2.3 and 2.4 can be combined to construct the wave equation

$$\vec{\nabla} \times \vec{\nabla} \times \vec{E} = -\mu_0 \frac{\partial^2 \vec{D}}{\partial t^2} \tag{2.22}$$

$$\vec{K}(\vec{K} \cdot \vec{E}) - K^2 \vec{E} = -\varepsilon(\vec{K}, \omega) \frac{\omega^2}{c^2} \vec{E} \tag{2.23}$$

in the time and frequency domain, respectively. We have defined $c = 1/\sqrt{\mu_0 \varepsilon_0}$ as the speed of light in vacuum. Two types of propagating waves can be identified, transverse and longitudinal waves.

For transverse waves $\vec{K} \cdot \vec{E} = 0$, giving the following dispersion relation

$$K^2 = \varepsilon(\vec{K}, \omega) \frac{\omega^2}{c^2} \tag{2.24}$$

On the other hand, for longitudinal waves the condition is simply that

$$\varepsilon(\vec{K}, \omega) = 0 \tag{2.25}$$

showing that longitudinal oscillations can only arise at zeros of the dielectric function.

Before exploring traveling transverse waves in more detail, we will examine the latter type of solution to the wave equations. For longitudinal oscillations under the small damping limit, Eq. 2.25 indicates that $\omega = \omega_p$. For $\varepsilon = 0$, combining Eqs. 2.7 and 2.8, we find that $\vec{P} = -\vec{E}/\varepsilon_0$. Therefore, at the plasma frequency, the material exhibits a purely depolarization field.

Throughout all the above derivation, the motion of the electrons has been

considered to be in phase, hence, this solution can be considered as a collective longitudinal oscillation of the electrons in the material. Within this framework, the electrons will collectively be displaced along a certain distance, creating a charge excess in the boundaries of the material, as shown in Fig. 2.2a. This will create an electric field, acting as a restoring force on the electrons, which in turn gives rise to a coherent collective oscillation of the electrons that resembles phonon vibrations in crystals. In this context, ω_p is the natural resonance frequency of the electron cloud in a material. The quanta of this oscillation are called *volume plasmons*. The longitudinal character of these oscillations precludes their coupling with electromagnetic waves, which means that they must often be excited by particle collisions. Notably, the early observations of such resonances were mainly conducted through electron energy loss spectroscopy experiments [81].

As for the transverse waves, described by Eq. 2.24, in the small damping limit the dispersion relation takes the form

$$\omega^2 = \omega_p^2 + K^2 c^2. \tag{2.26}$$

As shown in Fig. 2.2b, for $\omega > \omega_p$ there is always a solution to the wave equation with the form of a transverse electromagnetic wave propagating in the material with a velocity equal to the slope of the dispersion relation ($v = d\omega/dK$). These solutions will be thoroughly discussed in the following sections.

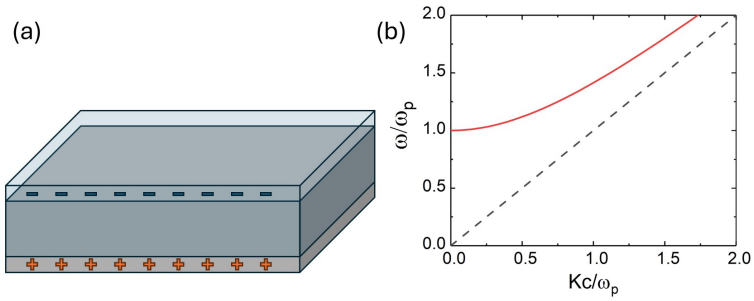

Fig. 2.2: (a)Schematic representation of the displacement of the electron gas for a volume plasmon in a finite metallic slab.(b)Dispersion relation of the free electron gas (solid red) and the photon in free space(dashed black).

Surface plasmon polaritons

3

Volume plasmons are a simple example of collective oscillations of the electron gas in a metal. However, there are other collective excitations of the electrons in a metal that can also take place. In particular those taking place at the interface between the metal and a surrounding dielectric medium, which are known as *surface plasmons*. In this section, we will briefly discuss the coupled oscillations of the electrons in the metal and the propagating electromagnetic wave at its surface, known as Surface Plasmon Polaritons, SPP.

In the absence of external charge and current sources we can rewrite the wave equation (Eq. 2.22) considering that in this case, $\vec{\nabla} \cdot \vec{D} = 0$, and ε is constant in space. We get to the central equation in electromagnetic wave theory, known as the Helmholtz equation

$$\nabla^2 \vec{E} - \frac{\varepsilon}{c^2} \frac{\partial^2 \vec{E}}{\partial t^2} = 0 \tag{3.1}$$

This equation can only be solved in regions of constant ε and then adapted through the appropriate boundary conditions.

In order to understand the generation of SPP, let us divide space into two regions. The first one, for $z > 0$, dielectric, and a second one, for $z < 0$, metallic, with dielectric constants ε_2 and ε_1, respectively, see Fig.3.1a. The insulator and metallic character of both materials require that $Re[\varepsilon_1] > 0$ and $Re[\varepsilon_2] < 0$. Note that in this section the suffixes 1 and 2 are used to denote the dielectric function of the two media involved in the calculations. In general ε_i will refer to the complex dielectric function as a whole, although, for the sake of simplicity, a negligible imaginary part will occasionally be assumed.

If we consider a wave propagating along the interface between these two

materials, the x direction, for instance. We can assume an harmonic dependence of the electric field of the form $\vec{E}(\vec{r},t) = \vec{E}(z)e^{i\beta x}e^{-i\omega t}$, where $\beta = K_x$ is a complex parameter corresponding to the wavevector in the propagation direction of the wave. Considering the symmetries of the problem, Eq. 3.1 can be written as follows.

$$\frac{\partial^2 \vec{E}(z)}{\partial z^2} + (K_0^2\varepsilon - \beta^2)\vec{E} = 0 \tag{3.2}$$

A similar procedure would yield an analogous equation for the magnetic field $\vec{H}$, thereby providing a priori two types of possible solutions for this problem. These two sets of equations correspond to two orthogonal polarizations of the electromagnetic wave, called TE and TM, characterized by the fact that the only non-zero components of the electric or magnetic fields are those along the direction transverse to the boundary plane.
It can be shown [74] that the excitation of SPP is only possible for the TM solutions. Finally, the continuity requirements on $\vec{H}_y$ and $\vec{D}_z$ lead to

$$\beta = K_0\sqrt{\frac{\varepsilon_1\varepsilon_2}{\varepsilon_1+\varepsilon_2}} \tag{3.3}$$

This expression holds for metals with and without attenuation, i.e. for real and complex ε_2. In Fig. 3.1b, the corresponding dispersion relation for the undamped limit is displayed. We recover the results from the previous section, for the propagation of electromagnetic waves in the transparency regime ($\omega > \omega_p$), but now the diagram presents a new branch corresponding to the excitation of SPP. There is a forbidden band for $\omega_{sp} < \omega < \omega_p$ that for metals with $\mathrm{Im}[\varepsilon_1] > 0$ will host lossy modes as well as the rest of the excitations. It is worth noting that the SPP curve falls under the line corresponding to the propagation of light in free space, the so-called *light line*, thus, a photon in free space will never be able to satisfy simultaneously the frequency and wavevector conditions necessary to excite a SPP. In addition, unlike the volume plasmons, whose excitation conditions solely rely on the metallic slab, SPP inherently depend on both materials, since they originate at the interface. Thus, the phase matching of an incoming photon has to be carried out through more complex strategies such as grating [82], prism coupling [83], or excitation via near field [84]. Despite the apparent difficulties to excite them, SPP have been extensively studied for their possibilities in unveiling new light matter interactions in the nanometer scale [35].

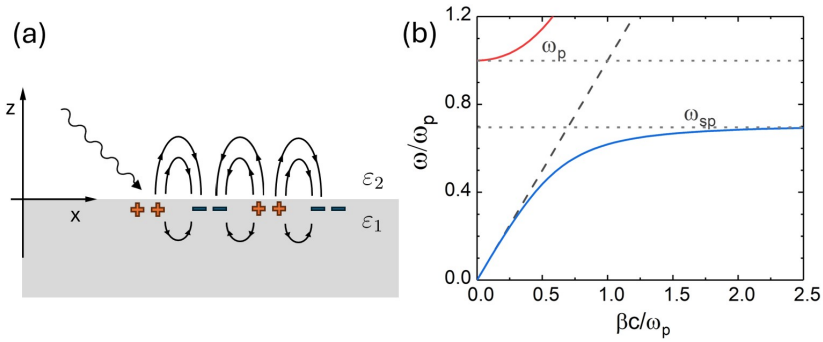

Fig. 3.1: (a)Schematic representation of a SPP. (b)Dispersion relation of SPP in the free electron gas (solid blue) and the photon in free space(dashed black). This model also includes the propagation of electromagnetic waves into the material in the transparency regime (solid red).

At low wavevectors, typically within the infrared or lower frequency ranges, the waves propagate over multiple wavelengths due to their propagation constant being close to that of the light line. In this regime, the SPP exhibit characteristics analogous to light propagating at grazing incidence. In contrast, for large wavevectors, these SPP attain a maximum frequency value known as the surface plasmon frequency. In the undamped free electron gas model, this frequency is simply

$$\omega_{sp} = \frac{\omega_p}{\sqrt{1+\varepsilon_2}} \tag{3.4}$$

As β approaches infinity, the slope of the dispersion relation, as shown in Fig. 3.1b, tends to be zero, leading to a null group velocity. In this large wavevector limit, a stationary oscillation with frequency ω_{sp} is formed, which is known as a surface plasmon.

Localized surface plasmons

4

Having introduced SPP in the previous section, which are propagating oscillations of the electron plasma coupled to a traveling electromagnetic wave at the metal-dielectric interface, we now turn the focus upon stationary excitations of electrons in metallic nanostructures, referred to as localized surface plasmons, LSP. The non-propagating nature of LSP arises from the fact that these excitations occur exclusively within nanostructures. The finite dimensions of a nanostructure supporting such oscillations will induce a restoring force on the electrons driven by an electromagnetic wave, similarly to the case of volume plasmons. However, unlike volume plasmons, the excitation of LSP modes is possible through direct illumination at the suitable frequency. The typical energy of LSP in noble metals falls within the optical range, leading to numerous applications based on this phenomenon. Nanostructures of these metals, with dimensions ranging from tens to hundreds of nanometers, are ideal for exciting LSP and can be utilized for enhanced emission and sub-wavelength confinement, among other applications.

4.1 The quasi-static approximation

Let us consider the interaction of a spherical homogeneous particle of radius a with an external electromagnetic field. Throughout most of this section we will consider that the particle is much smaller than the wavelength of the electromagnetic wave ($a << \lambda_0$). This is called the quasi-static approximation and will allow us to consider the electric field to be uniform in the whole volume of the particle. Once the problem is solved for the electrostatic case, the harmonic time dependence can be added to the solution.

Without losing generality, we can consider that the particle is placed at the origin of the coordinate system in a uniform electric field along the z

direction, $\vec{E} = E_0\hat{z}$. The particle is surrounded by a medium of dielectric constant ε_m, and its response is described by the complex dielectric constant $\varepsilon_m(\omega)$.

In the electrostatic approach, the response of the sphere can be found by solving the Laplace equation $\nabla^2\phi = 0$ for the potential, from which we will calculate the electric field using $\vec{E} = -\vec{\nabla}\phi$. Using Legendre's polynomials, together with the appropriate boundary conditions at the surface of the sphere, we get to the following solutions inside and outside of the sphere, respectively [85]

$$\phi_{in} = -\frac{3\varepsilon_m}{\varepsilon + 2\varepsilon_m} E_0 r\cos(\theta) \tag{4.1}$$

$$\phi_{out} = -E_0 r\cos(\theta) + \frac{\varepsilon - \varepsilon_m}{\varepsilon + 2\varepsilon_m} E_0 a^3 \frac{\cos(\theta)}{r^2}, \tag{4.2}$$

where θ is the angle between $\vec{r}$ (position of the point where ϕ is computed) and the z axis, taking the center of the nanoparticle as the origin.

It is easy to infer that the potential in the outer region is directly the superposition of the external driving field and the field created by an electric dipole. This is made evident if we rewrite Eq. 4.2 in terms of the dipole moment $\vec{p}$

$$\phi_{out} = -E_0 r cos(\theta) + \frac{\vec{p}\cdot\vec{r}}{4\pi\varepsilon_0\varepsilon_m r^3}, \tag{4.3}$$

where the dipole moment is defined as

$$\vec{p} = 4\pi\varepsilon_0\varepsilon_m a^3 \frac{\varepsilon - \varepsilon_m}{\varepsilon + 2\varepsilon_m}\vec{E}_0. \tag{4.4}$$

Finally, we can rewrite the dipole moment as $\vec{p} = \varepsilon_0\varepsilon_m\alpha\vec{E}_0$, since it is is proportional to the applied field. From this definition, we get the expression for the polarizability α of a spherical metallic particle smaller than the wavelength of the exciting electromagnetic wave[1]

$$\alpha = 4\pi a^3 \frac{\varepsilon - \varepsilon_m}{\varepsilon + 2\varepsilon_m}. \tag{4.5}$$

[1] This expression can be generalized[86]

$$\alpha = \frac{4}{3}\pi a^3(1+\kappa)\frac{\varepsilon - \varepsilon_m}{\varepsilon + \kappa\varepsilon_m}$$

where κ is a geometric factor that captures the predisposition of the structure to be polarized. For the case of a sphere $\kappa = 2$, which gets us back to Eq. 4.5

Fig. 4.1 illustrates both the absolute value and the real and imaginary components of the polarizability. This complex quantity will diverge when the denominator approaches zero. For instance, in the case of Au, this divergence occurs at approximately 2.5 eV. Considering the surrounding medium as a dielectric with negligible absorption ($\mathrm{Im}[\varepsilon_m] \approx 0$), the resonant condition for α can be written, in general, as

$$\mathrm{Re}[\varepsilon(\omega)] = -2\varepsilon_m. \tag{4.6}$$

For a spherical nanoparticle with a Drude dielectric function, surrounded by air, i.e. following Eq. 2.18, the resonance in the polarizability will happen at a frequency $\omega_0 = \omega_p/\sqrt{3}$. Note the strong dependence of this resonant frequency on ε_m.

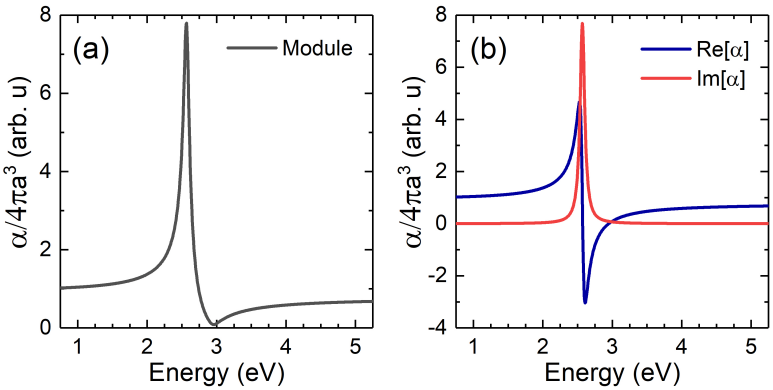

Fig. 4.1: (a) Module and (b) real and imaginary part of the polarizability of a spherical nanoparticle with ϵ obtained from a Drude fit for Au in Fig. 2.1.

In order to fully comprehend the utility of the expressions developed thus far, we will move beyond the electrostatic framework to provide a complete description of the response of a sub-wavelength metallic particle subjected to excitation by an electromagnetic wave. Assuming a harmonic time dependence $\vec{E}(\vec{r},t) = \vec{E}_0 e^{-i\omega t}$, the induced dipole moment will be $\vec{p} = \varepsilon_0 \varepsilon_m \alpha \vec{E}_0 e^{-i\omega t}$. In this new scenario, it is important to note that an oscillating dipole will radiate into the medium. To describe the response of an oscillating electric dipole, let us write the scattering and absorption

cross-sections as

$$C_{scat} = \frac{K^4}{6\pi}|\alpha|^2 = \frac{8\pi}{3}K^4 a^6 \left|\frac{\varepsilon - \varepsilon_m}{\varepsilon + 2\varepsilon_m}\right|^2 \tag{4.7}$$

$$C_{abs} = KIm[\alpha] = 4\pi K a^3 Im\left[\frac{\varepsilon - \varepsilon_m}{\varepsilon + 2\varepsilon_m}\right]. \tag{4.8}$$

Details on the derivation of these expressions can be found in [87].

The first interesting feature to point out is that the efficiency of absorption scales as a^3 while in the case of scattering, the dependence goes as a^6. Hence, for small particles, absorption serves as the principal mechanism of interaction with electromagnetic radiation. Conversely, for larger particles, scattering will increasingly prevail.

Finally, it is useful to define a third quantity that characterizes the total interaction efficiency of a system with electromagnetic radiation. This interaction occurs through two mechanisms: a change in the wave's energy (absorption) and a change in its momentum (scattering). The extinction is defined as the sum of both contributions, with the extinction cross-section expressed as follows

$$C_{ext} = C_{scat} + C_{abs}. \tag{4.9}$$

An important side note is that the expressions derived in Eqs.4.7 and 4.8 are not exclusive for metallic nanoparticles. If no specific dependence of ε is assumed, they can also be valid for dielectric nanoparticles. However, the absorption in dielectric nanoparticles, even for small sizes, will be strongly hindered by the small imaginary part of the dielectric function. For this reason, in most cases, dielectric nanoparticles will be assumed to only interact with electromagnetic waves through scattering.

Thus far in this section, we have discussed the physics behind the excitation of LSP in metallic nanostructures. Nevertheless, the assumptions adopted throughout this discussion can readily be adapted to the case of dielectric inclusions within metals, such as nanoholes or nanocavities.

We will begin our treatment of such systems with a spherical nanocavity of radius $a << \lambda_0$. The dielectric functions in this case will be ε_m for the

nanocavity, and $\varepsilon(\omega)$ for the surrounding metal. This nanostructure can sustain a plasmonic resonance, similar to that of a metallic sphere in a dielectric medium. However, in this case, the resulting dipole will be aligned antiparallel to the driving field, as evidenced by its polarizability

$$\alpha = 4\pi a^3 \frac{\varepsilon_m - \varepsilon}{\varepsilon_m + 2\varepsilon}. \tag{4.10}$$

Note that the only differences with Eq. 4.5 arises from the substitutions $\varepsilon \rightarrow \varepsilon_m$ and $\varepsilon_m \rightarrow \varepsilon$. This new polarizability leads to the resonant condition

$$Re[\varepsilon(\omega)] = -\frac{1}{2}\varepsilon_m. \tag{4.11}$$

Similarly to Eq. 4.6 this resonant condition is valid only in the quasi-static regime, meaning that the nanocavity must be significantly smaller than the wavelength of the exciting radiation. Non-spherical cavities will present a polarizability with slight variations from Eq. 4.10. However, the resonant condition will remain unaltered as it does not depend on geometric parameters of the system.

It is important to note that larger particles, for which the quasi-static approximation is no longer applicable, will exhibit different resonance conditions. Generally, these conditions will be significantly influenced by the size of the nanostructure and other geometric factors.

4.2 Beyond the quasi-static approximation: Mie theory

We have seen that, by modelling a small particle as a point dipole, a resonant field enhancement is predicted by considering the relation between the polarizability of the particle and its scattering and absorption cross sections. This model successfully describes particles up to 100 nm illuminated by light in the optical regime. However, an accurate description of larger particles requires a model that can appropriately describe the phase changes of the driving field inside the particle. In addition to variations in size, an increase in the aspect ratio leads to greater anisotropy in the particle, resulting in the emergence of additional resonant modes. Consequently, a more complex

description of the system becomes necessary, as illustrated schematically in Fig. 4.2.

In 1908, Mie developed a complete description of the scattering and absorption of a spherical scatterer as an expansion of the internal and external fields into normal modes described by vector harmonics[88]. This is known as Mie theory.

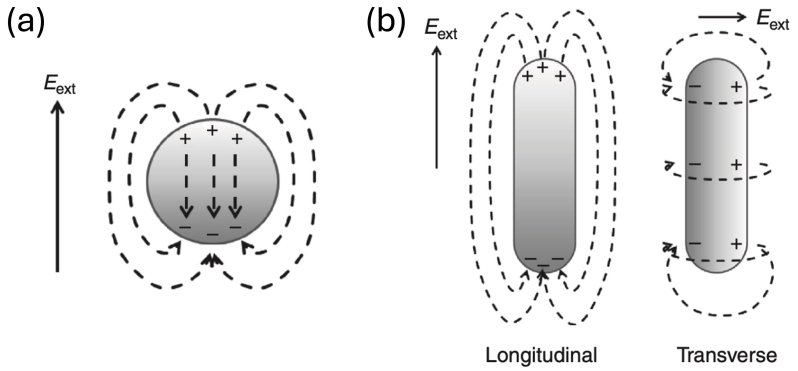

Fig. 4.2: Schematic representations of the electric field and charge distributions for (a) a spherical nanoparticle and (b) for a nanorod. Note that for the case of a nanorod, two possible dipole excitations are possible. Adapted from [89].

It is important to remark that the results of the quasi-static approximation can be derived from Mie theory by considering only the first terms of the Mie expansion.

The primary objective of this section is to analyze the spectral shift and broadening of LSP in nanoparticles as their size increases. To achieve this, we will consider the first TM mode from Mie theory and express the polarizability of a sphere with volume V as follows [90]

$$\alpha_{sphere} = \frac{1 - (\frac{1}{10})(\varepsilon + \varepsilon_m)x^2 + O(x^4)}{(\frac{1}{3} + \frac{\varepsilon_m}{\varepsilon - \varepsilon_m}) - \frac{1}{30}(\varepsilon + 10\varepsilon_m)x^2 - i\frac{4\pi^2\varepsilon_m^{3/2}V}{3\lambda_0} + O(x^4)}V, \quad (4.12)$$

where $x = \frac{\pi a}{\lambda_0}$, called the size parameter, describes the ratio between the radius of the sphere and the wavelength of the driving electromagnetic field.

In this section we will restrict our discussion to large particles.
In this regime, the size of the nanostructures is such that the exciting electric field cannot be regarded as constant throughout the entire volume of the particle with a straightforward harmonic time dependence. Instead, the phase of the electric field will exhibit spatial variation across the system. The spatially varying phase of the external electric field can influence the behavior of LSP and their interactions with electromagnetic radiation, leading to what are known as retardation effects. These effects become more pronounced as the size of the nanostructure increases.

A comparison between Eqs. 4.5 and 4.12 reveals several additional terms in the numerator and denominator, compared to the quasi-static regime. For Drude and noble metals, the quadratic terms in numerator and denominator lead to an overall shift to lower energies as the particle size increases (and the size parameters increases as well). This can be intuitively understood by considering that, as the particles get larger, the distance between the charges accumulated in opposite regions of the particle also increases. Therefore, the restoring force acting on the electrons diminishes and the frequency of the resonance is lowered. This is experimentally shown in Fig. 4.3. The imaginary term in the denominator accounts for radiation damping, which refers to the decay of coherently oscillating electrons into photons. In other words, this process effectively transforms the energy of the oscillating electrons into radiation that exits the system. This is the main mechanism behind the decay of the strength of the dipole resonance as the particle size increases, and it is closely associated with the spectral broadening of the LSP.

Eq. 4.12 describes the polarizability of a spherical metallic nanoparticle that exceeds the size limit of the quasi-static approximation. Using Mie's theory, we have shown that a relation between the polarizability of the nanoparticle and its size can be found. Likewise, the shape of the nanostructure will also play a key role in determining its polarizability. A change in the shape of the nanoparticle will alter the significance of different multipoles within Mie's expansion, thereby modifying the expression for the polarizability. This phenomenon has been experimentally demonstrated in [92, 93, 94]. Fig. 4.4 shows a representative example of a simple spectral shift due to shape effects. Nonetheless, the differences in spectral response based on nanoparticle shape can manifest an arbitrarily high level of complexity.

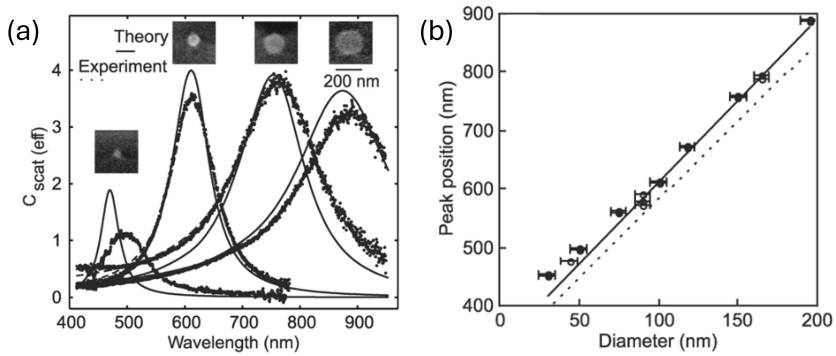

Fig. 4.3: (a) Scattering spectra and corresponding SEM images of single isolated cylindrical particles of different diameters (50, 100, 150 and 200 nm). The solid lines show scattering spectra calculated theoretically. The experimental and theoretical spectra have been normalized to the geometrical cross section. (b) Experimental LSP position vs particle diameter as determined by SEM analysis. The solid and dashed lines correspond to calculations considering particles of 25 and 30 nm in thickness, respectively. Adapted from [91].

The experimental excitation and observation of LSP, can be carried out using a wide variety of techniques. One of the most convenient features of LSP is their ability to directly excite electromagnetic waves, sallowing for their observation through optical measurements of reflection or transmission in samples that support LSP. For instance, FTIR spectroscopy has been employed throughout this thesis to characterize LSPs in the far-field regime. Additionally, excitation can also be induced through the impact of charged particles, as demonstrated in EELS experiments. This method offers the added benefit of enabling resonance mapping at the nanoscale.

4.3 Coupled localized surface plasmon resonances

In the preceding sections, we identified the characteristic frequency for LSP in small nanoparticles (Eq. 4.4), and showed that this frequency can modified through changes in the size and shape of the nanoparticle. If such particle is placed in close proximity of other nanostructures holding LSP, the dipole induced in the second nanostructure will alter the effective electric

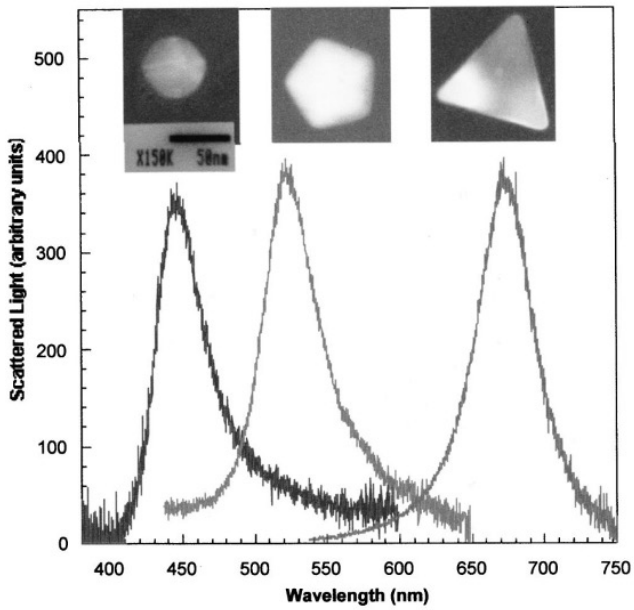

Fig. 4.4: Typical optical spectroscopy measurements of individual Ag nanoparticles. The figure shows the spectra of individual nanoparticles with different shapes, and their high-resolution TEM images. Reproduced from [93].

field acting on the particle, thus, shifting the resonant frequency.

Within this framework, the LSP of the two interacting particles will couple, resulting in the emergence of resonances that are not achievable for a single particle. In this context, a proper description of the resonances in the coupled system can no longer be given as a combination of resonant modes in a single element; instead the couple modes must be regarded as the fundamental basis of this new system. This concept is visually depicted in Fig. 4.5, where it is illustrated that within the model of coupled dipoles (analogous to the coupled harmonic oscillators), each pair of nanorods can exhibit two types of excitations: one in which the dipoles oscillate in phase and another in which they oscillate out-of-phase.

It is worth noting that among all the new resonant modes available, not all of them are efficiently excited by electromagnetic radiation, since the coupling with radiation is governed by the resulting dipole moment for each resonance. If the charge distribution of a given resonance has no net dipole moment, it can be considered optically dark, which means that it will not

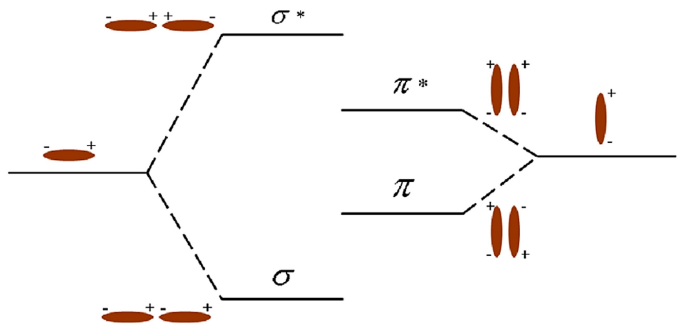

Fig. 4.5: Hibridization model of LSP modes in coupled nanorods. Analogously to the case of molecular orbitals, in phase and out-of-phase dipoles are formed in the end-to end situation (σ and σ^*) and in the side by side configuration (π and π^*). Note that the modes labeled as σ^* and π present no net dipole moment, hence, they are optically dark. Reproduced from [97].

be easily excited by light. However, dark modes can normally be excited by breaking a symmetry of the system. Changing the geometry or simply varying the incidence angle of the exciting radiation is enough to break the *dark* nature of the mode. In this context, these modes are called *subradiant modes* due to their low net dipole moment [95, 96]. Consequently, the excitation of emergent resonances in a coupled system, characterized by a new spectral position, is frequently observed experimentally as a shift in the peak position rather than as peak splitting, as the energy level diagram in Fig. 4.5 might imply. While spectral splitting does occur, it is primarily the energy modes associated with a non-zero net dipole moment (optically bright modes) that are significantly populated.

Considering the excitations of a pair of nanoparticles, similarly to coupled harmonic oscillators, a change in the coupling strength will affect the resonant frequencies of the coupled modes. The strength of the coupling can depend on several parameters such as the shape of the nanoparticle, the metal used, or the dielectric surrounding medium. This is exemplified in Fig. 4.6 with experimental data corresponding to a simple system of two neighboring Au disks.

Among the many factors controlling the spectral position of coupled LSP, probably the interparticle distance s is one of the most relevant. It is also experimentally easy to control and measure it, so a study of the coupling

strength in terms of the interparticle distance offers a remarkable opportunity to derive quantitative conclusions.

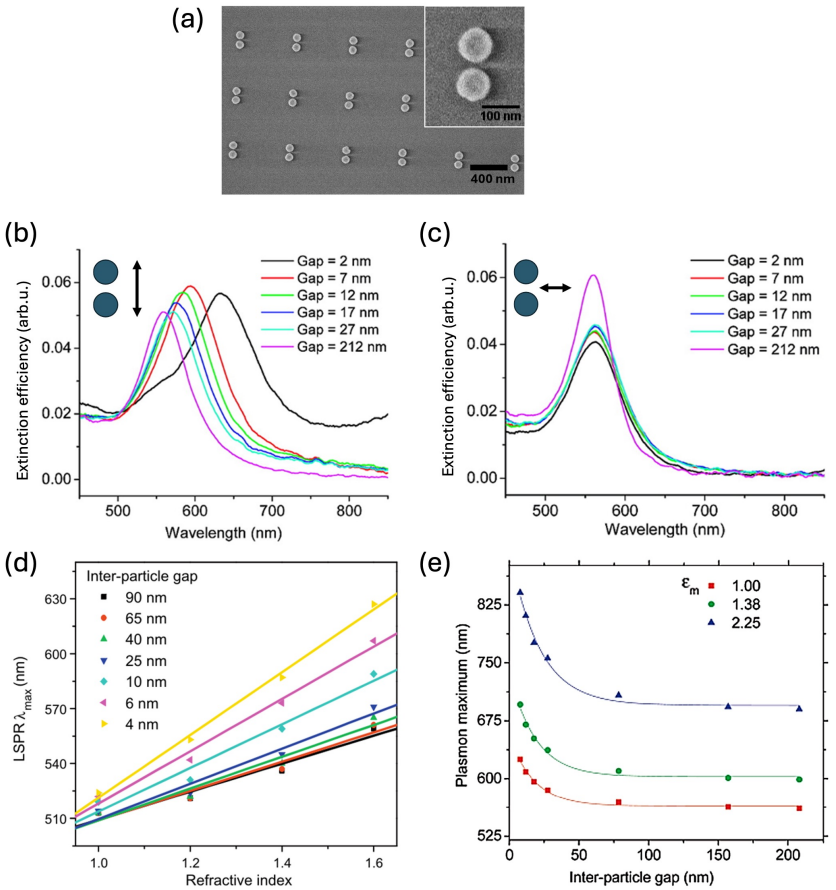

Fig. 4.6: (a) Scanning electron microscopy SEM image of pairs of Au nanodiscs with an inter-particle gap of 12 nm. (b)(c) Experimental absorption spectra for nanopairs excited by light polarized in the directions parallel and perpendicular to the nanopair axis for different gap values. (d)(e)Simulations of the position of the LSP as a function of the nanopair gap and the refractive index of the surrounding medium. Adapted from [86, 98].

For this parameter, an approximate relation can be found [98]:

$$\frac{\Delta\lambda}{\lambda_0} \approx ke^{-s/0.2D}, \tag{4.13}$$

where s is the surface-to-surface distance between particles, D is the diameter of the particle, k is a parameter that will depend on the system and can be determined experimentally, λ_0 is the wavelength of the resonance for the non-interacting case, and $\Delta\lambda$ is the shift of the resonance position.

Remarkably, the functional dependence observed exhibits a significant degree of universality, as it does not impose any constraints on the specific details of the interacting nanoparticles, such as their metallic composition or the properties of the surrounding medium. All these parameters are captured within the coefficient k, which will differ for each system. However, in all cases, the exponential dependence with $-s/(0.2D)$ is preserved.

The origin of the general distance-decay behavior described in Eq. 4.13 can be attributed to two key factors that influence the strength of inter-particle coupling: the polarizability of the particles and the distance between them. The first parameter scales as D^3, where D is a characteristic length of the particle (see Eq. 4.5 and [98]), while the electric field created by a dipole in the near field decays as r^{-3}. Summarizing, the strength of the coupling, determined by $\frac{\Delta\lambda}{\lambda_0}$, must have a functional dependence on $(r/D)^{-3}$.

A closer inspection of Fig. 4.6b and c demonstrates a distinctly different behavior of the coupled system depending on the polarization of the exciting electric field. Here, the connection between the electric field direction and the coupling strength is evident, as the orientation of the electric field dictates the direction from which each electric dipole arises in the particles, thereby affecting the angle between the electric dipole and its neighboring particle.

4.4 Surface lattice resonances

So far, we have discussed the interactions of plasmonic nanoparticles in close proximity. A thorough description of the interactions between pairs of nanoparticles has been given. The characteristic properties could be expanded to clusters of a few nanoparticles. However, a fundamentally different model is required for large arrays of nanostructures due to the long

distances among different elements compared to the excitation wavelength. Within this framework, the plasmonic nanoparticles will still be treated as dipoles. Nevertheless, they will now be coupled through far-field mechanisms, a phenomenon known as diffractive coupling [99, 100]. Specifically, under particular excitation conditions, additional plasmonic modes emerge in the system, called Surface Lattice Resonances (SLR). These are collective and coherent excitations of all the nanoelements in an array that typically yield very intense and spectrally narrow resonances, offering an additional degree of freedom to control the plasmonic response of a nanostructure.

For the sake of simplicity, let us take an ordered array of N metallic nanoparticles whose polarization can be considered to be an electric dipole $\vec{p}_i = \varepsilon_0 \varepsilon_m \alpha_i \vec{E}_i$. The electric field acting on a particle located at the position $\vec{r}_i$ will be the sum of the incident electric field and the total electric field created by the induced dipoles in the remaining $N-1$ nanoparticles within the array. For a fixed wavelength this yields

$$\vec{E}_i = \vec{E}_0 e^{i\vec{k}\cdot\vec{r}_i} - \sum_{j\neq i} A_{ij}\vec{p}_j, \tag{4.14}$$

where $\vec{E}_0$ and $\vec{k}$ are the amplitude and the wavevector of the incident wave, respectively. A_{ij} is the dipole interaction matrix (the negative sign in the previous equation is simply due to a sign convention), describing the effect of the whole dipole array. This term is explicitly written as

$$A_{ij}\vec{p}_j = e^{ikr_{ij}}\left[k^2 \frac{\vec{r}_{ij}\times(\vec{r}_{ij}\times\vec{p}_j)}{r_{ij}^3} + (1-ikr_{ij})\frac{r_{ij}^2\vec{p}_{ij} - 3\vec{r}_{ij}(\vec{r}_{ij}\cdot\vec{p}_j)}{r_{ij}^5}\right], \tag{4.15}$$

where $\vec{r}_{ij}$ measures the position of the j dipole with respect to the i position. For the particular case of an infinitely large array of particles with identical polarization α, considering the electric field acting on every particle defined by Eq. 4.14, the modulus of the total dipole moment for each particle of the array can be written as

$$P = \frac{E_0}{1/\alpha - S} \tag{4.16}$$

where S is known as the *dipole sum* and is strongly related to the dipole interaction matrix.

Moreover, under normal incident illumination, the dipole sum can be written

as follows

$$S = \sum_{j \neq i} e^{ikr_{ij}} \left[\frac{(1 - ikr_{ij}(3cos^2\theta_{ij} - 1)}{r_{ij}^3} + \frac{k^2 sin^2\theta_{ij}}{r_{ij}} \right], \tag{4.17}$$

where θ_{ij} is the angle between r_{ij} and the direction of the electric field, i.e. the polarization direction of the incident wave. In this thesis we will primarily focus on the excitation of SLR under normal incidence.

The SLR will correspond to maxima of the dipole moment of the particles of the array. Similarly to the derivation of the conditions for LSP, the collective excitation of a plasmonic lattice depends on the generation of large values of P. In other words, the condition for the generation of LSR is $\mathrm{Re}[1/\alpha] = \mathrm{Re}[S]$. Similarly to the case of LSP, the width of the resonance is determined by $\mathrm{Im}[1/\alpha - S]$.

Considering that the effective polarizability of a particle in the array is $(1/\alpha - S)^{-1}$, for the simple case of a square lattice of nanoparticles we can take a look of its extinction cross section (Eq. 4.9) and compare it with the values of the terms involved in Eq. 4.16. In Fig.4.7a we can see that SLR present a much more intense and narrow resonance, compared with the LSP of a single nanoparticle. It is clear from Fig. 4.7b that, despite the fact that the denominator in Eq. 4.16 vanishes for two wavelengths in Fig. 4.7, the intensity only becomes maximum when the real part of the denominator in Eq. 4.16 becomes zero and the imaginary part is small, since both $\mathrm{Im}[1/\alpha]$ and $\mathrm{Im}[S]$ have the same sign. This constitutes the fundamental condition for the generation of SLR. In practice, a spectral overlap between the resonant LSP frequency for the particle and the geometric diffraction condition of a given array is required. This information is contained in $1/\alpha$ and S, respectively. It should be noted that varying the angle of incidence will alter the diffraction condition, thereby changing the wavelength at which SLR can be excited.

The dipole sum reaches a sharp maximum at the wavelength that satisfies the diffraction condition because, at this precise wavelength, all dipoles in the array oscillate coherently, leading to perfectly constructive interference. To summarize, in general, for the excitation of a SLR, we will be able to distinguish three main spectral regions, as shown Fig. 4.7. The first one refers

to a broad extinction maximum corresponding to the first crossing of $\mathrm{Re}[1/\alpha]$ and $\mathrm{Re}[S]$. This peak is severely broadened due to the large imaginary part of the denominator in Eq. 4.16. The following region of interest is a narrow region of maximum transparency, marked by near zero extinction, corresponding to the geometric diffraction condition. At this wavelength, the lattice behaves similarly to a system composed entirely of passive (dielectric) particles. Subsequently, a second extinction maximum emerges. Again, we see that for this excitation the real part of the denominator in Eq. 4.16 vanishes. However, this resonance becomes both narrower and more intense, since the imaginary part of that denominator approaches zero too [101].

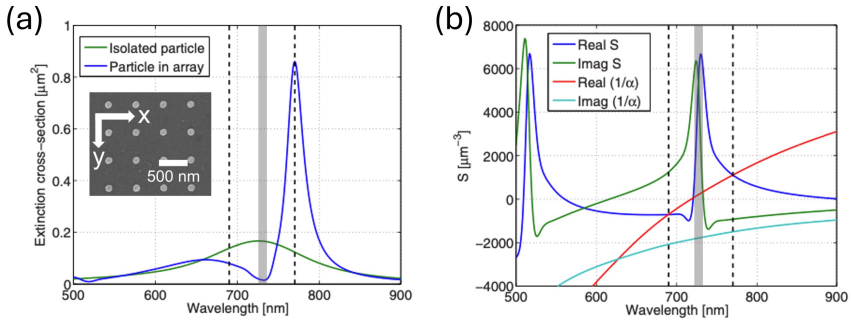

Fig. 4.7: (a) Extinction spectra for a LSP in a single nanoparticle and a SLR in an array of nanoparticles. (b) Real and imaginary parts of the inverse of the polarizability of the particles forming the array and the dipole sum. The calculations have been performed assuming a square array of Ag discs (shown in the inset) of 30 nm in thickness, 120 nm in diameter, and a periodicity of 480 nm. The array is surrounded by a dielectric material with no absorption and n=1.515. Adapted from [39].

SLR can also be studied from the perspective of Fano resonances. These, almost ubiquitous resonances arise from the spectral superposition of a narrow, well defined resonance, and a much broader resonance, considered to be a pseudo-continuum collection of states [24]. The case of a SLR can be tackled using this formalism by considering the narrow resonance to be the diffraction of the array, while the role of the broad resonance is played by the LSP of the individual nanoelements [102]. Despite the success of this approach, in this thesis, we have adopted the dipole sum formalism due to its direct derivation from basic interactions and its direct interpretation.

4.4.1 Experimental considerations

As discussed in preceding sections, there are many factors that influence the behavior of SLR, such as the size and shape of the nanoparticles that constitute the array [103], the disorder in the array [104], the angle of incidence [105], or the array geometry [39, 38]. Nevertheless, we will only briefly address a few critical factors that are important for the experimental detection of these resonances. For a more comprehensive overview, we refer the reader to the extensive reviews that can be found in the literature, such as [25, 106].

Number of scatterers in the lattice:

The size of the array has proven to be a critical factor in the excitation of SLR since the excitation of these modes relies on the coherent excitation of all the elements in the array. Given that, for the typical distances between particles in this regime (which are of the order of the wavelength), the interaction between pairs of particles is small but decays as $1/r$, the effect is only noticed when a large number of particles is involved. After a few hundreds of nanoparticles the quality of the resonance saturates to the maximum value [107, 108], see Fig. 4.8a. A similar effect can be observed for infinite arrays and finite width beams, as shown in [109]. Finally, it is important to note that the coupled dipole approximation is based on the coherent excitation of the dipoles in the array. However, experimental conditions may rely on the use of an incoherent source, i.e. a halogen lamp. The effect of the coherence of the source is studied in [110] and can be seen in Fig. 4.8b

Surrounding media:

The excitation of SLR is enhanced when the array of nanoelements is situated in a homogeneous surrounding medium. However, due to fabrication limitations, it is often the case that the substrate and superstrate surrounding the nanoparticle array do not posess matching refractive indices. The refractive index asymmetry severely hinders the excitation of SLR and can even lead to their complete destruction [111, 112], as shown in Fig. 4.9. The contrast in refractive indices and the distance to the interface between the two media are key

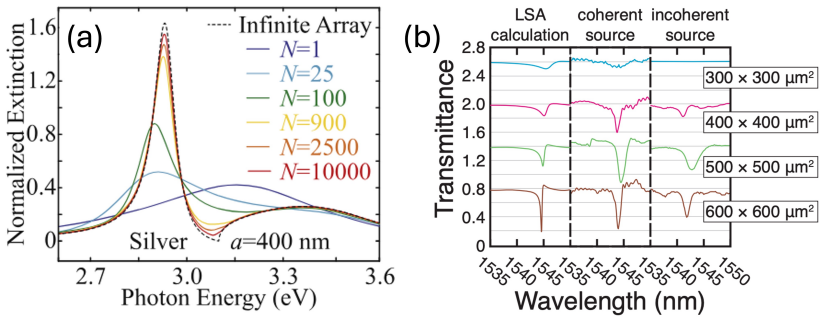

Fig. 4.8: (a) Extinction spectra shown by arrays on N particles of Ag nanodiscs of 400 nm in diameter. (b) Dipole sum calculations, and experimental detection of SLR using both coherent and incoherent illumination, for different array sizes. Adapted from [107, 110].

factors defining the quality of the SLR. This is because a change in the refractive index will create reflections at the interface. The diffracted beams, which will propagate as grazing waves along the interface, will interfere with the dipole coupling between the nanoparticles in the array. Hence, diffracted beams destroy the long-range coupling in the presence of a substrate [111].

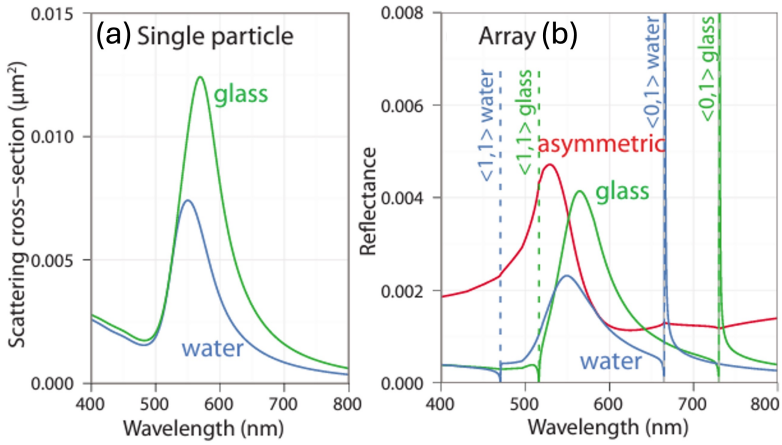

Fig. 4.9: (a) Scattering spectra for a LSP in a Au spherical nanoparticle surrounded by glass and water. (b)SLR in a square array of nanoparticles for different surrounding media. Glass, water and a hybrid medium (glass substrate and water superstrate). The nanoparticle diameter is 35 nm, and the periodicity is 500 nm. Adapted from [113].

A lot of factors can be engineered to transform the symmetry of the surrounding medium to a "soft" requirement. An array composed of larger or more complex nanoparticles will exhibit greater resilience to variations in refractive index. The increased size of the particles reduces the significance of reflected diffracted beams [114]. Furthermore, this larger size facilitates the excitation of out-of-plane resonances, which are less critically dependent on the homogeneity of the refractive index [115].

4.5 Chiral plasmonics

Chirality is the geometric property of objects that can not be superimposed onto their mirror image. This seemingly straightforward definition has profound implications across many aspects of life, especially in biochemistry. Many biomolecules, such as amino acids, DNA, and enzymes, exhibit chirality, highlighting the importance of developing methods to ascertain the chirality of molecules. Chirality is not limited to physical objects; electromagnetic fields can also possess chiral properties [56, 116]. Given that chiral characteristics can only be investigated using chiral probes, chiral electromagnetic waves serve as an ideal means to interact with physical systems through their chiral properties. The nature of this interaction will depend on the handedness of both the electromagnetic wave and the system under study. Therefore, we will begin by defining what is meant by optical chirality.

If we go back to Eq. 3.1, we can propose another solution to this equation. Considering a wave that propagates along the z direction, we now have $\vec{E}(\vec{r},t) = E_0\,\vec{J}\,e^{i(kz-\omega t)}$. Where $\vec{J}$ is the Jones vector that contains the information regarding the polarization of the wave, and E_0 is the amplitude. For linearly polarized LP light forming an angle φ with the x direction, the Jones vector is, simply

$$\vec{J}^{\varphi}_{LP} = \begin{pmatrix} \cos\,\varphi \\ \sin\,\varphi \\ 0 \end{pmatrix}. \tag{4.18}$$

Note that this solution, despite the slightly different notation, is perfectly compatible with all the previous derivations.

For CP light, the Jones vector takes the form

$$\vec{J}_{CP}^{\pm} = \frac{1}{\sqrt{2}} \begin{pmatrix} 1 \\ \pm i \\ 0 \end{pmatrix}. \tag{4.19}$$

From the Jones vector for CP light we can see that there are two orthogonal polarizations depending on whether the y component is advanced or retarded $\pi/2$ with respect to the x component. These are, usually, referred to as RCP and LCP. Note that the assignment of RCP or LCP to the "+" or "-" case is arbitrary[2].

4.5.1 A first approach to chiral plasmonics: the Born-Kuhn model

In section 2.2, we have described the response of the free electron gas in a metal as a harmonic oscillator. However, this model is fails to reproduce the behavior of chiral systems. This is because the quasi-static case is always considered in section 2.2, neglecting retardation effects. These play a key role in the chiral excitation of a system, since the handedness of both the fields and the system can only be defined taking into account the propagation of the wave and hence, its phase change. The quasi-static approximation is analogous to consider the plasmonic system to be two-dimensional, preventing any chiroptical effects from arising due to reciprocity constraints [69].

A simple approach that takes into account de-phasing effects arises from considering two coupled electrons oscillating harmonically in orthogonal directions under an external driving force. This is known as the Born-Kuhn model [117]. Considering the two oscillating electrons along x and y directions, respectively, and an electromagnetic wave propagating in the z direction; the equations of motion for a chiral system located at $\vec{r} =$

[2] For any given chiral object, two versions of the same object, so-called enantiomers, can be defined. Each one of these enantiomers has an opposite handedness. However, none of them can be assigned the right or left handed label. It is ultimately due to convention.

(x_o, y_0, z_0) are as follows

$$\frac{d^2u_x}{dt^2} + \gamma\frac{du_x}{dt} + \omega_0^2 u_x + \omega_c^2 u_y = -\frac{e}{m}E_{0\,x}e^{i(k(z_0+d/2)-\omega t)} \tag{4.20}$$

$$\frac{d^2u_y}{dt^2} + \gamma\frac{du_y}{dt} + \omega_0^2 u_y + \omega_c^2 u_x = -\frac{e}{m}E_{0\,y}e^{i(k(z_0-d/2)-\omega t)}, \tag{4.21}$$

where u_x and u_y are the displacement of the electrons oscillating along the x and y directions, respectively, m is the mass of electron, γ is the damping frequency, ω_0 is the resonant frequency of the oscillator, and ω_c acts as a coupling parameter. However, a mere coupling between the two oscillators is insufficient to create a chiral system, a phase difference in the driving field is also required. Consequently, the two coupled oscillators are not positioned at the same z-coordinate, as there must be a non-zero distance d between them, as illustrated in Fig. 4.10. This model can be directly applied to plasmonic systems, as demonstrated in [65]. Furthermore, it is applicable to more complex geometries or smaller parts of intricate systems.

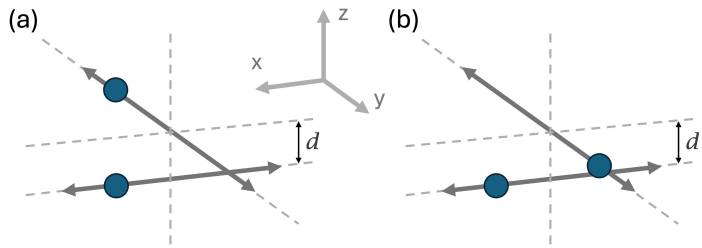

Fig. 4.10: Schematic depiction of the coupled oscillators model, in which two electrons oscillate along perpendicular directions, in planes separated by a distance d. The two orthogonal coupled modes are represented.

This description is similar to the model used to describe the coupling of harmonic oscillators (briefly discussed for the case of coupled LSP, see Fig. 4.5). This problem is solved by finding then new base of the excitations in the coupled system. Using the following change of variables

$$u_\pm = \frac{1}{\sqrt{2}}(x \pm y), \tag{4.22}$$

the system gets the following decoupled solutions

$$u_{\pm} = -\frac{e}{m}\frac{1}{(\omega_0^2 \pm \omega_c^2) - i\gamma\omega - \omega^2} E_{\pm} e^{i(kz_0 - \omega t)} \tag{4.23}$$

with

$$E_{\pm} = \frac{1}{\sqrt{2}}(E_{0\,x} e^{ikd/2} \pm E_{0\,y} e^{-ikd/2}). \tag{4.24}$$

As intended, we obtain two uncoupled oscillators with two different energies, determined by the coupling constant. These two normal modes are depicted in Fig. 4.11a and consist of in-phase and out-of-phase oscillations of the two oscillators. Note that if we assume that the system is illuminated with a wavelength such that $\lambda = 4d$

$$e^{\pm ikd/2} = e^{\pm i\pi/4} = \frac{1}{\sqrt{2}}(1 \pm i). \tag{4.25}$$

recovering the definition given in Eq. 4.19.

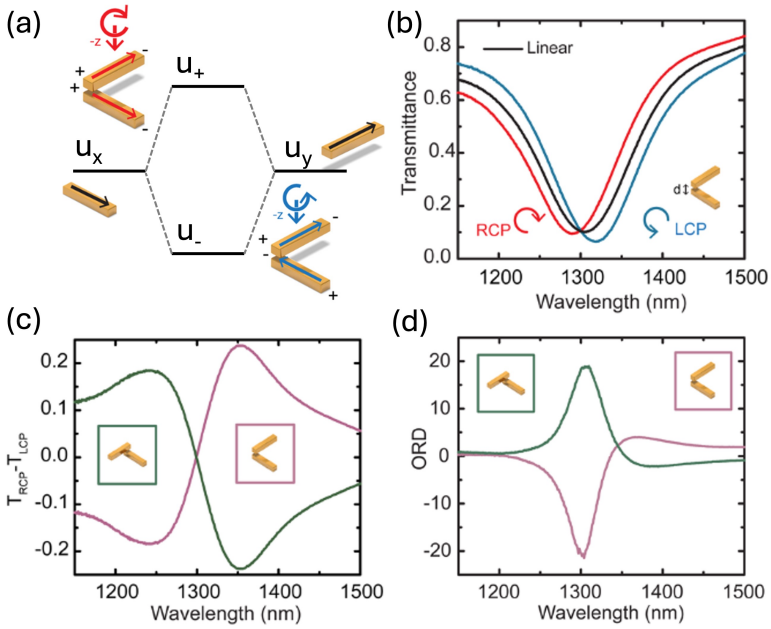

Fig. 4.11: (a) Hybridization scheme for the coupled modes. (b) Transmittance spectra for RCP, LCP, and for linear polarization for two Au nanorods at a distance of 120 nm forming an angle of 90°. (c) and (d) CD and ORD computed from the transmittance spectra in (c). Adapted from [65].

In this framework, the polarization of a chiral system can be calculated. The displacement of the electron cloud can be computed from 4.23, and after averaging for all the possible orientations, the polarization of the structure is given by the following expression for the displacement field [55]:

$$\vec{D}(\omega,\vec{r}) = \varepsilon_0 \varepsilon_{BK} \vec{E}(\omega,\vec{r}) + \varepsilon_0 \Gamma \vec{\nabla} \times \vec{E}(\omega,\vec{r}), \tag{4.26}$$

where the following definitions have been used

$$\varepsilon_{BK} = 1 - \frac{2}{3} \frac{\omega_p^2(\omega_0^2 - i\gamma\omega - \omega^2)}{(\omega_0^2 - i\gamma\omega - \omega^2)^2 - \omega_c^4} \tag{4.27}$$

$$\Gamma = -\frac{d}{3} \frac{\omega_p^2 \omega_c^2}{(\omega_0^2 - i\gamma\omega - \omega^2)^2 - \omega_c^4}. \tag{4.28}$$

This expression in the Born-Kuhn model is analogous to Eq. 2.8. Due to the averaging process that accounts for all possible orientations, this expression is also applicable to modeling the behavior of chiral media in general, extending beyond plasmonic systems.

Solving the Fresnel equation for the propagation in the z direction, we find the expression for the refractive index of the system that now will depend on the polarization of the incident light

$$n_\pm^2 = \bar{n}^2 \pm \Gamma \bar{n}, \tag{4.29}$$

where $\bar{n} = (n_+ + n_-)/2$ is the average refractive index of the material and $n_\pm$ is the refractive index of the material for the two orthogonal CP light modes (Eq. 4.24).[3] These expression gives us a relation between the Born-Kuhn model and the far-field response of the system. In particular, it allows us to understand the optical rotatory dispersion ORD and the circular dichroism CD depicted in Fig. 4.12.

Given that any polarization of the light can be expressed in the base of CP waves. In particular, linearly polarized light can be expressed as the sum of "+" and "−" modes. The polarization angle will be controlled by the phase difference between "+" and "−". From Eq. 4.29 we see that there is a

[3] It can be shown that any possible polarization state can be written as a linear combination of $+$ and $-$ modes. This yields that for the case of linearly polarized light the refractive index is simply $\bar{n}$.

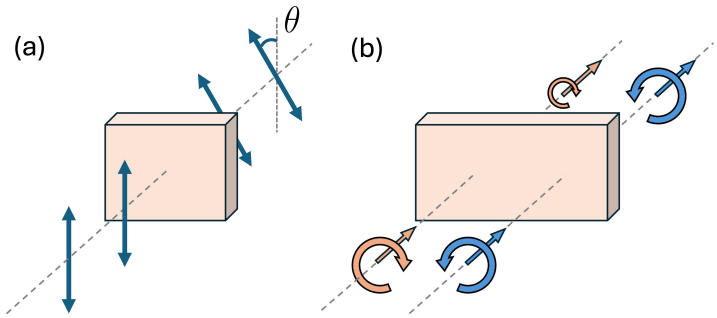

Fig. 4.12: Schematic representation of (a) ORD and (b) CD.

different complex refractive index for each of the polarizations of CP light. The consequences of this are twofold.

First, for linearly polarized light, the "+" and "−" components will experience different phase velocities. Following their interaction with the material, the relative phase between the two components of CP light will change, resulting in a modification of the polarization angle of the linearly polarized light. This effect underlies the principle of ORD. The ORD is the variation in the polarization direction that a linearly polarized wave experiences after interaction with the material. It can be computed using

$$\theta = \frac{\Delta n\, k}{2} = \frac{\omega}{2c}\mathrm{Re}[\Gamma], \tag{4.30}$$

where $\Delta n = n_+ - n_-$ is the difference between the two refractive indices. By looking at Eq. 4.29 we can see that $\Delta n = \Gamma$.

Second, a different complex refractive index implies a differential absorption for each circular polarization. Moreover, the CD is defined as the difference in absorption (or extinction) under illumination by RCP or LCP light.

$$CD = Abs_+ - Abs_- = 2\frac{\omega}{c}\mathrm{Im}[\Gamma]. \tag{4.31}$$

Note that these two quantities are related through Kramers-Kroning relations, since both reflect different aspects of the same phenomenon, thus containing the same information.

The typical spectral signature of these quantities around a chiral plasmonic

resonance is shown in Fig. 4.11. Depending on the desired application, one or the other may be emphasized.

4.5.2 Chiral response in coupled nanostructures and near-field chirality

The previous section presents a valuable model to understand the behavior of physical systems with chiroptical activity. However, it is far from a complete description. Notably, plasmonic systems are characterized by the important role played by near field, a consequence of their small length scale. To fully capture the potential of chiral plasmonic systems, we will focus on simple structures whose chiroptical activity arises from the near-field interactions within the system, often replicating properties of the molecular systems [54].

A closer examination of the system described in the previous section reveals that reducing the distance between the elements to 60 nm drastically changes the system's response, as shown in Fig. 4.13. While two peaks, corresponding to in-phase and out-of-phase resonances, are still discernible, the spectral splitting between them is significantly increased. Both RCP and LCP excite these two modes, with the main distinction being the resonance intensity. This leads to a substantial increase in chiroptical activity, as indicated by the Circular dichroism (CD) in Fig. 4.13b, which is twice that in Fig. 4.11c. The change in phase of the exciting radiation remains a crucial factor, as

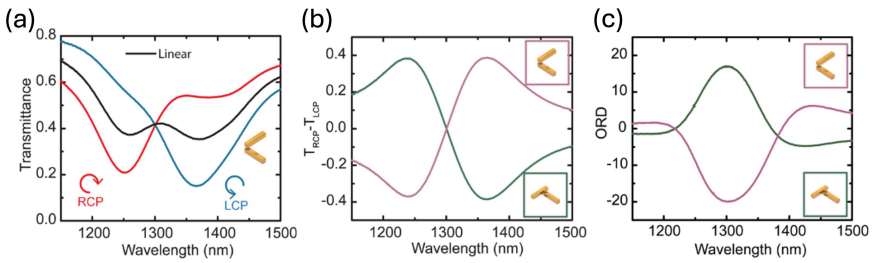

Fig. 4.13: (a) Transmittance spectra for RCP, LCP, and for linear polarization for two Au nanorods at a distance of 60 nm forming an angle of 90°. (b) and (c) CD and ORD computed from the transmittance spectra in (c). Adapted from [65].

it is the source of the differential response between RCP and LCP light. However, the phase change alone is insufficient to explain the behavior in this regime. The close proximity between the elements enables near-field coupling between the structures, resulting in a strongly interacting system. This strong interaction is responsible for the enhanced splitting between the resonances.

Numerous examples of stacked pair of nanoelements can be found in the literature, following the presented approach, from bars [62, 118], to crosses [63], to gammadions [70], among others [64, 119]. All rely on simple coupled elements whose response can be controlled by tuning the rotation angle between them. Publications III and IV, which are discussed in the subsequent sections, investigate a similar system by characterizing the coupling between the elements as a function of the system's geometrical parameters. Further details on this topic can be found in Part III.

Now that we have proven the importance of the near field in the chiral response of a plasmonic structure, it is worth to provide some insight into the particularities of these near fields. Considering harmonically oscillating electric and magnetic fields in vacuum, from Maxwell equations, we can define the local OC as follows [55, 120]

$$C = -\frac{\varepsilon_0 \omega}{2} \mathrm{Im}[\vec{E}^* \cdot \vec{B}], \tag{4.32}$$

where $\vec{E}^*$ refers to the complex conjugate of the electric field. This expression is only valid for a monochromatic electromagnetic field, but clearly exemplifies the importance of the electric and magnetic parts of the resonance, as well as the relative phase between them. From numerical simulations, one can compute this quantity for a variety of systems. One of the most popular configurations, building on the system described in the previous section, is the use of twisted stacks of plasmonic elements, as illustrated in Fig. 4.14. The highest values of OC are found in the middle plane between the structures and for the handedness opposite to that of the system. Additional details on this phenomenon can be found in Part III.

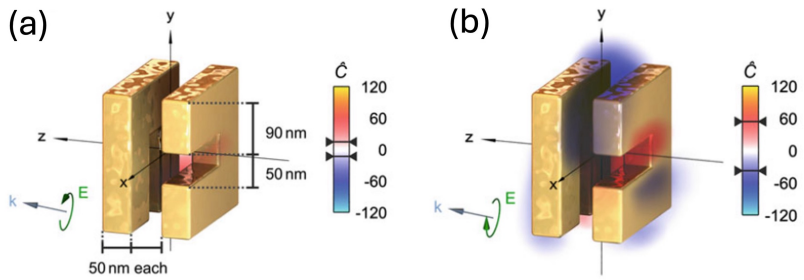

Fig. 4.14: Calculation of the OC, normalized to the exciting electric field, under (a) LCP and (b) RCP illumination at 1340 nm. Reproduced from [55].

Finite-difference time-domain simulations

5

Analytical solutions to Maxwell's equations can be obtained for simple geometries or systems with a high degree of symmetry. However, the solution for the electric and magnetic fields from Maxwell's equations for an arbitrary structure can only be obtained through numerical methods. Due to the interest of the community in modeling the response of complex structures, a lot of methods have been developed to find the solutions in 1D and 2D cases. In recent years, methods to find the solution to problems in 3D have also been developed, such as discrete dipole approximation [121, 122], finite elements method [123], boundary element method [124], and the FDTD method [125, 126]. In this section, only the latter will be discussed, since all the simulations in this thesis have been performed using this method.

FDTD was chosen, due to its simplicity and versatility. These qualities owe to the fact that the method does not impose any conditions to the system and does not rely on any approximations. Thus, by providing the software with the initial state of the system and the dielectric function for all the points in the simulation domain (i.e. the response of each point in the system to electromagnetic fields), it simply integrates Maxwell's equations and uses a leap-frog algorithm to simulate the evolution of the system. Such a simplistic approach allows for a complete description without introducing any spurious results due to any approximations. The only uncertainties in the simulation will be generated by the numerical precision of the calculations and the finite-sized discretization of the system, both in time and space.

Another significant advantage of this simulation framework is that the calculations are conducted in the time domain. This naturally facilitates broadband simulations and the study of temporal phenomena, such as the relaxation of specific plasmonic resonances. This method is especially efficient in the wave optics regime, where the features of the structure are in the order of the wavelength used. Thus, effects like diffraction, interference,

and coherence play a relevant role. All the simulations performed using the FDTD method have been implemented using the commercially available software Lumerical [127].

5.1 Working principle

The FDTD method, named after mathematician K. S. Yee, belongs to a broad family of differential methods. Within this paradigm, Maxwell's equations in differential form are solved in the time domain by approximating the derivatives as finite differences and employing a leap-frog algorithm [126].

Let us divide the simulation domain in a mesh with cells of dimensions Δx, Δy, and Δz in cartesian coordinates for 3D, and a time step Δt. Now we can rewrite any function as:

$$f(x, y, z, t) \rightarrow f(i\Delta x, j\Delta y, k\Delta z, n\Delta t) = f\big|_{ijk}^{n} \tag{5.1}$$

where $f\big|_{ijk}^{n}$ is the function f evaluated at the cell with indices i, j, and k at the time step n.

For the sake of simplicity, the 1D case will be discussed in the rest of the section. However, it is important to note that the discussions and derivations presented here are equally valid for the 3D case. In this discrete approximation, within a 1D system, a simple Taylor expansion allows us to write the first and second derivatives of a function in terms of the values of the function in other cells in the mesh.

$$\left.\frac{df}{dx}\right|_{i} = \frac{f\big|_{i+1} - f\big|_{i-1}}{2\Delta x} + \mathcal{O}(\Delta x^2) \tag{5.2}$$

Note that the derivatives of a function for a given cell in the mesh (or time step) depend on the values of the function in the neighboring cells. For a uniform mesh, this numerical approximation achieves second-order accuracy.

With these basic elements for a finite-difference description, we can finally try to solve Maxwell's equations. In particular, the evolution of the electric

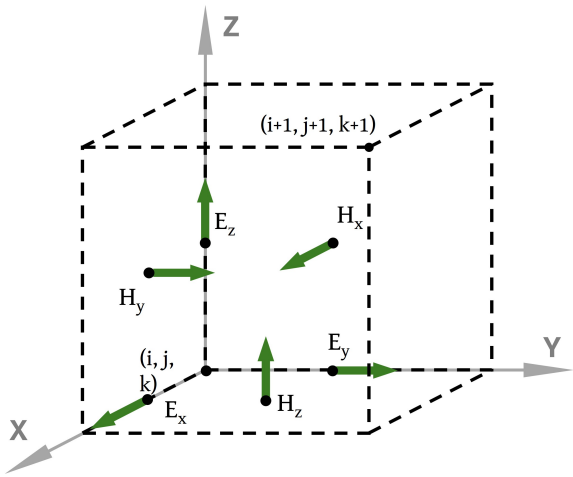

Fig. 5.1: Schematic depiction of the points in space for which the components of the electric and magnetic fields are calculated.

and magnetic fields can be computed using only the curl equations (Eqs. 2.3 and 2.4). For the 1D case, these equations are:

$$\frac{\partial H_y}{\partial x} = \varepsilon \frac{\partial E_z}{\partial t} \tag{5.3}$$

$$\frac{\partial E_z}{\partial x} = -\mu \frac{\partial H_y}{\partial t}. \tag{5.4}$$

If we use Eq. 5.2, we can find the following recurrence function:

$$E_z\big|_i^{n+1} = E_z\big|_i^n + \frac{\Delta t}{\varepsilon\big|_i \Delta x}\left(H_y\big|_{i+1/2}^{n+1/2} - H_y\big|_{i-/2}^{n+1/2}\right) \tag{5.5}$$

$$H_y\big|_{i+1/2}^{n+1/2} = H_y\big|_{1+1/2}^{n-1/2} + \frac{\Delta t}{\mu\big|_{1+1/2} \Delta x}\left(E_z\big|_{i+1}^n - E_z\big|_i^n\right). \tag{5.6}$$

These equations serve as the basis for the FDTD method, as they enable the computation of the electric and magnetic field components at all times from a known initial state. An interesting consequence of the finite element approximation is that, for a given position in the mesh, the fields are computed using the values of the fields at a different spatial and temporal positions. Moreover, none of the field components are calculated mesh points themselves, but rather at the centers between them. This is shown in Eqs. 5.5 and 5.6 and seen in Fig. 5.1. An important consequence of the approxima-

tions employed to solve Maxwell's equations using finite differences is the inherent introduction of numerical uncertainties. These uncertainties can accumulate at every step of the simulation, potentially inducing spurious results or even causing instabilities that may result in the divergence of calculated values, ultimately resulting in the failure of the simulation. In order to avoid these convergence issues, it is important to bear in mind the Courant-Friedrichs-Lewy stability criterion, that in 3D reads

$$\Delta t \leq \frac{1}{c\sqrt{\frac{1}{\Delta x^2}+\frac{1}{\Delta y^2}+\frac{1}{\Delta z^2}}}. \tag{5.7}$$

This convergence criterion is commonly applied in different algorithms [128]. In the FDTD case, it relates the spatial and temporal step sizes so that a finer mesh will imply a smaller time step to adequately describe the system. This will determine that, for a given simulation, the memory requirements increase as $(\lambda/\Delta x)^3$, while the simulation time goes as $(\lambda/\Delta x)^4$.

5.2 Simulation elements

In conducting an FDTD simulation, numerous factors must be considered. The subsequent section will address the basic components of a simulation and elaborate on the most relevant types in each case. This discussion will be framed within the context of Ansys' Lumerical [127], the commercial software predominantly used in the simulations presented in this thesis.

5.2.1 Sources

The source object *injects* light into the simulation. That is, for a given region in space, which can be a plane or a point depending on the type of source employed, the initial values of the electric and magnetic fields are set. For a short number of iterations, determined by the specified pulse length for the simulation, the electric and magnetic fields at the injection plane (or point) will attain the required values to ensure that the desired wave propagates throughout the simulation domain. Depending on the source type, setting appropriate type of BC will be necessary. This will be further discussed in the next section.

A wide variety of source types can be implemented, ranging from plane waves, Gaussian beams, dipole sources, or custom-made sources that can be imported from an external file. Among all of them, the relevant sources to the simulations presented in the thesis are the following:

Planewave:

A *planewave* defines a plane in which infinitely wide waves with perfectly parallel wavefronts are generated, see Fig. 5.2a. This source can only be implemented under periodic boundary conditions PBC. Planewaves are suitable for both infinite and finite systems, although their implementation in the latter requires some additional considerations, as shown in the next sources discussed. Additional precautions should be taken if the wavefronts are not initialized with a propagation direction parallel to the boundaries used for PBC. For these two cases, there are additional options that will adequately change the BC. There are three different source types, *Bloch/Periodic*, *BFAST*, and *Diffractive*. In this thesis only the first two will be discussed.

The *Bloch/Periodic* type is ideal for normally incident waves in simulations with PBC, regardless of the spectral range. For incident angles other than normal with single frequency illumination, a *Bloch/Periodic* planewave and *Bloch* BC should be used, while in the broadband case *BFAST* planewave and *BFAST* BC should be set.

Total-field scattered-field (TFSF):

This source defines two regions within the simulation. The first region is inside the source box, where a plane wave with a finite span is generated, similar to the planewave source. The second region is the outer area where the incident field is not considered. This configuration effectively creates a region where the total field (both incident and scattered) is present, and an external region where only the field scattered by the structures exists, as illustrated in Fig. 5.2b.

This source is indicated to analyze all the quantities related to the light scattered by a nanostructure, such as the scattering cross-section or the angular profile of the scattered light. Note that the injection direction of the planewave inside the total field region must be parallel to the

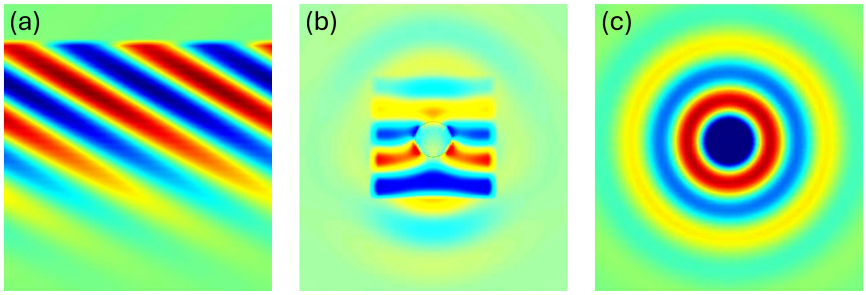

Fig. 5.2: Illustrative snapshot of the simulated z-component of the electric field (perpendicular to the plane) generated by three different sources. (a) Planewave source with an incidence angle of 45° with PBC. (b) Illumination of a Au sphere excited using a TFSF source. Note the scattered field following a radial propagation out of the total field region. (c) Emission of a dipole source. In this case, this is modeled after by electric dipole oscillating in the out-of-plane direction.

region boundaries. Other angles of incidence would cause spurious results due to the lack of proper BC inside the TFSF box.

Dipole:

This source is a point source that emits a radiation pattern that follows that of a dipole, either electric or magnetic. The electric dipole will create a radiation pattern of an oscillation charge, see Fig. 5.2c, whereas the magnetic dipole will have the emission of a current loop. Note that the two dipoles will generate orthogonal polarizations of the propagating waves in the radial direction.

5.2.2 Boundary conditions

A simulation domain must always have a finite volume, since it is impossible to compute the evolution of Maxwell's equations for an infinite number of cells. Hence, the simulation domain must be finite in space. Real systems, despite being finite in space, are generally not confined in space. For this reason it is necessary to introduce certain conditions on the values of the fields in the cells that form the boundaries of the simulation in order to avoid this limitation. These conditions can be broadly classified in two categories

depending on whether we are simulating the response of an infinite, but periodic structure, or the response of a finite structure.

Periodic:

In the case of periodic systems, the simulation of a single unit cell is usually the most efficient way to compute the response of an infinitely periodic system. To achieve this, BC must be established to account for the spatial periodicity of the system. This can be implemented by ensuring that the components of the fields on opposite boundaries in the same direction are equal at all time. For this purpose, two types of BC can be used in Lumerical, *Periodic* and *Bloch* BC. Both options implement PBC, but the latter introduces an additional phase shift in the fields between the boundaries. This phase shift is necessary to accurately capture the propagation of waves that are not parallel to the boundaries. It is calculated taking into account the size of the simulation domain in that particular direction and the wavelength of the propagating wave. As a result, Bloch BC are suitable only for single-frequency simulations. For broadband simulations with angled injection the *BFAST* method should be selected for both the source and the BC. See the previous "Sources" section for futher details.

Non-periodic:

If the simulation involves the study of a structure completely surrounded by free space, all the radiated energy should reach the boundaries without reflecting back into the simulation domain. In this case, the best option is to define the boundaries as "perfect absorbers", so that all the energy is absorbed at the boundaries, and reflections are avoided. However, due to the numerical approximations inherent to the method, a sudden change of the dielectric function (as it is the case of a finite boundary) will always create back reflections. In fact, changing the propagating fields to a null value at the boundaries will have the same effect as placing a slab of a perfect conductor (i.e. the field is perfectly canceled), and therefore, it will act like a perfect reflector [125]. In order to avoid this, in 1994 J. Berenger developed the formalism called PML [129] based on the implementation of an absorbing material and a smooth change in the refractive index so that there is an impedance matching between the simulation domain and

the absorbing material. Several improvements to this method have been implemented since then. By default, Lumerical uses a variation called "Stretched coordinate PML" [130]. Note that, as a general practice, PML should be placed at least half a wavelength away from any nanostructure, to avoid their interaction with evanescent fields.

5.2.3 Meshing

FDTD simulations using Lumerical only admit a rectangular mesh, formed by orthoedrical cells that can vary in size across the simulation domain. The minimum cell size to accurately describe a system will vary depending on several variables. As a rule of thumb, absorbing materials and small features of the nanostructure will require a smaller cell size to accurately model the response of the system. The optimal cell size will decrease as the refractive index of the material increases. A larger refractive index will increase the optical path, decreasing the effective wavelength of the radiation thus requiring a smaller cell size to properly capture the oscillations of the electric and magnetic fields in the system.

When specifying meshing for the simulation domain, three main types of meshing algorithms can be used:

Auto non-uniform:

The software automatically generates a mesh that varies throughout the simulation domain to keep the number of cells per wavelength constant and correctly capture the amplitude decay of an absorbed wave, etc. It is the default option and can be adjusted by choosing a value in the *mesh accuracy* slider from 1 to 8, which will affect the number of cells per wavelength, as described in Tab. 5.1.

Tab. 5.1: Correspondence between the value of the *mesh accuracy* parameter and the number of cells per wavelength ensured by the meshing algorithm.

Mesh accuracy	1	2	3	4	5	6	7	8
Cells per wavelength	6	10	14	18	22	26	30	34

Custom non-uniform:

This feature enables the manual specification of cell sizes and allows for the variation of this parameter based on predefined criteria.

Uniform:

This option provides a simulation domain with uniform cell size in the whole simulation region. This allows for a high degree of control over the mesh of the simulation, but can result in long simulations due to the excessive spatial resolution in some parts of the system. Note that, if a mesh override region is defined, the changes will be applied to the whole system.

In all cases, a mesh refinement option is available, allowing for additional resolution (potentially sub-cell size) can be achieved. This option precisely controls how the fields are computed at material interfaces. A detailed list on the several mesh-refinement algorithms can be found in Lumerical's documentation [127].

By using the FDTD method, the spatial and temporal discretization are strongly related to each other. For this reason, given a Δx, Δy, and a Δz, the optimal time step can easily be found. In Lumerical, this can be handled by defining the "*dt stability factor*". This is a quantity, usually slightly smaller than 1, which is used to compute the time step, *dt*. Following the stability criterion presented in Eq. 5.7, the time step will just be defined as the maximum Δt given by the stability criterion multiplied by the *dt stability factor*. Note that for values of the stability factor greater than 1 the simulation will become unstable.

Finally, the mesh can be directly defined in a small region of the system by means of the mesh override object. This simulation element allows for the definition of a uniform mesh within a specific simulation volume.

5.2.4 Material parameters

The implementation of different materials in the FDTD simulations is done by defining the optical response of the medium for each cell in the mesh. TCells not assigned to any specific material are automatically identified as background and are assigned a predefined refractive index with no absorption. As discussed in previous sections, the response of a material to an external electromagnetic field is fully described by either the dielectric function or the complex refractive index, as these two quantities are equivalent and related

to each other through the Kramers-Kronig relations. Therefore, specifying one of these quantities is sufficient to accurately model the material. Lumerical provides a vast database of dielectric functions and complex refractive indices based on experimental data from the literature. Alternatively, experimental data or a mathematical expresion can also be used in the simulation to model the system's response.

After a data set is supplied, discrete points are interpolated by fitting a function that models the response of each material during the simulation, following Eqs. 5.5 and 5.6. During the fitting process, various parameters can be adjusted, including the wavelength range for fitting and the number of coefficients used in the analysis. Especial attention should be paid to the sign of both real and imaginary parts of the dielectric function (or complex refractive index). Selecting the "make fit passive" option ensures that the imaginary part of the dielectric function remains positive throughout the fitting range, thereby preventing any gain from appearing and facilitating convergence in the simulations.

5.2.5 Monitors

Monitors record data from simulation. Different types of monitors retrieve different types of data from the simulation, such as the values of the electric and magnetic field as a function of time and spatial position, or the power transmitted through a surface as a function of the frequency. In addition to that, raw data can be further processed to provide complex information through analysis groups also available in the FDTD solver. The main types of monitors are described below.

- **Refractive index monitor:** obtains the value of the complex refractive index for each cell, in the specified region of the simulation.
- **Time monitor:** measures the electric and magnetic fields over time.
- **Frequency-domain field monitor:** measures the electric and magnetic field in the frequency domain in the specified region. It can also measure the power transmitted through a surface. Especially useful to simulate transmission and reflection of a structure.

An analysis group facilitates the integration of multiple monitors and enables the combined analysis of the data collected from those monitors. Some analysis groups are predefined, while others can be custom-created through scripting to measure and analyze simulation data. Additionally, several analysis groups are constructed by default.

- **Cross-section:** combining 6 frequency-domain monitors, this analysis group creates a closed box and measures the power that escapes the box for each frequency/wavelength in units of cross-section. Combining this analysis group with a TFSF source, the absorption and scattering cross-section of small objects can be computed.

- **Far field from a closed box:** computes both, the scattering cross-section and the far field projection, giving information about the radiated power in each direction. Note that, if the environment of the scatterer is not homogeneous (i.e. there is a substrate), results may not be reliable.

- **Current charge density:** Using Eq. 2.8 the current and charge density is computed for every point in the specified region. Note that the current density is a 3D vector with complex components and the charge density is a complex number.

Nanofabrication and characterization techniques

6

6.1 Nanofabrication overview

The manufacture and characterization of systems at progressively smaller size scales have been instrumental in the discoveries made over the last few decades. In nanotechnology, material properties can be substantially altered when the system size approaches a characteristic length scale. For plasmonics, the near-field decay length at the metal-dielectric interface is of particular interest, with typical decay lengths on the order of tens of nanometers.

Although complete control at the nanometer scale remains elusive, substantial efforts have been dedicated to the fabrication of diverse arrays of systems incorporating metallic nanoparticles and nanopatterned arrays with various shapes and features, consistently below 100 nm. Furthermore, thin film deposition techniques regularly achieve homogeneous layers with thicknesses ranging from 10 to 30 nm, often exhibiting sub-5 nm surface roughness.

The fabrication of nanostructures can be achieved through either a "bottom-up" or a "top-down" approach. The bottom-up method relies on chemical synthesis techniques, such as self-assembly, where structures are formed through the controlled agglomeration of materials, effectively growing the structure from the substrate [85, 86]. In contrast, the top-down approach utilizes photons, electrons, or ions to define a pattern on the substrate, which is then etched away to create the desired structure by removing material from the top layer. This family of methods includes traditional lithographic techniques, as well as advanced methods such as focused ion beam lithography and nanoimprinting lithography.

In this section, we will exclusively focus on the top-down methods used in the fabrication of the samples presented in this thesis.

6.2 Material choice

Before beginning the discussion on the fabrication methods we should address the issue of the material used for the nanostructures. In all cases, regardless of the particular design, we will be dealing with metallic-dielectric structures. Regarding the dielectric material, SiO_2 was typically used due to its easy access, chemical stability, and transparency in the optical and near-infrared regimes. In addition, Si_3N_4 or Si can also be used, depending on the thickness of the substrate and the spectral range, and they were also occasionally used in this thesis.

The choice of metal is more restricted. An optimal plasmonic response in the visible and near-infrared regimes favors the use of noble metals, in particular Ag and Au that exhibit a long electron relaxation time [22, 131]. These two metals can be approximated by a Drude metal in most of the spectral range of interest (see Fig. 2.1). Despite the fact that Ag presents a sharper, more intense peak at optical frequencies, Ag nanostructures degrade rapidly in contact with air. This is mainly due to reactions involving compounds with sulfur, present in the air [132]. For this reason, Ag nanostructures require to be manipulated and stored in inert atmospheres or be immediately capped in-situ with protective layers. In contrast, Au is chemically stable, making it a perfect candidate for the fabrication of plasmonic nanostructures [22].

6.3 Electron beam lithography

Lithographic methods generally rely on the transfer of a predefined 2D pattern from a flat surface to a thin metallic layer on a substrate. For that purpose, they include other techniques such as different types of etching and the deposition of thin metallic layers [133]. One of the most widely used techniques for nano- and micro-fabrication is photolithography [134]. This method involves carving the desired pattern onto a metallic plate known as a mask. Subsequently, light is passed through the mask onto a

photosensitive material, thereby transferring the pattern from the mask to the photosensitive layer. However, the resolution of this process is limited by the diffraction of light through the mask [135]. According to classical optics, light cannot be confined to a volume smaller than half of its wavelength [136, 137]. Advanced strategies, together with advanced extreme ultraviolet optical lithography equipment, have successfully extended the capabilities of photolithography to resolutions below 10 nm [138]. However, the high cost of this technology makes it impractical for the fabrication of sub-100 nm features in research laboratories.

Electron beam lithography (EBL) serves as a reliable, high-resolution, and highly versatile method for the manufacture of nanostructures [139]. Although it is not ideal for large-area fabrications, this technique excels in prototyping due to its flexibility in pattern design and the high resolution it achieves. The process involves defining patterns through the deposition of a specific amount of charge, or dose, by the electron beam. However, the pattern definition is typically limited by the speed at which the electron beam can be reliably deflected and the current it carries. Despite these limitations, EBL is particularly well-suited to create complex and precise designs with resolutions as fine as 10 nm.

Similar to photolithography, EBL involves the transfer of a 2D pattern to a thin layer of metal. However, unlike photolithography, this process does not rely on shining light through a mask. Instead, it utilizes an electron beam to alter the chemical properties of an electron-sensitive resist. The main advantage is that the electrons used in this procedure have a wavelength on the order of Å, similar to those used in electron microscopy. This characteristic means that EBL is not limited by diffraction, enabling the definition of nanometer patterns with high precision. A scheme of the process can be found in Fig. 6.1 and Fig. 6.2 and is subsequently described:

Spin coating and resist choice:

For EBL the first step is to deposit a thin layer of a electron-sensitive resist on top of the chosen substrate. This is done using a technique called *spin coating* that consists in the deposition of a polymer layer, whose thickness is controlled by a few experimental parameters[140]. A solution of the desired polymer in a volatile solvent is deposited onto the substrate, which is placed on a spinning plate. The viscosity of

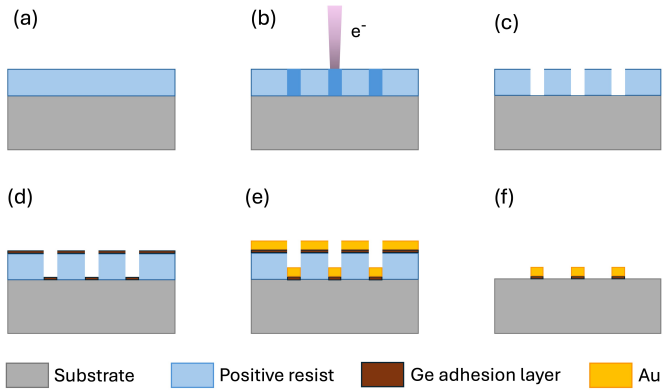

Fig. 6.1: Steps of a typical EBL process for the fabrication of plasmonic nanostructures using a positive tone resist. (a) Resist spin coating. (b) Pattern exposure. (c) Pattern development. (d) Adhesion layer deposition (e) Au layer deposition. (f) Lift-off.

the solution will vary depending on the solvent and the concentration. The thickness of the remaining layer can be accurately determined by controlling the spinning time and angular velocity. Once a calibration curve is established, increased rotation speeds can be used to achieve thinner layers. Following the spinning process, the solvent is evaporated by increasing the temperature, leaving a polymer layer behind.

There are two main types of electron sensitive resists: *positive* and *negative tone* resists. Positive tone resists are formed by polymer chains that, when exposed to an electron beam, break apart increasing their solubility, hence revealing the patterned areas after the development stage (see below) as the direct transfer of the exposed design. Positive resists, such as PMMA, are used as a straightforward, safe and reproducible tool to build sub 100 nm features [141, 142]. On the other hand, in the negative tone resists, the polymer chains exposed to the electron beam undergo a cross-linking process that reduces their solubility in water, producing the opposite effect. This resists can offer enhanced resolution, such as hydrogen silsesquioxane HSQ[1] [143], but are not efficient to define thin structures since the exposure times

[1] HSQ is used in the fabrication process of the work presented in a Publication 4. However, it is only used as a separation layer, avoiding its EBL capabilities

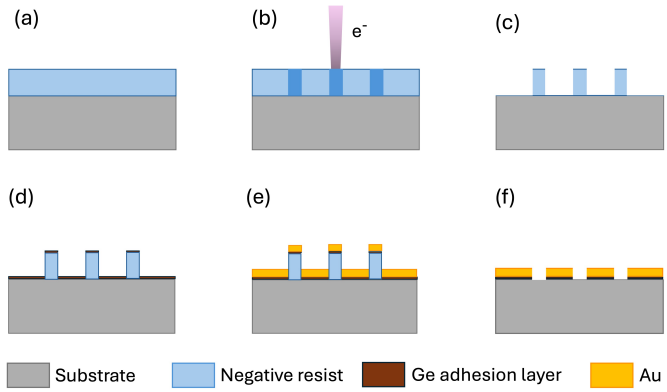

Fig. 6.2: Steps of a typical EBL process for the fabrication of plasmonic nanostructures using a negative tone resist. (a) Resist spin coating. (b) Pattern exposure. (c) Pattern development. (d) Adhesion layer deposition (e) Au layer deposition. (f) Lift-off.

would increase significantly.

- **Exposure:**

  The dose[2] for each pixel in the design can be controlled by adjusting parameters such as the resist thickness, beam current, dwelling time[3], and acceleration voltage, among others. Exposure calculations must also account for the resist thickness to ensure that the patterned geometry remains constant in the vertical direction. As illustrated in Fig. 6.3, the dispersion of electrons in 500 nm of PMMA is nearly negligible for a 100 kV case. However, Fig. 6.3c shows how the exposed profile varies significantly with depth.

- **Development:**

  After defining the regions of the polymer with enhanced or decreased solubility by the electron beam, an immersion in the right solvent allows for the removal of the sacrificial polymer. This solvent is called the developer. The suitability of a developer will depend on the type of polymer used in the lithography process. Following immersion in the developer solution, the sample is treated with a stopper solution to remove all the developer from the sample and ensure that only the

[2] Relates to the amount of charge deposited per unit area in the substrate.
[3] Indicates the time the beam is focused on a specific spot.

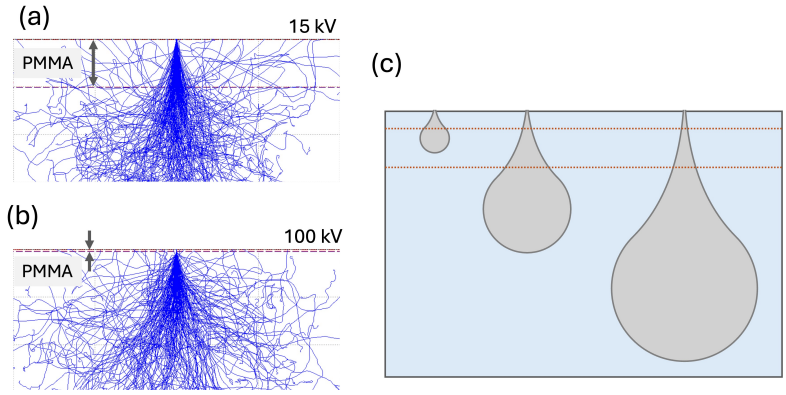

Fig. 6.3: Simulated electron trajectories into a 500 nm layer of PMMA in a Si substrate for (a) 15 kV and (b) 100 kV of acceleration voltage. Note the change of scale between (a) and (b). (c) Schematic depiction of the exposed volume for increasing acceleration voltages. Adapted from [144]. Simulations performed using [145].

desired resist is removed. The developing time is a critical parameter to control. Insufficient developing time can result in a poorly defined pattern, as the removal of the polymer may not be complete. Conversely, excessive developing time can have the opposite effect, as the solubility of the exposed polymer, although small, is not negligible over extended periods.

- **Metallic layer deposition:**

  Once the negative of the desired pattern is defined in the resist layer, the following step involves the deposition of the metallic layer. Besides achieving a smooth and uniform deposited layer, it is crucial to consider the directionality of the evaporation. The evaporation process should be as vertical as possible to prevent undesired connections between the metallic layer on top of the resist and at the bottom of the patterned areas. Controlling the deposited thickness is also crucial to avoid these effects. As a rule of thumb, the thickness of the polymer layer should be approximately three times that of the desired metal layer.

  Even after an ideal deposition, certain metals may exhibit poor adhesion to specific substrates, such as Au on Si or glass. To enhance the adhesion of a metallic layer to a substrate, it is often beneficial to in-

clude a thin adhesion layer, typically 5-10 nm thick, made of materials like Ti, Pt, or Cr [146]. This procedure, greatly enhances the reproducibility of the fabrication process, but it has been proven to severely hinder or modify the plasmonic response of the nanostructures [147]. For this reason, the structures studied in this thesis were fabricated without any adhesion layer, whenever possible, or alternatively, using a seed layer of Ge (less than 2 nm) [148]. This approach has been shown to improve the adhesion of the Au layer without compromising the plasmonic response [149].

- **Lift-off:**
  Following the deposition of the metallic layer on the patterned resist, the final step involves the removal of the resist to reveal the desired pattern. This is achieved by immersing the sample in an appropriate solvent, which dissolves the resist. The metal deposited on top of the resist is removed along with the polymer, while the metal deposited directly on the substrate remains intact. To ensure complete removal of the resist, the sample and solvent are often placed in an ultrasound bath. However, if the exposed features are too small, the solvent may not penetrate sufficiently under the metallic layer, preventing the resist from dissolving.

EBL is a versatile direct writing tool for the fabrication of 2D structures that has multiple applications. In this section, we have presented a general introduction to the technique, with special emphasis on the protocols used to manufacture the plasmonic nanostructures that will be discussed in detail later in Publications I and IV. Other variations of EBL include exposures with changing profile in the vertical direction [150], or using the patterned resist as a protection for etching process, instead of lift-off [151, 143].

6.4 Focused ion beam

Another common fabrication tool is FIB. This direct writing, top-down approach relies on the use of a highly focused ion beam in order to remove material from the sample. While FIB equipment can be utilized for various nanoscale manipulation techniques [152], we will concentrate on two

specific applications: FIB milling and the use of the equipment for characterization purposes.

FIB milling uses a setup similar to that of an EBL system, as it also relies on a controlled beam to pattern a surface. However, unlike EBL, the FIB beam is more energetic due to the higher mass of the accelerated ions. Typically, Ga ions are used, but other ion sources, such as Ge [153] or Au [154, 155] can be employed depending on specific applications.

This energetic beam of ions is focused on a spot of a few nm in size. This allows for carving the sample with a very high resolution, as depicted in Fig. 6.4a. A scan across the sample combined with the selective blanking of the beam allow the FIB system to mechanically etch away the first nanometers of the sample following a given design. Control over the acceleration voltage and the dwelling time allows also to finely tune the depth of the etched portion of the material [156, 152].

It is important to note that the material removed in the patterning process is typically deposited on another region of the sample, usually at the edges of the carved areas. This can become a problem as the amount of removed material increases. FIB equipments incorporate a SEM system, allowing for real-time monitoring of the patterning process.

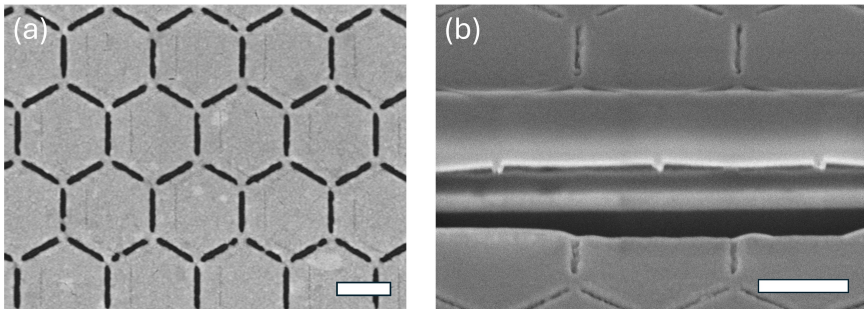

Fig. 6.4: (a) SEM image of a honeycomb lattice fabricated by FIB milling on a 20 nm layer of Au. (b) SEM image of a honeycomb lattice fabricated by EBL. The image of the cross-section has been obtained by carving a wide trench in the sample using FIB and tilting the SEM stage. Note that a Pt layer has been deposited over the sample to preserve the features during the carving process. The scale bars are 500 nm in both cases.

Secondly, FIB systems can be integrated with electron microscopy systems to facilitate advanced cross-sectional imaging and characterization. By carving a trench with the sufficient width and tilting the stage inside the microscope chamber, a SEM image of the sample's cross-section can be obtained, as illustrated in Fig. 6.4b. Moreover, another trench can be carved on the sample so that a thin lamella is produced. This ultra-thin slice of material, usually a few nanometers thick, is electron-transparent and can be subjected to further analysis using techniques like high-resolution TEM [157] or additional characterizations, such as EDX spectroscopy [158, 159], with enhanced precision. This technique usually benefits from the previous sputtering of an inert material, such as Pt (see Fig. 6.4b) over the studied sample in order to prevent damage to the structures in the carving process.

6.5 Characterization techniques

The ability to fully characterize the response of plasmonic nanostructures is a crucial point in understanding light-matter interactions at the nanoscale. The macroscopic, or far-field, characterization, consists in spectroscopic measurements aimed to determine the proportion of the incident wave that has interacted with the sample for each energy. Theses measurements require a background measurement that will serve as a reference and can be performed using table top equipments that can vary in complexity depending on the energy range and resolution.

In contrast, the inherent small dimensions of plasmonic systems pose some challenges regarding the microscopic, or far-field, measurements. A key distinction between plasmonic nanostructures and other optically responsive systems is that the features of these structures are comparable in size to the exciting wavelength. Since the system's response is highly dependent on the geometry of these features, obtaining spatially-resolved information about the spectral response of the structure becomes a critical issue.

Various techniques can provide insights into both the far-field and near-field properties of a sample, each employing different strategies to probe the system. In this section, we will focus on two techniques used in this thesis to characterize the far-field and near-field responses of plasmonic

nanostructures: FTIR for far-field characterization and EELS for near-field characterization.

6.5.1 Fourier-transform infrared spectroscopy

The objective of all the techniques that acquire the spectral signature of a sample is to measure the intensity transmitted or reflected by the sample at each frequency. Measuring the desired spectrum and comparing it to a reference spectrum (usually, the emission spectrum of the source used to excite the system) the spectrum of the sample can be obtained. Table top spectrometers, are able to measure reliable spectra, with a moderate spectral resolution. They rely on using a dispersive element -e.g. some type of diffraction grating- to project each wavelength to a selected group of pixels in a CCD sensor. By adjusting the dispersive power of the grating, the spectral resolution can be enhanced. However, since the number of pixels in the CCD array remains constant, this increase in resolution is achieved at the cost of reducing the spectral bandwidth of the measurement. This type of set-up, although robust and accessible, lacks the ability of performing high resolution measurements with a high spectral range. In addition, the efficiency of the sensors decreases as the wavelength increases, loosing potential for the infrared region.

As an alternative, FTIR spectroscopy is able to provide high resolution spectra across a wide spectral range using interferometric techniques. The basic configuration is very similar to a Michelson interferometer [160]. In the basic configuration, presented in Fig. 6.5, the light coming from a broadband source is divided by a beam-splitter. One of the resultant beams is sent to a fixed mirror at a distance l, whereas the other goes to a movable mirror at a distance $l + d$. When both beams get together again, they interact with the sample, and the resulting signal is captured by the detector.

The signal acquired by the detector is the sum of the two identical beams after their interaction with the sample, with the particularity that both signals have a relative phase due to a difference in their optical paths of $2d$. The advantage of this technique lies on measuring an interferogram, which represents the intensity of the total signal as a function of the distance d. By analyzing the Fourier transform of the interferogram we can retrieve high

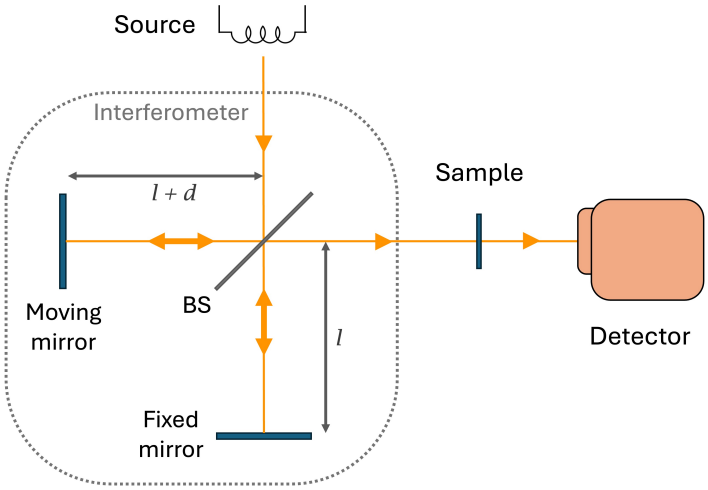

Fig. 6.5: Conventional FTIR spectroscopy setup configured for measuring sample transmission.

resolution spectra while maintaining a wide spectral range.

A single measurement requires for the movable mirror to travel a certain distance. The larger the distance, the better the spectral resolution of the measurement.

In addition to the main FTIR measurement setup, these far-field measurements easily allow for the addition of a microscopy system that can be used to select the region of interest in a microscopic scale. The magnification is constrained by the inherent limitations of optical microscopy; nevertheless, this technique facilitates the measurement of structures within the micrometer-squared μm^2 range. It is important to note that the addition of optical elements to the system introduces additional diaphragms and can modify the illumination angle, thereby introducing additional variables into the measurements. This is particularly significant when measuring SLR, as discussed in Section 4.4.1.

6.5.2 Electron energy loss spectroscopy

To perform measurements with spatial resolution of tens or hundreds of nanometers, far-field, visible and infra-red photons are no longer suitable.

This is because propagating radiation is inherently diffraction-limited, restricting its resolution to a volume of the order of half its wavelength. To overcome this limitation, two approaches can be taken: either reducing the wavelength of the probe by using electrons, or utilizing electromagnetic radiation in the non-propagating near-field regime to avoid the diffraction limit, as illustrated in Fig. 6.6.

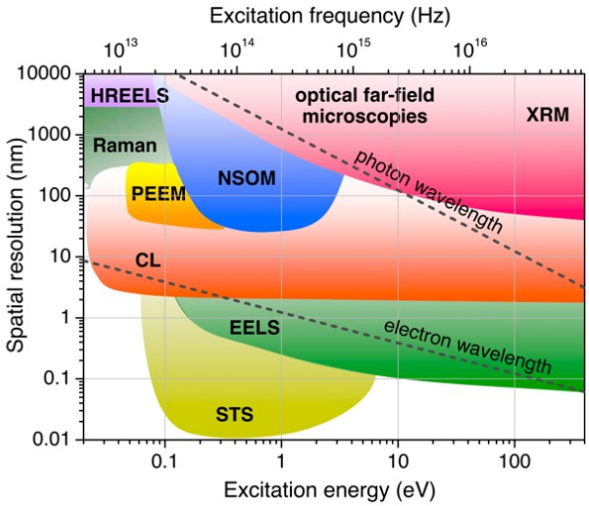

Fig. 6.6: Atlas of spatially resolved spectroscopy techniques, organized by their spatial and energy resolution. Note both the extensive energy range accessible via EELS and its exceptional spatial resolution. Adapted from [161].

This thesis focuses on EELS as a prominent example of a technique offering spatially resolved information about plasmonic nanostructures, given its significance to this research. Publication II specifically presents detailed characterization results of plasmonic near fields using EELS. For an extensive discussion on the techniques relying on near field excitations and other methods for imaging plasmons with nanometer resolutions, numerous reviews are available in the literature [162, 163, 164].

EELS utilizes the energy distribution of inelastically scattered electrons to probe nanostructures. The short wavelength of high-energy electrons ensures exceptional spatial resolution, while the technique simultaneously offers detailed spectral information about the sample's electronic structure. An overview of the equipment is presented in Fig. 6.7, and the working principle

goes as follows. The sample is positioned in a high vacuum chamber, where a highly monochromated electron beam is directed onto the sample. The transmitted electrons are then collected using two different detectors. A HAADF detector, typical in high resolution TEM, while others can be collected and sorted by their energy at an EELS spectrometer.

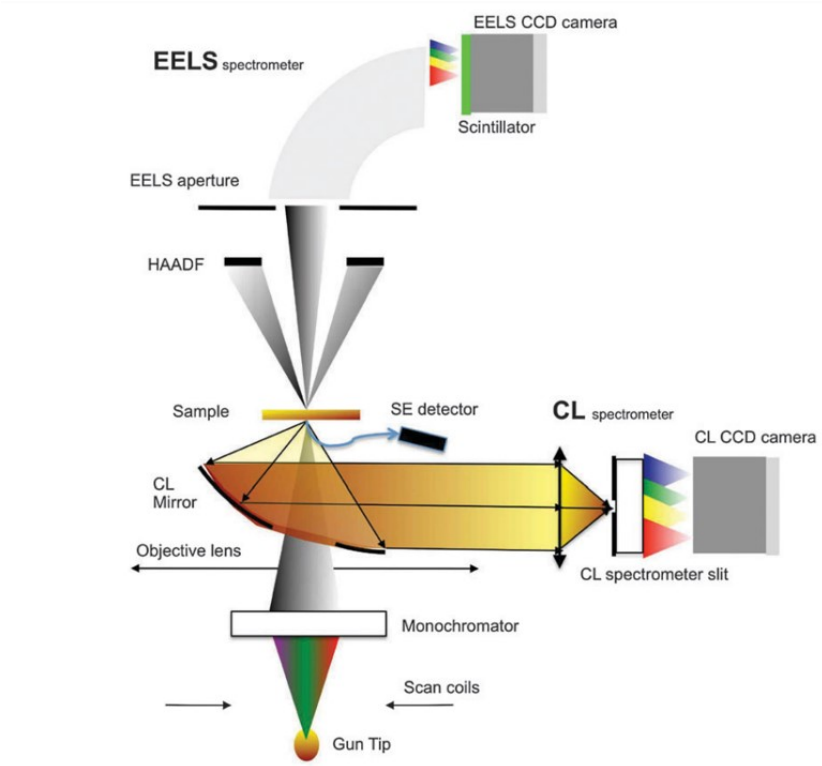

Fig. 6.7: Schematic depiction of the basic set-up to perform EELS measurements. The system uses a STEM as a platform, with a secondary electrons (SE) detector for the SEM mode, and a HAADF for the TEM mode. Integration of a CL measurement system is also included. Reproduced from [165].

The first set of electrons is used to generate a high-resolution image of the sample, while the second set provides the energy loss probability spectrum for each pixel of the image. In essence, for each pixel corresponding to a specific position on the sample, the technique can determine the EELS probability for each energy loss value. This means that the information collected in an EELS measurement is both spatially and spectrally resolved. In Fig. 6.8a, the spectra for two different regions of the sample are displayed. Fig. 6.8b shows the spatial distribution with the energy fixed. The measured

EELS probability is found to closely match the predicted excitations, as illustrated in Fig. 6.8c.

Additional signals, such as those from the CL detector, can be measured to provide complementary information about the sample. The potential integration of a CL detector is also illustrated in Fig. 6.7. EELS is a valuable

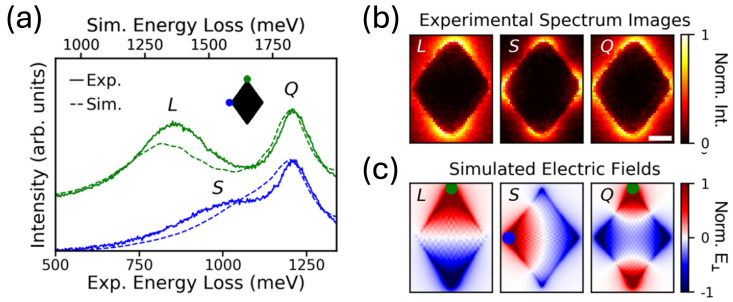

Fig. 6.8: (a)Energy loss spectra of electrons traversing two distinct points in the sample. (b) and (c) depict the EELS signal and simulated electric fields at energies corresponding to the spectral peaks in (a). Adapted from [166].

tool for investigating plasmonic resonances, as the electron energy loss probability is directly proportional to the local density of states within the plasmonic system [167]. This relationship is intimately linked to the near-field distribution generated by surface plasmons [161].

Despite its exceptional spatial and spectral resolution, EELS requires samples that are sufficiently thin to be electron-transparent. The technique must be conducted under high vacuum conditions and requires highly specialized equipment, including state-of-the-art aberration-corrected microscopes and monochromators.

Part II

Inverted Honeycomb Plasmonic Lattices

Introduction

Arrays of plasmonic nanostructures are a hot topic in nanophotonics due to their ability to excite both LSP resonances and their collective counterparts, SLR, to achieve highly localized field enhancement and tailored optical responses. Among the myriad configurations of plasmonic arrays, inverted designs have garnered significant attention due to their unique properties that include sharp spectral features and relatively large out-of-plane hot spots. These structures, defined by their two-dimensional arrangement of nanoholes or nanoslits in a metallic thin film, provide versatile platforms for supporting complex plasmonic modes, while ensuring compatibility with scalable fabrication methods, integration into planar optical systems, and they can be easily functionalized with biomolecules for sensing applications.

This chapter presents two peer-reviewed articles delving into the unique optical properties and applications of inverted honeycomb plasmonic lattices. Publication I, "An Inverted Honeycomb Plasmonic Lattice as an Efficient Refractive Index Sensor", translates these planar architectures into practical sensing devices. Here, the inverted honeycomb lattice is embedded within a planar heterostructure comprising a dielectric spacer and a metallic mirror, optimizing the excitation of out-of-plane SLR. This planar configuration not only enhances the electric field distribution within and around the lattice but also achieves exceptional sensitivity to refractive index changes, with figures of merit as high as 199 RIU^{-1}. Such performance underscores the relevance of planar plasmonic systems for chemical and biological sensing, particularly for detecting nanoscale variations in dielectric environments.

Publication II, "Imaging of Antiferroelectric Dark Modes in an Inverted Plasmonic Lattice", examines the excitation and mapping of bright and dark plasmonic modes within a similar honeycomb lattice. By leveraging advanced EELS and FDTD simulations, the study identifies numerous plasmonic resonances. Furthermore, we also observe a collection of dark plasmonic modes arising from antiferroelectric arrangements of slit polarizations across the lattice. These modes, confined within the planar structure, exhibit vanishing net dipole moments, minimizing radiative losses and enabling superior en-

ergy confinement. These modes are particularly interesting due to the fact that their periodicity is twice that of the plasmonic lattice.

Collectively, these studies underscore the transformative potential of planar inverted honeycomb plasmonic lattices as platforms for investigating fundamental plasmonic phenomena and facilitating high-sensitivity sensing applications. Through the integration of FDTD simulations, nanofabrication techniques, and advanced characterization methods, they establish a comprehensive compendium of the optical and plasmonic responses exhibited by such lattices.

nanomaterials

MDPI

Article

An Inverted Honeycomb Plasmonic Lattice as an Efficient Refractive Index Sensor

Javier Rodríguez-Álvarez [1,2,*], Lorenzo Gnoatto [1], Marc Martínez-Castells [1], Albert Guerrero [3], Xavier Borrisé [4], Arantxa Fraile Rodríguez [1,2], Xavier Batlle [1,2] and Amílcar Labarta [1,2]

[1] Departament de Física de la Matèria Condensada, Universitat de Barcelona, 08028 Barcelona, Spain; lgnoatgn26@alumnes.ub.edu (L.G.); martinezcastellsmarc@gmail.com (M.M.-C.); arantxa.fraile@ub.edu (A.F.R.); xavierbatlle@ub.edu (X.B.); amilcar.labarta@ub.edu (A.L.)
[2] Institut de Nanociència i Nanotecnologia (IN2UB), 08028 Barcelona, Spain
[3] Institut de Microelectrónica de Barcelona (IMB-CNM, CSIC), 08193 Bellaterra, Spain; albert.guerrero@imb-cnm.csic.es
[4] Catalan Institute of Nanoscience and Nanotechnology (ICN2), CSIC and The Barcelona Institute of Science and Technology, Campus UAB, Bellaterra, 08193 Barcelona, Spain; xavier.borrise@imb-cnm.csic.es
* Correspondence: javier.rodriguez@ub.edu

Abstract: We present an efficient refractive index sensor consisting of a heterostructure that contains an Au inverted honeycomb lattice as a main sensing element. Our design aims at maximizing the out-of-plane near-field distributions of the collective modes of the lattice mapping the sensor surroundings. These modes are further enhanced by a patterned SiO_2 layer with the same inverted honeycomb lattice, an SiO_2 spacer, and an Au mirror underneath the Au sensing layer that contribute to achieving a high performance. The optical response of the heterostructure was studied by numerical simulation. The results corresponding to one of the collective modes showed high sensitivity values ranging from 99 to 395 nm/RIU for relatively thin layers of test materials within 50 and 200 nm. In addition, the figure of merit of the sensor detecting slight changes of the refractive index of a water medium at a fixed wavelength was as high as 199 RIU^{-1}. As an experimental proof of concept, the heterostructure was manufactured by a simple method based on electron beam lithography and the measured optical response reproduces the simulations. This work paves the way for improving both the sensitivity of plasmonic sensors and the signal of some enhanced surface spectroscopies.

Keywords: Au plasmonic nanostructures; inverted honeycomb lattice; surface lattice resonances; refractive index sensor

Citation: Rodríguez-Álvarez, J.; Gnoatto, L.; Martínez-Castells, M.; Guerrero, A.; Borrisé, X.; Fraile Rodríguez, A.; Batlle, X.; Labarta, A. An Inverted Honeycomb Plasmonic Lattice as an Efficient Refractive Index Sensor. *Nanomaterials* **2021**, *11*, 1217. https://doi.org/10.3390/nano11051217

Academic Editor: Daniela Iacopino

Received: 9 April 2021
Accepted: 1 May 2021
Published: 4 May 2021

1. Introduction

The design and manipulation of plasmonic nanostructures have rapidly become one of the most active topics in nanophotonics over the last years. Specifically, several plasmonics-based approaches have been applied to improve the detection limit and sensitivity of sensing devices. Good examples of these new capabilities are the potential to prove volumes beyond the diffraction limit [1–3] or to achieve single-molecule sensitivity [4]. Moreover, plasmonic nanostructures have contributed to largely enhancing the signal of surface spectroscopies, such as surface-enhanced Raman scattering or plasmon-enhanced fluorescence [5–9].

One of the most promising niches for plasmonic nanostructures is their integration in refractive index sensors [10]. This kind of sensor benefits from the fact that the wavelengths at which the plasmonic excitations arise depend strongly on the features of the medium mapping the corresponding near-field distributions. However, the inherent nature of localized surface resonances (LSRs) hinders their efficiency as sensing devices as the evanescent electric fields excited in an LSR decrease rapidly with the distance from the metal–dielectric interface. In this way, the regions in which the electric field is enhanced, the so-called "hotspots", extend only a few tens of nanometers away from the metal–dielectric

interface and, in many cases, are confined in the space between neighboring plasmonic elements. In contrast, inverted structures, in which dielectric holes are carved through a continuous metallic layer, have proven to be a valid approach to tackle this issue [11] and are known to improve the efficiency of light–matter interaction in some situations [12–16]. Unlike other realizations of inverted plasmonic structures [17–19], such as nanoholes or nanoarrays with a more complex pattern, the heterostructure proposed in this work benefits from the inclusion of a mirror layer. By adding this element, the device can collect all the optical responses solely in the reflection spectrum, given the null transmission.

In addition, our system is based on the detection of surface lattice resonances (SLRs) in a honeycomb lattice, which implies sharper peaks associated with higher-energy modes involving the collective excitation of all the elements in the plasmonic array [20–23]. These modes usually present hotspots encompassing larger areas than those associated with local excitations. Besides, the three-fold symmetry of the honeycomb lattice may hamper the excitation of LSR in favor of SLR, making collective modes much more intense [20,21], as will be further discussed in Section 3.2.

Overall, the heterostructure presented in this work constitutes a proof of concept for a simple realization of a highly sensitive refractive index sensor that can be manufactured by a relatively easy lithographic process.

2. Materials and Methods

As shown in Figure 1, the main part of the studied heterostructure is composed of two layers of Au and SiO_2 of 30 and 80 nm in thickness, respectively, where an inverted honeycomb lattice—with a pitch of 866 nm and bar-shaped trenches of 400 nm in length and 30 nm in width—is carved through the whole Au/SiO_2 bilayer. On the bottom of the trenches, there is an Au layer of 30 nm in thickness that shapes the direct honeycomb lattice complementary to that at the top. Thus, the two plasmonic honeycomb lattices are placed at an edge-to-edge distance of 50 nm. Between them, there is a sort of two-dimensional photonic crystal that is formed by the contrast in the refractive indices of the SiO_2 and the material filling the trenches (air, water, and so on). Consequently, the interactions among the three lattices feed back into each other because they share the same pitch and symmetry. Specifically, one of the collective modes of the two plasmonic structures gives rise to a spatial distribution of the near-field enhancement around the heterostructure that is well suited for sensing applications, as discussed later. This heterostructure rests on top of a second bilayer, composed of an SiO_2 spacer and an Au mirror of 120 nm and 100 nm in thickness, respectively, which enhances the intensity of the collective modes and ensures that the transmission through the entire system is negligible.

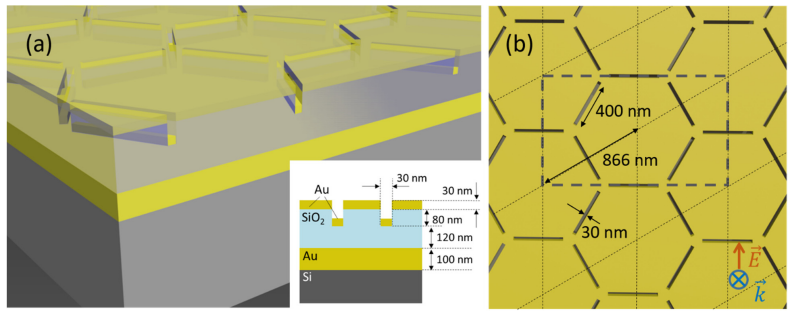

Figure 1. (**a**) Scheme of the heterostructure. The inset shows a schematic cross-sectional view. (**b**) Top view showing the honeycomb lattice, the hexagonal Bravais lattice (dotted lines), a rectangular unit cell (dashed grey lines), and some relevant parameters of the design. Regular rhombus are primitive cells of the hexagonal lattice. The cell for the simulations is the rectangular unit cell. At the bottom left corner of the panel, there is a schematic representation of the electric field and propagation vectors of the incident radiation.

The simulations presented in this work were performed using the finite-difference time-domain (FDTD) method, implemented in the solver provided by Lumerical^R [24].The method defines a simulation spatial domain, which is discretized. Then, the incident electromagnetic field is set by defining the initial state of the system. The software solves Maxwell's equations to determine the evolution of the electric and magnetic fields using a discrete time-step. This approximation, as well as the inherent mesh step necessary to discretize the space in the simulation domain, introduce a certain error into the calculations. However, the method allows for direct observation of the physical phenomena taking place without imposing any further assumption on the behavior of the system.

The configuration of the simulations was as follows: a short pulse of linearly polarized light was sent perpendicularly to the surface of the heterostructure from a source placed above the metal (see the inset of Figure 1b). Placing different monitors in several spots, we obtained the transmission and reflection cross sections, as well as the electric field distribution as a function of the wavelength of the incident radiation. Owing to the periodicity of the system, periodic boundary conditions of a rectangular unit cell of the honeycomb lattice are used to perform the simulations (see Figure 1b). The dielectric functions for the materials used in these simulations were obtained by fitting analytical functions to the data from [25] for SiO_2 and Au, respectively.

In the manufacturing of the samples, a bilayer made up of Au (mirror) and SiO_2 (spacer) layers of 100 nm in thickness each was deposited on top of a standard Si wafer by electron beam evaporation (ATC Orion, AJA International, Inc) and plasma enhanced chemical vapor deposition (PECVD), respectively. A pattern of 500 μm × 500 μm in size following the inverted honeycomb design shown in Figure 1 was exposed by electron beam lithography (EBL) on an additional third layer of poly methyl methacrylate (950 PMMA, MicroChem) with a thickness of 90 nm. After removing the exposed areas, the sample was metallized with 30 nm of Au deposited by electron beam evaporation. The outcome of the evaporation process was a 30 nm Au layer on top of the heterostructure shaping an inverted honeycomb lattice and the complementary direct version of the same lattice on the bottom of the trenches, as shown in Figure 1a, at an edge-to-edge distance of 60 nm. Between them, a two-dimensional photonic crystal is formed by the contrast in the refractive indices of the 950 PMMA and the material filling the trenches. No further lift-off was necessary owing to the design of the samples. As SiO_2 and 950 PMMA have very similar refractive indices, the optical spectra of the simulated and manufactured heterostructures may be compared right away, even though some geometrical parameters are slightly different than in the simulations, namely, the edge-to-edge distances between the inverted Au layer and both the mirror (190 nm) and the direct Au structure (60 nm).

The optical characterization was carried out by a Vertex 70 Fourier transform infrared (FTIR) spectrophotometer attached to an optical microscope (Bruker Hyperion). Experiments were performed in the reflection configuration with a 4× objective and under the illumination of unpolarized light. The measured signal of an Ag mirror was used as a background in all the experiments.

3. Results

3.1. Optical Response of the Heterostructure

Several peaks are exhibited by the simulated reflection spectrum of this heterostructure (see Figure 2). Nevertheless, they can be classified into only two groups depending on either the local or collective nature of the resonances associated with them. The first group includes the peaks located around 729 and 1789 nm, which arise from the excitation of LSR related to local modes of the bar-shaped trenches and the Au bars in the inverted and direct plasmonic structures, respectively. Accordingly, the near-field distributions for these modes are mainly confined inside either the trenches through the Au layer or around the Au bars at the bottom of the SiO_2 trenches. For instance, the corresponding near-field distributions for these two peaks show mostly dipolar excitations of the trenches perpendicular to the polarization axis of the incoming radiation with some multipolar or dipolar polarizations

of the tilted trenches for the peaks at 729 and 1789 nm, respectively (see Figure S1a,c,d,f in the Supplementary Materials).

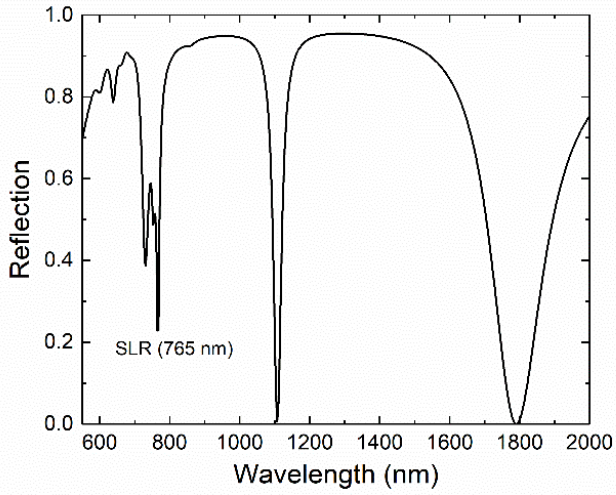

Figure 2. Simulated reflection spectrum as a function of the wavelength of the incident radiation. The sharp peaks at about 765 and 1107 nm correspond to the surface lattice resonance (SLR) of the Au inverted honeycomb lattice at the air–Au and Au–SiO_2 interfaces, respectively.

It is also worth noting that the positions of these two peaks can be tuned just by adding the Au mirror and varying the edge-to-edge distance between the inverted Au lattice and the Au mirror as there is a certain coupling with the images of these modes at the mirror. In such a way, 200 nm was chosen for the edge-to-edge distance so that the peak at 729 nm was blue-shifted to be on the left-hand side of the sharp peak at 765 nm, which is the one we are intending to use for sensing applications. In a similar way, the edge-to-edge distance between the inverted Au lattice and the direct one was optimized to be 50 nm to reduce the overlap between the peaks at 729 and 765 nm.

In the second group of excitations shown in Figure 2, there are those with a collective character that are associated with SLRs. The corresponding peaks are the aforementioned one at 765 nm and the ones located about 754 and 1107 nm. These three peaks arise from the constructive interference between the incident radiation and the collective modes of the direct and inverted honeycomb plasmonic lattices. Considering that SLRs are excited at the interface between the Au and the surrounding dielectric media, two SLRs should be expected for each honeycomb lattice as both the direct and the inverted Au arrays are in contact with two different dielectric media, namely air (above) and SiO_2 (below). For a hexagonal lattice, which is the Bravais lattice of the honeycomb array, the condition for the excitation with perpendicular incidence of the most intense SLR is

$$\lambda_i = n_i \, p \cos 30, \tag{1}$$

where λ_i is the resonant wavelength of the incident radiation, p is the pitch of the hexagonal lattice ($p = 866$ nm; see Figure 1b), and n_i is the effective refractive index of the dielectric medium forming the interface with the Au layer. Taking average values of the refractive indices of air and SiO_2 as 1 and 1.45, respectively, the expected wavelengths that fulfill Equation (1) are 750 nm and 1087 nm, respectively, in very close agreement with the positions of the peaks found by numerical simulation.

Thus, the small peak around 754 nm is mainly related to the SLR at the interface with the air of the direct honeycomb lattice on the bottom of the SiO_2 trenches. This is supported by both the near-field distribution shown in Figure S1b,e in the Supplementary Materials

and the fact that this peak does not appear when the direct Au honeycomb lattice is not present, and the trenches are carved through the whole thickness of the SiO_2 layer down to the Au mirror (see Figure S2 in the Supplementary Materials). Interestingly, in the latter case, the peak around 729 nm remains almost unchanged, strengthening the argument that it is only associated with local modes of the trenches in the inverted Au lattice. The second SLR mode corresponding to the Au–SiO_2 interface of the direct honeycomb lattice may be likely overlapped with the intense peak around 1107 nm.

On the contrary, the two peaks around 765 and 1107 nm are associated with the two SLRs at the air–Au and Au–SiO_2 interfaces of the inverted honeycomb lattice, respectively. Both peaks are very intense and relatively sharp, which makes them suitable for applications. It is also worth noting that the overlap between the two peaks at 729 and 765 nm is somehow reduced by the coupling with the two-dimensional photonic crystal underneath the inverted plasmonic lattice, which is beneficial for sensing purposes. As a comparison, Figure S2 in Supplementary Materials shows the spectra for the cases of a continuous SiO_2 spacer of 200 nm in thickness and the same spacer, but with trenches carved through its entire thickness.

In addition, simulations of the near-field distributions on the heterostructure at 765 and 1107 nm reveal the formation of patterns of extended hotspots compatible with the translational symmetry of the hexagonal lattice. For the peak at 1107 nm, there are also some extra excitations inside the trenches of the inverted Au layer (Figure 3b) arising from the coupling between the SLR modes of the direct and the inverted lattices through the polarization of the regions of the trenches in between the two plasmonic lattices (see Figure 3d). Although the two peaks show very similar near-field patterns outside the trenches, it is interesting to note that, for the peak at 765 nm, the hotspots following the lattice symmetry are found on top of the plasmonic Au layer, whereas in the case of the peak at 1107 nm, the electric field enhancement takes place at the bottom interface with the SiO_2 layer (see Figure 3c,d). In both cases, the pattern of hotspots yields an out-of-plane electric field that extends hundreds of nanometers away from the corresponding interfaces. The corresponding distributions of the electric field enhancement spread deep inside the air and the SiO_2, respectively (see Figure 3c,d). It is precisely these out-of-plane near-field distributions associated with the SLR of the inverted honeycomb lattice that provide the heterostructure with strong sensing capabilities, as will be discussed in the following subsection.

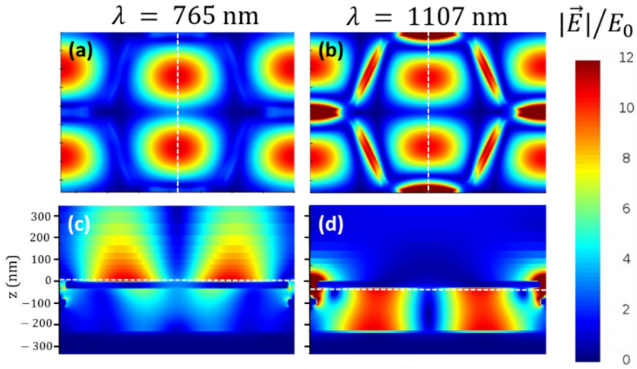

Figure 3. Near-field distributions associated with the SLR at 765 nm (**a**,**c**) and 1107 nm (**b**,**d**). (**a**,**b**) correspond to in-plane views 10 nm above and below the inverted honeycomb lattice, respectively, at the heights indicated by the dashed lines in the corresponding panels (**c**,**d**). (**c**,**d**) depict transversal cross sections of the heterostructure along the dashed lines plotted in the corresponding in-plane view panels (**a**,**b**), respectively. $|\vec{E}|/E_0$ stands for the normalized modulus of the electric field with respect to the modulus of the incident radiation.

3.2. Performance of the Refractive Index Sensor

The design of the plasmonic heterostructure following a lattice with three-fold symmetry hampers the excitation of the LSRs that are not fully compatible with the symmetry of a hexagonal lattice, because local modes imply polarizations with an even number of charge poles [20,21]. For instance, the three bar-shaped elements of the honeycomb lattice converging on each corner of the hexagons are not compatible with a simple dipolar mode within the gap between them. This favors the excitation of the SLRs yielding more intense absorption peaks, which in turn may improve the optical response of the system for sensing purposes. While preserving the honeycomb design, the system presented in this work does not follow direct realizations of a honeycomb lattice based on arrays of plasmonic nanoelements [26–28]. Instead, it takes advantage of the inverted version of the direct lattice. The main plasmonic structure presented here is, as opposed to a honeycomb array of bars, a continuous layer of Au where bar-shaped trenches are carved through its full thickness. According to Babinet's principle, the direct and the inverted structures should be equivalent in terms of their optical properties [14,29], showing the same excitations at the same values of the wavelength, but the nature of the excitations is different in the two structures. The electric dipoles formed in the direct structure are magnetic dipoles in the corresponding inverted realization and vice versa, because the role of the charge accumulation is played by the currents induced in the system in the complementary structure. Previous works show that, despite the similarities in the spectral behavior, inverted structures can perform better in terms of their interaction with the surrounding medium or an externally exciting source [7–9]. One particularly appealing characteristic of the inverted structures is that the near-field distributions tend to spread further away compared with the direct structure. The near-field distributions for the peaks at 765 and 1107 in Figure 3 are good examples of this spreading. In particular, the SLR at about 765 nm exhibits hotspots that extend out-of-plane largely away from the top Au–air interface. Then, any changes in the properties of the surrounding medium above the heterostructure will especially affect this excitation because the electric field is distributed in a relatively large volume that extends up to about 400 nm from the Au–air interface (see Figure 3c,d). This allows both to detect slight changes in the optical properties of a relatively distant region of the medium above and to boost the sensitivity of surface enhanced spectroscopies, such as Raman scattering.

In this work, we aim at presenting a sensing application based on the detection of small changes in the refractive index of the medium above the heterostructure by measuring the shift in the wavelength of the SLR at the interface with the top Au layer. More precisely, a 50 nm layer of a test material with a given refractive index is placed on top of the heterostructure. This layer is intended to model the adsorption on top of the heterostructure of some biological species, such as macromolecules or viruses (with refractive index values in the range of our test layer) or any other materials to be detected not fitting inside the trenches because of their relatively small width (30 nm). We decided to use a thin test layer to evidence the high sensitivity of the sensor. In Figure 4, the reflection spectra around the two SLR peaks of the inverted plasmonic structure are depicted for values of the refractive index of the test layer ranging from 1 to 1.45. Although the two peaks show remarkable shifts, the one for the SLR at the top test layer–Au interface is much larger, as expected from the corresponding near-field distributions shown in Figure 3. The fact that the near-field enhancement for this excitation is mostly distributed outside of the heterostructure makes its wavelength highly susceptible to changes in the surrounding medium.

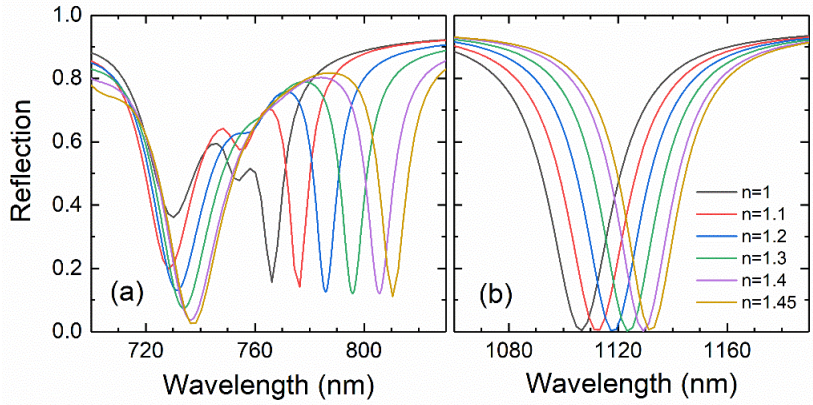

Figure 4. Reflection spectra around the wavelength ranges where the SLRs corresponding to the top (**a**) and bottom (**b**) interfaces of the Au inverted honeycomb lattice take place. The spectra were simulated for several values within 1.1 and 1.45 of the refractive index of a test layer of 50 nm in thickness resting on top of the heterostructure. The spectrum in Figure 2 without the test layer is included as a reference (black line).

It is worth noting that the shift in the wavelength of this resonance follows an almost perfectly linear dependence on the refractive index of the test layer (see Figure 5a). This can be easily understood considering that the resonant wavelength satisfying a SLR is linearly dependent on the effective refractive index of the dielectric medium that forms the interface with the Au layer, as shown in Equation (1). Hence, the sensitivity of the sensor computed from the slope of the linear dependence shown in Figure 5a is 99 nm/RIU (RIU stands for refractive index unit), which is a very remarkable result considering the small thickness of the test layer.

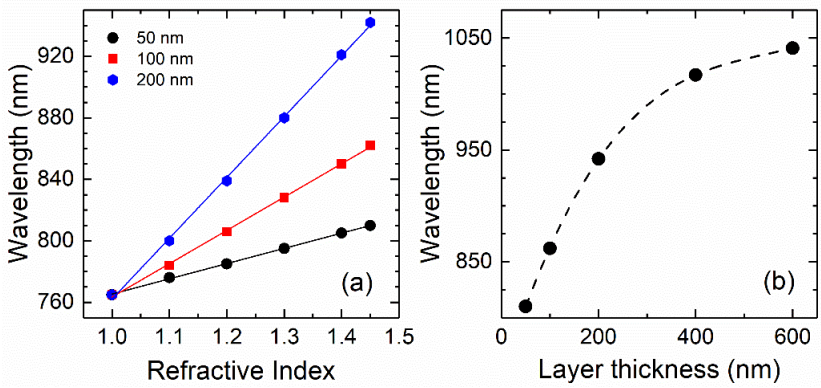

Figure 5. (**a**) Wavelength of the peak corresponding to the SLR at the test layer–Au interface as a function of the refractive index for three values of the test layer thickness, namely, 50, 100, and 200 nm. (**b**) Wavelength of the SLR peak corresponding to the test layer–Au interface for $n = 1.45$ as a function of the layer thickness. The dashed line is only a guide to the eye.

To determine the dependence of the sensitivity on the amount of test material, the same study was repeated for sensing layers of 100 and 200 nm in thickness, obtaining sensitivities of 216 and 395 nm/RIU, respectively (see Figure 5a). These results show an almost linear dependence of the sensor sensitivity on the thickness of the test material, at least in this range of relatively small thicknesses. This enables to quantify the amount of material deposited on the sensor provided its refractive index is known. In Figure 5b, the

wavelength of the SLR is depicted as a function of the thickness of the test layer. For a thickness larger than 400 nm (560 nm/RIU), the sensitivity significantly departs from the linear dependence tending to a maximum value slightly greater than that of the 600 nm layer (613 nm/RIU). Therefore, the sensitivity for test layers thicker than about 1000 nm can be considered thickness independent.

The performance of the heterostructure as a detector of an analyte present in a water medium was also tested. For this purpose, water was modelled by a 600 nm thick layer with a refractive index of 1.33 that also filled the bar-shaped trenches of the inverted honeycomb lattice. The presence of an analyte was simulated by changing the refractive index of the medium to 1.34. To ensure high sensitivity to such small changes of the refractive index, the variation of the intensity of the reflection peak at a given wavelength was measured, instead of the peak shift as in the previous cases, as the simplicity in detecting a signal at a fixed wavelength is of key importance for biosensing. The figure of merit (*FOM*) [30] for this kind of measurements is defined as follows:

$$FOM = \frac{dI/dn}{I_m}, \tag{2}$$

where dI is the variation in the intensity of the reflection peak corresponding to the SLR at the air–Au interface as a function of the wavelength, n is the refractive index of the medium, and I_m is the average of the intensities of the two spectra used in the calculation as a function of the wavelength. Thus, the shift in the position of the SLR peak as n varies is translated into a change of its intensity for a fixed wavelength. The computed values of the *FOM* as a function of the wavelength are shown in Figure 6 together with the two spectra used in the calculations. The maximum value of the *FOM* is 199 RIU^{-1} at a wavelength of 974 nm. This value can be compared with the sensitivity computed from Figure 4 (613 nm RIU^{-1} for a test layer of 600 nm in thickness) divided by the full width at half maximum of the peak, which is about 9 nm [31]. Finally, the minimum detectable change in the refractive index can be estimated. For a fixed wavelength of 981 nm, for which the *FOM* is maximized, there is a change of 0.48 in the reflection signal induced by a change of 0.01 RIU in the refractive index (see Figure 6). Considering a minimum detectable variation of 0.1 in the signal intensity, the minimum change in the refractive index that could be detectable by the system would be 0.002 RIU. These results are a solid proof of concept for further applications of these heterostructures for biosensing purposes.

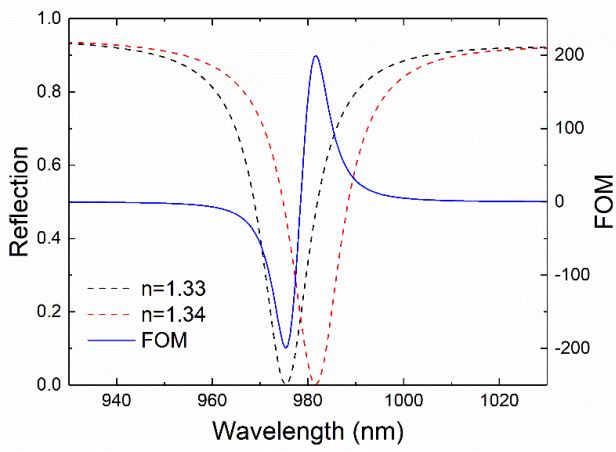

Figure 6. Reflection peak corresponding to the SLR at the test layer–Au interface for a test layer of 600 nm in thickness with values of the refractive index of 1.33 (black dashed line) and 1.34 (red dashed line). The blue solid line corresponds to the computed *FOM* from these two spectra using Equation (2).

3.3. Experimental Realization of the Heterostructure

In addition to the results of the simulations shown throughout this article, a preliminary experimental realization and optical characterization of the heterostructure were also carried out. We aimed at replicating as much as possible the design studied in the simulations while keeping in mind the ease and potential scalability in the manufacturing process. Hence, the parameters of the modelled system were followed, apart from the nanostructured layer of SiO_2 that was substituted by a PMMA layer with a thickness of 90 nm, giving an edge-to-edge distance between the inverted honeycomb lattice and the Au mirror of 190 nm instead of 200 nm, as was the case of the simulations. In this way, the PMMA layer was etched following a much more direct and easy lithographic method than would have been necessary for the SiO_2 layer, while preserving an almost equal value of the refractive index. The final metallization of the heterostructure yielded the Au inverted honeycomb lattice on top of the PMMA layer, but also an additional direct lattice on the bottom of the bar-shaped trenches carved through the PMMA layer. This was the reason the Au direct lattice was also included in the simulated model, because it is hard to avoid its formation following a simple manufacturing process. Nevertheless, the presence of this extra Au direct lattice does not significantly affect the collective excitations of the inverted Au layer, as proven by the simulation of the system without the direct lattice shown in Figure S2 in Supplementary Materials, while it hinders the excitation of the LSR at 729 nm by partially shielding the interaction of this mode and its corresponding image at the mirror (compare the intensity of this peak in the spectra in Figure 2 and Figure S2 in Supplementary Materials). Figure 7a shows an scanning electron microscopy (SEM) top-view image of the final heterostructure from which the overall good quality of the manufactured sample can be assessed.

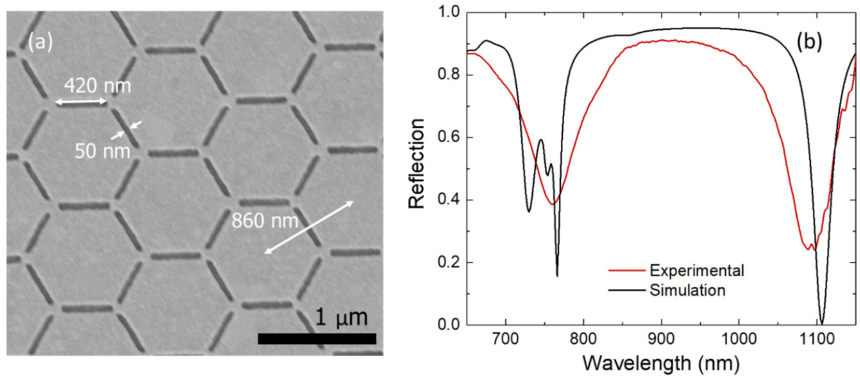

Figure 7. (**a**) SEM image of the manufactured sample. (**b**) Experimental (red curve) and simulated data (black curve) corresponding to the reflection spectrum as a function of the wavelength. The simulated curve is the same as in Figure 2 and is included here for the sake of comparison.

The optical characterization of the manufactured sample by FTIR spectroscopy showed the excitation of the two collective modes associated with the two interfaces of the inverted honeycomb lattice, as shown in Figure 7b. The peak corresponding to the SLR excited in the air–Au interface was broader than that of the SLR in the Au–PMMA interface. Experimental imperfections on the manufactured sample together with the existence of other excitations in the vicinity of the peak around 765 nm may cause their overlap, giving rise to a single broad peak. Nevertheless, the measured spectrum and the simulation results were in good agreement, thus proving the experimental feasibility of this heterostructure.

4. Discussion

The results shown in this work evidence the high performance of the presented heterostructure based on an Au inverted honeycomb lattice for sensing purposes. Owing to the chosen lattice pitch and because local excitations are hindered by the three-fold symmetry of the honeycomb array, this heterostructure exhibits very intense and narrow reflection peaks corresponding to its collective excitations at wavelengths in the near infrared that are well suited for sensing applications. The intensity of these peaks is further enhanced by the underneath layers within the heterostructure, namely, the patterned SiO_2 layer with the inverted honeycomb lattice, the SiO_2 spacer, and the Au mirror that ensures total reflection. Among the collective excitations shown by this heterostructure, the most suitable for sensing the refractive index of the environment is that associated with the peak around 765 nm. This peak is particularly susceptible to changes in the nearby environment because it arises at the top interface of the sensing Au layer, thus yielding an out-of-plane near-field distribution that spreads up and far away from the interface. The sensitivity associated with the shift of this peak was assessed by changing the refractive index of a thin layer of a test material resting on top of the heterostructure. Under these conditions, simulations showed a sensitivity of 99 nm/RIU for a layer of 50 nm in thickness with a full width at half maximum of the peak of only 9 nm. These results become especially relevant when compared with those of previous studies in which the refractive index change was tested in layers of infinite thickness [32,33]. Moreover, a further large shift in the resonant wavelength was also found for an increasing thickness of the test layer. This yielded a rising sensitivity for thicker test layers, opening another possible application of the studied heterostructure as a sensor of the amount of test material, provided its refractive index is known. The sensitivity of the sensor tended to a maximum value greater than about 613 nm/RIU for a thickness larger than about 600 nm, which is a very remarkable performance for this kind of sensor. Finally, the sensitivity of the sensor detecting slight changes of the refractive index at a fixed wavelength of a thick layer of a water medium was also checked. The computed *FOM* at 974 nm was as high as 199 RIU^{-1}. This value constitutes a solid improvement over other plasmonic sensors operating in a similar fashion that exhibit values of the *FOM* about one order of magnitude smaller [30,33–35].

As an experimental proof of concept, the heterostructure was manufactured by a simple method based on EBL. The FTIR spectrophotometry measurements showed intense and relatively narrow excitations around the wavelengths predicted by the simulations. These results show that an easy experimental realization of this heterostructure is possible, in a similar way to in [22], but avoiding the final lift-off process.

All in all, this work paves the way for the application of heterostructures based on inverted plasmonic lattices with three-fold symmetry to improve the performance of a wide range of plasmonic sensors and surface enhanced spectroscopies.

Supplementary Materials: The following are available online at https://www.mdpi.com/article/10.3390/nano11051217/s1, Figure S1: Near-field distributions for the peaks at 729, 754, and 1789 nm; Figure S2: Reflection spectra for a heterostructure without the Au direct lattice, where the trenches are carved through the whole thickness of the SiO_2 spacer, and for a heterostructure with a solid SiO_2 spacer of 200 nm in thickness with no trenches carved through it.

Author Contributions: Conceptualization, A.L., X.B. (Xavier Batlle), and A.F.R.; methodology, A.L. and J.R.-Á.; numerical simulations, J.R.-Á., L.G., and M.M.-C.; analysis of the results, J.R.-Á. and A.L.; design and manufacturing of the samples, A.G. and X.B. (Xavier Borrisé); writing—original draft preparation, J.R.-Á. and A.L.; writing—review and editing, A.L., X.B. (Xavier Batlle), and A.F.R. All authors have read and agreed to the published version of the manuscript.

Funding: This research was funded by Spanish MINECO, grant number PGC2018-097789-B-I00, and the European Union FEDER funds.

Institutional Review Board Statement: Not applicable.

Informed Consent Statement: Not applicable.

Data Availability Statement: Not applicable.

Acknowledgments: We want to thank Pau Molet and A. Mihi, Institut de Ciència de Materials de Barcelona (ICMAB-CSIC), for the FTIR measurements.

Conflicts of Interest: The authors declare no conflict of interest.

References

1. Frey, H.G.; Bolwien, C.; Brandenburg, A.; Ros, R.; Anselmetti, D. Optimized apertureless optical near-field probes with 15 nm optical resolution. *Nanotechnology* **2006**, *17*, 3105–3110. [CrossRef]
2. Kim, J.H.; Song, K.B. Recent progress of nano-technology with NSOM. *Micron* **2007**, *38*, 409–426. [CrossRef]
3. Carrara, A.; Maccaferri, N.; Cerea, A.; Bozzola, A.; De Angelis, F.; Proietti Zaccaria, R.; Toma, A. Plasmon Hybridization in Compressible Metal–Insulator–Metal Nanocavities: An Optical Approach for Sensing Deep Sub-Wavelength Deformation. *Adv. Opt. Mater.* **2020**, *8*, 1–8. [CrossRef]
4. Kneipp, K.; Kneipp, H.; Bohr, H.G. Single-Molecule SERS Spectroscopy. In *Surface-Enhanced Raman Scattering: Physics and Applications*; Springer: Berlin/Heidelberg, Germany, 2006; pp. 261–277. ISBN 978-3-540-33566-5.
5. Vo-dinh, T.; Wang, H.; Scaffidi, J. Plasmonic nanoprobes for SERS biosensing and bioimaging. *J. Biophotonics* **2010**, *102*, 89–102. [CrossRef]
6. Cho, W.J.; Kim, Y.; Kim, J.K. Ultrahigh-Density Array of Silver Nanoclusters for SERS Substrate with High Sensitivity and Excellent Reproducibility. *ACS Nano* **2012**, *6*, 249–255. [CrossRef] [PubMed]
7. Shanmukh, S.; Jones, L.; Driskell, J.; Zhao, Y.; Dluhy, R.; Tripp, R.A. Rapid and Sensitive Detection of Respiratory Virus Molecular Signatures Using a Silver Nanorod Array SERS Substrate. *Nano Lett.* **2006**, *6*, 2630–2636. [CrossRef] [PubMed]
8. Article, R.; Dong, J.; Zhang, Z.; Zheng, H.; Sun, M.; Access, O. Recent Progress on Plasmon-Enhanced Fluorescence. *Nanophotonics* **2015**, *4*, 472–490. [CrossRef]
9. Bauch, M.; Toma, K.; Toma, M. Plasmon-Enhanced Fluorescence Biosensors: A Review. *Plasmonics* **2014**, *9*, 781–799. [CrossRef] [PubMed]
10. Chen, Q.; Liang, L.; Zheng, Q.L.; Zhang, Y.X.; Wen, L. On-chip readout plasmonic mid-IR gas sensor. *Opto-Electron. Adv.* **2020**, *3*, 1–13. [CrossRef]
11. Liu, N.; Weiss, T.; Mesch, M.; Langguth, L.; Eigenthaler, U.; Hirscher, M.; Sönnichsen, C.; Giessen, H. Planar metamaterial analogue of electromagnetically induced transparency for plasmonic sensing. *Nano Lett.* **2010**, *10*, 1103–1107. [CrossRef]
12. Hrtoň, M.; Konečná, A.; Horák, M.; Šikola, T.; Křápek, V. Plasmonic Antennas with Electric, Magnetic, and Electromagnetic Hot Spots Based on Babinet's Principle. *Phys. Rev. Appl.* **2020**, *13*, 054045. [CrossRef]
13. Horák, M.; Křápek, V.; Hrtoň, M.; Konečná, A.; Ligmajer, F.; Stöger-Pollach, M.; Šamořil, T.; Paták, A.; Édes, Z.; Metelka, O.; et al. Limits of Babinet's principle for solid and hollow plasmonic antennas. *Sci. Rep.* **2019**, *9*, 4004. [CrossRef] [PubMed]
14. Falcone, F.; Lopetegi, T.; Laso, M.A.G.; Baena, J.D.; Bonache, J.; Beruete, M.; Marques, R.; Martín, F.; Sorolla, M. Babinet principle applied to the design of metasurfaces and metamaterials. *Phys. Rev. Lett.* **2004**, *93*, 2–5. [CrossRef] [PubMed]
15. Qin, F.; Ding, L.; Zhang, L.; Monticone, F.; Chum, C.C.; Deng, J.; Mei, S.; Li, Y.; Teng, J.; Hong, M.; et al. Hybrid bilayer plasmonic metasurface efficiently manipulates visible light. *Sci. Adv.* **2016**, *2*, 1–9. [CrossRef] [PubMed]
16. Huck, C.; Vogt, J.; Sendner, M.; Hengstler, D.; Neubrech, F.; Pucci, A. Plasmonic Enhancement of Infrared Vibrational Signals: Nanoslits versus Nanorods. *ACS Photonics* **2015**, *2*, 1489–1497. [CrossRef]
17. Stewart, M.E.; Mack, N.H.; Malyarchuk, V.; Soares, J.A.N.T.; Lee, T.W.; Gray, S.K.; Nuzzo, R.G.; Rogers, J.A. Quantitative multispectral biosensing and 1D imaging using quasi-3D plasmonic crystals. *Proc. Natl. Acad. Sci. USA* **2006**, *103*, 17143–17148. [CrossRef]
18. Kannegulla, A.; Liu, Y.; Wu, B.; Cheng, L. Plasmonic Open-Ring Nanoarrays for Broadband Fluorescence Enhancement and Ultrasensitive DNA Detection. *J. Phys. Chem. C* **2018**, *122*, 770–776. [CrossRef]
19. Ni, X.; Ishii, S.; Kildishev, A.V.; Shalaev, V.M. Ultra-thin, planar, Babinet-inverted plasmonic metalenses. *Light Sci. Appl.* **2013**, *2*, e72. [CrossRef]
20. Conde-Rubio, A.; Fraile Rodríguez, A.; Espinha, A.; Mihi, A.; Pérez-Murano, F.; Batlle, X.; Labarta, A. Geometric frustration in ordered lattices of plasmonic nanoelements. *Sci. Rep.* **2019**, *9*, 1–10. [CrossRef]
21. Conde-Rubio, A.; Rodríguez, A.F.; Borrisé, X.; Perez-Murano, F.; Batlle, X.; Labarta, A. Geometric frustration in a hexagonal lattice of plasmonic nanoelements. *Opt. Express* **2018**, *26*, 20211. [CrossRef]
22. Chen, Y.; Dai, J.; Yan, M.; Qiu, M. Metal-insulator-metal plasmonic absorbers: Influence of lattice. *Opt. Express* **2014**, *22*, 30807. [CrossRef]
23. Humphrey, A.D.; Barnes, W.L. Plasmonic surface lattice resonances on arrays of different lattice symmetry. *Phys. Rev. B Condens. Matter Mater. Phys.* **2014**, *90*, 1–8. [CrossRef]
24. Lumerical Inc. Innovative Photonic Design Tools. Available online: https://www.lumerical.com/ (accessed on 11 January 2021).
25. Palik, E.D. *Handbook of Optical Constants of Solids*; Palik, E.D., Ed.; Academic Press: Washington, DC, USA, 1985; ISBN 978-0-08-054721-3.
26. Johnson, P.B.; Christy, R.W. Optical Constant of the Nobel Metals. *Phys. Rev. B* **1972**, *6*, 4370–4379. [CrossRef]
27. Tok, R.U.; Şendur, K. Engineering the broadband spectrum of close-packed plasmonic honeycomb array surfaces. *J. Quant. Spectrosc. Radiat. Transf.* **2013**, *120*, 70–80. [CrossRef]

28. Chen, Y.; Dai, J.; Yan, M.; Qiu, M. Honeycomb-lattice plasmonic absorbers at NIR: Anomalous high-order resonance. *Opt. Express* **2013**, *21*, 20873. [CrossRef] [PubMed]
29. Zhang, T.; He, J.; Xie, W.; Sun, C. Plasmonic properties of a honeycomb structure formed by metallic nanoparticles. *Phys. E Low-Dimens. Syst. Nanostructures* **2020**, *118*, 113901. [CrossRef]
30. Hentschel, M.; Weiss, T.; Bagheri, S.; Giessen, H. Babinet to the half: Coupling of solid and inverse plasmonic structures. *Nano Lett.* **2013**, *13*, 4428–4433. [CrossRef]
31. Becker, J.; Trügler, A.; Jakab, A.; Hohenester, U.; Sönnichsen, C. The optimal aspect ratio of gold nanorods for plasmonic bio-sensing. *Plasmonics* **2010**, *5*, 161–167. [CrossRef]
32. Sherry, L.J.; Chang, S.-H.; Schatz, G.C.; Duyne, R.P.V. Localized surface plasmon resonance of single silver nanocubes. *Nano Lett.* **2005**, *5*, 2034–2038. [CrossRef]
33. Agharazy Dormeny, A.; Abedini Sohi, P.; Kahrizi, M. Design and simulation of a refractive index sensor based on SPR and LSPR using gold nanostructures. *Results Phys.* **2020**, *16*, 102869. [CrossRef]
34. Wang, X.; Zhu, J.; Wen, X.; Wu, X.; Wu, Y.; Su, Y.; Tong, H.; Qi, Y.; Yang, H. Wide range refractive index sensor based on a coupled structure of Au nanocubes and Au film. *Opt. Mater. Express* **2019**, *9*, 3079. [CrossRef]
35. Hicks, E.M.; Zhang, X.; Zou, S.; Lyandres, O.; Spears, K.G.; Schatz, G.C.; Van Duyne, R.P. Plasmonic properties of film over nanowell surfaces fabricated by nanosphere lithography. *J. Phys. Chem. B* **2005**, *109*, 22351–22358. [CrossRef] [PubMed]

Supplementary Materials

An inverted honeycomb plasmonic lattice as an efficient refractive index sensor

Javier Rodríguez-Álvarez[1,2,*], Lorenzo Gnoatto[1], Marc Martinez-Castells[1], Albert Guerrero[3], Xavier Borrisé[4], Arantxa Fraile Rodríguez[1,2], Xavier Batlle[1,2] and Amílcar Labarta[1,2]

Departament de Física de la Matèria Condensada, Universitat de Barcelona, 08028 Barcelona, Spain
[2] Institut de Nanociència i Nanotecnologia (IN2UB), Barcelona, 08028, Spain
[3] Institut de Microelectrónica de Barcelona (IMB-CNM, CSIC), Bellaterra, 08193, Spain
[4] Catalan Institute of Nanoscience and Nanotechnology (ICN2), CSIC and The Barcelona Institute of Science and Technology, Campus UAB, Bellaterra, 08193 Barcelona, Spain
* E-mail:javier.rodriguez@ub.edu

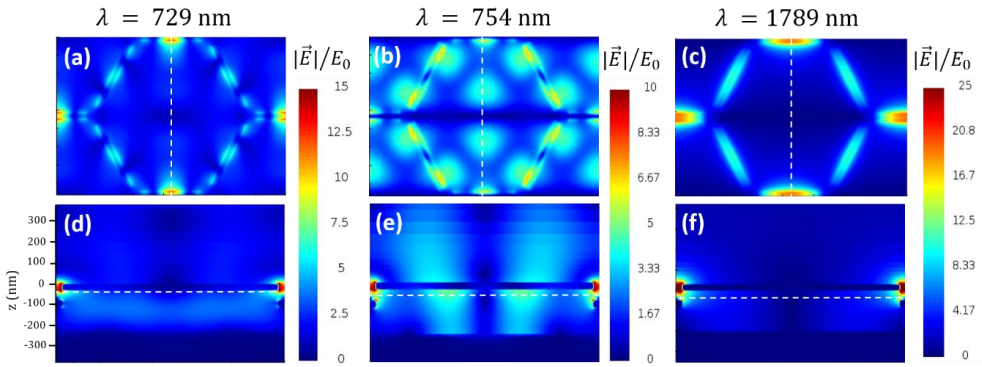

Figure S1. Near-field distributions for the peaks at 729 nm (a) and (d), 754 nm (b) and (e), and 1789 nm (c) and (f). (a), (b), and (c) correspond to in-plane views at the heights indicated by the dashed lines in the corresponding panels (d), (e), and (f). (d), (e), and (f) depict transversal cross sections of the heterostructure along the dashed lines plotted in the corresponding in-plane view panels (a), (b) and (c), respectively. They share a common vertical scale. $|\vec{E}|/E_0$ stands for the normalized modulus of the electric field with respect to the modulus of the incident radiation.

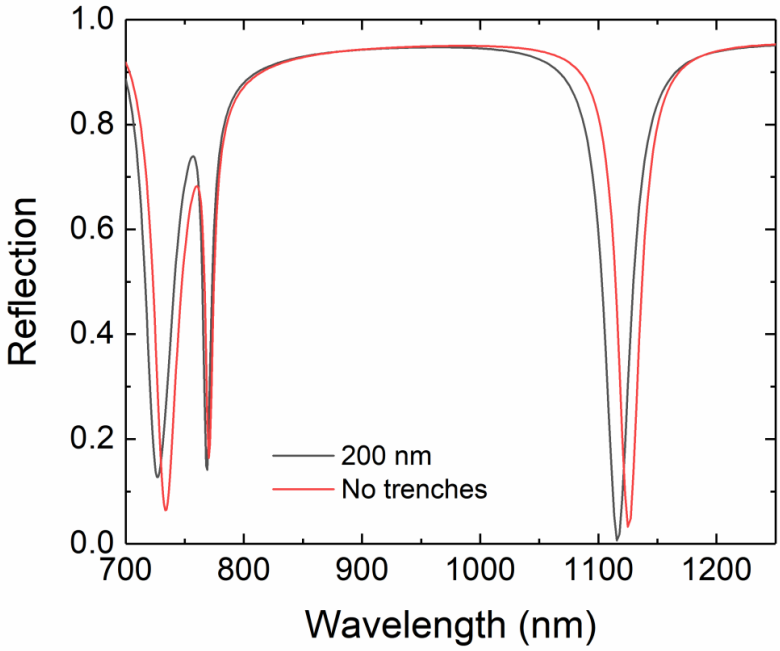

Figure S2. Reflection spectra for a heterostructure without the direct Au honeycomb lattice for the following two cases: a system with trenches carved through the whole thickness of 200 nm of the SiO_2 layer within the top-Au and mirror layers (black solid line) and a system with no trenches and a continuous SiO_2 layer (red solid line). The rest of the parameters are the same as those for the heterostructure in Figure 1.

ACSNANO

www.acsnano.org

ARTICLE

Imaging of Antiferroelectric Dark Modes in an Inverted Plasmonic Lattice

Javier Rodríguez-Álvarez,* Amílcar Labarta, Juan Carlos Idrobo, Rossana Dell'Anna, Alessandro Cian, Damiano Giubertoni, Xavier Borrisé, Albert Guerrero, Francesc Perez-Murano, Arantxa Fraile Rodríguez, and Xavier Batlle

Cite This: *ACS Nano* 2023, 17, 8123–8132

Read Online

ACCESS | Metrics & More | Article Recommendations | Supporting Information

ABSTRACT: **Plasmonic lattice nanostructures are of technological interest because of their capacity to manipulate light below the diffraction limit. Here, we present a detailed study of dark and bright modes in the visible and near-infrared energy regime of an inverted plasmonic honeycomb lattice by a combination of Au^+ focused ion beam lithography with nanometric resolution, optical and electron spectroscopy, and finite-difference time-domain simulations. The lattice consists of slits carved in a gold thin film, exhibiting hotspots and a set of bright and dark modes. We proposed that some of the dark modes detected by electron energy-loss spectroscopy are caused by antiferroelectric arrangements of the slit polarizations with two times the size of the hexagonal unit cell. The plasmonic resonances take place within the 0.5−2 eV energy range, indicating that they could be suitable for a synergistic coupling with excitons in two-dimensional transition metal dichalcogenides materials or for designing nanoscale sensing platforms based on near-field enhancement over a metallic surface.**

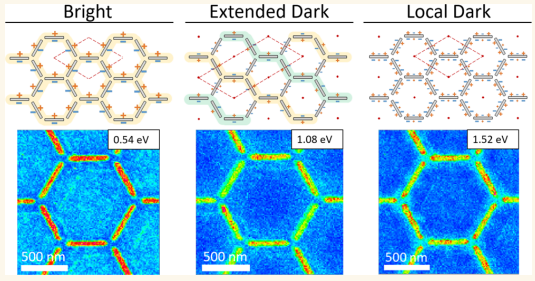

KEYWORDS: *plasmonic, honeycomb lattice, inverted lattice, dark modes, EELS, antiferroelectric, SLR*

Localized surface plasmons (LSP) can be excited at the interface between a metallic nanostructure and a dielectric medium by coupling with an external electromagnetic wave under the appropriate conditions.[1] LSP excitations create subwavelength confinement of the light in the vicinity of the nanostructures, as well as an enhanced intensity of such a near-field distribution.[2−4] Consequently, they have extensively been used in a wide variety of applications involving electromagnetic radiation in the infrared-visible-ultraviolet range, such as nanoantennas,[5] high sensitivity spectroscopies,[6,7] biomedical applications,[8−10] nonlinear harmonic generation,[11] ultrafast phase modulation,[12] and sensors[13] among others.

An additional level of complexity arises when metallic nanostructures are organized in a periodic array. In this case, the radiative coupling between the LSP and the diffracted waves in the plane of the array enables the appearance of coherent excitations of the scatterers in the lattice, known as surface lattice resonances (SLR). Introduced by Carron and co-workers[14] and found experimentally by Hicks and co-workers,[15] the excitation of these resonances occurs near the frequency at which the diffracted wave is radiating in the plane of the array, that is, at the Rayleigh anomaly. Experimental realizations of lattices of plasmonic nanostructures vary considerably, both in design and functionality.[16−18] Although the LSP of neighboring nanoparticles can also be coupled, the corresponding excitations are severely affected by radiative damping. SLR, in contrast, often exhibit highly tunable, intense and narrow resonances.[19]

In this work, we focus on geometrically frustrated honeycomb lattices, which have previously been studied for its unique plasmonic band structure and its similarities with the behavior of graphene and other 2D materials.[20−22] We investigate the plasmonic properties of an inverted honeycomb lattice (inverted as the nanostructure is carved in a continuous layer). The interest for inverted structures arises, among other applications, from further increasing the sensitivity of surface enhanced Raman spectroscopy (SERS) to ultrasmall amounts

Received: November 4, 2022
Accepted: April 11, 2023
Published: April 24, 2023

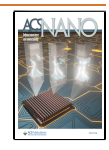

of a given analyte,[20,23] which is relevant for the detection of diseases in early stages[24] and traces of contaminants in wastewater.[25] According to Babinet's principle[21,22], the optical response of a plasmonic nanostructure must be equivalent to that of its inverted counterpart. Besides, the excitation of SLR is perfectly possible in these type of inverted systems.[20] This enables designing inverted structures with a very similar spectral behavior to their counterparts, in terms of the excitation energy and spectral features of the resonances - while corresponding to a very different near-field distribution around the structure.[22,26,27]

Here we show that the manufacture of a honeycomb array of slits fosters the formation of out-of-plane hotspots related to the SLR that present large enhancement factors of the electric field, even hundreds of nanometers away from the 2D array into the surrounding medium. Such an out-of-plane electric field enhancement is crucial for their integration in sensing and advanced spectroscopic architectures such as refractive index sensors.[28]

The implementation of any design pathway for enhanced plasmonic nanoarchitectures requires of an understanding of the plasmonic near-field response. A possible route to obtain a clear picture of the plasmonic resonances supported by a particular structure is to use electron energy loss spectroscopy (EELS). This technique, probing the local photonic density of states,[29] allows the excitation and mapping of the local distribution of electromagnetic modes by measuring a spectrum of the energy loss resulting from local interactions with the sample, thereby becoming an important tool for near-field imaging of plasmonic optical excitations.[30] When performed in a monochromated aberration-corrected scanning transmission electron microscope (STEM), the achieved energy resolution of EELS can be of the order of 10 meV while preserving sub-Å spatial resolution.[31−34] A crucial advantage of this technique is the combination of the spectral features with their 2D projected intensity maps, allowing high sensitivity to subtle spatial modifications.[35] In the case of studying plasmonic responses with a STEM, an acquired EELS signal is closely related to the optical extinction spectra, and has proven to be a useful tool for studying localized and surface plasmon resonances of a variety of structures, including films, pillars, and holes of varying diameters, as well as slots and coaxial resonators,[36] metallic nanostructures,[37−39] nanocavities,[40,41] nanowires,[42] surface-plasmon modes in nanoparticles,[43,44] coupled nanoparticles,[45] molecular excitations,[46] or excitation of modes in 3D.[47] In addition to the experimental contributions, advances in EELS simulations and theoretical modeling have also been crucial for interpretation of the results.[35,48−50]

A key aspect regarding our work is the fact that, in addition to bright modes, EELS can also reveal optically dark modes,[35,36,51−54] that is, modes with a vanishing net dipole moment, thereby providing a full modal spectral map of a plasmonic system. Dark modes can store electromagnetic energy more efficiently than bright modes due to suppression of radiative losses. This results in narrower line widths and longer lifetimes than their radiative counterpart, making them ideal candidates for lossless nanoscale waveguides and subwavelength high-Q optical cavities,[55] as well as enhanced biological and chemical sensors or nanolasing applications.[56−59]

In this work, we focus on the excitation and mapping of the bright and dark plasmonic resonances associated with the SLR and LSP modes in the optical range, which was achieved through the combination of state-of-the-art manufacturing of the samples and the outstanding spectral and spatial resolution of the STEM. A comprehensive spectral analysis of both the far-field and near-field measurements from Fourier-transform infrared spectroscopy (FTIR) and EELS, respectively, and the good agreement with the numerical electromagnetic simulations have enabled the identification of a variety of both bright and dark modes, the latter unable to be detected using light. Furthermore, dark modes that are be caused by arrangements of the slit polarizations that divide the system into two antiferroelectric sublattices have been found. These modes present a primitive unit cell twice that of the fabricated honeycomb lattice.

RESULTS AND DISCUSSION

The studied sample consists in a 20 nm thick continuous layer of Au deposited on a thin (50 nm) Si_3N_4 membrane. The Au layer is patterned by carving slits through the entire thickness of the Au layer. The slits are approximately 400 nm long and 45 nm wide. They follow the arrangement of a honeycomb lattice with a pitch of p = 906 nm. This structure can be considered as a dielectric (air) planar honeycomb lattice embedded in a metallic (Au) layer (see Figure 1).

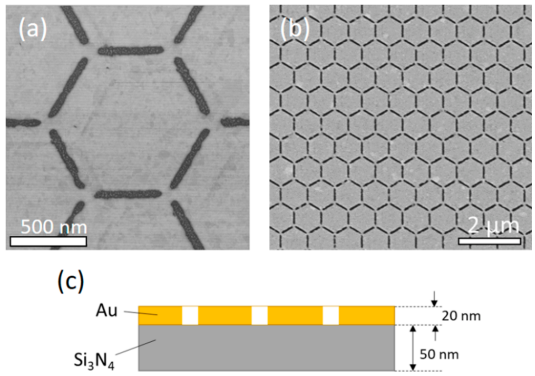

Figure 1. (a, b) Scanning electron microscopy images of the manufactured sample. (c) Schematic cross-sectional view of the studied sample.

The response of the structure presents a plethora of resonances in the visible and near-infrared (NIR) ranges. This is clear from the finite-difference time-domain (FDTD) simulations, FTIR measurements, and the data acquired during the EELS experiments. The corresponding spectral results are presented in Figure 2. Prior to an in-depth discussion, it is important to stress the differences between the three data sets shown in Figure 2.

FDTD simulations and FTIR measurements show the response of the system under the excitation of unpolarized light with normal incidence onto the array. However, EELS data rely on the energy-loss of a highly monochromatic beam of electrons that are inelastically scattered by the system. Therefore, FDTD simulation and FTIR data show only peaks associated with bright modes since electromagnetic radiation can only couple with modes exhibiting a net dipole moment.[55] In contrast, the scattering of electrons in an EELS experiment will excite all the available resonances in the structure,[50,60]

https://doi.org/10.1021/acsnano.2c11016
ACS Nano 2023, 17, 8123−8132

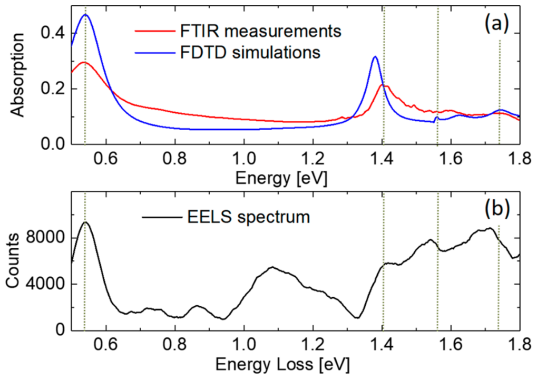

Figure 2. Absorption spectra obtained through (a) FDTD simulations (blue line) and FTIR measurements (red line). (b) EEL spectrum computed as the integral of the counts across the whole hexagon (black line). Peaks and anomalies only present in the EELS spectrum are associated with the excitation of dark modes by electron scattering. EELS and FTIR measurements were performed on the same sample. Vertical dashed lines indicate the energy of the bright modes that are discussed in the text.

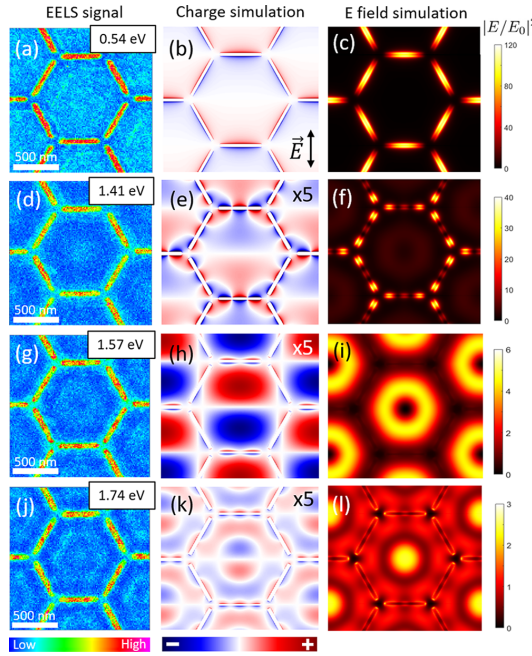

Figure 3. Left hand-side panels (a, d, g, and j) show colormaps of the EELS signal across the sample for the four bright modes indicated in Figure 2. The color scale bar represents the intensity of the EELS signal. Middle panels (b, e, h, and k) depict the calculated charge distribution on the surface of the array for the same bright modes from the FDTD simulations under the illumination of linearly polarized light along the vertical axis. Blue and red colors represent negative and positive net charge densities, respectively. The charge intensity has been multiplied by a factor, indicated by the number on the top-right side of the panels, for an easier comparison between resonances. Right hand-side panels (c, f, i, and l) show simulations of the corresponding electric field intensity under the illumination of unpolarized light. These colormaps were obtained 10 nm above the structure.

including not only bright modes but also dark ones (those showing zero net dipole moment). This constitutes a key point in understanding the differences and similarities among the three curves shown in Figure 2. We also point out that the peaks shown by the FDTD simulated absorption do not exactly match the location of those on the FTIR and EELS curves because of the imperfections of the experimental sample due to manufacturing defects, such as slight variations in size or vertical profile of the slits.

The lowest energy mode of the honeycomb array of slits appears around 0.54 eV and corresponds to a relatively intense broad peak that is clearly visible in the three spectra shown in Figure 2. It is a dipolar mode caused by the distribution of opposite charges round the longitudinal facing edges of each slit, as it is disclosed by the FTDT simulations of charge distributions shown in Figure 3b. Moreover, it is a bright mode since the net dipole moment corresponding to the three slits emanating from every vertex (primitive unit element of the lattice) in Figure 3b is nonzero along the vertical direction parallel to the polarization axis of the exciting radiation in the FDTD simulations. Note that the charge distributions shown in Figure 3 were obtained from an FDTD simulation with linearly polarized light in the vertical direction. EELS measurements and the distribution of the intensity of the electric field for unpolarized light obtained from FDTD simulations support the occurrence of significant values of the electric field only in the hollow space inside the slits (Figure 3a and c) in accordance with the major dipolar nature of the mode in the directions perpendicular to the slits.

To get a deeper insight into the energy of the rest of the bright modes, the values of the integral of the EELS signal computed in several specific regions of the hexagon are shown in Figure 4 as a function of the energy loss within 1.2 and 1.8 eV, the energy range where most of the bright modes appear.

The next bright mode can be found at about 1.41 eV in the EELS and FTIR curves, and at 1.38 eV in the simulated absorption (see Figure 2). At 1.41 eV, there is also a clear peak in the light brown curve in Figure 4a (region III), as well as some anomalies in the curves for region I in Figure 4a. Based on the results of the EELS mapping and the FDTD simulations for unpolarized light, the near-field distribution of this resonance presents a diffuse hotspot around the center of each hexagon accompanied by a multipolar excitation of the slits (Figure 3d and f).

The charge distribution shown in Figure 3e, which was obtained from an FDTD simulation with linearly polarized light in the vertical direction, also indicates a multipolar excitation of the slits. Each slit contains three parallel dipoles of alternating sign. So, as in the case of the previous excitation at 0.54 eV, every three converging slits at each vertex has a net dipole moment in the vertical direction. At the same time, the inferior and superior halves of the hexagons exhibit diffuse charges of opposite sign that contribute to the total dipole moment of the structure in the vertical direction (Figure 3e) and cause the central diffuse hotspot found under unpolarized radiation (see Figure 3d and f).

The mode at 1.57 eV corresponds to the coherent excitation of the whole lattice in a SLR. The small peak in the absorption spectrum obtained by FDTD simulations around this energy

https://doi.org/10.1021/acsnano.2c11016
ACS Nano 2023, 17, 8123−8132

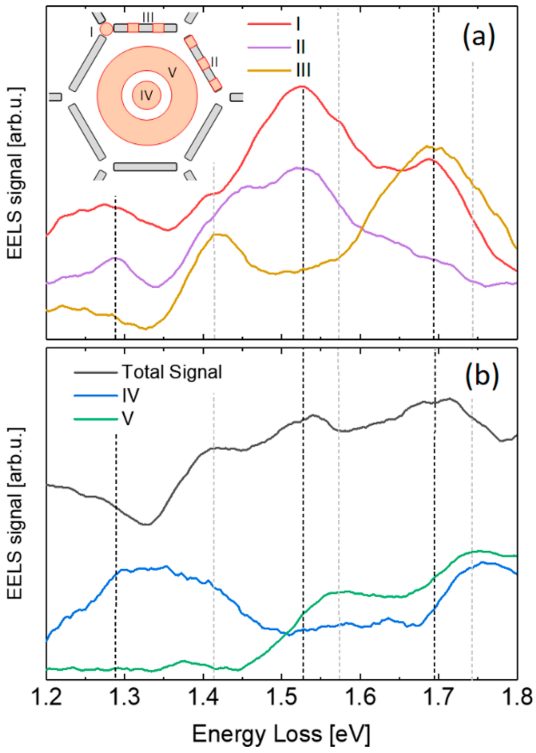

Figure 4. EEL spectra computed as the integral of the counts across the regions of the hexagon colored in orange in the inset of panel (a). (a) Red, purple, and light brown solid curves correspond to the integrals of the EELS signal over regions I, II, and III, respectively. (b) Blue and green solid curves correspond to the integrals of the EELS signal over regions IV and V, respectively. The total signal across the whole hexagon is also shown as the black solid line in panel (b) for the sake of comparison. The vertical dashed lines indicate the energy of the bright (gray lines) and dark (black lines) modes discussed in the text.

(blue curve in Figure 2a) is associated with the diffraction condition of the lattice at the interface between the metal and the air. In fact, a photon of 1.57 eV in air has a wavelength of 790 nm, which is very close to $p\cos 30 = 785$ nm, the first diffraction condition of the lattice for normal incidence, being p the pitch of the lattice. Interestingly, the imperfections of the experimental sample do not affect its pitch (see Figure 1a and b). This means that the SLR of the lattice takes place at the same energy as the FDTD simulations and experimental results. In this case, most of the excited charge is found to spread inside the hexagons, relatively far from the slits forming the array (see Figure 3h for FDTD results with linearly polarized light). The two opposite sign charge distributions in the upper and lower halves of each hexagon cause a large electric field with an out-of-plane component that extends hundreds of nanometers from the structure[28] (see Figure S1 in the Supporting Information). For unpolarized radiation with normal incidence, the charge distribution will oscillate from the center of the hexagon to the outer part following a kind of breathing mode and giving rise to the EELS signal and electric-field distribution depicted in Figure 3g and i. Moreover, the *xy*-plane crosscut for the *z*-component of the electric field shown in Figure S1 in the Supporting Information is also characteristic of a breathing mode.

Besides, for this mode, the intensity of the electric field for unpolarized light shows a central hotspot with a ring shape, revolving around a minimum of intensity at the center of the hexagon (see Figure 3i). It is worth noting that a central structure like that of Figure 3i is clearly distinguishable in the EELS colormap (Figure 3g). This qualitative interpretation of the EELS colormap is also quantitatively confirmed by the local maximum of the green curve in Figure 4b corresponding to the integral of the EELS signal in region V (central ring). It should also be noted that, in relation to this mode, a small shoulder is shown in the red curve in Figure 4a (region I corresponding to the vertex).

Finally, at an energy of 1.74 eV we find an excitation in the EELS experiment (Figure 3j) with a maximum in the center of the hexagons surrounded by an approximately hexagonal hotspot. This central structure may appear due to an averaging along the directions perpendicular to the edges of the hexagon of charge distributions such that in Figure 3k for linearly polarized light in the vertical direction. The existence of this central structure can also be confirmed by the maxima in the green and blue curves in Figure 4b for the EELS signal integrated in regions V (central ring) and IV (central hotspot), respectively. In addition, the EELS map also suggests a multipolar excitation of the slits in agreement with the FDTD simulation for the electric field distribution in Figure 3l.

The four modes discussed so far are bright, since they display a net dipole moment per primitive unit cell of the hexagonal lattice. In this respect, they can be considered ferroelectric modes of the system, since the dipole moment per primitive cell forms a ferroelectric lattice with the same symmetry as that of the hexagonal array of slits.

In addition, dark modes are also excited in the structure. In this work, we present the detection of two types of dark modes. Depending on whether the unit cell of the charge distribution fits into a single primitive cell of the honeycomb lattice, or it extends outside of it, we will denote these modes as local or extended, respectively. A first approach to understanding the local charge distributions excited in a dark mode is to consider the behavior of three slits converging on the same vertex (Figure S2 in the Supporting Information) that will act as the unit element of the lattice. Bearing in mind that we are dealing with an inverted lattice, most of the excitation of this unit element will take place through currents flowing around the central vertex, giving rise to a central out-of-plane magnetic moment.[61] Therefore, by placing a perpendicular magnetic dipole source above the vertex shared by these three slits, several dark modes of increasing multipolar order can be simulated as the energy increases. The lowest energy dark mode (Figure S2a in the Supporting Information) shows a dipolar excitation across the slits, akin to the bright mode at 0.54 eV but, in this case, all the slits are equivalent due to the 3-fold symmetry of the element, and the net dipole moment vanishes. The other local dark modes shown by the simulations as the energy increases follow the same overall behavior but with multipolar excitation of the slits (see Figure S2b,c in the Supporting Information).

Homologous dark modes can be found in the inverted honeycomb lattice by exciting the system with an array of in-phase magnetic dipoles situated on those vertices of the hexagons that coincide with the Bravais lattice (see Methods

https://doi.org/10.1021/acsnano.2c11016
ACS Nano 2023, 17, 8123–8132

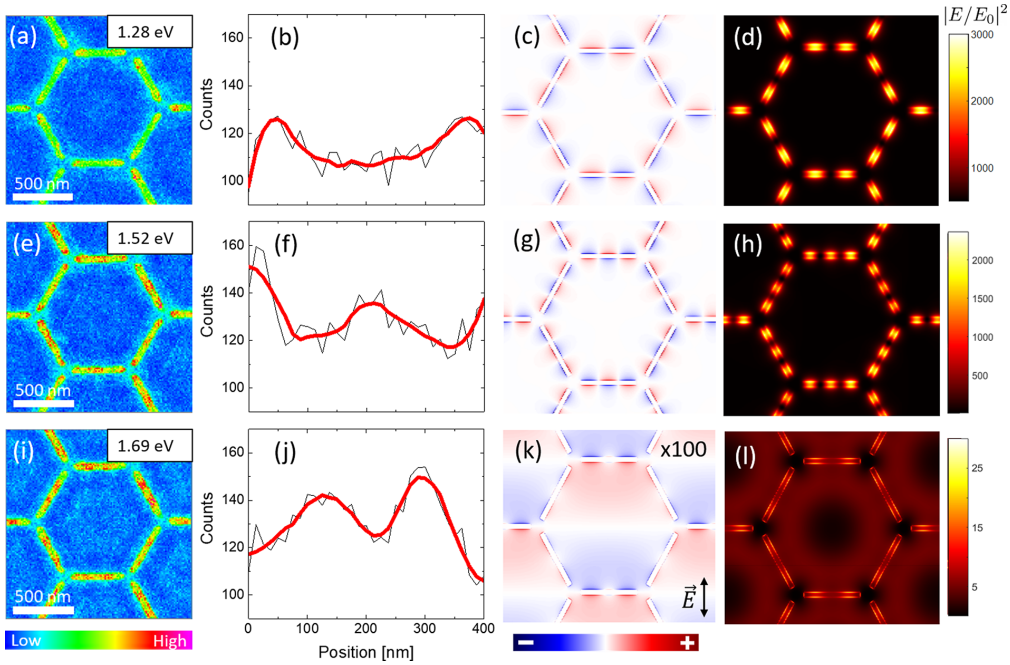

Figure 5. Left hand-side panels (a, e, and i) show colormaps of the EELS signal across the sample for the three dark modes indicated in Figure 4a. The color scale bar represents the intensity of the EELS signal. Panels (b, f, and j) depict the average of the profile of the EELS signal along the slits computed integrating the counts across the slits. Panels (c, g, and k) show the simulated charge distributions of these three dark modes. Right hand-side panels (d, h, and l) show the near field distribution for each energy computed 10 nm above the structure. Note that for the modes arising at 1.28 and 1.52 eV an array of magnetic dipoles has been used to excite the system, whereas for the mode at 1.69 eV the system has been excited using a combination of an array of magnetic dipoles and a plane wave with normal incidence. Panel (k) shows the charge distribution for the vertical polarization of the plane wave while panel l is the average between two orthogonal polarizations. These colormaps were obtained 10 nm above the structure.

section). The lowest energy dark mode found by simulation is shown in Figure S3 in the Supporting Information. However, due to the similarity between the near-field distributions of this mode and that of the broad bright one at 0.54 eV and the spectral proximity of both, this excitation cannot be distinguished in the EELS spectrum in Figure 2. The rest of the local dark modes are presented in Figure 5, in order of increasing energy. Figure 5b shows the average of the profile of the EELS signal at 1.28 eV computed as the integral across the slits, where the purple curve in Figure 4a (EELS signal from the ends and center of the slits) exhibits a local maximum. This profile supports the fact that most of the excitation occurs at both ends of the slits following a quadrupolar polarization, and is in good agreement with the simulated charge and near-field distributions in Figure 5c,d. We point out that any quadrupolar arrangement of the charge distribution around the slits nonhaving 3-fold symmetry gives rise also to dark modes of similar energies.

At 1.52 eV there are local maxima in the red (EELS signal at the vertices of the hexagonal lattice) and purple (EELS signal from the ends and center of the slits) curves in Figure 4a that are associated with a dark mode with the sextupole polarization of the slits. Accordingly, the respective EELS profile along the slits (see Figure 5f) shows three approximately equidistant poles. The results of the simulations using magnetic dipole sources shown in Figure 5g,h support this interpretation.

Finally, at about 1.69 eV there are maxima in the red (EELS signal at the vertices of the hexagonal lattice) and light brown (EELS signal from regions of the slits that exclude their ends and center) curves in Figure 4a that coincide with a broad maximum in the curve for the total signal (black solid line in Figure 4b). In accordance with the results of the simulations with magnetic dipoles, this should be a dark mode with octupole polarization of the slits and relatively low intensity. However, only two poles close to the center of the slits are shown by both the EELS color map in Figure 5i and the profile of the EELS signal along the slits in Figure 5j. In addition, EELS color map in Figure 5i shows a distinctive ring around the center of the hexagon. Such an electric field pattern does not arise from the sole excitation of charge across the slits, but from a charge arrangement in the continuous gold layer found in the hexagons formed by the honeycomb lattice of slits. Therefore, this mode may result from the hybridization of the octupole dark mode and a bright mode like that at 1.74 eV. To simulate this mode, we have used the simultaneous excitation of the system by an array of in-phase magnetic dipoles like in the previous cases and a plane wave with normal incidence, aiming at exciting both dark and bright modes. The charge distribution depicted in Figure 5k, which was obtained for the polarization axis of the plane wave along the vertical direction, shows a kind of quadrupolar excitation close to the center of the horizontal slits (those perpendicular to the polarization axis

https://doi.org/10.1021/acsnano.2c11016
ACS Nano 2023, 17, 8123−8132

of the plane wave) that is compatible with the EELS profile shown in Figure 5j. Moreover, the near-field distribution computed for an unpolarized plane wave in Figure 5l shows overall features in qualitative agreement with EELS color map in Figure 5i, including the ring around the center of the hexagon and the two central poles in the slits.

In addition to the local dark modes discussed so far, there are several other ways to get an extended dark mode in an ordered lattice. For instance, the system can be divided into two sublattices of opposite net dipole moment per primitive unit cell, so that the net dipole moment cancels out in pairs of two primitive cells. This implies that there is a net dipole moment associated with each threesome of slits converging in a vertex coincident with the Bravais lattice (unit element of the lattice) that cancels out with the opposite net dipole moment of a neighboring threesome of slits. Therefore, the excitation of the slits in each of these threesomes must be nonequivalent under the 3-fold symmetry to have a net dipole moment, like in the bright modes.

Examples of this kind of dark modes can be simulated by FDTD using a tailored source of radiation that excites neighboring primitive unit cells in opposition of phase, in such a way that they form two antiparallel ferroelectric sublattices. An array of magnetic dipoles in phase opposition and placed above the vertices coincident with the Bravais lattice was the excitation source used for this purpose (see more details in the Methods section). Thus, Figure 6a,b shows an example of these extended dark modes at 0.68 eV where the charge across the slits alternates along the zigzag chains, and the remaining slits, rotated 60 degrees from the horizontal, are less charged and show a kind of quadrupolar excitation. This results in two antiferroelectric sublattices whose net dipole moments (indicated by arrows in Figure 6b) per primitive cell of the honeycomb lattice point in the direction of the zigzag chains and are arranged antiparallel to each other, so they cancel out in pairs of primitive cells. Note that the unit cell of the antiferroelectric mode is indicated by the dashed black line in Figure 6b and is two times bigger than that of the honeycomb lattice. It is worth noting that for this kind of extended dark modes, one of the slits of each threesome shows a different excitation (different multipolarity and/or intensity) than the other two, as expected. This is a distinctive feature of these extended dark modes that can be checked in the results of the simulations for the near-field distribution at other energies that are shown in Figure S4 in the Supporting Information. Consequently, there exists an almost continuous family of extended dark modes with increasing energy, where the differences among them come from the multipolarities of the slits in each threesome, and/or their relative intensities of excitation.

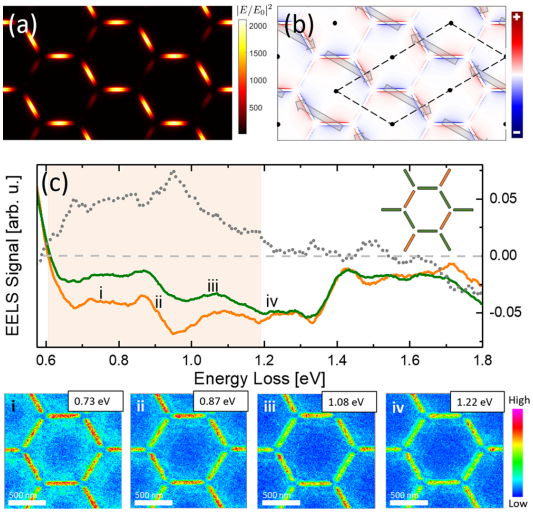

Figure 6. (a, b) Simulated electric field and charge distribution, respectively, corresponding to the antiferroelectric mode at 0.68 eV. The arrows in panel (b) indicate the total electrical dipole moments for threesomes of slits converging at points of the Bravais lattice. The dashed lines show a primitive unit cell of the antiferroelectric mode. (c) Average integral of the EELS signal computed separately over the two subsets of slits (the green and orange curves correspond to the green and orange subsets of slits in the inset showing a unit cell of the lattice, respectively). EELS color maps labeled with Roman numerals show some representative examples of the extended dark modes taking place in the energy range within 0.6 and 1.22 eV.

This kind of extended dark mode can be excited by EELS in the experimental sample as discussed below. Previous observations of local dark modes by EELS, among other techniques, have been reported.[36,45,62] Nevertheless, the finding of extended (antiferroelectric) dark modes is also reported in this work.

Between 0.6 and 1.4 eV, there are no bright modes in the spectral response of the system, so all the peaks and anomalies shown by the EELS signal in this range in Figure 2b could be assigned to dark modes. To find out the nature of these dark modes, we represent in Figure 6c the average integral of the EELS signal as a function of energy computed separately over two subsets of slits (those forming zigzag chains and the remaining ones, colored in green and orange in the inset of Figure 6c, respectively). Interestingly, the EELS signals for the green and orange slits coincide for the bright mode at 0.54 eV, as expected. But as the energy increases and becomes larger than 0.6 eV, the two curves in Figure 6c start to separate and stay that way until around 1.2 eV, from where they coincide again within the experimental error. In this energy range (light brown region in Figure 6c) the slits forming the zigzag chains (shown in green in the inset of Figure 6c) are excited more strongly than the remaining isolated slits (shown in orange in the inset of Figure 6c), indicating that the system cannot be excited through local dark modes, since, if that were the case, the intensity of excitation of the slits in each threesome would be equal. Consequently, there should be a net dipole moment associated with each threesome of slits converging in a vertex since the excitations of them are not equivalent under the 3-fold symmetry, and the system may be excited through a kind of extended dark mode, as described above. However, it is worth noting that, in an EELS experiment with an ideal sample, all the mode variants equivalent by symmetry (three in a honeycomb lattice) are simultaneously excited with the same probability, in such a way that the resulting state exhibits always the same average intensity and multipolarity for all the slits, even for an extended dark mode. In our case, the imperfections in the fabrication of the sample (especially in the oblique slits) enable a distinct excitation of the three variants of the extended mode, yielding an average state where the signature of an extended dark mode can be inferred by the

https://doi.org/10.1021/acsnano.2c11016
ACS Nano 2023, 17, 8123−8132

different excitation intensity of the three slits of each threesome.

The EELS color maps labeled with Roman numerals i, ii, iii, and iv in Figure 6c show some representative examples of the excitation of the system corresponding to three local maxima of the EELS signal in this energy range and the limit of the energy range where extended dark modes can be excited, respectively. The EELS color maps i and ii in Figure 6c and the EELS profiles along the slits in Figure S4,a,b in the Supporting Information indicate a dipolar excitation of the slits but with stronger intensity for the slits forming zigzag chains. The results of the simulations for the electric field and the average profile along the slits obtained with the array of magnetic dipoles in phase opposition (Figure S4e,f,i,j in the Supporting Information) are in qualitative agreement, since the average of the excitation of the three slits in a threesome has major dipolar character. On the contrary, the EELS color maps iii and iv in Figure 6 and the EELS profiles along the slits in Figures S4,c,d in the Supporting Information indicate a quadrupole excitation of the slits. The corresponding results of the simulations for the electric field and the average profiles along the slits (Figure S4g,h,k,l in the Supporting Information) point toward the quadrupole character of the average excitation of the slits. Therefore, as the energy increases from 0.6 eV, the average polarity of the extended dark modes progressively becomes of higher order, until the local dark mode corresponding to quadrupole excitation with the same intensity of all the slits in a threesome is reached at 1.28 eV.

At energies higher than about 1.7 eV, the EELS signals for the green and orange slits in the inset of Figure 6c start to significantly separate again, indicating the onset of a second range of energies where antiferroelectric dark modes may be excited, but with the intensity of the excitation of the two subsets of slits swapped with respect to those within 0.6 and 1.2 eV.

CONCLUSIONS

This work constitutes a comprehensive study of the plasmonic properties of an inverted honeycomb lattice of slits. The patterning quality of the samples, together with the spectral and spatial resolution of the EELS measurements has led to the direct observation and mapping of bright and dark plasmonic modes. A detailed description of the charge and near-field distributions in the structure has been given by virtue of the good agreement between the EELS measurements, the optical measurements, and simulations. Some of the dark modes found are caused by antiferroelectric arrangements of the slit polarizations, giving rise to charge arrangements with a unit cell two times larger than that of the original honeycomb lattice. Additionally, plasmonic modes exhibiting hotspots far from the discontinuities of the metallic layer are found, ranging from 1.3 to 1.8 eV approximately.

The behavior of the inverted honeycomb plasmonic lattice is relevant not only from a fundamental point of view. As shown in a previous work,[24] the appearance of hotspots far from the slits that form the lattice is highly correlated with a strong out-of-plane electric field ranging hundreds of nanometers away from the lattice. This electric field could foster a strong coupling of the plasmonic lattice with other materials allocated on top of the structure. Moreover, the inverted nature of this lattice, thanks to its large mostly planar surface, presents this system as a platform for exploiting new synergies with 2D materials. The exciton energies for 2D WSe_2 and MoS_2 on an Au substrate, 1.75 and 1.9 eV, respectively,[63] could be targeted by easily tuning manufacturing parameters such as the pitch of the lattice, thus changing the spectral position of the plasmonic resonances.

Other applications include transport measurements in 2D materials in which a local gating could be done by means of the hotspot in the nanostructure and the introduction of localized defects in the lattice.

METHODS

Manufacture Process. A thin Au film was deposited on a 50 nm thick Si_3N_4 membrane using an ultrahigh vacuum (UHV) electron beam evaporator. The Si_3N_4 membrane is 500 × 500 μm^2 wide. These types of structures are normally used as substrate for Transmission Electron Microscopy (TEM). The square membrane windows are centered on 200 μm thickness silicon frames.[64]

The measured Au film thickness was 19.4 nm with a root-mean-square roughness of 0.3 nm as measured by atomic force microscopy (AFM). The Au film was then patterned using a Raith Velion focused ion beam (FIB) equipped with an Au−Ge−Si liquid metal alloy ion source (LMAIS). A 35 keV Au^+ beam, ∼5 pA ion current intensity and ∼15 nm diameter, was used for patterning the hexagonal array of slits. Au^+ beam was chosen to avoid lateral contaminations along the milled lines that would occur with other commonly used ion species in FIB like Ga^+. The 350 × 350 μm^2 wide array was milled using 200 × 200 μm^2 writing fields and applying a 3000 pC/cm linear dose of Au^+ (single loop passage, 10 nm step between ion spots, and dwell time of 0.52 ms). This allowed for the patterning of the designed structures through the Au film while keeping the line width in plane of ∼45 nm.

FTIR Measurements. The optical characterization was carried out using a Vertex 70 Fourier transform infrared (FTIR) spectrophotometer attached to an optical microscope (Bruker Hyperion). Experiments were performed in the reflection and transmission configuration with 2× and 4× objectives, respectively, under unpolarized light illumination. A shutter was used to select the signal coming from the nanostructured area. The measured signal of the plain Au of a non-nanostructured area of the sample was used as a background for the reflection measurements, whereas the transmission of the light in air was used for calibrating the transmission measurements.

EELS Measurements. EEL spectra were collected using a Nion aberration-corrected high energy resolution monochromated EELS−STEM (Nion HERMES) operating at a 60 kV accelerating voltage, using a convergence semiangle of 30 mrad, a collection semiangle of 20 mrad, and a beam current of ∼10 pA.[52−54] The resulting energy resolution of the spectra, measured by the full-width half-maximum (fwhm) of the zero-loss peak was 60 meV.

FDTD Simulations. The simulations were performed using the finite-difference time-domain (FDTD) method, implemented in the solver provided by Lumerical.[65] The computation procedure starts by setting a 3D FDTD simulation with perfectly matched layers (PMLs) in the z-direction, perpendicular to the plane of the lattice and periodic boundary conditions in the other two directions, the x−y plane. Given the initial conditions, the software solves Maxwell's equations to determine the Fourier components of the electric and magnetic fields by using discrete time and spatial steps. The method allows for a direct observation of the physical phenomena taking place without imposing any further assumption on the behavior of the system. We obtained the transmission and reflection spectra by placing two monitors that compute the total power that flows through a surface. In addition, other monitors were placed on the surface of the sample and 10 nm above, from which we computed the charge and the electric field distributions, respectively.

An override mesh region was defined along the structure to ensure a correct level of detail in the description of the lattice. The cell size used was 3.816 × 3.824 × 1 nm^3 in the x-, y- and z-directions, respectively. The dielectric functions for the materials used in these

https://doi.org/10.1021/acsnano.2c11016
ACS Nano 2023, 17, 8123−8132

simulations were obtained by fitting analytical functions to the data from refs 66 and 67 for Si_3N_4 and Au, respectively.

In these simulations, four different types of excitation sources were used, depending on the targeted modes. Plane waves were the source of excitation for all the bright modes. The plane waves were injected at 500 nm from the structure following normal incidence and setting periodic boundary conditions in the $x-y$ plane for a unit cell of the system like that of the snapshots in Figure 3. For the simulations showing local dark modes, an array of in-phase magnetic dipoles, perpendicular to the system plane and placed 50 nm above the vertices of the hexagons coincident with the Bravais lattice, was the excitation procedure. Bloch boundary conditions in the x-y directions were set for the same unit cell than the one for the bright modes. The hybrid mode at 1.69 eV was simulated by the simultaneous excitation of a plane wave with normal incidence and the array of in-phase magnetic dipoles. Finally, for the antiferroelectric dark modes, an array of magnetic dipoles in phase opposition were placed 50 nm above the vertices coincident with the Bravais lattice (see Figure S5 in the Supporting Information). The simulation unit cell, as shown in Figure S5 in the Supporting Information, was larger than in the previous cases to enable the excitation of extended modes. Bloch boundary condition were used in the x-y directions.

ASSOCIATED CONTENT

Supporting Information

The Supporting Information is available free of charge at https://pubs.acs.org/doi/10.1021/acsnano.2c11016.

> Transversal electric field distribution for the SLR at 1.57 eV; simulated electric field and charge distributions for a threesome of slits; simulated electric field and charge distributions for the simplest local dark mode of the inverted honeycomb lattice; profiles of the EELS signal and the simulated electric field along the slits for the antiferroelectric dark modes; array of the magnetic dipoles over the structure used to simulate antiferroelectric dark modes (PDF)

AUTHOR INFORMATION

Corresponding Author

Javier Rodríguez-Álvarez − *Departament de Física de la Matèria Condensada, Universitat de Barcelona, Barcelona 08028, Spain; Institut de Nanociència i Nanotecnologia (IN2UB), Universitat de Barcelona, Barcelona 08028, Spain;* orcid.org/0000-0001-5822-4013; Email: javier.rodriguez@ub.edu

Authors

Amílcar Labarta − *Departament de Física de la Matèria Condensada, Universitat de Barcelona, Barcelona 08028, Spain; Institut de Nanociència i Nanotecnologia (IN2UB), Universitat de Barcelona, Barcelona 08028, Spain;* orcid.org/0000-0003-0904-4678

Juan Carlos Idrobo − *Materials Science and Engineering Department, University of Washington, Seattle, Washington 98195, United States*

Rossana Dell'Anna − *Sensors & Devices Center, FBK - Bruno Kessler Foundation, Povo, TN 38123, Italy;* orcid.org/0000-0001-7147-6127

Alessandro Cian − *Sensors & Devices Center, FBK - Bruno Kessler Foundation, Povo, TN 38123, Italy*

Damiano Giubertoni − *Sensors & Devices Center, FBK - Bruno Kessler Foundation, Povo, TN 38123, Italy;* orcid.org/0000-0001-8197-8729

Xavier Borrisé − *Catalan Institute of Nanoscience and Nanotechnology (ICN2), CSIC and BIST, Campus UAB, Bellaterra, Barcelona 08193, Spain*

Albert Guerrero − *Institut de Microelectrònica de Barcelona (IMB-CNM, CSIC), Bellaterra 08193, Spain*

Francesc Perez-Murano − *Institut de Microelectrònica de Barcelona (IMB-CNM, CSIC), Bellaterra 08193, Spain*

Arantxa Fraile Rodríguez − *Departament de Física de la Matèria Condensada, Universitat de Barcelona, Barcelona 08028, Spain; Institut de Nanociència i Nanotecnologia (IN2UB), Universitat de Barcelona, Barcelona 08028, Spain;* orcid.org/0000-0003-2722-0882

Xavier Batlle − *Departament de Física de la Matèria Condensada, Universitat de Barcelona, Barcelona 08028, Spain; Institut de Nanociència i Nanotecnologia (IN2UB), Universitat de Barcelona, Barcelona 08028, Spain;* orcid.org/0000-0001-7897-2692

Complete contact information is available at: https://pubs.acs.org/10.1021/acsnano.2c11016

Author Contributions

The manuscript was written through contributions of all authors. All authors have given approval to the final version of the manuscript.

Notes

The authors declare no competing financial interest.

ACKNOWLEDGMENTS

The authors want to thank Pau Molet and Agustín Mihi, Institut de Ciència de Materials de Barcelona (ICMAB-CSIC), for the FTIR measurements, and Paolo Mattevi of FBK for the UHV evaporation of Au on the Si_3N_4 membranes. This work was supported by Spanish ICTS Network MICRONANOFABS. The authors from Universitat de Barcelona thank the funding from Spanish MICIIN, grant numbers PGC2018-097789−B-I00 and PID2021-127397NB-I00, and the European Union FEDER funds. The EELS measurements were supported by the Center for Nanophase Materials Sciences (CNMS), which is a U.S. Department of Energy, Office of Science User Facility, and using instrumentation within ORNL's Materials Characterization Core provided by UT-Batelle, LLC, under Contract No. DE-AC05-00OR22725 with the U.S. Department of Energy, and sponsored by the Laboratory Directed Research and Development Program of Oak Ridge National Laboratory, managed by UT-Battelle, LLC, for the U.S. Department of Energy.

REFERENCES

(1) Maier, S. A. *Plasmonics fundamentals an applications*, 1st ed.; Springer: New York, 2007.

(2) Marinica, D. C.; Kazansky, A. K.; Nordlander, P.; Aizpurua, J.; Borisov, A. G. Quantum plasmonics: Nonlinear effects in the field enhancement of a plasmonic nanoparticle dimer. *Nano Lett.* **2012**, *12*, 1333−1339.

(3) Lee, B.; Lee, I. M.; Kim, S.; Oh, D. H.; Hesselink, L. Review on subwavelength confinement of light with plasmonics. *J. Mod. Opt.* **2010**, *57*, 1479−1497.

(4) Khurgin, J.; Tsai, W. Y.; Tsai, D. P.; Sun, G. Landau Damping and Limit to Field Confinement and Enhancement in Plasmonic Dimers. *ACS Photonics* **2017**, *4*, 2871−2880.

(5) Novotny, L.; Van Hulst, N. Antennas for light. *Nat. Photonics* **2011**, *5*, 83−90.

(6) Maccaferri, N.; Barbillon, G.; Koya, A. N.; Lu, G.; Acuna, G. P.; Garoli, D. Recent advances in plasmonic nanocavities for single-molecule spectroscopy. *Nanoscale Adv.* **2021**, *3*, 633−642.
(7) Cho, W. J.; Kim, Y.; Kim, J. K. Ultrahigh-Density Array of Silver Nanoclusters for SERS Substrate with High Sensitivity and Excellent Reproducibility. *ACS Nano* **2012**, *6*, 249−255.
(8) Vo-dinh, T.; Wang, H.; Scaffidi, J. Plasmonic nanoprobes for SERS biosensing and bioimaging. *J. Biophotonics* **2010**, *3*, 89−102.
(9) Bauch, M.; Toma, K.; Toma, M.; Zhang, Q.; Dostalek, J. Plasmon-Enhanced Fluorescence Biosensors : a Review. *Plasmonics* **2014**, *9*, 781−799.
(10) Sharifi, M.; Attar, F.; Saboury, A. A.; Akhtari, K.; Hooshmand, N.; Hasan, A.; El-Sayed, M. A.; Falahati, M. Plasmonic gold nanoparticles: Optical manipulation, imaging, drug delivery and therapy. *J. Controlled Release* **2019**, *311*−*312*, 170−189.
(11) Ahmadivand, A.; Gerislioglu, B. Deep- and vacuum-ultraviolet metaphotonic light sources. *Mater. Today* **2021**, *51*, 208−221.
(12) Smolyaninov, A.; El Amili, A.; Vallini, F.; Pappert, S.; Fainman, Y. Programmable plasmonic phase modulation of free-space wavefronts at gigahertz rates. *Nat. Photonics* **2019**, *13*, 431−435.
(13) Ahmadivand, A.; Gerislioglu, B. Photonic and Plasmonic Metasensors. *Laser Photonics Rev.* **2022**, *16*, 2100328.
(14) Carron, K. T.; Lehmann, H. W.; Fluhr, W.; Meier, M.; Wokaun, A. Resonances of two-dimensional particle gratings in surface-enhanced Raman scattering. *J. Opt. Soc. Am. B* **1986**, *3*, 430.
(15) Hicks, E. M.; Zou, S.; Schatz, G. C.; Spears, K. G.; Van Duyne, R. P.; Gunnarsson, L.; Rindzevicius, T.; Kasemo, B.; Käll, M. Controlling plasmon line shapes through diffractive coupling in linear arrays of cylindrical nanoparticles fabricated by electron beam lithography. *Nano Lett.* **2005**, *5*, 1065−1070.
(16) Rodriguez, S. R. K.; Abass, A.; Maes, B.; Janssen, O. T. A.; Vecchi, G.; Gómez Rivas, J. Coupling Bright and Dark Plasmonic Lattice Resonances. *Phys. Rev. X* **2011**, *1*, 1−7.
(17) Humphrey, A. D.; Barnes, W. L. Plasmonic surface lattice resonances on arrays of different lattice symmetry. *Phys. Rev. B - Condens. Matter Mater. Phys.* **2014**, *90*, 1−8.
(18) Conde-Rubio, A.; Fraile Rodríguez, A.; Espinha, A.; Mihi, A.; Pérez-Murano, F.; Batlle, X.; Labarta, A. Geometric frustration in ordered lattices of plasmonic nanoelements. *Sci. Rep.* **2019**, *9*, 1−10.
(19) Vecchi, G.; Giannini, V.; Gómez Rivas, J. Surface modes in plasmonic crystals induced by diffractive coupling of nanoantennas. *Phys. Rev. B - Condens. Matter Mater. Phys.* **2009**, *80*, 1−4.
(20) Huck, C.; Vogt, J.; Sendner, M.; Hengstler, D.; Neubrech, F.; Pucci, A. Plasmonic Enhancement of Infrared Vibrational Signals: Nanoslits versus Nanorods. *ACS Photonics* **2015**, *2*, 1489−1497.
(21) Hentschel, M.; Weiss, T.; Bagheri, S.; Giessen, H. Babinet to the half: Coupling of solid and inverse plasmonic structures. *Nano Lett.* **2013**, *13*, 4428−4433.
(22) Hrtoň, M.; Konečná, A.; Horák, M.; Šikola, T.; Křápek, V. Plasmonic Antennas with Electric, Magnetic, and Electromagnetic Hot Spots Based on Babinet's Principle. *Phys. Rev. Appl.* **2020**, *13*, 054045.
(23) Cetin, A. E.; Turkmen, M.; Aksu, S.; Etezadi, D.; Altug, H. Multi-resonant compact nanoaperture with accessible large nearfields. *Appl. Phys. B: Laser Opt.* **2015**, *118*, 29−38.
(24) Moore, T.; Moody, A.; Payne, T.; Sarabia, G.; Daniel, A.; Sharma, B. In Vitro and In Vivo SERS Biosensing for Disease Diagnosis. *Biosensors* **2018**, *8*, 46.
(25) Wei, H.; Hossein Abtahi, S. M.; Vikesland, P. J. Environmental Science Plasmonic colorimetric and SERS sensors for environmental analysis. *Environ. Sci. Nano* **2015**, *2*, 120−135.
(26) Falcone, F.; Lopetegi, T.; Laso, M. A. G.; Baena, J. D.; Bonache, J.; Beruete, M.; Marques, R.; Martín, F.; Sorolla, M. Babinet principle applied to the design of metasurfaces and metamaterials. *Phys. Rev. Lett.* **2004**, *93*, 2−5.
(27) Zentgraf, T.; Meyrath, T. P.; Seidel, A.; Kaiser, S.; Giessen, H.; Rockstuhl, C.; Lederer, F. Babinet's principle for optical frequency metamaterials and nanoantennas. *Phys. Rev. B - Condens. Matter Mater. Phys.* **2007**, *76*, 4−7.
(28) Rodríguez-Álvarez, J.; Gnoatto, L.; Martínez-Castells, M.; Guerrero, A.; Borrisé, X.; Fraile Rodríguez, A.; Batlle, X.; Labarta, A. An inverted honeycomb plasmonic lattice as an efficient refractive index sensor. *Nanomaterials* **2021**, *11*, 1217.
(29) García De Abajo, F. J.; Kociak, M. Probing the photonic local density of states with electron energy loss spectroscopy. *Phys. Rev. Lett.* **2008**, *100*, 1−4.
(30) Wu, Y.; Li, G.; Camden, J. P. Probing Nanoparticle Plasmons with Electron Energy Loss Spectroscopy. *Chem. Rev.* **2018**, *118*, 2994−3031.
(31) Hage, F. S.; Kepaptsoglou, D. M.; Ramasse, Q. M.; Allen, L. J. Phonon Spectroscopy at Atomic Resolution. *Phys. Rev. Lett.* **2019**, *122*, 16103.
(32) Bellido, E. P.; Rossouw, D.; Botton, G. A. Toward 10 meV electron energy-loss spectroscopy resolution for plasmonics. *Microsc. Microanal.* **2014**, *20*, 767−778.
(33) Egerton, R. F. *Electron energy-loss spectroscopy in the electron microscope*, 3rd ed.; Springer Science & Business Media: New York, 2011;.
(34) Lagos, M. J.; Trügler, A.; Hohenester, U.; Batson, P. E. Mapping vibrational surface and bulk modes in a single nanocube. *Nature* **2017**, *543*, 529−532.
(35) Koh, A. L.; Bao, K.; Khan, I.; Smith, W. E.; Kothleitner, G.; Nordlander, P.; Maier, S. A.; Mccomb, D. W. Electron energy-loss spectroscopy (EELS) of surface plasmons in single silver nanoparticles and dimers: Influence of beam damage and mapping of dark modes. *ACS Nano* **2009**, *3*, 3015−3022.
(36) Isoniemi, T.; Maccaferri, N.; Ramasse, Q. M.; Strangi, G.; De Angelis, F. Electron Energy Loss Spectroscopy of Bright and Dark Modes in Hyperbolic Metamaterial Nanostructures. *Adv. Opt. Mater.* **2020**, *8*, 2000277.
(37) Wu, Y.; Li, G.; Cherqui, C.; Bigelow, N. W.; Thakkar, N.; Masiello, D. J.; Camden, J. P.; Rack, P. D. Electron Energy Loss Spectroscopy Study of the Full Plasmonic Spectrum of Self-Assembled Au-Ag Alloy Nanoparticles: Unraveling Size, Composition, and Substrate Effects. *ACS Photonics* **2016**, *3*, 130−138.
(38) Schoen, D. T.; Atre, A. C.; García-Etxarri, A.; Dionne, J. A.; Brongersma, M. L. Probing complex reflection coefficients in one-dimensional surface plasmon polariton waveguides and cavities using STEM EELS. *Nano Lett.* **2015**, *15*, 120−126.
(39) Song, F.; Wang, T.; Wang, X.; Xu, C.; He, L.; Wan, J.; Van Haesendonck, C.; Ringer, S. P.; Han, M.; Liu, Z.; et al. Visualizing plasmon coupling in closely spaced chains of Ag nanoparticles by electron energy-loss spectroscopy. *Small* **2010**, *6*, 446−451.
(40) Alexander, D. T. L.; Flauraud, V.; Demming-Janssen, F. Near-Field Mapping of Photonic Eigenmodes in Patterned Silicon Nanocavities by Electron Energy-Loss Spectroscopy. *ACS Nano* **2021**, *15*, 16501−16514.
(41) Raza, S.; Esfandyarpour, M.; Koh, A. L.; Mortensen, N. A.; Brongersma, M. L.; Bozhevolnyi, S. I. Electron energy-loss spectroscopy of branched gap plasmon resonators. *Nat. Commun.* **2016**, *7*, 1−10.
(42) Rossouw, D.; Couillard, M.; Vickery, J.; Kumacheva, E.; Botton, G. A. Multipolar plasmonic resonances in silver nanowire antennas imaged with a subnanometer electron probe. *Nano Lett.* **2011**, *11*, 1499−1504.
(43) Nelayah, J.; Kociak, M.; Stéphan, O.; De Abajo, F. J. G.; Tencé, M.; Henrard, L.; Taverna, D.; Pastoriza-Santos, I.; Liz-Marzán, L. M.; Colliex, C. Mapping surface plasmons on a single metallic nanoparticle. *Nat. Phys.* **2007**, *3*, 348−353.
(44) Schaffer, B.; Hohenester, U.; Trügler, A.; Hofer, F. High-resolution surface plasmon imaging of gold nanoparticles by energy-filtered transmission electron microscopy. *Phys. Rev. B - Condens. Matter Mater. Phys.* **2009**, *79*, 1−4.
(45) Koh, A. L.; Fernández-Domínguez, A. I.; McComb, D. W.; Maier, S. A.; Yang, J. K. W. High-resolution mapping of electron-beam-excited plasmon modes in lithographically defined gold nanostructures. *Nano Lett.* **2011**, *11*, 1323−1330.

https://doi.org/10.1021/acsnano.2c11016
ACS Nano 2023, 17, 8123−8132

(46) Konečná, A.; Neuman, T.; Aizpurua, J.; Hillenbrand, R. Surface-Enhanced Molecular Electron Energy Loss Spectroscopy. *ACS Nano* **2018**, *12*, 4775−4786.
(47) Nicoletti, O.; De La Peña, F.; Leary, R. K.; Holland, D. J.; Ducati, C.; Midgley, P. A. Three-dimensional imaging of localized surface plasmon resonances of metal nanoparticles. *Nature* **2013**, *502*, 80−84.
(48) Hohenester, U. Simulating electron energy loss spectroscopy with the MNPBEM toolbox. *Comput. Phys. Commun.* **2014**, *185*, 1177−1187.
(49) Bernasconi, G. D.; Butet, J. my; Flauraud, V.; Alexander, D.; Brugger, J.; Martin, O. J. F. Where does energy go in electron energy loss spectroscopy of nanostructures? *ACS Photonics* **2017**, *4*, 156−164.
(50) García De Abajo, F. J. Optical excitations in electron microscopy. *Rev. Mod. Phys.* **2010**, *82*, 209−275.
(51) Schmidt, F. P.; Ditlbacher, H.; Hohenester, U.; Hohenau, A.; Hofer, F.; Krenn, J. R. Dark plasmonic breathing modes in silver nanodisks. *Nano Lett.* **2012**, *12*, 5780−5783.
(52) Krivanek, O. L.; Lovejoy, T. C.; Dellby, N.; Aoki, T.; Carpenter, R. W.; Rez, P.; Soignard, E.; Zhu, J.; Batson, P. E.; Lagos, M. J.; et al. Vibrational spectroscopy in the electron microscope. *Nature* **2014**, *514*, 209−212.
(53) Hachtel, J. A.; Lupini, A. R.; Idrobo, J. C. Exploring the capabilities of monochromated electron energy loss spectroscopy in the infrared regime. *Sci. Rep.* **2018**, *8*, 1−10.
(54) Lovejoy, T. C.; Corbin, G. C.; Dellby, N.; Hoffman, M. V.; Krivanek, O. L. Advances in Ultra-High Energy Resolution STEM-EELS. *Microsc. Microanal.* **2018**, *24*, 446−447.
(55) Gómez, D. E.; Teo, Z. Q.; Altissimo, M.; Davis, T. J.; Earl, S.; Roberts, A. The dark side of plasmonics. *Nano Lett.* **2013**, *13*, 3722−3728.
(56) Cuerda, J.; Rüting, F.; García-Vidal, F. J.; Bravo-Abad, J. Theory of lasing action in plasmonic crystals. *Phys. Rev. B - Condens. Matter Mater. Phys.* **2015**, *91*, 1−5.
(57) Hakala, T. K.; Rekola, H. T.; Väkeväinen, A. I.; Martikainen, J. P.; Nečada, M.; Moilanen, A. J.; Törmä, P. Lasing in dark and bright modes of a finite-sized plasmonic lattice. *Nat. Commun.* **2017**, *8*, 1−7.
(58) Omaghali, N. E. J.; Tkachenko, V.; Andreone, A.; Abbate, G. Optical sensing using dark mode excitation in an asymmetric dimer metamaterial. *Sensors (Switzerland)* **2014**, *14*, 272−282.
(59) Banerjee, S.; Amith, C. S.; Kumar, D.; Damarla, G.; Chaudhary, A. K.; Goel, S.; Pal, B. P.; Roy Chowdhury, D. Ultra-thin subwavelength film sensing through the excitation of dark modes in THz metasurfaces. *Opt. Commun.* **2019**, *453*, 124366.
(60) Zeng, Y.; Madsen, S. J.; Yankovich, A. B.; Olsson, E.; Sinclair, R. Comparative electron and photon excitation of localized surface plasmon resonance in lithographic gold arrays for enhanced Raman scattering. *Nanoscale* **2020**, *12*, 23768−23779.
(61) Mayerhöfer, T. G.; Popp, J. Periodic array-based substrates for surface-enhanced infrared spectroscopy. *Nanophotonics* **2018**, *7*, 39−79.
(62) Yoshimoto, D.; Saito, H.; Hata, S.; Fujiyoshi, Y.; Kurata, H. Characterization of Nonradiative Bloch Modes in a Plasmonic Triangular Lattice by Electron Energy-Loss Spectroscopy. *ACS Photonics* **2018**, *5*, 4476−4483.
(63) Park, S.; Mutz, N.; Schultz, T.; Blumstengel, S.; Han, A.; Aljarb, A.; Li, L. J.; List-Kratochvil, E. J. W.; Amsalem, P.; Koch, N. Direct determination of monolayer MoS2 and WSe2 exciton binding energies on insulating and metallic substrates. *2D Mater.* **2018**, *5*, 025003.
(64) Norcada. Available online: https://www.norcada.com/tech-info/ (accessed on Jan 10, 2023).
(65) Lumerical Inc. Available online: https://www.lumerical.com/ (accessed on Jan 10, 2023).
(66) Philipp, H. R. Optical Properties of Silicon Nitride. *J. Electrochem. Soc.* **1973**, *120*, 295.
(67) Johnson, P. B.; Christy, R. W. Optical Constant of the Nobel Metals. *Phys. Rev. B* **1972**, *6*, 4370−4379.

https://doi.org/10.1021/acsnano.2c11016
ACS Nano 2023, 17, 8123−8132

Supporting information for:

Imaging of Antiferroelectric Dark Modes in an Inverted Plasmonic Lattice

Javier Rodríguez-Álvarez[1,2,], Amílcar Labarta[1,2], Juan Carlos Idrobo[3], Rossana Dell'Anna[4], Alessandro Cian[4], Damiano Giubertoni[4], Xavier Borrisé[5], Albert Guerrero[6], Francesc Perez-Murano[6], Arantxa Fraile Rodríguez[1,2] and Xavier Batlle[1,2]*

[1] Departament de Física de la Matèria Condensada, Universitat de Barcelona, 08028 Barcelona, Spain

[2] Institut de Nanociència i Nanotecnologia (IN2UB), Universitat de Barcelona, 08028, Spain

[3] Materials Science and Engineering Department, University of Washington, Seattle, WA, 98195, USA

[4] Sensors & Devices Center, FBK - Bruno Kessler Foundation, via Sommarive, 18, Povo, TN 38123 Italy

[5] Catalan Institute of Nanoscience and Nanotechnology (ICN2), CSIC and BIST, Campus UAB, Bellaterra, 08193 Barcelona, Spain

[6] Institut de Microelectrónica de Barcelona (IMB-CNM, CSIC), Bellaterra, 08193, Spain

E-mail: javier.rodriguez@ub.edu

- **S1.** Transversal electric field distribution for the SLR at 1.57 eV.
- **S2.** Simulated electric field and charge distributions for a threesome of slits.
- **S3.** Simulated electric field and charge distributions for the simplest local dark mode of the inverted honeycomb lattice.
- **S4.** Profiles of the EELS signal and the simulated electric field along the slits for the antiferroelectric dark modes.
- **S5.** Array of the magnetic dipoles over the structure used to simulate antiferroelectric dark modes.

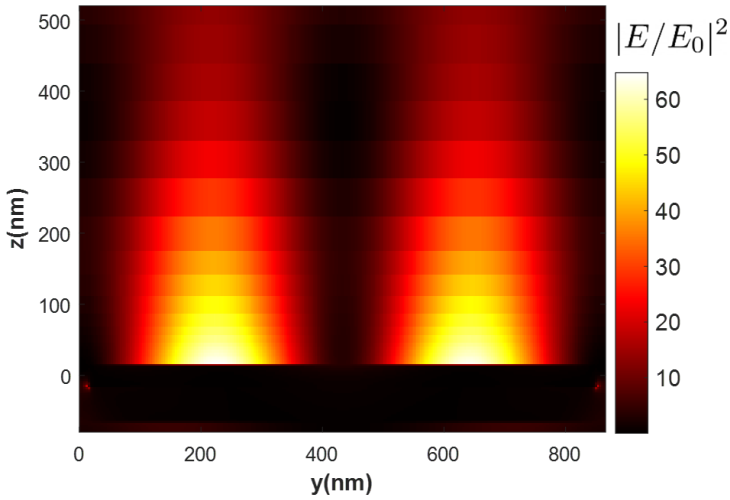

Figure S1. Simulated electric field for the SLR at 1.57 eV. The zy plane, transversal to the structure, shows the strong out-of-plane electric field of a unit cell. Each one of the two hotspots corresponds to transversal cuts to the ring shown in Fig. 3i. z = 0 nm corresponds to the center of the metallic gold layer.

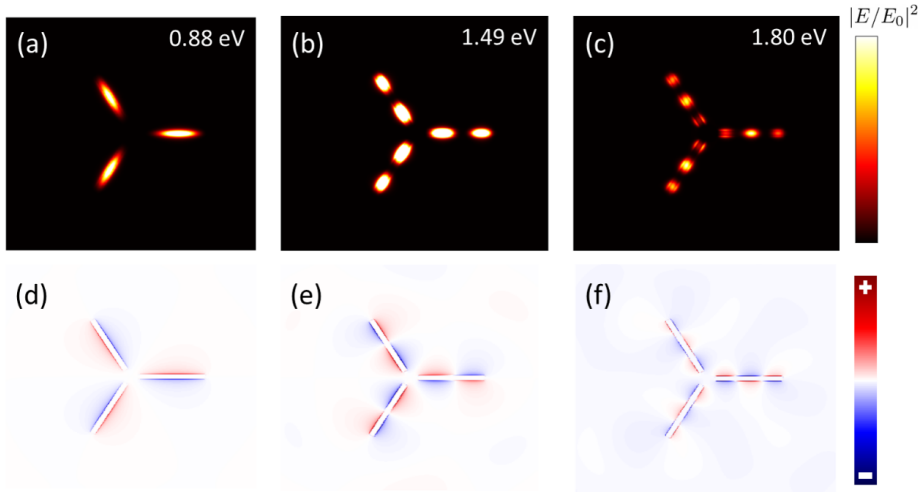

Figure S2. (a, b, c) Electric field and (d, e, f) charge distributions for the dark modes with the lowest energies in the three slits system. The plasmonic modes have been excited by placing a magnetic dipole 50 nm above the vertex of the slits.

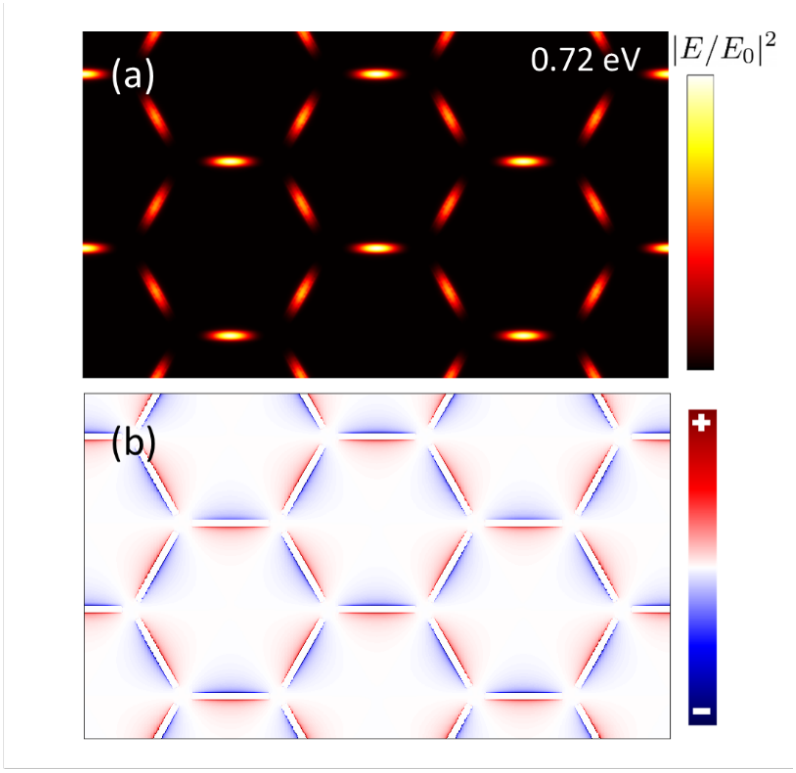

Figure S3. (a) Electric field and (c) charge distributions for the simplest local dark mode. Note that despite the non-zero dipole moment of the slits, the net moment is zero if the whole unit cell is considered. This plasmonic mode has been excited by placing an array of magnetic dipoles 50 nm above the vertices of the hexagons coincident with the Bravais lattice.

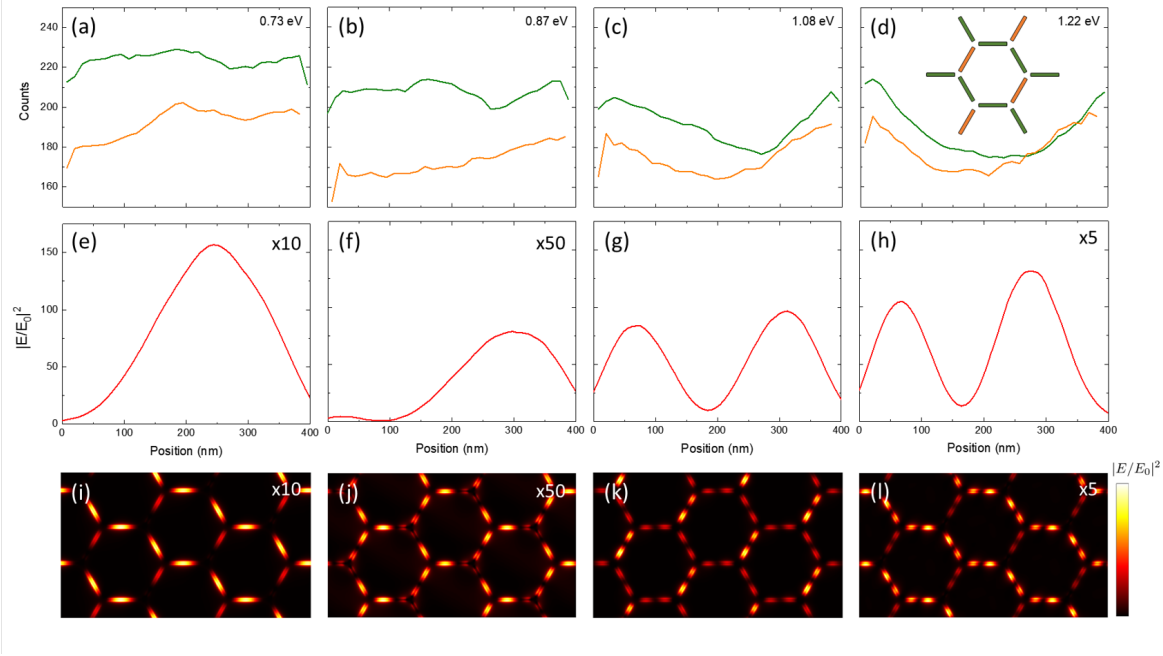

Figure S4. (a,b,c,d) EELS intensity profile along the slits for four energies corresponding to the range where antiferroelectric dark modes are detected by EELS. The green and orange curves depict the average intensity of the EELS signal as a function of the position for the two subsets of slits depicted in the inset. (e,f,g,h) Simulated intensity of the electric-field profile along a slit for each energy, computed averaging the three variants of the modes shown in panels (i,j,k,l). The charge intensity has been multiplied by a factor indicated in the top-right side of the panels for an easier comparison between resonances. (i,j,k,l) Near-field distributions corresponding to one of the three variants (equivalent by three-fold symmetry) for each energy. Note that the energies correspond to those of the EELS color maps shown in Figure 6.

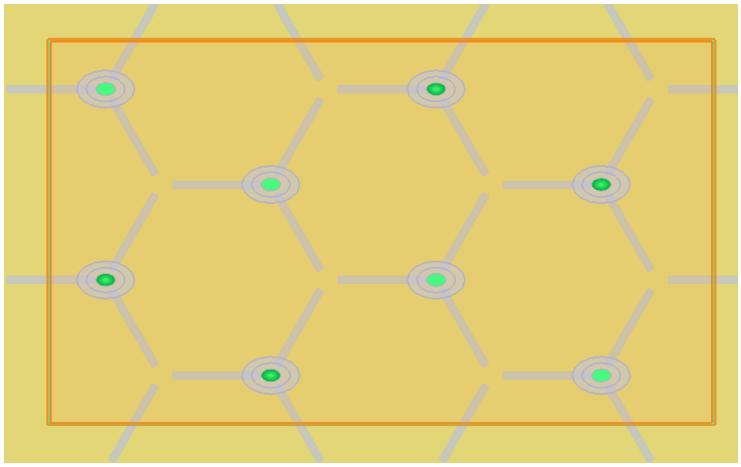

Figure S5. Schematics of the unit cell for the simulations of the antiferroelectric modes where the excitation source is an array of magnetic dipoles. There are two subsets of magnetic dipoles (lighter and darker green circles) in phase opposition with respect to each other. Note the simulation region denoted by an orange rectangle. The magnetic dipoles are placed 50 nm above the vertices of the hexagons that are coincident with the Bravais lattice.

Part III

Chiral Plasmonic Nanostructures

Introduction

Chirality is the fundamental geometrical property of systems that cannot be superimposed with their mirror images. It plays a pivotal role in numerous natural and artificial systems. In particular, chiral plasmonic structures have garnered increasing interest due to their ability to exhibit CD)—a difference in the optical response to left- and right-handed circularly polarized light. This property enables a range of applications, including polarization-sensitive detectors, chiral molecule sensing, and enhanced spectroscopies. Among these structures, twisted stacks of planar plasmonic nanoelements, such as triskelion-shaped monomers, offer a compelling combination of design simplicity and tunable optical properties, making them ideal for experimental and theoretical exploration. Moreover, the 3-fold symmetry of the triskelion is shown to enhance the excitation of resonances presenting CD due to the geometrical frustration of the system.

This chapter presents two articles that explore the chiroptical behavior of twisted triskelia stacks, providing a comprehensive perspective on their optical properties and technological potential. Publication III, "Tunable Circular Dichroism through Absorption in Coupled Optical Modes of Twisted Triskelia Nanostructures", examines a two-layered system of stacked planar triskelia using FDTD simulations. These chiral nanoelements, characterized by their threefold rotational symmetry, exhibit tunable CD through the careful manipulation of the relative twist angle and vertical separation between the layers. The study demonstrates that interaction-driven optical modes within the triskelia stack are responsible for high CD values, reaching up to 60% in the visible and near-infrared range. This behavior arises from the coupling between plasmonic modes localized within each layer, which generates helicity-dependent near-field interactions and resonance enhancement. These findings underline the potential of triskelion stacks for helicity-sensitive applications, including polarization-dependent spectroscopy and single-photon polarization control.

Publication IV, "Dichroism of Coupled Multipolar Plasmonic Modes in Twisted Triskelion Stacks", extends the exploration of these systems by investigating

their multipolar nature. This work investigates the spectral and intensity shifts of multipolar modes as a function of the twist angle, using a combination of FTIR spectroscopy and FDTD simulations. The results reveal that the coupling between stacked triskelia gives rise to hybrid plasmonic modes with strong handedness-dependent optical responses. In particular, the low-energy multipolar modes exhibit significant dephasing between the two triskelia layers, enabling large and tunable CD in the near-infrared region. Furthermore, the integration of these stacks into triangular plasmonic arrays demonstrates their ability to generate SLR, further amplifying their chiral optical response and paving the way for advanced photonic devices with a high spectral selectivity.

Collectively, these studies offer a comprehensive examination of twisted triskelion stacks as versatile and tunable platforms for chiroptical applications, emphasizing the understanding of the coupling between multipolar plasmonic modes. This chapter aims to present a simple yet realistic model for understanding chiral stacked systems, highlighting the advantages of employing a threefold geometry.

scientific reports

Check for updates

OPEN

Tunable circular dichroism through absorption in coupled optical modes of twisted triskelia nanostructures

Javier Rodríguez-Álvarez[1,2]✉, Antonio García-Martín[3], Arantxa Fraile Rodríguez[1,2], Xavier Batlle[1,2] & Amílcar Labarta[1,2]

We present a system consisting of two stacked chiral plasmonic nanoelements, so-called triskelia, that exhibits a high degree of circular dichroism. The optical modes arising from the interactions between the two elements are the main responsible for the dichroic signal. Their excitation in the absorption cross section is favored when the circular polarization of the light is opposite to the helicity of the system, so that an intense near-field distribution with 3D character is excited between the two triskelia, which in turn causes the dichroic response. Therefore, the stacking, in itself, provides a simple way to tune both the value of the circular dichroism, up to 60%, and its spectral distribution in the visible and near infrared range. We show how these interaction-driven modes can be controlled by finely tuning the distance and the relative twist angle between the triskelia, yielding maximum values of the dichroism at 20° and 100° for left- and right-handed circularly polarized light, respectively. Despite the three-fold symmetry of the elements, these two situations are not completely equivalent since the interplay between the handedness of the stack and the chirality of each single element breaks the symmetry between clockwise and anticlockwise rotation angles around 0°. This reveals the occurrence of clear helicity-dependent resonances. The proposed structure can be thus finely tuned to tailor the dichroic signal for applications at will, such as highly efficient helicity-sensitive surface spectroscopies or single-photon polarization detectors, among others.

Chiral structures play a key role in the working mechanism of a wide variety of biological processes and biochemical interactions, and thus hold promise for several technological applications. The term "chiral" refers to structures which are not superimposable with their mirror image. Therefore, any chiral structure can be found in two different handedness formed of the same building blocks. One of the most relevant properties of chiral structures is that the two versions of the system react differently under the illumination of left-handed (LCP) and right-handed (RCP) circularly polarized light. This chiroptical activity has been extensively used in many fields, such as chemistry[1,2], pharmaceuticals[3], and optics[4,5]. For a given chiroptical system, the differences in the signal of the optical functions f of the system under the two circular polarizations is usually named circular dichroism (CD) and can be quantified by the dimensionless figure of merit (FOM)

$$CD_f = \frac{f_{LCP} - f_{RCP}}{f_{LCP} + f_{RCP}}, \tag{1}$$

where f stands for any of the studied optical cross-sections (CS), namely, the absorption, scattering, and the extinction, recorded under either LCP or RCP light. Although there are other alternatives, Eq. (1) is a common definition in the literature[6,7] to ascertain the significance of any dichroism present in the spectra of the optical functions of a system.

Due to the versatility of plasmonic metamaterials, several plasmonic chiral systems have been proposed in the last years in response to a growing interest in the experimental realization of such chiral nanostructures. The approaches to their manufacture comprehend the realization of three-dimensional (3D) structures[8], the manipulation of nanoparticle assemblies[9,10] or the stacking of pseudo-planar structures[11,12], among others. Even

[1]Departament de Física de la Matèria Condensada, Universitat de Barcelona, 08028 Barcelona, Spain. [2]Institut de Nanociència i Nanotecnologia (IN2UB), 08028 Barcelona, Spain. [3]Instituto de Micro y Nanotecnología IMN-CNM, CSIC, CEI UAM + CSIC, Isaac Newton 8, 28760 Tres Cantos, Madrid, Spain. ✉email: javier.rodriguez@ub.edu

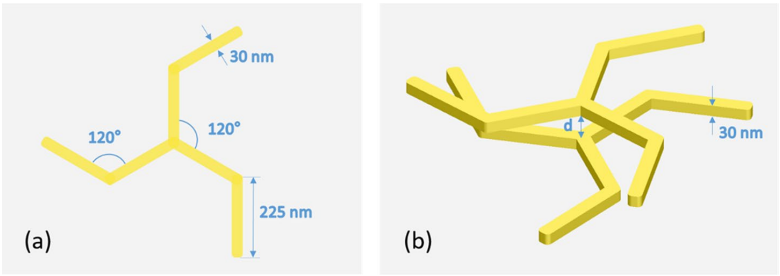

Figure 1. (**a**) Schematic top view of one triskelion showing the values of the main in-plane geometrical parameters. The thickness of the triskelion was set to 30 nm. (**b**) 3D-view showing the parallel stacking of the two triskelia in the system. The edge-to-edge distance *d* between the two triskelia is also depicted. Note that the triskelion on top of the stack is twisted 30° anticlockwise with respect to the bottom one.

though planar structures can be easily manufactured by standard lithography processes[13], in the recent years, 3D plasmonic structures have gained interest because of their enhanced chiral response and simple tunability, compared to their 2D counterparts[14–16]. Despite the good performance of 3D structures, their manufacture can be highly demanding and limited by practically attainable feature sizes and complex manufacturing procedures, especially if a strong CD in the visible range is desired. To address this issue, stacked 2D nanostructures made of simple elements following a multilayered design can fill in the gap as they have shown to exhibit broadband dichroic signals[12,17–24]. Although the twice exposure of the pattern with high alignment precision during nanofabrication makes stacked 2D nanostructures also challenging, they might be easier to manufacture when based on simple designs than 3D structures. Thus, stacked 2D structures can be broadly found in many applications related to nanophotonics[25–27]. Despite their apparent simple design, complex interactions among the plasmonic nanoelements acting as basic building blocks of these structures enable to manipulate light in a highly efficient way. For instance, the optical response of the system can be tuned by simply controlling the spatial arrangement of the building blocks in the structure.

Unlike previous realizations of stacked structures[12,28], the plasmonic nanoelements used as building block in this work has a handedness such that they are optically active in nature. This yields to the arising of additional resonances driven by the interaction between the two elements. Consequently, the CD of the structure can be controlled by the in-plane relative rotation angle (twist angle) between the basic elements with respect to the handedness of the element itself together with the distance between the elements. We therefore present a system consisting of two stacked chiral plasmonic nanoelements with three-fold rotational symmetry, so-called triskelia, providing a high degree of CD in the visible to near-infrared range that could be easily tuned in a manufacturing process.

System and numerical methods

Numerical simulations. The simulations presented hereafter have been performed using a commercial Finite Difference Time Domain (FDTD) method providing a robust and reliable solver for Maxwell's equations (Lumerical[29]). We use an impinging plane wave along the *z*-axis (perpendicular to the surface of the triskelia) of unit amplitude everywhere. The simulation cell is large enough (1.2 μm × 1.2 μm × 4 μm) to ensure that perfectly absorbing boundary conditions exert a negligible effect on the electromagnetic fields obtained. We employ a parallelepiped mesh in the nanostructures and near field region of 1.5 nm × 1.5 nm × 1 nm, *dx-dy-dz*, respectively, growing uniformly in *dz* up to a maximum of 25 nm out of the nearfield close to the simulation boundaries, so that convergence (to the best of our numerical capabilities) is attained. The total and scattered fields are then collected to give rise to the nearfield intensity color maps and the cross-sections. All fields are normalized to the amplitude of the impinging plane wave.

Design of the triskelia stacking. Prior to the design of more complex chiral structures, it is convenient to choose a planar monomer showing some dichroism in its optical response that can be appropriate as building block of 3D chiral systems. We have chosen a monomer made up of three elements emanating from a center with three-fold rotational symmetry so that its electric polarization is not fully compatible with an even number of poles[30,31]. This introduces a certain geometric frustration that favors the formation of more complex polar distributions, which in turn may make the structure more prone to show dichroism under circularly polarized illuminations. In addition, the three elements of the monomer are bent at their midpoint forming the same clockwise angle so that the three-fold rotational symmetry is preserved while not presenting any mirror plane parallel to the rotation axis. Figure 1a depicts the design of the monomer used in this work as the primary source of planar CD. It has been named "triskelion" in view of its resemblance to the artistic motif and the three-legged clathrin molecule[32]. Interestingly, any planar structure embedded in a homogeneous dielectric medium, even fulfilling the stated properties, is not truly chiral because of reciprocity and the existence of an inherent symmetry mirror plane[33–35], and although significant CD signals can be exhibited by both the absorption and the scattering CS, they cancel out when the total extinction is considered. One way to induce true 3D chirality in a planar structure

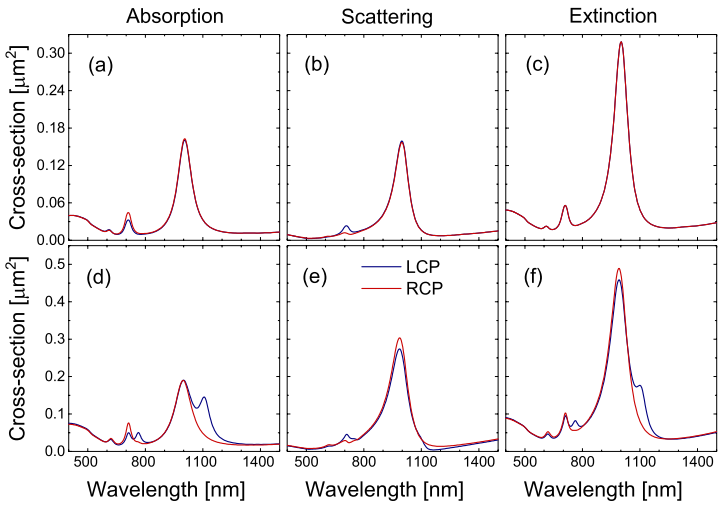

Figure 2. (**a**) Absorption, (**b**) scattering, and (**c**) extinction cross-sections under LCP (blue solid line) and RCP (red solid line) light for a single triskelion (see Fig. 1a). (**d**) Absorption, (**e**) scattering, and (**f**) extinction CS under LCP (blue solid line) and RCP (red solid line) light for a double triskelion system forming an anticlockwise 30° twist angle and at an edge-to-edge distance d = 30 nm (see Fig. 1b).

is just to put it on a dielectric substrate, so that both sides of the structure are not equivalent[35,36]. Nevertheless, in this work we propose a 3D arrangement of two of these planar motifs in a homogeneous medium that consists of a stack of two parallel interacting triskelia separated by an edge-to-edge distance d (Fig. 1b) aiming to improve both the tunability and the intensity of the dichroic signal. This design is somehow similar to those in Refs.[28,37], where the monomers have no in-plane mirror symmetry, but here we take advantage as well from the interactions between the electric polarizations of monomers with three-fold rotational symmetry. Additionally, the parallel stacking provides a simple platform to study the CD of the system as a function of both the edge-to-edge distance between the two triskelia and the twist angle φ with respect to each other (the twist angle refers to the relative in-plane rotation between elements). It is worth stressing that these two geometric parameters could be easily tuned in a manufacture process. The material chosen for the study of the optical response of the system is gold owing to its well-known plasmonic properties and chemical inertness[38,39]. Numerical simulations of the absorption and scattering CS for a single triskelion with 30 nm in thickness show that the corresponding CD signals are maximized (not shown) when all the angles in Fig. 1a are kept equal to 120°.

Results and discussion

Optical responses of the single triskelion *vs* the stacking. A priori, the planar nature of a single triskelion in combination with reciprocity[33,35] is known to prevent any CD in the total optical extinction. However, as shown in Fig. 2a,b, neither the absorption nor the scattering holds this suppression by themselves. A close look at Fig. 2a,b reveals different signals for RCP and LCP light both in the absorption and scattering channels, predominantly around the peak at 710 nm, whereas the CD perfectly vanishes in the extinction CS (Fig. 2c) since a planar triskelion embedded in a uniform dielectric medium is not a truly chiral structure[33]. However, when triskelia are set to form a non-planar structure, the optical properties of the whole system are expected to change drastically, enabling the existence of CD in the extinction CS.

As an example, Fig. 2d,e show the absorption and scattering CS for a triskelion stack with and edge-to-edge distance of 30 nm and anticlockwise 30° twist angle between the top and bottom triskelia (see Fig. 1b). Similar peaks around 710 and 1000 nm than those for a single triskelion can be identified in the absorption and scattering CS under both RCP and LCP illuminations. Nevertheless, the absorption CS under LCP light also exhibits two extra peaks, which are redshifted with respect to those around 710 and 1000 nm and are the main cause of CD in the extinction CS since they have no counterparts in any of the scattering CS for the two light polarizations (see Fig. 2d–f). Therefore, the interaction between the electric polarizations of the two triskelia under LCP illumination is causing these two extra excitation modes in the absorption CS that are in turn responsible for the CD in the extinction CS.

Tuning interactions: relative in-plane angle between the triskelia. As shown earlier in Fig. 2d–f, the optical response of the system can be tuned by changing the twist angle φ between the two triskelia in the stack. This will effectively modify the distance between the legs of the two triskelia, as well as induce a "sense of turn"[13,35]. In fact, when $\varphi = 0$ (or an integer multiple of 120°, as a single triskelion has three-fold rotational symmetry), from the point of view of the CD the system can be regarded as equivalent to the planar case of a single

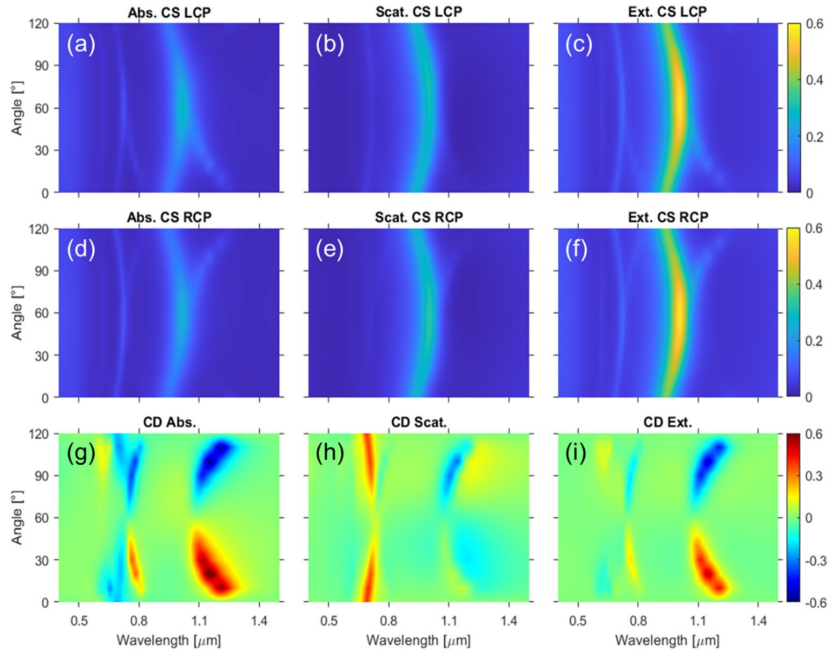

Figure 3. Absorption, scattering, and extinction CS for LCP (**a**–**c**), and RCP (**d**–**f**), illuminations, respectively, as a function of the twist angle φ for a fixed edge-to-edge distance of 30 nm. FOM defined in Eq. (1) for the CD of the absorption (**g**), scattering (**h**), and extinction (**i**) as a function of the twist angle.

element irrespective of the edge-to-edge distance between the two triskelia since no additional helicity is associated with the 3D stacking, as also shown in Ref.[37]. Therefore, for those twist angles, the system only displays some differences in the absorption and scattering CS mostly around the peak at 710 nm and smaller around 1000 nm but not in the extinction CS as in the case of a single triskelion (see Fig. S1 in the Supplementary Information) since this parallel stack does not modify the planar nature of each triskelion. Thus, the CS are very much like those of a single triskelion in Fig. 2a,b, but with some important distinctions. First, the scattering CS is almost twice as intense as for the single triskelion, whereas the absorption CS remains equally intense. Second, there are two extra peaks (resonances) in the absorption CS caused by the interaction between the two triskelia, one barely noticeable around 850 nm and another one more visible around 1250 nm that appear under both LCP and RCP light with the same intensities so that they do not contribute to the CD in agreement with the no 3D helicity of the stack for this special value of the angle. As will be discussed later, the spectral positions of these two extra peaks depend on the distance between the triskelia as they are driven by interactions.

Figure 3a–f shows the absorption, scattering, and extinction CS, for both LCP and RCP incidence, as a function of anticlockwise φ (see Fig. 1), for an edge-to-edge distance of 30 nm, together with their respective FOM for the CD of the three CS (Fig. 3g–i). By varying φ, the spectra of all CS display the two main excitations at ca. 710 and 1000 nm (already shown by a single triskelion) that are always present under both circular polarizations and, more importantly, the emergence of two extra excitations with intensities which vary greatly as a function of the handedness of the circular polarization. For instance, it is found that the extra excitations in the absorption, which are clearly visible under LCP incidence at an anticlockwise $\varphi \leq 60°$ (see Fig. 3a and Fig. 2d for the case of 30°), are then predominant under RCP illumination for $60° < \varphi < 120°$ anticlockwise (see Fig. 3d and Fig. S1 in the Supplementary Information for $\varphi = 90°$). Maximum values for the CD in the extinction CS can be found for $\varphi = 20°$ (and $\varphi = 100°$) for the excitation around 1000 nm, reaching CD values up to 60%. High values of the CD can also be found in a broad range of parameters around the maximal value. In addition, remarkable CD values are also shown at the resonance in the vicinity of 710 nm. For twist angles of 30° and 90° we can observe a sharp increase in the CD. These results show that our structure presents values of the CD perfectly comparable to those of the state of the art, even outperforming similar works[7,40].

Since the range of anticlockwise twist angles within 0° and 60° is *almost* optically equivalent to that of the clockwise ones starting from 120°[12,41,42] (for instance, the optical response for 110° clockwise should be equivalent to that of 10° anticlockwise), these results put forward the occurrence of clear helicity-dependent excitations (chiral resonances) that are manifested as enhanced absorption peaks. We would like to point out the interesting features associated with two special angles. These are the aforementioned highly symmetric case of $\varphi = 0°$ that shows no CD (despite being driven by near-field interactions) and that of $\varphi = 60°$, which shows a peculiar

behavior since the only element that breaks perfect symmetry is the bending angle at the midpoint of the legs of each triskelion.

Interesting enough is the case of $\varphi = 60°$, where the CD in the extinction CS vanishes (see Fig. S1 in the Supplementary Information and Fig. 3g–i), similarly to Ref.[20]. This angle represents a highly symmetric arrangement of the triskelia in the stack, for which symmetric dispersions (with opposite sign) of the main excitations in the absorption and the scattering CS occur when φ is increased or decreased from 60°. These symmetric dispersions of the absorption (Fig. 3a,d) and the scattering (Fig. 3b,e) are equal under LCP and RCP, while only some differences are exhibited by the intensities of the peaks for the two polarizations. However, those differences yield CD signals almost canceling each other out in the extinction CS (Fig. 3i) because of the opposite sign of the two contributions. In fact, the only noticeable differences between the CS for the triskelion stack at $\varphi = 60°$ and those for the single triskelion are the intensities of the signals since the two extra excitations are not present in the spectra of the latter (see Fig. S1 in the Supplementary Information). It is also worth noting that 60° is the angle for which the distance between equivalent points in the legs of the two triskelia is maximum for a fixed value of the edge-to-edge distance such that the interaction among the legs of the two triskelia in the stack is minimum. Besides, this distance is equal for both clockwise and anticlockwise screw rotation through the stack, so no dependence of the excitation on the handedness of the light can be expected.

The incomplete complementarity of the double triskelion structure comes from the bending angle at the midpoints of the legs of each triskelion. Perfect complementarity would be achieved if the sign of the bending angle of the legs were fully reversed[12], and thus LCP and RCP spectra could be interchanged for anticlockwise and clockwise in-plane angles within 0–60° and 120–60°, respectively. In terms of the CS spectra, the incompleteness arises from the fact that the extra excitations are also discernible in the scattering CS (Fig. 3b,e) for twist angles within 120–60°, although the contribution of the absorption to the CD in the extinction is still much more prominent. A clear example of the lack of perfect complementarity is set by the comparison of the scattering CS for 30° and 90° shown in Fig. 2d and Fig. S1 in the Supplementary Information, respectively. One of the extra excitations is perfectly discernible on the right-hand side of the peak around 1000 nm for 90° whereas it is not present at all for 30°.

Regarding the spectral dependence of the excitations on φ, the peaks arising from the single triskelion (denoted as main peaks) and those owing to the interactions between the two triskelia in the stack (so-called extra excitations) must be analyzed separately. Both kinds of excitations, exhibit spectral shifts of the corresponding CS as a function of φ, as expected for interacting systems (Fig. 3a–f). The main peaks are redshifted for $0° < \varphi < 60°$ or for $60° < \varphi < 120°$ owing to the symmetry around the 60° case. In contrast, the extra peaks evolve in a complementary fashion: they are blueshifted for angles $0° < \varphi < 60°$ or $60° < \varphi < 120°$.

Concerning the CD spectra, most of the interest lies in the contributions from the extra excitations. Despite being non-negligible for the main peaks, remarkable values are only obtained for the extra ones. Increasing the twist angle from 0°, for which the extra peaks have the same intensities under LCP and RCP illuminations and there is no contribution to the CD in the extinction cross-section (Fig. S1 in the Supplementary Information), the extra peaks under RCP light rapidly decrease and vanish above about $\varphi = 10°$, while their intensities monotonously increase for LCP light (see Fig. S1 in the Supplementary Information for $\varphi = 10°$ and Fig. 3 for 30°). An almost complementary behavior of these extra peaks under the two circular polarizations is found within 120° and 60° (see Fig. 3a–f). The contributions of the extra peaks to the CD spectra are redshifted from the highly symmetric angle of 60°, having opposite sign depending on the circular polarization of the light at which the corresponding extra excitations appear, as depicted in Fig. 3g–i. It must be pointed out that the high values of the CD in the scattering CS in the long wavelength range are mostly due to the intrinsically low values of the scattering CS for both polarizations.

Tuning interactions: edge-to-edge distance. As mentioned above, the other important geometrical parameter influencing the mutual interactions between the triskelia is the vertical separation (edge-to-edge distance) between them. In Sect. "Optical responses of the single triskelion *vs* the stacking", it was mentioned that the interaction between the two triskelia in the stack causes the emergence of extra peaks in the spectra of the CS. Some are only visible under the proper circular polarization of the impinging light. In Fig. 4, we show the absorption, scattering, and extinction CS for both LCP and RCP light, and the corresponding FOM for the CD, as a function of the edge-to-edge distance between the two triskelia upon a fixed anticlockwise twist angle $\varphi = 30°$. For this value, the extra peaks in the absorption CS are solely present under LCP illumination (Fig. 4a, d), as expected from the prior discussion in Sect. "Optical responses of the single triskelion *vs* the stacking". These extra excitations are blueshifted while the main excitations are redshifted as the distanceOptical responses of the single triskelion *vs* the stacking between the triskelia increases, tending to overlap and resulting in only two peaks as the interaction between the two triskelia decreases. Therefore, at a sufficiently large edge-to-edge distance the positions of the peaks coincide with those of a single triskelion but almost doubling the intensities. In contrast, the scattering CS does not exhibit any extra excitations (Fig. 4b,e) for either of the two circular polarizations. Nevertheless, there is an underlying effect arising from the interaction between the triskelia that causes the redshift of the main excitations as the separation between the triskelia increases. Consequently, the main features shown by the extinction CS (see Fig. 4c,f) as the edge-to-edge distance increases are driven by those of the absorption CS. Similar dependencies of the main and extra excitations on the edge-to-edge distance are found at 0° (not shown), but with the extra excitations appearing under both circular polarizations and larger values of the splitting between the main and extra excitations due to the lower twist angle.

A quick inspection of the CD of the absorption and scattering CS (Fig. 4g,h) reveals that the CD in the extinction signal arises mainly due to the two extra excitations found in the absorption CS under LCP light only (see Fig. 4i). In addition, and as discussed before, there are also small differences between the intensities of the two

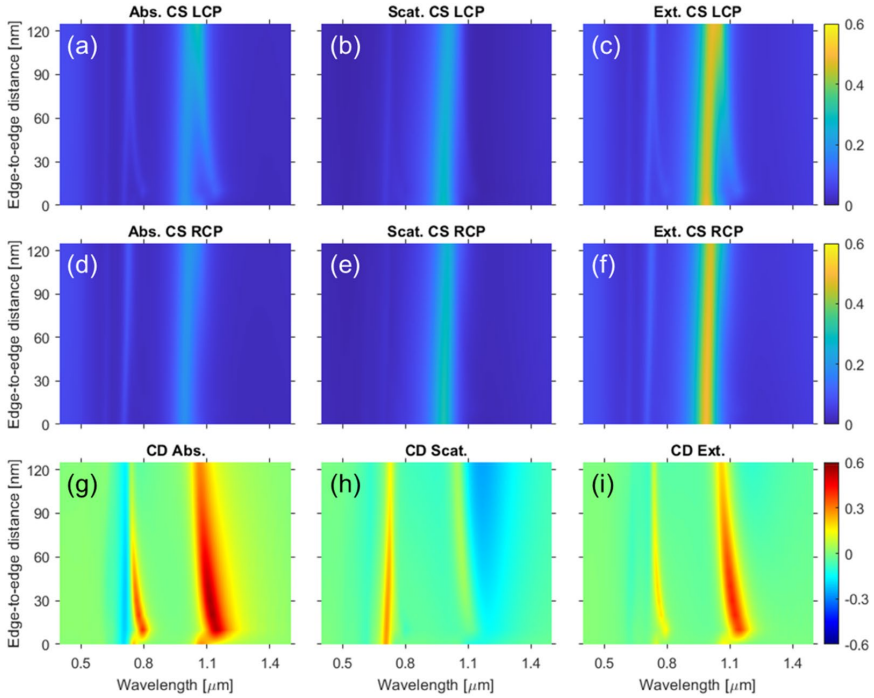

Figure 4. Absorption, scattering, and extinction CS for LCP (**a**–**c**), and RCP (**d**–**f**), illuminations, respectively, as a function of the edge-to-edge distance for a fixed twist angle $\varphi = 30°$. FOM defined in Eq. (1) for the CD of the absorption (**g**), scattering (**h**), and extinction (**i**) as a function of the edge-to-edge distance.

main excitations under LCP and RCP illuminations that yield some dichroism in the absorption and scattering CS as well, but almost cancelling each other out in the CD of the extinction CS due to the opposite sign of these two contributions as they are associated with less interacting modes of the two triskelia in the stack that are similar to those of a single triskelion. Thus, the extra excitations present in the absorption under LCP light give rise to a distinctive CD in the absorption CS without counterpart in the scattering CS that in turn causes most of the CD in the extinction CS.

Finally, it is worth stressing that the study of the optical response as a function of the twist angle φ in Sect. 6 was performed at an edge-to-edge distance of 30 nm. At this value of the distance, there is a certain overlap in the absorption between the LCP extra excitations and the main ones (see Fig. 4a). It happens in such a way that the absolute difference between the LCP and RCP signals is large around the excitations, while the CD in the extinction CS is still high enough, as shown in Fig. 4i. Besides, 30 nm is the midpoint of the range within about 10 and 50 nm for which the CD associated with the extra peaks is maximum.

Near-field distributions of the modulus of the electric field. The near-field distributions of the modulus of the electric field (intensity) in the vicinity (2 nm above) of each triskelion are shown in Fig. 5 and Fig. S2 in the Supplementary Information. The edge-to-edge distance between the two triskelia is 30 nm and the twist angles φ are 30° and 60° (Fig. 5), and 0° and 90° (Fig. S2 in the Supplementary Information), respectively. The excitation of the extra resonances causing the CD in the extinction discussed in the previous section can now be easily correlated with the near-field distribution around the triskelia in each case. For instance, when the angle is 30°, the two triskelia display high intensity of the electric field around the metal for LCP illumination, corresponding to the excitation of the extra modes. It is also possible to observe the signature of the top triskelion on the plane of the bottom one as a blurry electric-field distribution resembling the spatial arrangement of the triskelion on top. On the contrary, under RCP illumination the overall electric response of the system is several times smaller since no extra resonances are excited for this polarization. Interestingly, the system shows a higher degree of optical activity under incident light with opposite polarization to the helicity of the structure, as previously reported in the literature[43]. The electric-field distributions are similar for 90° (see Fig. S2 in the Supplementary Information) but swapping the images corresponding to LCP and RCP light with respect to the 30° case, similarly to Ref[7] always showing the highest near-field activity in the case in which the helicity of the stack is opposite to that of the incident light.

Alternatively, when considering the configurations yielding no CD at all (60° and 0° in Fig. 5 and Fig. S2 in the Supplementary Information, respectively), the intensity distributions are almost indistinguishable for the two

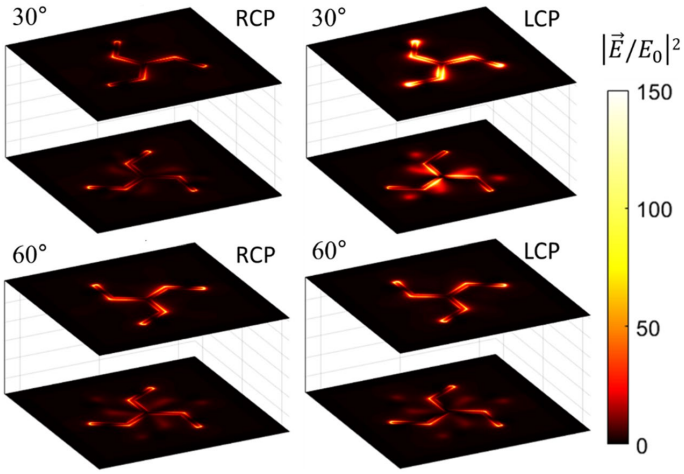

Figure 5. Near-field distributions of the square modulus of the electric field normalized to that of the incident light under RCP and LCP illumination at a wavelength of 1100 nm for twist angles φ of 30° and 60°.

light polarizations. The case for 0° is like that of a single element because the two triskelia are parallelly aligned so that there is no chirality associated with the screw-like arrangement of the elements. In addition, the top element has a shadowing effect of the impinging radiation over the bottom one, hampering its excitation (more evident for the 0° case in Fig. S2 in the Supplementary Information). Even though there is no CD for 60° in any of the three studied optical functions, the intensity distributions look qualitatively different from those for 0° because the two triskelia display almost the same excitation regardless of the light polarization (see Fig. 5). It is worth stressing that for twist angles smaller than 60° the stack is more active under LCP illumination, whereas for angles higher than 60° the converse applies. Therefore, for 60° the system cannot show any differences on its excitation under either LCP or RCP light due to symmetry reasons.

A deeper insight into the differences in the activity of the stack under LCP and RCP light for the extra excitations around 760 and 1100 nm (those mainly driven by interactions) can be gained by the near-field distributions of the modulus of the electric field in the middle plane between the two triskelia for $d = 30$ nm and $\varphi = 30°$ (see Fig. 6). As shown in Fig. 6b,d, under LCP light (opposite to the helicity of the stack), there is high intensity of the electric field between the two triskelia for both extra modes caused by the strong interactions between them, so that the near-field distributions have high 3D character and can be considered as excitations of the stack as a whole. Consequently, they give rise to CD in the extinction CS according to their true 3D nature. On the contrary, the stack under RCP light (see Fig. 6a,c) shows much lower activity in between the two triskelia as the excitations correspond to more independent modes of the two triskelia (more planar character), and, consequently, they do not significantly contribute to the CD in the extinction CS.

All things considered, following the results presented in previous sections, the study of the near-field distributions in the system reveals big differences in the intensity of the evanescent field under the two polarizations of light, providing a further proof of its chiral response.

Conclusions

To summarize, the CD in the extinction CS exhibited by the twisted stack of triskelia is determined by the arrangement of the two elements. The extra resonances yielding the dichroic signal mostly appear in the absorption CS and are not intrinsic to a single triskelion. Most of the previous work found in the literature exploits and manipulates resonances already shown by the single element used to build the chiral structure. On the contrary, our work shows that the excitations responsible for the CD in the extinction CS are arising from the interaction between the two triskelia and are not present in the single triskelion case. Moreover, they are clearly interaction-driven since they show strong tunability by adjusting both the distance between the elements and their twist angle.

In addition, the helicity of the system strongly favors the excitation of the extra resonances under the illumination of one of the circular polarizations only (that opposite to the helicity of the structure) yielding near-field distributions between the two triskelia with 3D character that cause strong CD in the extinction CS. Special cases are those for 0° and 120°, for which the extra resonances show the same intensity for both RCP and LCP light (no helicity of the stack) and their contributions cancel each other in the extinction CS. As the angle increases/decreases from these values, the intensity for one polarization raises while rapidly vanishes for the opposite polarization. Thus, at an angle of 10° (110°) the extra resonances are only noticeable for one of the polarizations.

Finally, we have shown that by finely tuning the relative distance between the two triskelia and the twist angle of the structure, total control over the CD in the extinction can be achieved, obtaining tunable values up to 60%

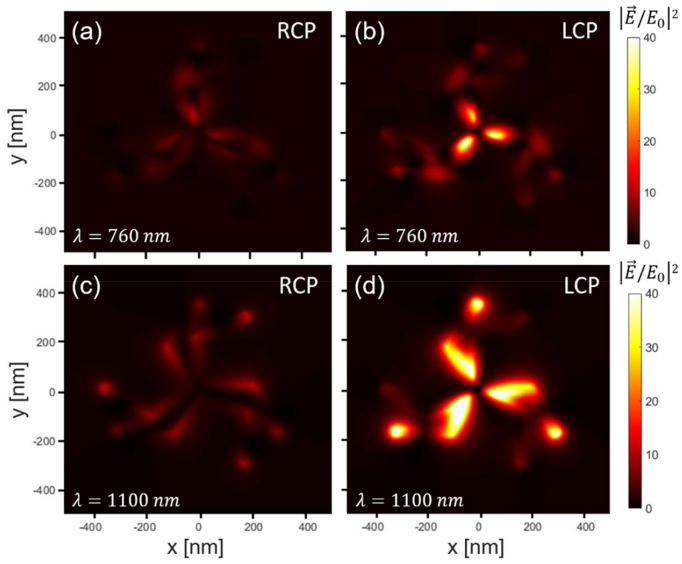

Figure 6. Near-field distributions of the square modulus of the electric field normalized to that of the incident light under RCP and LCP illumination at wavelengths of 760 nm (**a**, **b**), and 1100 nm (**c**, **d**), for twist angles φ of 30° in a plane perpendicular to the axis of the stacking and equidistant to both triskelia.

in the visible to near-infrared range. The simplicity with which these parameters can be manipulated and finely defined through successive lithographic and thin film deposition processes makes our design of special interest for the realization of more reliable and efficient chiral plasmonic nanostructures.

This work constitutes a solid contribution to the polarization-dependent manipulation of light and holds promise for applications such as highly efficient helicity-sensitive surface spectroscopies or single-photon polarization detectors.

Received: 21 October 2021; Accepted: 10 December 2021
Published online: 07 January 2022

References

1. Wang, Y. *et al.* Active control and biosensing application of induced chirality between symmetric metal and graphene nanostructures. *J. Phys. Chem. C* **123**, 24754–24762. https://doi.org/10.1021/acs.jpcc.9b07576 (2019).
2. Fasman, G. D. *Circular Dichroism and the Conformational Analysis of Biomolecules* (Springer, 2013).
3. Hutt, A. J. & O'Grady, J. Drug chirality: A consideration of the significance of the stereochemistry of antimicrobial agents. *J. Antimicrob. Chemother.* **37**, 7–32. https://doi.org/10.1093/jac/37.1.7 (1996).
4. Pendry, J. B. A chiral route to negative refraction. *Science* **306**, 1353–1355. https://doi.org/10.1126/science.1104467 (2004).
5. Kitzerow, H. & Bahr, C. *Chirality in Liquid Crystals*; 2001; ISBN 0387986790.
6. Luo, Y. *et al.* Plasmonic chiral nanostructures: chiroptical effects and applications. *Adv. Opt. Mater.* **5**, 1–18. https://doi.org/10.1002/adom.201700040 (2017).
7. Petronijevic, E. *et al.* Chiral effects in low-cost plasmonic arrays of elliptic nanoholes. *Opt. Quantum Electron.* **52**, 1–10. https://doi.org/10.1007/s11082-020-02279-8 (2020).
8. Gansel, J. K. *et al.* Gold helix photonic metamaterial as broadband circular polarizer. *Science* **325**, 1513–1515. https://doi.org/10.1126/science.1177031 (2009).
9. Govorov, A. O. *et al.* Chiral nanoparticle assemblies: Circular dichroism, plasmonic interactions, and exciton effects. *J. Mater. Chem.* **21**, 16806–16818. https://doi.org/10.1039/c1jm12345a (2011).
10. Li, J. *et al.* Tunable chiral optics in all-solid-phase reconfigurable dielectric nanostructures. *Nano Lett.* **21**, 973–979. https://doi.org/10.1021/acs.nanolett.0c03957 (2021).
11. Huttunen, M. J. *et al.* Nonlinear chiral imaging of twisted-cross gold nano-objects. *Opt. Mater. Express* **1**, 2501–2503 (2011).
12. Decker, M. *et al.* Strong optical activity from twisted-cross photonic metamaterials. *Opt. Lett.* **34**, 2501. https://doi.org/10.1364/ol.34.002501 (2009).
13. Valev, V. K., Baumberg, J. J., Sibilia, C. & Verbiest, T. Chirality and chiroptical effects in plasmonic nanostructures: Fundamentals, recent progress, and outlook. *Adv. Mater.* **25**, 2517–2534. https://doi.org/10.1002/adma.201205178 (2013).
14. Hu, G., Wang, M., Mazor, Y., Qiu, C. W. & Alù, A. Tailoring light with layered and Moiré metasurfaces. *Trends Chem.* **3**, 342–358. https://doi.org/10.1016/j.trechm.2021.02.004 (2021).
15. Kuzyk, A. *et al.* Reconfigurable 3D plasmonic metamolecules. *Nat. Mater.* **13**, 862–866. https://doi.org/10.1038/nmat4031 (2014).
16. Schreiber, R. *et al.* Chiral plasmonic DNA nanostructures with switchable circular dichroism. *Nat. Commun.* **4**, 1–6. https://doi.org/10.1038/ncomms3948 (2013).

17. Pfeiffer, C., Zhang, C., Ray, V., Guo, L. J. & Grbic, A. High performance bianisotropic metasurfaces: Asymmetric transmission of light. *Phys. Rev. Lett.* **113**, 1–5. https://doi.org/10.1103/PhysRevLett.113.023902 (2014).
18. Wu, Z. & Zheng, Y. Moiré Chiral Metamaterials. *Adv. Opt. Mater.* **5**, 1–9. https://doi.org/10.1002/adom.201700034 (2017).
19. Zhao, Y., Belkin, M. A. & Alù, A. Twisted optical metamaterials for planarized ultrathin broadband circular polarizers. *Nat. Commun.* https://doi.org/10.1038/ncomms1877 (2012).
20. Rogacheva, A. V., Fedotov, V. A., Schwanecke, A. S. & Zheludev, N. I. Giant gyrotropy due to electromagnetic-field coupling in a bilayered chiral structure. *Phys. Rev. Lett.* **97**, 1–4. https://doi.org/10.1103/PhysRevLett.97.177401 (2006).
21. Wang, Y. *et al.* Strong circular dichroism enhancement by plasmonic coupling between graphene and h-shaped chiral nanostructure. *Opt. Express* **27**, 33869. https://doi.org/10.1364/oe.27.033869 (2019).
22. Wang, Y. *et al.* Dynamically adjustable-induced THz circular dichroism and biosensing application of symmetric silicon-graphene-metal composite nanostructures. *Opt. Express* **29**, 8087. https://doi.org/10.1364/oe.419614 (2021).
23. Wang, Y. *et al.* Circular dichroism enhancement in grapheme with planar metal nanostructures: A computational study. *Appl. Surf. Sci.* https://doi.org/10.1016/j.apsusc.2019.145070 (2020).
24. Wang, Y. *et al.* Circular dichroism enhancement and dynamically adjustment in planar metal chiral split rings with graphene sheets arrays. *Nanotechnology* https://doi.org/10.1088/1361-6528/ac0ac6 (2021).
25. Wang, H. *et al.* Full color generation using silver tandem nanodisks. *ACS Nano* **11**, 4419–4427. https://doi.org/10.1021/acsnano.6b08465 (2017).
26. Zhou, Y. *et al.* Multifunctional metaoptics based on bilayer metasurfaces. *Light Sci. Appl.* https://doi.org/10.1038/s41377-019-0193-3 (2019).
27. Menzel, C., Sperrhake, J. & Pertsch, T. Efficient treatment of stacked metasurfaces for optimizing and enhancing the range of accessible optical functionalities. *Phys. Rev. A* **93**, 1–12. https://doi.org/10.1103/PhysRevA.93.063832 (2016).
28. Liu, N., Liu, H., Zhu, S. & Giessen, H. Stereometamaterials. *Nat. Photonics* **3**, 157–162. https://doi.org/10.1038/nphoton.2009.4 (2009).
29. Lumerical Inc. Innovative Photonic Design Tools. Available online: https://www.lumerical.com/
30. Conde-Rubio, A. *et al.* Geometric frustration in a hexagonal lattice of plasmonic nanoelements. *Opt. Express* **26**, 20211. https://doi.org/10.1364/oe.26.020211 (2018).
31. Conde-Rubio, A. *et al.* Geometric frustration in ordered lattices of plasmonic nanoelements. *Sci. Rep.* **9**, 1–10. https://doi.org/10.1038/s41598-019-40117-4 (2019).
32. Ernst, U. & Daniel, B. Assembly units of clathrin coats. *Nature* **289**, 420–422 (1981).
33. Hopkins, B., Poddubny, A. N., Miroshnichenko, A. E. & Kivshar, Y. S. Circular dichroism induced by Fano resonances in planar chiral oligomers. *Laser Photonics Rev.* **10**, 137–146. https://doi.org/10.1002/lpor.201500222 (2016).
34. Ogier, R., Fang, Y., Svedendahl, M., Johansson, P. & Käll, M. Macroscopic layers of chiral plasmonic nanoparticle oligomers from colloidal lithography. *ACS Photonics* **1**, 1074–1081. https://doi.org/10.1021/ph500293u (2014).
35. Kuwata-Gonokami, M. *et al.* Giant optical activity in quasi-two-dimensional planar nanostructures. *Phys. Rev. Lett.* **95**, 1–4. https://doi.org/10.1103/PhysRevLett.95.227401 (2005).
36. Schwanecke, A. S. *et al.* Broken time reversal of light interaction with planar chiral nanostructures. *Phys. Rev. Lett.* **91**, 1–4. https://doi.org/10.1103/PhysRevLett.91.247404 (2003).
37. Auguié, B., Alonso-Gómez, J. L., Guerrero-Martínez, A. & Liz-Marzán, L. M. Fingers crossed: Optical activity of a chiral dimer of plasmonic nanorods. *J. Phys. Chem. Lett.* **2**, 846–851. https://doi.org/10.1021/jz200279x (2011).
38. Chu, Y., Schonbrun, E., Yang, T. & Crozier, K. B. Experimental observation of narrow surface plasmon resonances in gold nanoparticle arrays. *Appl. Phys. Lett.* https://doi.org/10.1063/1.3012365 (2008).
39. Cheng, Y., Wang, M., Borghs, G. & Chen, H. Gold nanoparticle dimers for plasmon sensing. *Langmuir* **27**, 7884–7891. https://doi.org/10.1021/la200840m (2011).
40. Liu, S. D., Liu, J. Y., Cao, Z., Fan, J. L. & Lei, D. Dynamic tuning of enhanced intrinsic circular dichroism in plasmonic stereometamolecule array with surface lattice resonance. *Nanophotonics* **9**, 3419–3434. https://doi.org/10.1515/nanoph-2020-0130 (2020).
41. Yin, X. *et al.* Active chiral plasmonics. *Nano Lett.* **15**, 4255–4260. https://doi.org/10.1021/nl5042325 (2015).
42. Mattioli, F. *et al.* Plasmonic superchiral lattice resonances in the mid-infrared. *ACS Photonics* **7**, 2676–2681. https://doi.org/10.1021/acsphotonics.0c00161 (2020).
43. Decker, M., Zhao, R., Soukoulis, C. M., Linden, S. & Wegener, M. Twisted split-ring-resonator photonic metamaterial with huge optical activity. *Opt. Lett.* **35**, 1593. https://doi.org/10.1364/ol.35.001593 (2010).

Author contributions

J.R.-A. and A.G.-M. performed the simulations. J.R.-A, A.G.-M. and A.L. wrote the first version of the manuscript. All the authors participated in the discussion and review of the manuscript.

Competing interests

The authors declare no competing interests.

Additional information

Supplementary Information The online version contains supplementary material available at https://doi.org/10.1038/s41598-021-03908-2.

Correspondence and requests for materials should be addressed to J.R.

Reprints and permissions information is available at www.nature.com/reprints.

Publisher's note Springer Nature remains neutral with regard to jurisdictional claims in published maps and institutional affiliations.

Supplementary Information

Tunable Circular Dichroism through Absorption in Coupled Optical Modes of Twisted Triskelia Nanostructures

Javier Rodríguez-Álvarez*, Antonio García-Martín, Arantxa Fraile Rodríguez, Xavier Batlle and Amílcar Labarta

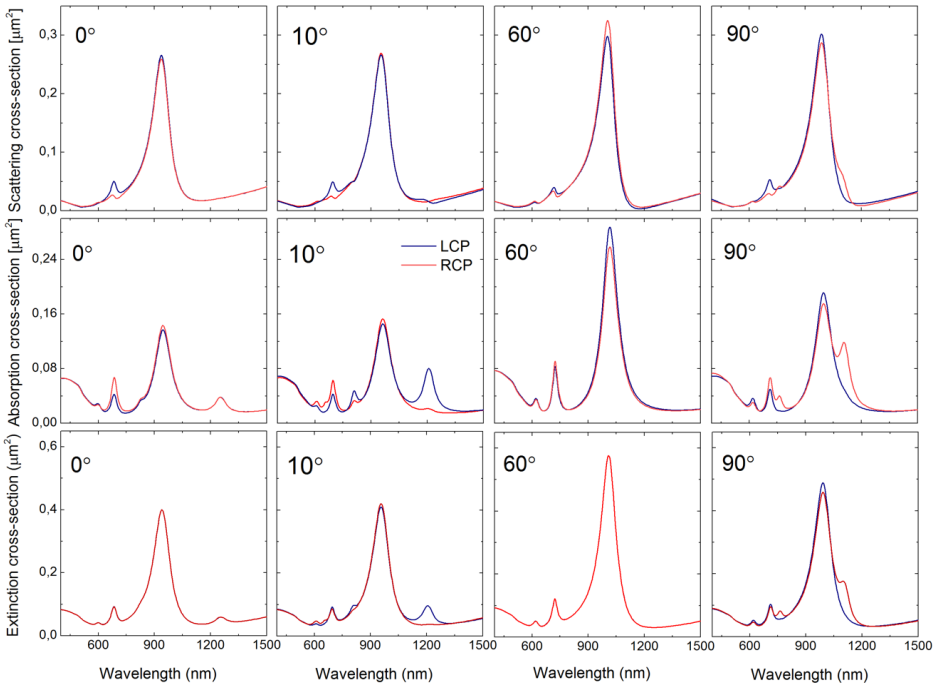

Figure S1. Absorption, scattering and extinction cross-sections under LCP (blue solid line) and RCP (red solid line) light for a double triskelia system forming an anticlockwise in-plane angle of 0°, 10°, 60° and 90° and at an edge-to-edge distance $d = 30$ nm (see Fig. 1(b)).

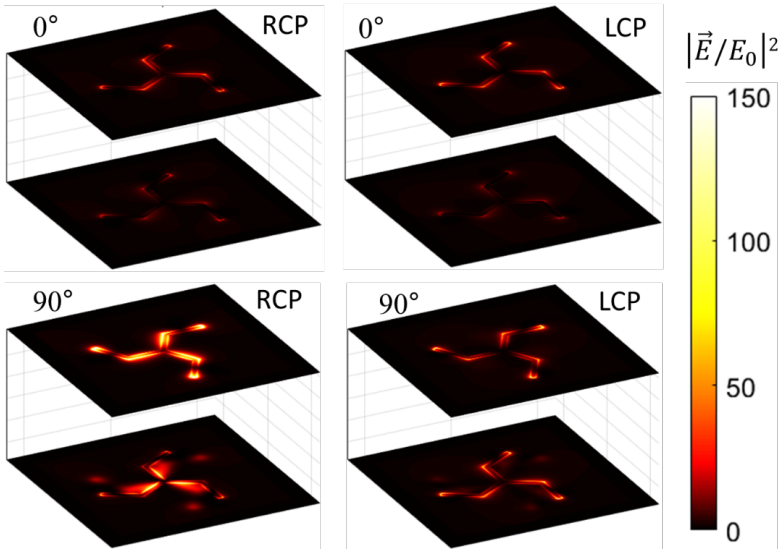

Figure S2. Near-field distributions of the square modulus of the electric field normalized to that of the incident light under RCP and LCP illumination for in-plane angles of 0° and 90°, at a wavelength of 1100 nm.

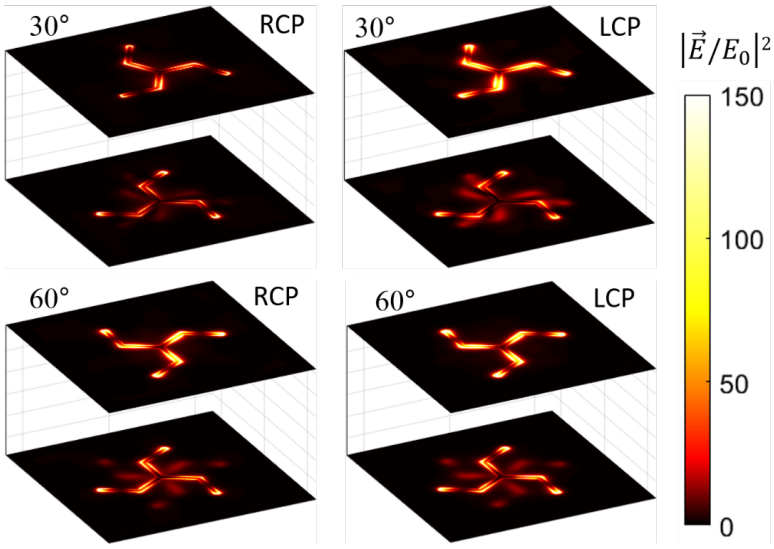

Figure S3. Near-field distributions of the square modulus of the electric field normalized to that of the incident light under RCP and LCP illumination for in-plane angles of 30° and 60°, at a wavelength of 1000 nm.

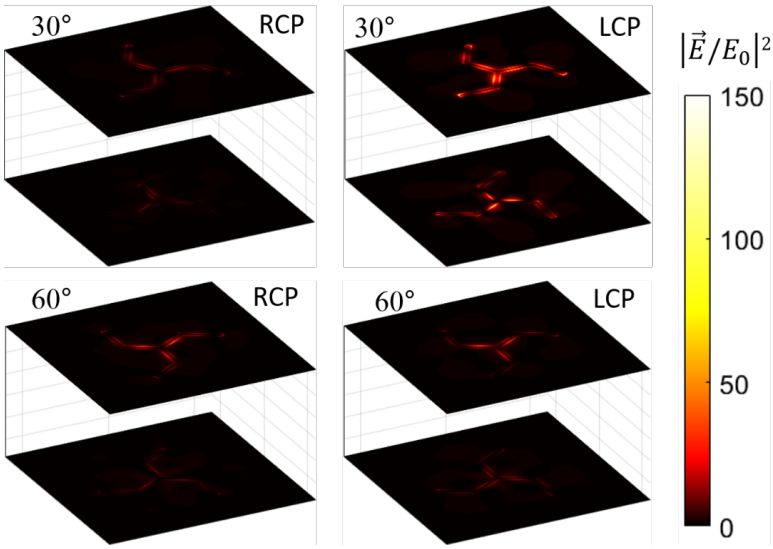

Figure S4. Near-field distributions of the square modulus of the electric field normalized to that of the incident light under RCP and LCP illumination for in-plane angles of 30° and 60°, at a wavelength of 760 nm.

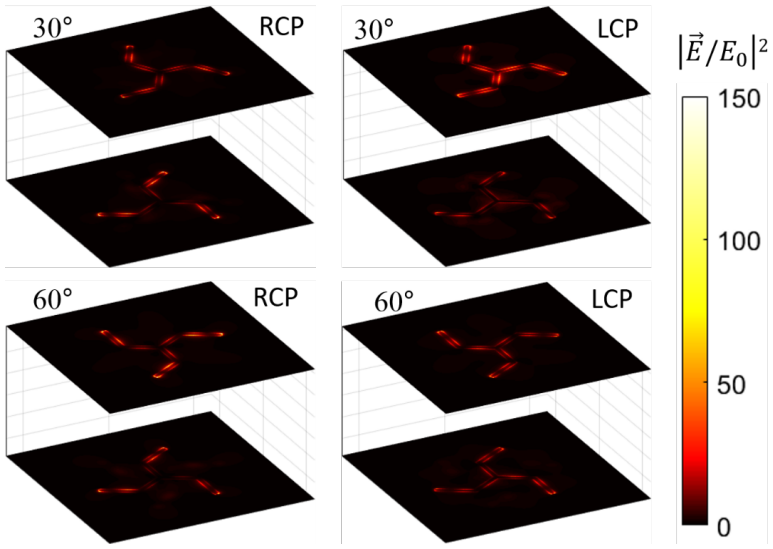

Figure S5. Near-field distributions of the square modulus of the electric field normalized to that of the incident light under RCP and LCP illumination for in-plane angles of 30° and 60°, at a wavelength of 710 nm.

Research Article

Javier Rodríguez-Álvarez*, Joan Vila-Comamala, Antonio García-Martín, Albert Guerrero, Xavier Borrisé, Francesc Pérez-Murano, Christian David, Alvaro Blanco, Carlos Pecharromán, Xavier Batlle, Arantxa Fraile Rodríguez, and Amílcar Labarta.

Dichroism of coupled multipolar plasmonic modes in twisted triskelion stacks

Abstract: We present a systematic investigation of the optical response to circularly polarized illumination in twisted stacked plasmonic nanostructures. The system consists in two identical, parallel gold triskelia, centrally aligned and rotated at a certain angle relative to each other. Sample fabrication was accomplished through a double electron beam lithography process. This stack holds two plasmonic modes of multipolar character in the near-infrared range, showing a strong dependence of their excitation intensities on the handedness of the circularly polarized in incident light. This translates in a large circular dichroism which can be modulated by adjusting the twist angle of the stack. Fourier-transform infrared (FTIR) spectroscopy and numerical simulations were employed to characterize the spectral features of the modes. Remarkably, in contrast to previous results in other stacked nanostructures, the system's response exhibits a behavior analogous to that of two interacting dipoles only at small angles. As the angle approaches 15°, where maximum dichroism is observed, more complex modes of the stack emerge. These modes evolve towards two in-phase multipolar excitations of the two triskelia as the angle increases up to 60°. Finally, simulations for a triangular array of such stacked elements show a sharp mode arising from the hybridization of a surface lattice resonance with the low-energy mode of the stack. This hybridized mode demonstrates the capability to be selectively switched on and off through the light polarization handedness.

Keywords: Plasmonics, Chirality, Dichroism, Triskelion, Twisted stack.

*** Corresponding author: Javier Rodríguez-Álvarez,** Departament de Física de la Matèria Condensada, Universitat de Barcelona, 08028 Barcelona, Spain and Institut de Nanociència i Nanotecnologia (IN2UB), Universitat de Barcelona, 08028, Spain.
E-mail: javier.rodriguez@ub.edu
Xavier Batlle, Arantxa Fraile Rodríguez, and Amílcar Labarta, Departament de Física de la Matèria Condensada, Universitat de Barcelona, 08028 Barcelona, Spain and Institut de Nanociència i Nanotecnologia (IN2UB), Universitat de Barcelona, 08028, Spain.
Joan Vila-Comamala and Christian David, Paul Scherrer Institute, Forschungsstrasse 111, Villigen 5232, Switzerland.
Antonio García-Martín, Instituto de Micro y Nanotecnología IMN-CNM, CSIC, CEI UAM + CSIC, Isaac Newton 8, 28760, Tres Cantos, Madrid, Spain.
Albert Guerreo and Francesc Pérez-Murano, Institut de Microelectrónica de Barcelona (IMB-CNM, CSIC), Bellaterra, 08193, Spain.
Xavier Borrisé, Catalan Institute of Nanoscience and Nanotechnology (ICN2), CSIC and BIST, Campus UAB, Bellaterra, 08193 Barcelona, Spain.
Alvaro Blanco and Carlos Pecharromán, Instituto de Ciencia de Materiales de Madrid (ICMM), Consejo Superior de Investigaciones Científicas (CSIC), Calle Sor Juana Inés de la Cruz 3, Madrid, E-28049 Spain.

1 Introduction

Chirality is an intrinsic geometrical property of objects that cannot be superimposed with their mirror image. This property gives rise to two distinct realizations, termed enantiomers, which exhibit opposite handedness. Although often overlooked, chirality plays a crucial role in numerous critical phenomena, particularly in the field of biochemistry. The handedness of biological molecules such as amino acids, DNA or enzymes, for instance, has been demonstrated to be of paramount importance in elucidating their properties [1], [2]. A remarkable example is limonene, where one enantiomer is responsible for the characteristic fragrance of citrus fruits, while its counterpart contributes significantly to the scent of numerous coniferous and broadleaved trees [3].

Chirality is not limited to physical objects but can also be a property of fields, as is the case with left-handed (LCP) and right-handed (RCP) circularly polarized light [4], [5]. Light with a specific handedness serves as a valuable probe for chiral media, since light-matter interaction can be dictated by the handedness of both entities [6], [7], when present. Such chiroptical activity is commonly quantified through the optical functions f of the system under the two circular polarizations by means of the circular dichroism (CD) that can be defined as:

$$CD_f = \frac{f_{LCP} - f_{RCP}}{f_{LCP} - f_{RCP}}, \quad (1)$$

where f stands for any of the optical cross-sections (CS), namely, the absorption, scattering, and extinction, under either RCP or LCP illumination.

The chiral interaction in naturally occurring systems is typically of low magnitude, presenting substantial challenges for detection and quantification. Consequently, engineered chiral plasmonic structures have gained relevance because of their enhanced light-matter interaction associated with large values of the near fields, showing enhancements of the chiral signal of several orders of magnitude [8]–[11]. Furthermore, their integration into hybrid nanostructures promises active control of chirality [12].

Nowadays, strategies to fabricate chiral nanostructures are very diverse. However, due to the inherent difficulty to manufacture 3D structures using conventional nanofabrication techniques, early approaches were based on planar plasmonic structures [13]–[17]. These planar configurations typically exhibited limited chiroptical activity due to their two-dimensional nature, as truly planar structures cannot manifest chiroptical activity without violating system reciprocity [18]. Consequently, the observed chiroptical activity in many such structures was primarily attributed to their interaction with the substrate, effectively breaking the planar approximation [14], [16], [19]. Alternative designs have relied on the interaction between two modes through the excitation of Fano resonances [20], [21]. While these systems present circular dichroism (CD) in the absorption and the scattering cross sections (CS), the opposite sign of those contributions result in mutual cancellation. As a result, the extinction CS remains polarization-independent, again in accordance with reciprocity principles [22].

Further developments in nanofabrication technology have enabled the realization of diverse 3D nanostructures showing large values of CD, such as spirals [23], helicoidal arrangements [24], [25], and various stacked planar nanostructures ranging from nanorods [26], crosses [27], split ring resonators [28], [29], and gammadions [30], [31], among others.

In this work, we present a twisted stack formed by two identical planar nanostructures, called triskelia, which are characterized by their inherent 2D chirality and threefold rotational symmetry. In contrast to previously reported systems [24]–[29], the monomers of the stack exhibit intrinsic chiroptical activity. Furthermore, their threefold symmetry hinders the excitation of simple modes with an even number of poles while promoting the mixing of higher-order multipolar modes. As elucidated in our previous work [32], the small distance between the stack elements facilitates strong inter-element interactions, resulting in the emergence of handedness-dependent resonances in the near infrared spectral region. This configuration gives rise to pronounced CD which can be modulated by adjusting the twist angle between the stacked elements. Here, we investigate the nature of those resonances as a function of the twist angle between the two stacked structures, demonstrating that higher-order multipolar modes play a crucial role in the excitation of the structure under circularly polarized illumination. Our study is based on Fourier transform infrared spectroscopy (FTIR) measurements and finite difference time domain (FDTD) simulations.

2 Triskelion stack

The motif constituting the building block of the stack, the triskelion, is designed as three identical gold elements extending from a common central point, with each element oriented at 120° intervals. These elements exhibit a clockwise bend of 120° at their respective midpoints, thereby preserving threefold rotational symmetry while eliminating mirror planes parallel to the axis of rotation (see Fig. 1a). This geometric arrangement confers 2D chirality to the triskelion structure. The specific dimensions and geometry of the studied monomer are shown in Fig. 1a. The thickness of the planar structure was set to 30 nm. The final 3D structure consisted of a twisted stack of two coupled plasmonic triskelia, a schematic of which is shown in Fig. 1b, where the twist angle α is defined so that the stack has right-handed chirality whenever $\alpha < 60°$. Note that the chirality of the stack is the opposite (left-handed) for $\alpha > 60°$ due to the threefold symmetry of the monomer. $\alpha = 60°$ is a symmetrical configuration without a distinct handedness. Samples with various twist angles were manufactured through sequential processes by electron beam lithography (EBL), all of them with a separation between the two stacked elements of about 20 nm. Additional information regarding the manufacturing process is shown in the Methods section. Some examples of the manufactured stacks are shown in Fig. 1c. The cross-sectional image in Fig. 1d indicates good parallelism and consistent separation between the two triskelia. To preserve optical equivalence across all interfaces of the structure, the stack was embedded in a homogeneous medium with a refractive index of n=1.42. Larger areas of some samples are shown in Fig. 1e and f, illustrating the uniformity of the stacks.

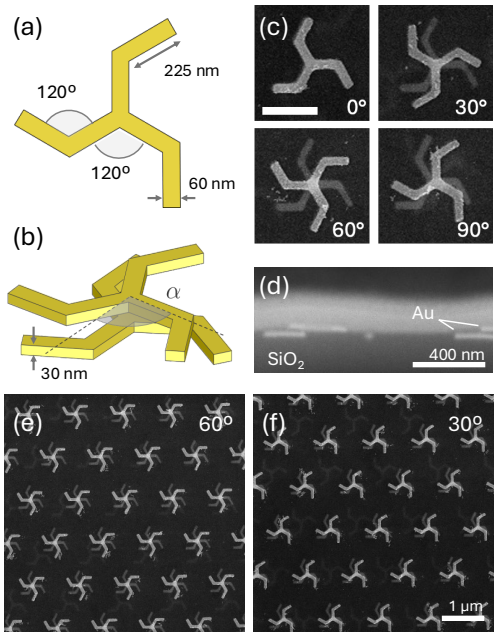

Fig. 1: (a) Diagram of a triskelion displaying the dimensions of the studied case. (b) Schematic depiction of the stack indicating the twist angle α, the vertical separation in the manufactured samples is 20 nm approximately. (c) Scanning Electron Microscopy (SEM) top-view images of some of the fabricated nanostructures. (d) Cross-section SEM image of one of the samples. Scale bars are 400 nm in length. (e) and (f) correspond to SEM images showing the spatial arrangement of the fabricated array of stacked triskelia. Note that the fabricated array has a pitch of 1200 nm.

3 Results and discussion

The structure exhibits two plasmonic resonances within the wavelength range of 1100 and 1600 nm. Both, FTIR measurements and simulations reveal two extinction peaks in this range, which undergo remarkable spectral shifts and intensity as the twist angle is modified. This is illustrated in Fig. 2a and b, where the intensity of the peaks, particularly the one at lower energy, is severely affected by the handedness of the circular polarization of the incident radiation. As a result, these handedness-dependent resonances yield large CD, as shown in Fig. 2c and d. It is worth noting that, while the studied excitations are of multipolar character and not as intense as the primary dipolar excitations (far in the infrared range, around 2000-3000 nm, for this structure), there is a general qualitative agreement between the experimental and

simulated curves in Fig. 2, including the opposite sign of the CD observed for the 30° and 90° cases.

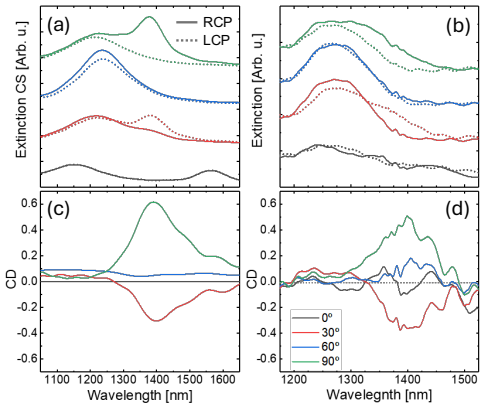

Fig. 2: (a) Simulated and (b) measured extinction spectra for different twist angles under LCP (solid line) and RCP (dashed line) illumination. The baselines of the spectra are shifted arbitrarily for clarity. (c) Simulated and (d) experimental CD extracted from the data in panels (a) and (b), respectively, using Eq. (1).

Moreover, owing to the threefold symmetry of the triskelion, both the spectral shifts and intensity variations are almost symmetric around 60° when the handedness of the light polarization is exchanged. Thus, the spectra for 30° and 90° under LCP and RCP light, respectively, appear remarkably similar (see Fig. 2a and b). The differences in the relative intensity of the peaks at these two angles can be attributed to the rightward bending of the triskelion branches, which breaks the symmetry when switching the light polarization between the 30° and 90° configurations. This also accounts for the minor differences observed in the spectra under LCP and RCP light at 60°, resulting in CD that is not strictly null, contrary to what would be expected solely from the threefold symmetry of the triskelion.

The typical approach to describing the optical response of a chiral medium would be to consider a simple and straightforward framework: the Born-Kuhn model [33]–[35]. This approximation supposes two interacting electrons oscillating in orthogonal directions in parallel planes separated a distance d. The coupling between the two particles results in two new eigenstates of the coupled oscillators system. This model yields results analogous to those of the hybridization of two plasmonic modes [36], [37] and was experimentally shown to be valid for plasmonic systems [38]. However, in prior studies, d was of the order of the excitation wavelength, while in the present work, d~20 nm. As a result, the phase shift of the incident radiation between the two monomers is rather small, weakening the chiral response. At the same time, since the interaction between plasmonic elements is mediated by their near fields, the close proximity between the two monomers in our study significantly enhances their coupling [26]. Consequently, a model based on the phase shift alone, such as the Born-Kuhn model, cannot account for the optical response of the triskelion stack. We propose instead an interpretation based on the hybridization of the plasmonic modes of individual triskelia. As shown in the charge distributions snapshots of the triskelia in Fig. 3, the complexity of the motif gives rise to multipolar excitations, especially fostered by geometric frustration; specifically, the threefold symmetry of the triskelion does not effectively accommodate an even number of poles, which are typically associated with simple dipole or multipolar modes. These plasmonic resonances, in turn, interact with those of the second triskelion in the stack resulting in a plethora of hybrid modes that deviate from the ideal in-phase/anti-phase excitations often considered in previous works involving two interacting dipoles [16], [29]. Moreover, the geometry of the system changes with the twist angle, favoring the excitation of low-energy resonances displaying variable dephasing between the polarizations of the two triskelia. This is clear in Fig. 3c and Fig. S1 in the Supplementary Information, where charge distributions and computed dipole moments for the two components of the stack as a function of α for the high- and low-energy modes are shown. Thus, while the high-energy mode maintains the two electric dipole moments relatively in-phase as α changes, the low energy mode exhibits a variable dephasing between the polarizations of both triskelia in the stack. Only at very small angles, the low-energy mode is sufficiently close to the anti-phase polar configuration (see Fig. 3a, Fig. 3c and Fig. S1 in the Supplementary Information). Around 30°, the polarizations of the two triskelia become perpendicular in the low-energy mode (see Fig. 3b, Fig. 3c and Fig. S1 in the Supplementary Information). As the angle α further increases, the polarizations corresponding to the low- and high-energy modes begin to resemble each other more closely (see Fig. 3c and Fig. S1 in the Supplementary Information). This observation indicates that, although only two peaks are detected for any value of α, the features of

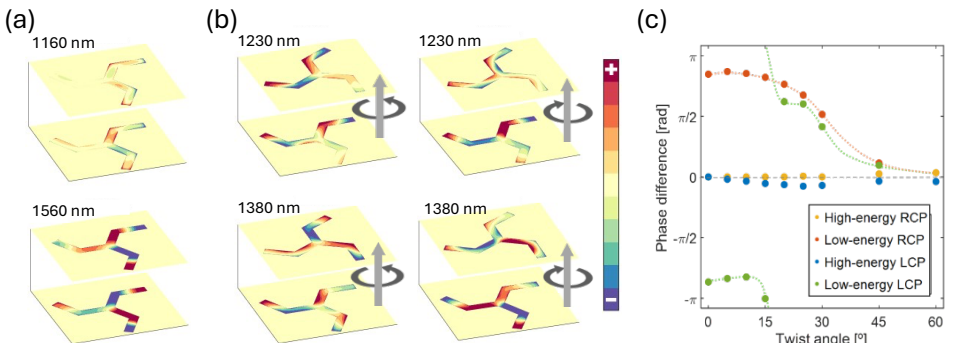

Fig. 3: Simulated charge distributions for facing triskelion interfaces for twist angles 0° (a) and 30° (b). Simulations at different angles correspond to arbitrary values of the phase of the incoming illumination. Panel (c) presents the phase difference in the orientations of the electric dipole moment of the top and bottom triskelia for each twist angle. All the information displayed shares a common scale. Note that a single polarization is presented for the case of 0° since the response is identical for both LCP and RCP. The geometry of the illumination is indicated by the vertical gray arrows and corresponds to that of the FTIR measurements.

the low-energy mode excited in each case are significantly different.

These findings suggest that the chiroptical activity in the stack arises from the dependence of the excitation intensity of these modes on the light-handedness, in accordance with previously reported results [26], [27], [32]. However, in this case, the resonances yielding CD are not sufficiently explained by the simplistic model involving the splitting of a triskelion mode into anti-phase and in-phase modes of the stack. Instead, they are better characterized by the excitation of an out-of-phase mode that is highly sensitive to the geometry of the stack at each angle α, in conjunction with the in-phase excitation. This continuous shift of the dephasing between the dipole moments of the monomers in the stack is shown in Fig. 3 and Fig. S1 in the Supplementary Information, for angles between 0° and 60°. In addition, the small net dipole moment of the out-of-phase, low-energy resonances agree with the fact that CD is typically associated with the selective excitation of modes exhibiting poor scattering [32].

In Fig. 4, the spectral response of the stack as a function of α is shown in colormaps obtained from FTIR and FDTD simulated data. Remarkably qualitative agreement between both sets of colormaps is found. Two Lorentzian functions, corresponding to the low- and high- energy resonances, were fitted to both the experimental and simulated spectra, with the position of some of these peaks also displayed for comparison in Fig. 4. The details of the fitting are presented in Fig. S2 in the Supplementary Information.

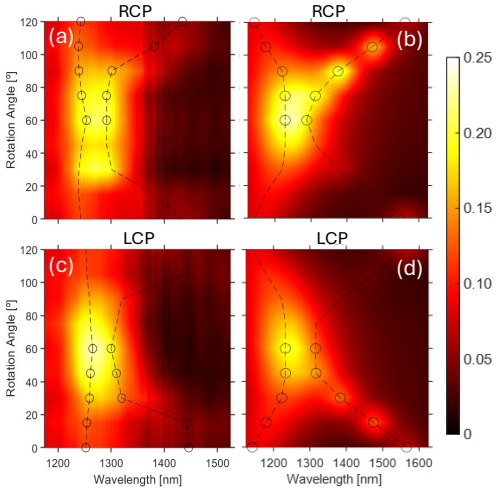

Fig. 4: Colormaps depicting the experimental ((a), (c)) and simulated ((b), (d)) extinction spectra for twist angles between 0° and 120° for both RCP ((a), (b)) and LCP ((c), (d)). Empty circles highlight the spectral position of the two Lorentzian peaks fitted to both the experimental and simulated data. Dashed lines are guidelines to the eye.

For angles between 0° and 60°, the structure favors the excitation of the out-of-phase, low-energy mode for the light-handedness opposite to that of the stack, i.e. LCP since the chirality of the stack is right-handed. Consequently, the out-of-phase mode is most efficiently excited by circular polarization that induces the greatest change in the relative orientation of the electric field with respect to the lower and upper triskelia (note that illumination is from bottom to top). In contrast, RCP light will excite both triskelia similarly due to the minimal phase shift of the light across *d*, thereby favoring the in-phase mode and significantly hindering the out-of-phase resonance. At 60°, the excitation features of the system are quite similar under both circular polarizations of the light, with only slight variations arising from the rightward bending of the triskelion branches. Despite this minor splitting at this angle, the intensity of the low-energy resonance is nearly negligible, as shown in Fig. S2 of the Supplementary Information, resulting in a single prominent peak in the extinction spectra. For angles greater than 60°, symmetric optical responses are observed with respect to those for α < 60° under reversed circular polarizations, except for small differences in the intensity of the low-energy mode. This slight asymmetry is owed to the fact that the triskelion is a chiral object in 2D, thus slightly altering the expected symmetric response around 60° due to its inherent threefold symmetry.

Finally, it is important to highlight that arranging these twisted triskelion stacks in a triangular array with an appropriate pitch (see Fig. 1e and f for details) can enhance the excitation of a surface lattice resonance (SLR). The intensity of this resonance strongly depends on the handedness of the circular polarization of the light and the twist angle, resulting in very large dichroism for angles larger than 10°. These results were obtained from numerical simulation of a lattice embedded in a medium of $n = 1.5$, where each element consisted of a twisted stack with 50 nm in separation between the two monomers and a twist angle range of $0° \leq \alpha \leq 30°$. Fig. 5 shows the simulated extinction CS under RCP an LCP light at four selected values of α, with a fixed pitch of 1200 nm. At this pitch, a SLR emerges as a sharp peak with a Fano profile located around 1550 nm, precisely in the region where anti-phase excitations of the triskelion stack become energetically favorable (as seen in the case for α = 0° in Fig. 5). Therefore, the Fano resonance originates from the hybridization of the SLR mode with the anti-phase plasmonic excitation of the stack, where the sharp and intense peak of the resonance corresponds to the coherent excitation of the anti-phase mode across the lattice of triskelion stacks through absorption of the incoming radiation. Consequently, the cooperative interaction among the near fields created by the elements in the lattice, due to the geometrical resonance condition, amplifies the excitation of the anti-phase mode in every stack (which would otherwise be very weak), leading to a large energy absorption. This excitation occurs with much greater efficiency when illuminated by light that matches the handedness of the stack (LCP in this case), as

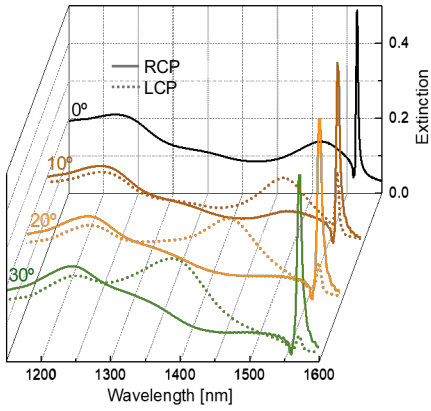

Fig. 5: Simulated extinction spectra for an array of stacked triskelia with a pitch of 1200 nm, embedded in a homogeneous medium of n=1.5 with a separation of 50 nm between triskelia. The response of the array under RCP and LCP illumination is presented for different values of the twist angle within the stack.

incoming radiation with the handedness of the stack favors a larger polarization of the first triskelion. This, in turn, induces a larger anti-phase polarization in the second triskelion through near-field interactions. It is important to note that in-phase modes cannot be excited in this range of relatively low energies. Under circular polarization with opposite handedness to that of the stack (RCP in this case), polarizations induced in both triskelia within each stack are reduced, leading to lower absorption associated with the lattice resonance. As a result, the spectra in Fig. 5 exhibit large differences in the intensity of the SLR modes under RCP and LCP illumination, resulting in high values of dichroism, except at $\alpha = 0°$ where the stack lacks chirality.

We attempted to experimentally reproduce these results using samples like those shown in Fig. 1e and f but were unsuccessful. This may be attributed to the narrow spectral width of the SLR, inadequate perpendicular illumination of the samples due to the numerical apertures of the optical systems used for light focusing, or insufficient patterned areas on the fabricated samples, which could lead to finite-size broadening effects.

4 Conclusions

We have presented a comprehensive study of the chiroptical response of a twisted stack of triskelion nanostructures, emphasizing the detailed characterization of two coupled multipolar modes in the near-infrared region. Our findings, supported by FTIR measurements and FDTD simulations, demonstrate that both the spectral position and intensity of the resonances can be precisely tuned by adjusting the angle between the two elements in the stack. The three-fold symmetry of the elements promotes complex multipolar excitations which are incompatible with an even number of pairs of equal poles with opposite sign. In particular, under illumination with an opposite handedness to that of the structure, two multipolar resonances are observed; conversely, illumination with light that matches the handedness of the structure reveals only the peak corresponding to the high-energy excitation. This results in large dichroism in the extinction CS of the system, except in the particularly symmetric cases at twist angles of 0° and 60°.

Our findings show that the high-energy mode originates from an in-phase excitation of the two triskelia under both RCP and LCP illumination. In contrast, the low-energy mode, which is enhanced by illumination under opposite handedness to that of the stack, corresponds to the excitation of the two monomers with a specific phase difference between their instantaneous polarizations. Thus, contrary to previous works, we demonstrate that anti-phase oscillations occur only at small twist angles; for angles greater than 15°, the polarizations of the two monomers progressively align in phase as α increases towards 60°. This draws a significantly more complex scenario depending on the twist angle, diverging from the descriptions provided by the Born-Kuhn model or the hybridization of two equivalent plasmonic resonances producing simple in phase- and antiphase-coupled modes of the stack.

Finally, simulations indicate that arranging such a chiral stack in a plasmonic triangular lattice leads to the selective excitation of a SLR depending on the light handedness. This configuration enables high CD values within a narrow wavelength range, that can be tuned by the pitch of the lattice and the geometry of the stack.

5 Methods

5.1 Sample fabrication

The samples were fabricated by consecutive EBL, following the steps depicted in Fig. S3 in the Supplementary Information. The samples were lithographed on a Si substrate (250 μm thick) coated with a SiO_2 layer on both sides (1.8 μm thick, deposited by wet thermal oxidation). The first EBL process aimed at defining the alignment markers, which consisted of Au squares of 100x100 nm^2 and 80 nm in thickness using an adhesion layer of 10 nm of Cr. The thickness of these markers has proven to be critical for their correct detection, and therefore, alignment of the EBL system for further lithography processes. The second step was to cover the markers with hydrogen silsesquioxane (HSQ) in solution in methyl isobutyl ketone (MIBK), commercially labelled as FOx (flowable oxide) [39], [40]. This diluted polymer was deposited through spin coating, pre-baked at 80 °C for 4 minutes and then annealed at 400 °C for a minimum of 1 hour. This produced a homogeneous layer of SiO_2 of 300 nm in thickness approximately following a cost-effective and controllable protocol.

Subsequently, an additional EBL step was carried out to pattern the first layer of triskelia, using the alignment markers as a reference. Following the corresponding exposure and development, 30 nm of Au was deposited on top of a 2 nm adhesion layer of Ge, which has been shown to better preserve the plasmonic properties of noble metal nanostructures compared to other common materials, such as Cr or Ti [41]. After completing the lift-off process, another layer of HSQ was deposited and then annealed, with this layer having a thickness of approximately 50 nm.

Finally, the third and final EBL step was performed. A second layer of twisted triskelia was patterned, ensuring that the centers of the triskelia in both layers were aligned, using the same alignment markers and parameters as in the previous step. Following this complex process, the two layers of twisted triskelia, separated by 20 nm, were embedded in SiO_2. Interestingly, despite the substrate consisting of a relatively thick layer of Si, the transparency of the entire double-oxidized Si wafer is approximately 50%, particularly for wavelengths larger than 1150 nm (see Fig. S4 in the Supplementary Information).

EBL was performed using a Raith/Vistec EBPG 5000Plus with a Gaussian-shaped beam, offering a maximum writing field size of 1024×1024 μm^2 and high beam stepping frequencies of up to 125 MHz, and operating at 100 keV acceleration and with an overlay precision around 20 nm for larger write fields and 10 nm for smaller ones (100×100 μm^2). The metallization was performed using physical vapor deposition (PVD) by evaporating the target using an electron gun.

5.2 FDTD simulations

The FDTD simulations presented in this work were performed using the commercial software provided by Lumerical [42]. All simulations were performed using a 2x2x2 nm^3 cell size setting a homogeneous background refractive index of 1.42 without absorption to better reproduce the optical properties of annealed HSQ. The optical coefficients for Au were obtained from [43]. The circularly polarized illumination was introduced using linearly polarized plane waves by setting two sources with orthogonal polarization angles and a $\pi/2$ phase difference between them. Two types of simulations were performed, those featuring single stacked elements, and others

where the response of an infinite triangular lattice of stacked elements was simulated.

The former relies on the use of total-field scattered-field (TFSF) sources and perfect absorbing boundary conditions. Absorption and scattering CS data were collected since only one element was being simulated. For these simulations the extinction CS was the sum of absorption and scattering CS. The second type of simulations require the use of plane wave sources and periodic boundary conditions at the in-plane boundaries. In this case, reflection and transmission through the structure were measured. The extinction in this framework was assigned to be 1 - *T*, where *T* stands for the transmission CS. It is worth noting that the reflection of the structure was very small compared to the extinction signal.

5.3 FTIR measurements

Bruker Vertex 70V Spectrophotometer with a microscope Hyperion 2000 was used to measure the extinction spectra. Transmission through the sample was measured using 4x magnification in order to minimize the numerical aperture of the system and to optimize normal incidence.

Research funding: Financial support from the Spanish Ministry of Science and Innovation (PID2021-127397NB-I00), the European Union FEDER funds, and the Generalitat de Catalunya (2021SGR00328) is acknowledged.

Author contributions: JRA has designed the structures, simulated the system, fabricated the samples, assisted in their characterization, and contributed to the draft and final manuscript. JVC and CD. have provided access to the facilities and the expertise necessary for the fabrication of the samples and have supported the process. AGM has contributed to the simulations and the discussion of the system. AGB, XB and FPM have contributed to the design and initial exploration of the fabrication process and the later characterization of the cross-section of the samples by SEM. AB and CP have performed the experimental characterization of the spectral response of the system by FTIR. XB and AFR have contributed to the design, discussion and revisions of the manuscript. AL has contributed to the design, discussion and elaboration of the draft and final manuscripts. All authors have accepted responsibility for the entire content of this manuscript and consented to its submission to the journal, reviewed all the results and approved the final version of the manuscript.

Data availability: The data that support the findings of this study are available from the corresponding author upon reasonable request.

References

[1] S. F. Mason, "Origins of biomolecular handedness," *Nature*, vol. 311, no. 5981, pp. 19–23, 1984, doi: 10.1038/311019a0.

[2] M. Novotny and G. J. Kleywegt, "A survey of left-handed helices in protein structures," *J. Mol. Biol.*, vol. 347, no. 2, pp. 231–241, 2005, doi: 10.1016/j.jmb.2005.01.037.

[3] A. Wibe, A. K. Borg-Karlson, M. Persson, T. Norin, and H. Mustaparta, "Enantiomeric composition of monoterpene hydrocarbons in some conifers and receptor neuron discrimination of α-pinene and limonene enantiomers in the pine weevil, Hylobius abietis," *J. Chem. Ecol.*, vol. 24, no. 2, pp. 273–287, 1998, doi: 10.1023/A:1022580308414.

[4] L. V. Poulikakos, J. A. Dionne, and A. García-Etxarri, "Optical helicity and optical chirality in free space and in the presence of matter," *Symmetry (Basel).*, vol. 11, no. 9, pp. 1–16, 2019, doi: 10.3390/sym11091113.

[5] M. Schäferling, *Chiral Nanophotonics*, vol. 205. 2017.

[6] Y. Tang and A. E. Cohen, "Optical chirality and its interaction with matter," *Phys. Rev. Lett.*, vol. 104, no. 16, pp. 1–4, 2010, doi: 10.1103/PhysRevLett.104.163901.

[7] A. O. Govorov, Z. Fan, P. Hernandez, J. M. Slocik, and R. R. Naik, "Theory of circular dichroism of nanomaterials comprising chiral molecules and nanocrystals: Plasmon enhancement, dipole interactions, and dielectric effects," *Nano Lett.*, vol. 10, no. 4, pp. 1374–1382, 2010, doi: 10.1021/nl100010v.

[8] Z. Fan and A. O. Govorov, "Chiral nanocrystals: Plasmonic spectra and circular dichroism," *Nano Lett.*, vol. 12, no. 6, pp. 3283–3289, 2012, doi: 10.1021/nl3013715.

[9] H. E. Lee *et al.*, "Amino-acid- A nd peptide-directed synthesis of chiral plasmonic gold nanoparticles," *Nature*, vol. 556, no. 7701, pp. 360–364, 2018, doi: 10.1038/s41586-018-0034-1.

[10] M. Hentschel, M. Schäferling, X. Duan, H. Giessen, and N. Liu, "Chiral plasmonics," *Sci. Adv.*, vol. 3, no. 5, pp. 1–12, 2017, doi: 10.1126/sciadv.1602735.

[11] C. Jack *et al.*, "Biomacromolecular Stereostructure Mediates Mode Hybridization in Chiral Plasmonic Nanostructures," *Nano Lett.*, vol. 16, no. 9, pp. 5806–5814, 2016, doi: 10.1021/acs.nanolett.6b02549.

[12] X. Yin *et al.*, "Active Chiral Plasmonics," *Nano Lett.*, vol. 15, no. 7, pp. 4255–4260, 2015, doi: 10.1021/nl5042325.

[13] R. Ogier, Y. Fang, M. Svedendahl, P. Johansson, and M. Käll, "Macroscopic Layers of Chiral Plasmonic Nanoparticle Oligomers from Colloidal Lithography," *ACS Photonics*, vol. 1, no. 10, pp. 1074–1081, 2014, doi: 10.1021/ph500293u.

[14] A. S. Schwanecke, A. Krasavin, D. M. Bagnall, A. Potts, A. V. Zayats, and N. I. Zheludev, "Broken time reversal of light interaction with planar chiral nanostructures," *Phys. Rev. Lett.*, vol. 91, no. 24, pp. 1–4, 2003, doi: 10.1103/PhysRevLett.91.247404.

[15] A. Papakostas, A. Potts, D. M. Bagnall, S. L. Prosvirnin, H. J. Coles, and N. I. Zheludev, "Optical Manifestations of Planar Chirality," *Phys. Rev. Lett.*, vol. 90, no. 10, p. 4, 2003, doi: 10.1103/PhysRevLett.90.107404.

[16] M. Kuwata-Gonokami *et al.*, "Giant optical activity in quasi-two-dimensional planar nanostructures," *Phys. Rev. Lett.*, vol. 95, no. 22, pp. 1–4, 2005, doi: 10.1103/PhysRevLett.95.227401.

[17] A. W. Clark, A. Glidle, D. R. S. Cumming, and J. M. Cooper, "Plasmonic split-ring resonators as dichroic nanophotonic DNA biosensors," *J. Am. Chem. Soc.*, vol. 131, no. 48, pp. 17615–17619, 2009, doi: 10.1021/ja905910q.

[18] P. Vincent and M. Nevière, "The Reciprocity Theorem for Corrugated Surfaces Used in Conical Diffraction Mountings," *Opt. Acta Int. J. Opt.*, vol. 26, no. 7, pp. 889–898, Jul. 1979, doi: 10.1080/713820075.

[19] B. Bai, Y. Svirko, J. Turunen, and T. Vallius, "Optical activity in planar chiral metamaterials: Theoretical study," *Phys. Rev. A - At. Mol. Opt. Phys.*, vol. 76, no. 2, 2007, doi: 10.1103/PhysRevA.76.023811.

[20] B. Hopkins, A. N. Poddubny, A. E. Miroshnichenko, and Y. S. Kivshar, "Revisiting the physics of Fano resonances for nanoparticle oligomers," *Phys. Rev. A - At. Mol. Opt. Phys.*, vol. 88, no. 5, pp. 1–10, 2013, doi: 10.1103/PhysRevA.88.053819.

[21] S. Zu, Y. Bao, and Z. Fang, "Planar plasmonic chiral nanostructures," *Nanoscale*, vol. 8, no. 7, pp. 3900–3905, 2016, doi: 10.1039/c5nr09302c.

[22] B. Hopkins, A. N. Poddubny, A. E. Miroshnichenko, and Y. S. Kivshar, "Circular dichroism induced by Fano resonances in planar chiral oligomers," *Laser Photonics Rev.*, vol. 10, no. 1, pp. 137–146, 2016, doi:

10.1002/lpor.201500222.

[23] V. K. Valev *et al.*, "Plasmonic ratchet wheels: Switching circular dichroism by arranging chiral nanostructures," *Nano Lett.*, vol. 9, no. 11, pp. 3945–3948, 2009, doi: 10.1021/nl9021623.

[24] A. Kuzyk *et al.*, "DNA-based self-assembly of chiral plasmonic nanostructures with tailored optical response," *Nature*, vol. 483, no. 7389, pp. 311–314, 2012, doi: 10.1038/nature10889.

[25] J. K. Gansel *et al.*, "Gold helix photonic metamaterial as broadband circular polarizer," *Science (80-.).*, vol. 325, no. 5947, pp. 1513–1515, 2009, doi: 10.1126/science.1177031.

[26] A. Wu, Y. Y. Tanaka, and T. Shimura, "Giant chiroptical response of twisted metal nanorods due to strong plasmon coupling," *APL Photonics*, vol. 6, no. 12, 2021, doi: 10.1063/5.0069371.

[27] M. Decker *et al.*, "Strong optical activity from twisted-cross photonic metamaterials," *Opt. Lett.*, vol. 34, no. 16, p. 2501, 2009, doi: 10.1364/ol.34.002501.

[28] M. Decker, R. Zhao, C. M. Soukoulis, S. Linden, and M. Wegener, "Twisted split-ring-resonator photonic metamaterial with huge optical activity," *Opt. Lett.*, vol. 35, no. 10, p. 1593, 2010, doi: 10.1364/ol.35.001593.

[29] N. Liu, H. Liu, S. Zhu, and H. Giessen, "Stereometamaterials," *Nat. Photonics*, vol. 3, no. 3, pp. 157–162, 2009, doi: 10.1038/nphoton.2009.4.

[30] T. Cao, L. Zhang, R. E. Simpson, C. Wei, and M. J. Cryan, "Strongly tunable circular dichroism in gammadion chiral phase-change metamaterials," *Opt. Express*, vol. 21, no. 23, p. 27841, 2013, doi: 10.1364/oe.21.027841.

[31] D.-H. Kwon, P. L. Werner, and D. H. Werner, "Optical planar chiral metamaterial designs for strong circular dichroism and polarization rotation," *Opt. Express*, vol. 16, no. 16, p. 11802, 2008, doi: 10.1364/oe.16.011802.

[32] J. Rodríguez-Álvarez, A. García-Martín, A. Fraile Rodríguez, X. Batlle, and A. Labarta, "Tunable circular dichroism through absorption in coupled optical modes of twisted triskelia nanostructures," *Sci. Rep.*, vol. 12, no. 1, pp. 1–10, 2022, doi: 10.1038/s41598-021-03908-2.

[33] V. A. Fedotov, P. L. Mladyonov, S. L. Prosvirnin, A. V. Rogacheva, Y. Chen, and N. I. Zheludev, "Asymmetric propagation of electromagnetic waves through a planar chiral structure," *Phys. Rev. Lett.*, vol. 97, no. 16, pp. 1–4, 2006, doi: 10.1103/PhysRevLett.97.167401.

[34] M. Born, "Über die natürliche optische aktivität von flüssigkeiten," *Phys. Z*, vol. 16, pp. 251–258, 1915.

[35] W. Kuhn, "Quantitative Verhältnisse und Beziehungen bei der natürlichen optischen Aktivität," *Zeitschrift für Phys. Chemie*, vol. 4, no. 1, pp. 14–36, 1929, doi: https://doi.org/10.1515/zpch-1929-0403.

[36] K. D. Osberg, N. Harris, T. Ozel, J. C. Ku, G. C. Schatz, and C. A. Mirkin, "Systematic study of antibonding modes in gold nanorod dimers and trimers," *Nano Lett.*, vol. 14, no. 12, pp. 6949–6954, 2014, doi: 10.1021/nl503207j.

[37] B. Auguié, J. L. Alonso-Gómez, A. Guerrero-Martínez, and L. M. Liz-Marzán, "Fingers crossed: Optical activity of a chiral dimer of plasmonic nanorods," *J. Phys. Chem. Lett.*, vol. 2, no. 8, pp. 846–851, 2011, doi: 10.1021/jz200279x.

[38] X. Yin, M. Schäferling, B. Metzger, and H. Giessen, "Interpreting chiral nanophotonic spectra: The plasmonic Born-Kuhn model," *Nano Lett.*, vol. 13, no. 12, pp. 6238–6243, 2013, doi: 10.1021/nl403705k.

[39] G. A. Loboda, Mark J and Toskey, "Understanding hydrogen silsesquioxane-based dielectric film processing," *Solid state Technol.*, vol. 41, no. 5, pp. 99–103, 1998.

[40] M. J. Loboda, C. M. Grove, and R. F. Schneider, "Properties of a - SiO x : H Thin Films Deposited from Hydrogen Silsesquioxane Resins," *J. Electrochem. Soc.*, vol. 145, no. 8, pp. 2861–2866, 1998, doi: 10.1149/1.1838726.

[41] V. J. Logeeswaran *et al.*, "Ultrasmooth silver thin films deposited with a germanium nucleation layer," *Nano Lett.*, vol. 9, no. 1, pp. 178–182, 2009, doi: 10.1021/nl8027476.

[42] "Lumerical Inc." https://www.lumerical.com/ (accessed Jan. 10, 2023).

[43] P. B. Johnson and R. W. Christy, "Optical Constant of the Nobel Metals," *Phys. Rev. B*, vol. 6, no. 12, pp. 4370–4379, 1972.

Supplementary Information for:

Dichroism of coupled multipolar plasmonic modes in twisted triskelion stacks

Javier Rodríguez-Álvarez[1,2,], Joan Vila-Comamala[3], Antonio García-Martín[4], Albert Guerreo[5], Xavier Borrisé[6], Francesc Pérez-Murano[5], Christian David[3,] Alvaro Blanco[7], Carlos Pecharromán[7], Xavier Batlle[1,2], Arantxa Fraile Rodríguez[1,2], and Amílcar Labarta[1,2].*

[1] Departament de Física de la Matèria Condensada, Universitat de Barcelona, 08028 Barcelona, Spain

[2] Institut de Nanociència i Nanotecnologia (IN2UB), Universitat de Barcelona, 08028, Spain

[3] Paul Scherrer Institute, Forschungsstrasse 111, Villigen 5232, Switzerland

[4] Instituto de Micro y Nanotecnología IMN-CNM, CSIC, CEI UAM + CSIC, Isaac Newton 8, 28760, Tres Cantos, Madrid, Spain

[5] Institut de Microelectrónica de Barcelona (IMB-CNM, CSIC), Bellaterra, 08193, Spain

[6] Catalan Institute of Nanoscience and Nanotechnology (ICN2), CSIC and BIST, Campus UAB, Bellaterra, 08193 Barcelona, Spain

[7] Instituto de Ciencia de Materiales de Madrid (ICMM), Consejo Superior de Investigaciones Científicas (CSIC), Calle Sor Juana Inés de la Cruz 3, Madrid, E-28049 Spain

*E-mail: javier.rodriguez@ub.edu

- **S1.** Electric dipole moment for both triskelia for the high- and low-energy resonances for several twist angles.
- **S2.** Lorentzian fitting of the measured and spectra for several twist angles.
- **S3.** EBL lithography steps involved in the fabrication of the structures.
- **S4.** Calculated transmission of the substrate.

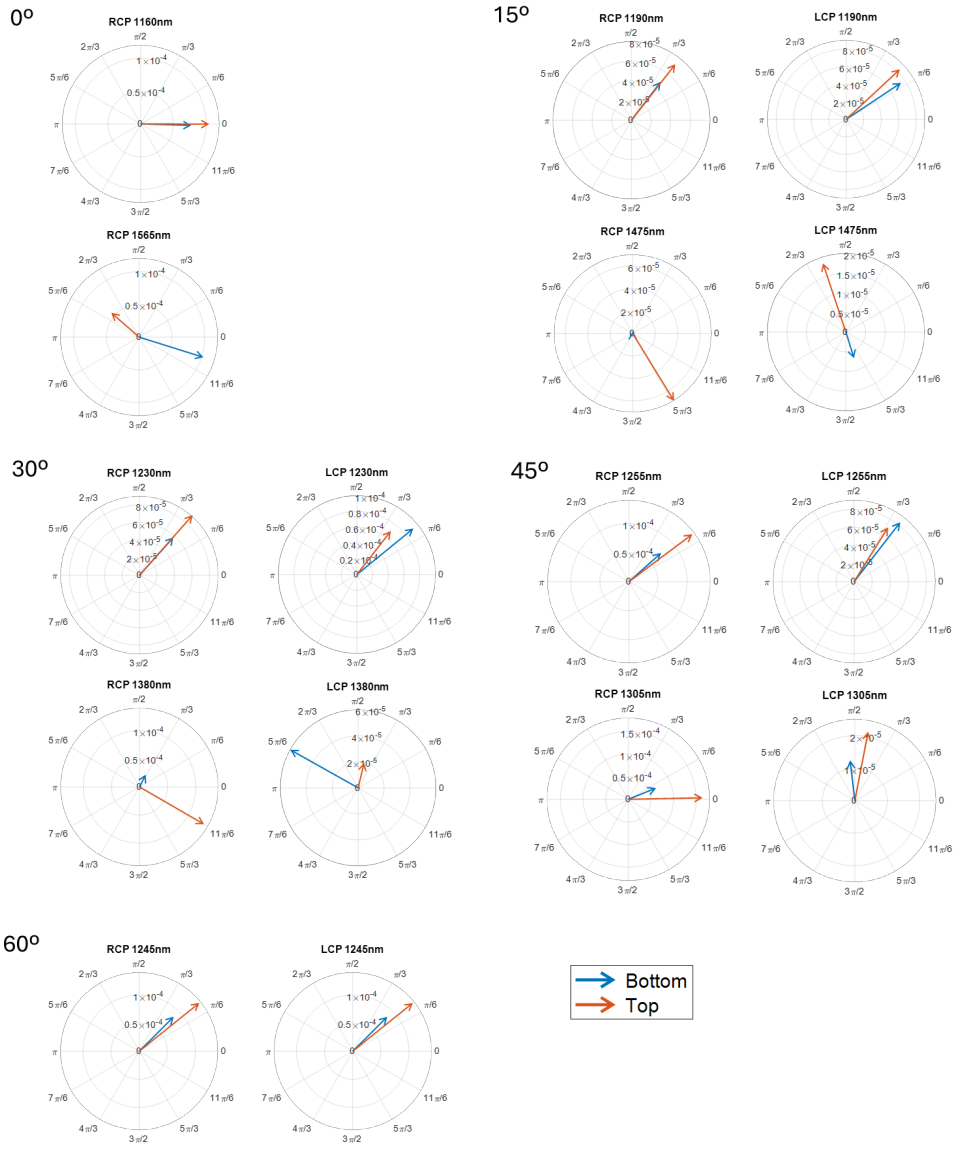

Fig. S1: Real part of the electric dipole moment computed for each of the two triskelia in the stack at an arbitrary phase of the incoming light. Data extracted from FDTD simulations for 0º, 15º, 30º, 45º, and 60º for wavelengths of interest under RCP and LCP. Note that for the 0º case, only RCP is represented since the structure is not chiral.

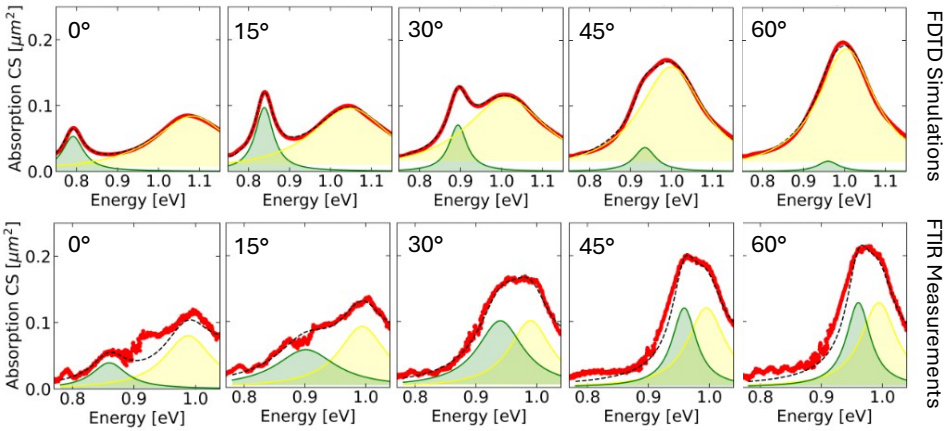

Fig. S2: Simulated (top row) and measured data (bottom row) fitted by the sum of two Lorentzian curves for several twist angles under RCP illumination.

Fig. S3: Schematic representation of the necessary steps in the double lithography process used in the fabrication of the samples.

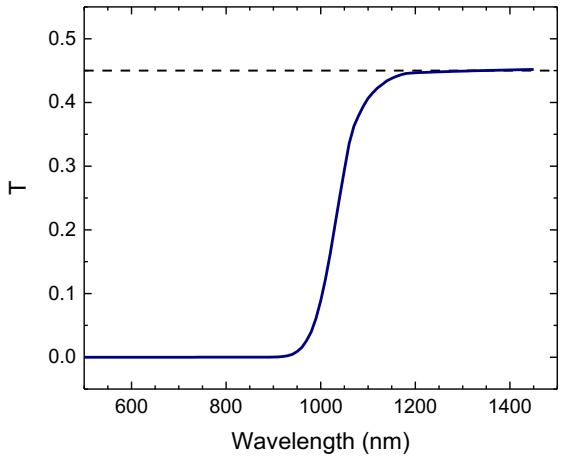

Fig. S4: Calculations of the transmission of the double oxidized Si substrate as a function of the wavelength. The transparency is almost 50% for wavelengths greater than 1200 nm. The calculation takes into account the energy lost by reflections in all the interphases of the substrate as well as the absorption of the Si layer, using the optical constants for Si in the literature [1].

REFERENCES

[1] D. E. A. and A. A. Studna, “Dielectric functions and optical parameters of Si, Ge, GaP, GaAs, GaSb, InP, InAs, and InSb from 1.5 to 6.0 eV,” *Phys. Rev. B*, vol. 27, no. 2, pp. 985–1009, 1983, doi: 10.1103/PhysRevB.27.985.

Discussion

This section aims to summarize and discuss the main findings presented in publications I to IV, which encompass the main findings of the research presented in this thesis on two distinct yet interrelated classes of plasmonic nanostructures.

On the one hand, the two articles delving into inverted plasmonic honeycomb lattices study a rich variety of bright and dark plasmonic modes. With a special emphasis on both SLR, due to their potential sensing applications, and extended antiferroelectric dark modes, due to their novelty in such plasmonic structures. On the other hand, the works on stacked, twisted plasmonic triskelion nanostructures study the control of chiroptical activity through tuning of plasmonic coupling between the two elements in the stack through near-field interactions. Although the underlying physical phenomena differ in detail, both classes of structures rely on a precise manipulation of geometry and plasmonic interactions to tailor their optical responses.

Publication I focuses on the integration of an inverted plasmonic lattice into a heterostructure designed for refractive index sensing. Here, the plasmonic lattice is combined with additional elements such as a SiO_2 spacer, and an underlying Au mirror to maximize the out-of-plane near-field enhancement. FDTD simulations show that the heterostructure supports SLR at both the Au–SiO_2 and the air–Au interfaces, manifesting as sharp spectral peaks whose positions are highly sensitive to changes in the refractive index of the surrounding medium. Moreover, the near-field distributions associated with these resonances extend hundreds of nanometers into the surrounding environment providing an enlarged interaction volume for analyte molecules, thereby improving the sensor's performance. The device exhibits high sensitivity, ranging from approximately 99 to 395 nm/RIU, and a notable figure of merit, up to 199 RIU^{-1}, underscoring the effectiveness of the inverted lattice design as a refractive index sensor.

Complementing these findings, Publication II provides an in-depth analysis of the plasmonic modes arising in an similar inverted honeycomb array.

By combining high-resolution EELS, FTIR, and FDTD simulations, several plasmonic resonances are characterized in the visible and near-infrared spectral ranges. The study successfully characterizes both bright and dark modes, using far- and near-field techniques. Notably, it also identifies a class of dark modes that rely on the excitation of antiferroelectric chains of slits in the honeycomb lattices, giving rise to complex excitations that present a unit cell with twice the area than that of the underlying lattice. These extended modes, arising from the out-of-phase excitation of adjacent chains of slits, have not been reported previously in the literature and constitute a prime example of plasmonic modes that present a larger periodicity than that of the plasmonic lattice.

On the topic of twisted triskelion, Publication III investigates a system composed of two stacked, chiral plasmonic elements, called triskelia through FDTD simulations. This work constitutes a first approach to this system. For this reason, simulations are used to study a simple standalone stack. Our results indicate that by controlling the twist angle and the separation between the triskelia, a significant CD can be achieved, attaining maximum values of up to 60% under optimal conditions. This is due to the interaction-based resonant modes arising in the stacked structure. In particular, due to a plasmonic resonance around 1100 nm that is preferentially excited by light with opposite handedness to that of the stacked system, producing a strong dichroism in the absorption cross-section. In addition, simulations indicate a distinct three-dimensional near-field distribution associated with the plasmonic modes displaying CD. The intensity of this near field also depends on the handedness of the exciting light. Similarly to the spectral response, the details on this near-field distribution strongly depend on the handedness of the light, the energy of the resonance and can be controlled through the geometric parameters of the structure.

Based on the results from the simulations, Publication IV aims to provide experimental evidence on the behavior of stacked twisted trikelion nanostructures. Owing to a state-of-the-art nanofabrication process by EBL and through a combination of FTIR spectroscopy and numerical simulations with realistic parameters, the study characterizes the effect of the twist angle between the triskelion layers on the plasmonic response of the structure. At small twist angles, the system behaves analogously to a pair of interacting dipoles, originating two hybrid modes with oscillating charges in phase and

out of phase, respectively. However, as the angle increases, the dipolar modes disapear in favor of more complex charge distributions as the relative phase difference between the charge oscillations in both structures also changes. This transition is accompanied by a pronounced change in the CD exhibited by the structure, with maximum dichroism observed at 20° approximately, where the hybridization of the modes and the chirality of the stack are both optimal. The results underscore the importance of plasmonic coupling to the generation of enhanced chiroptical response in stacked systems, and they highlight the feasibility of engineering plasmonic responses through controlled nanofabrication. In addition, simulations presented in this works indicate the presence of chiral SLR that can be selectively excited under CP illumination.

Both classes of plasmonic systems —namely, the inverted honeycomb lattices and the stacked triskelion nanostructures— exemplify how rigorous simulation and its analysis can be employed to tailor plasmonic resonances for specific applications. Moreover, thanks to a precise nanofabrication process, often requiring the development of new protocols, the simulated structures can be characterized. Furthermore, the combined use of advanced experimental techniques, such as EELS, FTIR, and electron beam lithography, with FDTD simulations has been crucial for unraveling the complex interplay between geometry, mode coupling, and optical response in these systems.This integrated approach not only validates the theoretical predictions but also provides practical guidelines for the design of next-generation plasmonic devices for innovative applications in sensing, optical communication, and beyond.

The discussed results successfully achieve the objectives of this thesis, which delves into the study of plasmonic lattices and stacked plasmonic systems with 3-fold symmetry using a methodology that combines FDTD simulations, innovative nanofabrication processes, and far- and near-field characterization of the fabricated samples.

Conclusions

This thesis has been devoted to the study of interacting plasmonic nanostructures that exhibit an enhanced optical response due to the interactions of simple elements and the inherent geometric frustration in the system. The most relevant contributions obtained through the design, simulations, fabrication and characterization of such structures are listed below.

Inverted honeycomb lattices

- Our work shows the promising performance of inverted plasmonic arrays, in particular following a honeycomb lattice, for sensing purposes. Due to the chosen pitch for the arrays and the layers of SiO_2 and Au underneath it, these structures are able to hold a collective SLR with an exceptionally intense and narrow reflection dip around 765 nm, despite the expected total reflection granted by the Au layer.

- The spectral signature of these inverted honeycomb lattices and their sensitivity to changes in the surrounding medium make them particularly suitable for sensing purposes. As a refractive index sensor, the proposed structure achieved a sensitivity of 99 nm/RIU for a layer of changing refractive index of 50 nm in thickness, reaching high sensitivity values even for small analyte thickness.

- For an infinite analyte thickness, the calculated sensitivity was 613 nm/RIU, yielding a figure of merit of 199 RIU^{-1}, which constitutes an improvement of an order of magnitude over other similar plasmonic nanosensors.

- From a fundamental perspective, plasmonic resonances in inverted honeycomb arrays have been studied by FDTD simulations and EELS, resulting in significant success in characterizing both bright and dark LSP within the structure. This characterization is achieved through the strong agreement between the charge and near-field distributions obtained from FDTD simulations and the EELS maps.

- Additional dark modes have also been reported. These resonances consist of an antiferroelectric polarization of chains of neighboring slits throughout the sample. The periodicity of these modes does not match that of the honeycomb lattice, as the unit cell of these periodic excitations of the lattice has twice the area.

- Both systems further strengthened the technical capabilities of nanofabrication techniques, the first employs an unconventional EBL process, that eliminates the lift-off step, while the second utilizes a FIB milling with Au ions to pattern a 20 nm layer of Au over a 50 nm Si_3N_4 membrane.

Stacked triskelia nanostructures

- We have shown that the stacked structure studied is capable of achieving large CD due to coupled modes between the building blocks of the stack. These building blocks, called triskelia, present an inherent 3-fold symmetry and are chiral in 2D.

- We demonstrate that, by changing the distance between the triskelia and their relative rotation angle, called "twist angle", both the spectral position and intensity can be precisely tuned.

- FDTD simulations indicate that the two pairs of resonances arise from this interaction in the visible (around to 800 nm) and NIR (around 1100 nm)range. The chiroptical response primarily originates from the lower-energy resonance in each pair of resonance. The dichroism arises mainly in the absorption CS, as these resonances present a negligible scattering signal.

- The chiroptically active resonances studied in Publication III are easily understood when considered in relation to their non-chiral counterparts. The model presented in Publication IV, considers two multipolar excitations arising on each triskelion that are coupled due to the close proximity of both elements, around 20 nm in the fabricated systems. These two hybrid modes exhibit in-phase and out-of-phase excitations of the net dipolar moments in each triskelion.

- As the twist angle changes, the mode arising at lower energy is only detected under illumination with the opposite handedness to that of the structure, corresponding to the out-of-phase mode. This phenomenon is the origin of the strong dichroism present in the system, except in the specific cases of 0°and 60°.

- Contrary to previous works, we show that as the twist angle increases from 0°to 60°, the out-of-phase mode exhibits a decreasing phase difference between the two polarizations that progressively transitions from the anti-phase case for angles under 15°to the in-phase case at 60°.

After presenting the main results of this thesis, it is worth discussing the open questions to be addressed by future research. While this thesis has highlighted the potential of inverted honeycomb plasmonic lattices as a sensing platform, future research should focus on their integration as a functional sensing devices. Efficient functionalization of the structure and optical readout of changes in the reflection signal are critical issues to tackle in order to achieve a functional device based on the principles explored in this work. The sensing capabilities of the structure could be expanded to include enhanced spectroscopies that would benefit from the intense and out-of-plane hotspots detected in the structure such as surface-enhanced Raman spectroscopy or surface enhanced IR absorption.

The fabrication of such structures should also be streamlined. EBL is an excellent technique for prototyping purposes due to its versatility. However, the iterative process required for calibrating a sensing platform would benefit from other nanofabrication techniques such as nanoimprinting lithography.

Fundamental research conducted using EELS has proven to be a valuable tool to characterize inverted honeycomb structures from a fundament perspective. Future characterization processes should involve surface-sensitive techniques that do not require the sample to be transparent to electrons, or necessitate that measurements be carried out in a vacuum chamber, such as photoemission electron microscopy or scanning near-field optical microscopy.

Regarding the stacked triskelion nanostructures, the remarkable versatility of

the structure enables its application as a filter or polarizer in a spectral range relevant to telecommunications. The main promise of these system lies in their integration in a plasmonic lattice that would excite a SLR in absorption only under the illumination of LCP or RCP, depending on the design. In order to achieve this response, the long-range order of the fabricated sample is crucial. Conductive oxides, such as indium tin oxide, simultaneously offer low absorption, while being conductive enough to avoid charging effects in the EBL process. These charging effects, together with beam astigmatism and stitching defects, severely hinder the long-range translation symmetry of the samples, undermining the possibility of achieving a chiral SLR.

Bibliography

[1] Vincenzo Giannini, Antonio I Fernández-Domínguez, Susannah C Heck, and Stefan A Maier. „Plasmonic nanoantennas: fundamentals and their use in controlling the radiative properties of nanoemitters“. In: *Chemical reviews* 111.6 (2011), pp. 3888–3912 (cit. on p. 7).

[2] Eliza Hutter and Janos H Fendler. „Exploitation of localized surface plasmon resonance“. In: *Advanced materials* 16.19 (2004), pp. 1685–1706 (cit. on p. 7).

[3] Kathryn M Mayer and Jason H Hafner. „Localized surface plasmon resonance sensors“. In: *Chemical reviews* 111.6 (2011), pp. 3828–3857 (cit. on p. 7).

[4] Katherine A Willets and Richard P Van Duyne. „Localized surface plasmon resonance spectroscopy and sensing“. In: *Annu. Rev. Phys. Chem.* 58.1 (2007), pp. 267–297 (cit. on p. 7).

[5] Ankit Agrawal, Shin Hum Cho, Omid Zandi, et al. „Localized surface plasmon resonance in semiconductor nanocrystals“. In: *Chemical reviews* 118.6 (2018), pp. 3121–3207 (cit. on p. 7).

[6] Christoph Langhammer, Markus Schwind, Bengt Kasemo, and Igor Zoric. „Localized surface plasmon resonances in aluminum nanodisks“. In: *Nano letters* 8.5 (2008), pp. 1461–1471 (cit. on p. 7).

[7] Jacob Khurgin, Anton Yu Bykov, and Anatoly V Zayats. „Hot-electron dynamics in plasmonic nanostructures: fundamentals, applications and overlooked aspects“. In: *Elight* 4.1 (2024), p. 15 (cit. on p. 7).

[8] Guang-Can Li, Dangyuan Lei, Meng Qiu, et al. „Light-induced symmetry breaking for enhancing second-harmonic generation from an ultrathin plasmonic nanocavity“. In: *Nature communications* 12.1 (2021), p. 4326 (cit. on p. 7).

[9] Grégory Barbillon, Andrey Ivanov, and Andrey K Sarychev. „Applications of symmetry breaking in plasmonics“. In: *Symmetry* 12.6 (2020), p. 896 (cit. on p. 7).

[10] Emiliano Cortés, Lucas V Besteiro, Alessandro Alabastri, et al. „Challenges in plasmonic catalysis“. In: *ACS nano* 14.12 (2020), pp. 16202–16219 (cit. on p. 7).

[11] Anderson GM da Silva, Thenner S Rodrigues, Jiale Wang, and Pedro HC Camargo. „Plasmonic catalysis with designer nanoparticles“. In: *Chemical Communications* 58.13 (2022), pp. 2055–2074 (cit. on p. 7).

[12] Umar Aslam, Steven Chavez, and Suljo Linic. „Controlling energy flow in multimetallic nanostructures for plasmonic catalysis“. In: *Nature nanotechnology* 12.10 (2017), pp. 1000–1005 (cit. on p. 7).

[13] Meijie Chen, Yurong He, Qin Ye, and Jiaqi Zhu. „Tuning plasmonic near-perfect absorber for selective absorption applications“. In: *Plasmonics* 14.6 (2019), pp. 1357–1364 (cit. on p. 7).

[14] Mehdi Keshavarz Hedayati, Franz Faupel, and Mady Elbahri. „Tunable broadband plasmonic perfect absorber at visible frequency“. In: *Applied Physics A* 109 (2012), pp. 769–773 (cit. on p. 7).

[15] Wei Zhou, Montacer Dridi, Jae Yong Suh, et al. „Lasing action in strongly coupled plasmonic nanocavity arrays“. In: *Nature nanotechnology* 8.7 (2013), pp. 506–511 (cit. on p. 7).

[16] TK Hakala, HT Rekola, AI Väkeväinen, et al. „Lasing in dark and bright modes of a finite-sized plasmonic lattice“. In: *Nature communications* 8.1 (2017), p. 13687 (cit. on p. 7).

[17] VV Popov, OV Polischuk, AR Davoyan, et al. „Plasmonic terahertz lasing in an array of graphene nanocavities“. In: *Graphene-Based Terahertz Electronics and Plasmonics*. Jenny Stanford Publishing, 2020, pp. 587–601 (cit. on p. 7).

[18] Roozbeh Siavash Moakhar, Somayeh Gholipour, Saeid Masudy-Panah, et al. „Recent advances in plasmonic perovskite solar cells“. In: *Advanced science* 7.13 (2020), p. 1902448 (cit. on p. 7).

[19] Prasanta Mandal. „Application of plasmonics in solar cell efficiency improvement: a brief review on recent progress“. In: *Plasmonics* 17.3 (2022), pp. 1247–1267 (cit. on p. 7).

[20] Nicolò Maccaferri, Grégory Barbillon, Alemayehu Nana Koya, et al. „Recent advances in plasmonic nanocavities for single-molecule spectroscopy“. In: *Nanoscale Advances* 3.3 (2021), pp. 633–642 (cit. on p. 7).

[21] Tamitake Itoh, Marek Procházka, Zhen-Chao Dong, et al. „Toward a new era of SERS and TERS at the nanometer scale: From fundamentals to innovative applications“. In: *Chemical Reviews* 123.4 (2023), pp. 1552–1634 (cit. on p. 7).

[22] Prashant K Jain and Mostafa A El-Sayed. „Plasmonic coupling in noble metal nanostructures“. In: *Chemical Physics Letters* 487.4-6 (2010), pp. 153–164 (cit. on pp. 7, 70).

[23] Alexander O Govorov, Zhiyuan Fan, Pedro Hernandez, Joseph M Slocik, and Rajesh R Naik. „Theory of circular dichroism of nanomaterials comprising chiral molecules and nanocrystals: plasmon enhancement, dipole interactions, and dielectric effects“. In: *Nano letters* 10.4 (2010), pp. 1374–1382 (cit. on pp. 7, 9).

[24] Andrey E Miroshnichenko, Sergej Flach, and Yuri S Kivshar. „Fano resonances in nanoscale structures“. In: *Reviews of Modern Physics* 82.3 (2010), pp. 2257–2298 (cit. on pp. 7, 45).

[25] Vasyl G Kravets, Andrei V Kabashin, William L Barnes, and Alexander N Grigorenko. „Plasmonic surface lattice resonances: a review of properties and applications“. In: *Chemical reviews* 118.12 (2018), pp. 5912–5951 (cit. on pp. 7, 46).

[26] Tal Ellenbogen, Kwanyong Seo, and Kenneth B Crozier. „Chromatic plasmonic polarizers for active visible color filtering and polarimetry“. In: *Nano letters* 12.2 (2012), pp. 1026–1031 (cit. on p. 8).

[27] Ming Lun Tseng, Jian Yang, Michael Semmlinger, et al. „Two-dimensional active tuning of an aluminum plasmonic array for full-spectrum response“. In: *Nano letters* 17.10 (2017), pp. 6034–6039 (cit. on p. 8).

[28] Cheng Zhang, Yonghua Lu, Yuan Ni, et al. „Plasmonic lasing of nanocavity embedding in metallic nanoantenna array“. In: *Nano letters* 15.2 (2015), pp. 1382–1387 (cit. on p. 8).

[29] Wei Zhou and Teri W Odom. „Tunable subradiant lattice plasmons by out-of-plane dipolar interactions“. In: *Nature nanotechnology* 6.7 (2011), pp. 423–427 (cit. on p. 8).

[30] Wei Zhou, Montacer Dridi, Jae Yong Suh, et al. „Lasing action in strongly coupled plasmonic nanocavity arrays“. In: *Nature nanotechnology* 8.7 (2013), pp. 506–511 (cit. on p. 8).

[31] Rithvik R Gutha, Seyed M Sadeghi, Christina Sharp, and Waylin J Wing. „Biological sensing using hybridization phase of plasmonic resonances with photonic lattice modes in arrays of gold nanoantennas“. In: *Nanotechnology* 28.35 (2017), p. 355504 (cit. on p. 8).

[32] Barbora Špačková, Piotr Wrobel, Markéta Bocková, and Jiří Homola. „Optical biosensors based on plasmonic nanostructures: a review“. In: *Proceedings of the IEEE* 104.12 (2016), pp. 2380–2408 (cit. on p. 8).

[33] Barbora Špačková and Jiří Homola. „Sensing properties of lattice resonances of 2D metal nanoparticle arrays: An analytical model“. In: *Optics express* 21.22 (2013), pp. 27490–27502 (cit. on p. 8).

[34] SM Sadeghi, WJ Wing, and Q Campbell. „Tunable plasmonic-lattice mode sensors with ultrahigh sensitivities and figure-of-merits“. In: *Journal of Applied Physics* 119.24 (2016) (cit. on p. 8).

[35] Päivi Törmä and William L Barnes. „Strong coupling between surface plasmon polaritons and emitters: a review“. In: *Reports on Progress in Physics* 78.1 (2014), p. 013901 (cit. on pp. 8, 28).

[36] Ankun Yang, Alexander J Hryn, Marc R Bourgeois, et al. „Programmable and reversible plasmon mode engineering“. In: *Proceedings of the National Academy of Sciences* 113.50 (2016), pp. 14201–14206 (cit. on p. 8).

[37] Said Rahimzadeh Kalaleh Rodriguez, Aimi Abass, Björn Maes, et al. „Coupling bright and dark plasmonic lattice resonances“. In: *Physical Review X* 1.2 (2011), p. 021019 (cit. on p. 8).

[38] Yasa Ekşioğlu, Arif E Cetin, and Jiří Petráček. „Optical response of plasmonic nanohole arrays: comparison of square and hexagonal lattices“. In: *Plasmonics* 11 (2016), pp. 851–856 (cit. on pp. 8, 46).

[39] Alastair D Humphrey and William L Barnes. „Plasmonic surface lattice resonances on arrays of different lattice symmetry“. In: *Physical Review B* 90.7 (2014), p. 075404 (cit. on pp. 8, 45, 46).

[40] Ana Conde-Rubio, Arantxa Fraile Rodríguez, Xavier Borrisé, et al. „Geometric frustration in a hexagonal lattice of plasmonic nanoelements“. In: *Optics express* 26.16 (2018), pp. 20211–20224 (cit. on p. 8).

[41] Ana Conde-Rubio, Arantxa Fraile Rodríguez, André Espinha, et al. „Geometric frustration in ordered lattices of plasmonic nanoelements“. In: *Scientific Reports* 9.1 (2019), p. 3529 (cit. on p. 8).

[42] Roderich Moessner and Arthur P. Ramirez. „Geometrical frustration“. In: *Physics Today* 59.2 (Feb. 2006), pp. 24–29. eprint: `https://pubs.aip.org/physicstoday/article-pdf/59/2/24/16665199/24\_1\_online.pdf` (cit. on p. 8).

[43] Zhongyang Li, Serkan Butun, and Koray Aydin. „Ultranarrow band absorbers based on surface lattice resonances in nanostructured metal surfaces“. In: *ACS nano* 8.8 (2014), pp. 8242–8248 (cit. on p. 8).

[44] Mario Hentschel, Thomas Weiss, Shahin Bagheri, and Harald Giessen. „Babinet to the half: coupling of solid and inverse plasmonic structures“. In: *Nano letters* 13.9 (2013), pp. 4428–4433 (cit. on p. 8).

[45] Fei Cheng, Jie Gao, Ting S Luk, and Xiaodong Yang. „Structural color printing based on plasmonic metasurfaces of perfect light absorption“. In: *Scientific reports* 5.1 (2015), p. 11045 (cit. on p. 8).

[46] Charles Cherqui, Marc R Bourgeois, Danqing Wang, and George C Schatz. „Plasmonic surface lattice resonances: Theory and computation“. In: *Accounts of chemical research* 52.9 (2019), pp. 2548–2558 (cit. on p. 8).

[47] Sebastian Baur, Stephen Sanders, and Alejandro Manjavacas. „Hybridization of lattice resonances“. In: *ACS nano* 12.2 (2018), pp. 1618–1629 (cit. on p. 8).

[48] TK Hakala, HT Rekola, AI Väkeväinen, et al. „Lasing in dark and bright modes of a finite-sized plasmonic lattice“. In: *Nature communications* 8.1 (2017), p. 13687 (cit. on p. 8).

[49] Benjamin D Thackray, Vasyl G Kravets, Fred Schedin, et al. „Narrow collective plasmon resonances in nanostructure arrays observed at normal light incidence for simplified sensing in asymmetric air and water environments“. In: *Acs Photonics* 1.11 (2014), pp. 1116–1126 (cit. on p. 8).

[50] Rui Guo, Tommi K Hakala, and Päivi Törmä. „Geometry dependence of surface lattice resonances in plasmonic nanoparticle arrays“. In: *Physical Review B* 95.15 (2017), p. 155423 (cit. on p. 8).

[51] Gianluca Ruffato, Denis Garoli, S Cattarin, Sonia Barison, and Filippo Romanato. „FIB lithography of nanoporous gold slits for extraordinary transmission“. In: *Microelectronic engineering* 98 (2012), pp. 419–423 (cit. on p. 8).

[52] Seung-Woo Lee, Kyeong-Seok Lee, Junhyoung Ahn, et al. „Highly sensitive biosensing using arrays of plasmonic Au nanodisks realized by nanoimprint lithography“. In: *ACS nano* 5.2 (2011), pp. 897–904 (cit. on p. 8).

[53] Matthew C Traub, Whitney Longsine, and Van N Truskett. „Advances in nanoimprint lithography“. In: *Annual review of chemical and biomolecular engineering* 7.1 (2016), pp. 583–604 (cit. on p. 8).

[54] Ventsislav K Valev, Jeremy J Baumberg, Concita Sibilia, and Thierry Verbiest. „Chirality and chiroptical effects in plasmonic nanostructures: fundamentals, recent progress, and outlook“. In: *Advanced Materials* 25.18 (2013), pp. 2517–2534 (cit. on pp. 9, 54).

[55] Martin Schäferling. *Chiral nanophotonics*. Vol. 205. Springer, 2017, p. 159 (cit. on pp. 9, 52, 55, 56).

[56] Lisa V Poulikakos, Jennifer A Dionne, and Aitzol García-Etxarri. „Optical helicity and optical chirality in free space and in the presence of matter“. In: *Symmetry* 11.9 (2019), p. 1113 (cit. on pp. 9, 48).

[57] Robert N Compton and Richard M Pagni. „The chirality of biomolecules“. In: *Advances in atomic, molecular, and optical physics*. Vol. 48. Elsevier, 2002, pp. 219–261 (cit. on p. 9).

[58] Marco Esposito, Vittorianna Tasco, Massimo Cuscuna, et al. „Nanoscale 3D chiral plasmonic helices with circular dichroism at visible frequencies“. In: *Acs Photonics* 2.1 (2015), pp. 105–114 (cit. on p. 9).

[59] Zhiyuan Fan and Alexander O Govorov. „Chiral nanocrystals: plasmonic spectra and circular dichroism“. In: *Nano letters* 12.6 (2012), pp. 3283–3289 (cit. on p. 9).

[60]Lei Wang and Luogen Deng. „Plasmonic circular dichroism of the helical nanosphere assemblies and the helical nanoellipsoid assemblies“. In: *Plasmonics* 10 (2015), pp. 399–409 (cit. on p. 9).

[61]Zhiyuan Fan and Alexander O Govorov. „Plasmonic circular dichroism of chiral metal nanoparticle assemblies“. In: *Nano letters* 10.7 (2010), pp. 2580–2587 (cit. on p. 9).

[62]An'an Wu, Yoshito Y Tanaka, and Tsutomu Shimura. „Giant chiroptical response of twisted metal nanorods due to strong plasmon coupling“. In: *APL Photonics* 6.12 (2021) (cit. on pp. 9, 10, 55).

[63]M Decker, M Ruther, CE Kriegler, et al. „Strong optical activity from twisted-cross photonic metamaterials“. In: *Optics letters* 34.16 (2009), pp. 2501–2503 (cit. on pp. 9, 10, 55).

[64]Na Liu, Hui Liu, Shining Zhu, and Harald Giessen. „Stereometamaterials“. In: *Nature Photonics* 3.3 (2009), pp. 157–162 (cit. on pp. 9, 10, 55).

[65]Xinghui Yin, Martin Schäferling, Bernd Metzger, and Harald Giessen. „Interpreting chiral nanophotonic spectra: the plasmonic Born–Kuhn model“. In: *Nano letters* 13.12 (2013), pp. 6238–6243 (cit. on pp. 9, 50, 51, 54).

[66]Euan Hendry, T Carpy, J Johnston, et al. „Ultrasensitive detection and characterization of biomolecules using superchiral fields“. In: *Nature nanotechnology* 5.11 (2010), pp. 783–787 (cit. on p. 10).

[67]Tarun Kakkar, Chantal Keijzer, Marion Rodier, et al. „Superchiral near fields detect virus structure“. In: *Light: Science & Applications* 9.1 (2020), p. 195 (cit. on p. 10).

[68]Jose García-Guirado, Mikael Svedendahl, Joaquim Puigdollers, and Romain Quidant. „Enantiomer-selective molecular sensing using racemic nanoplasmonic arrays“. In: *Nano letters* 18.10 (2018), pp. 6279–6285 (cit. on p. 10).

[69]Makoto Kuwata-Gonokami, Nobuyoshi Saito, Yusuke Ino, et al. „Giant optical activity in quasi-two-dimensional planar nanostructures“. In: *Physical review letters* 95.22 (2005), p. 227401 (cit. on pp. 10, 49).

[70]E Plum, VA Fedotov, AS Schwanecke, NI Zheludev, and Y Chen. „Giant optical gyrotropy due to electromagnetic coupling“. In: *Applied Physics Letters* 90.22 (2007) (cit. on pp. 10, 55).

[71]E Plum, J Zhou, J Dong, et al. „Metamaterial with negative index due to chirality“. In: *Physical Review B—Condensed Matter and Materials Physics* 79.3 (2009), p. 035407 (cit. on p. 10).

[72] Jiangfeng Zhou, Dibakar Roy Chowdhury, Rongkuo Zhao, et al. „Terahertz chiral metamaterials with giant and dynamically tunable optical activity". In: *Physical Review B—Condensed Matter and Materials Physics* 86.3 (2012), p. 035448 (cit. on p. 10).

[73] R Zhao, L Zhang, J Zhou, Th Koschny, and CM Soukoulis. „Conjugated gammadion chiral metamaterial with uniaxial optical activity and negative refractive index". In: *Physical Review B—Condensed Matter and Materials Physics* 83.3 (2011), p. 035105 (cit. on p. 10).

[74] Stefan A. Maier et al. *Plasmonics: fundamentals and applications*. Vol. 1. Springer, 2007 (cit. on pp. 20, 28).

[75] N. W. Ashcroft and N.D. Mermin. *Solid State Physics*. Holt-Saunders, 1976 (cit. on p. 21).

[76] Paul Drude. „Zur elektronentheorie der metalle". In: *Annalen der physik* 306.3 (1900), pp. 566–613 (cit. on p. 22).

[77] Paul Drude. „Zur elektronentheorie der metalle; II. Teil. galvanomagnetische und thermomagnetische effecte". In: *Annalen der physik* 308.11 (1900), pp. 369–402 (cit. on p. 22).

[78] Felix Bloch. „Über die quantenmechanik der elektronen in kristallgittern". In: *Zeitschrift für physik* 52.7 (1929), pp. 555–600 (cit. on p. 22).

[79] Krystyna Kolwas and Anastasiya Derkachova. „Impact of the interband transitions in gold and silver on the dynamics of propagating and localized surface plasmons". In: *Nanomaterials* 10.7 (2020), p. 1411 (cit. on p. 24).

[80] Peter B Johnson and R-WJPrB Christy. „Optical constants of the noble metals". In: *Physical review B* 6.12 (1972), p. 4370 (cit. on p. 24).

[81] David Pines. „Collective energy losses in solids". In: *Reviews of modern physics* 28.3 (1956), p. 184 (cit. on p. 26).

[82] Fernando López-Tejeira, Sergio G Rodrigo, Luis Martín-Moreno, et al. „Efficient unidirectional nanoslit couplers for surface plasmons". In: *Nature Physics* 3.5 (2007), pp. 324–328 (cit. on p. 28).

[83] John F O'Hara, Richard D Averitt, and Antoinette J Taylor. „Prism coupling to terahertz surface plasmon polaritons". In: *Optics Express* 13.16 (2005), pp. 6117–6126 (cit. on p. 28).

[84] Ramona Dallapiccola, C Dubois, A Gopinath, Francesco Stellacci, and L Dal Negro. „Near-field excitation and near-field detection of propagating surface plasmon polaritons on Au waveguide structures". In: *Applied Physics Letters* 94.24 (2009) (cit. on p. 28).

[85] John David Jackson. *Classical electrodynamics*. John Wiley & Sons, 2012 (cit. on p. 32).

[86]Prashant K Jain and Mostafa A El-Sayed. „Noble metal nanoparticle pairs: effect of medium for enhanced nanosensing“. In: *Nano letters* 8.12 (2008), pp. 4347–4352 (cit. on pp. 32, 41).

[87]Craig F Bohren and Donald R Huffman. *Absorption and scattering of light by small particles*. John Wiley & Sons, 2008 (cit. on p. 34).

[88]Gustav Mie. „Beiträge zur Optik trüber Medien, speziell kolloidaler Metallösungen“. In: *Annalen der physik* 330.3 (1908), pp. 377–445 (cit. on p. 36).

[89]Matthew Pelton and Garnett W. Bryant. *Introduction to metal-nanoparticle plasmonics*. John Wiley & Sons, 2013 (cit. on p. 36).

[90]Hitoshi Kuwata, Hiroharu Tamaru, Kunio Esumi, and Kenjiro Miyano. „Resonant light scattering from metal nanoparticles: Practical analysis beyond Rayleigh approximation“. In: *Applied physics letters* 83.22 (2003), pp. 4625–4627 (cit. on p. 36).

[91]Linda Gunnarsson, Tomas Rindzevicius, Juris Prikulis, et al. „Confined plasmons in nanofabricated single silver particle pairs: experimental observations of strong interparticle interactions“. In: *The Journal of Physical Chemistry B* 109.3 (2005), pp. 1079–1087 (cit. on p. 38).

[92]Yi Hua, Kavita Chandra, Duncan Hieu M Dam, Gary P Wiederrecht, and Teri W Odom. „Shape-dependent nonlinear optical properties of anisotropic gold nanoparticles“. In: *The journal of physical chemistry letters* 6.24 (2015), pp. 4904–4908 (cit. on p. 37).

[93]JJ Mock, M Barbic, DR Smith, DA Schultz, and Sh Schultz. „Shape effects in plasmon resonance of individual colloidal silver nanoparticles“. In: *The Journal of Chemical Physics* 116.15 (2002), pp. 6755–6759 (cit. on pp. 37, 39).

[94]Colleen L Nehl and Jason H Hafner. „Shape-dependent plasmon resonances of gold nanoparticles“. In: *Journal of Materials Chemistry* 18.21 (2008), pp. 2415–2419 (cit. on p. 37).

[95]Feng Hao, Yannick Sonnefraud, Pol Van Dorpe, et al. „Symmetry breaking in plasmonic nanocavities: subradiant LSPR sensing and a tunable Fano resonance“. In: *Nano letters* 8.11 (2008), pp. 3983–3988 (cit. on p. 40).

[96]Benjamin Gallinet and Olivier JF Martin. „Refractive index sensing with subradiant modes: a framework to reduce losses in plasmonic nanostructures“. In: *ACS nano* 7.8 (2013), pp. 6978–6987 (cit. on p. 40).

[97]Prashant K Jain, Susie Eustis, and Mostafa A El-Sayed. „Plasmon coupling in nanorod assemblies: optical absorption, discrete dipole approximation simulation, and exciton-coupling model“. In: *The Journal of Physical Chemistry B* 110.37 (2006), pp. 18243–18253 (cit. on p. 40).

[98] Prashant K Jain, Wenyu Huang, and Mostafa A El-Sayed. „On the universal scaling behavior of the distance decay of plasmon coupling in metal nanoparticle pairs: a plasmon ruler equation“. In: *Nano letters* 7.7 (2007), pp. 2080–2088 (cit. on pp. 41, 42).

[99] VG Kravets, F Schedin, and AN Grigorenko. „Extremely Narrow Plasmon Resonances Based on Diffraction Coupling<? format?> of Localized Plasmons in Arrays of Metallic Nanoparticles“. In: *Physical review letters* 101.8 (2008), p. 087403 (cit. on p. 43).

[100] G Vecchi, V Giannini, and J Gómez Rivas. „Surface modes in plasmonic crystals induced by diffractive coupling of nanoantennas“. In: *Physical Review B—Condensed Matter and Materials Physics* 80.20 (2009), p. 201401 (cit. on p. 43).

[101] Andrey G Nikitin, Andrei V Kabashin, and Hervé Dallaporta. „Plasmonic resonances in diffractive arrays of gold nanoantennas: near and far field effects“. In: *Optics express* 20.25 (2012), pp. 27941–27952 (cit. on p. 45).

[102] Vincenzo Giannini, Yan Francescato, Hemmel Amrania, Chris C Phillips, and Stefan A Maier. „Fano resonances in nanoscale plasmonic systems: a parameter-free modeling approach“. In: *Nano letters* 11.7 (2011), pp. 2835–2840 (cit. on p. 45).

[103] Ana Conde-Rubio, Arantxa Fraile Rodríguez, André Espinha, et al. „Geometric frustration in ordered lattices of plasmonic nanoelements“. In: *Scientific Reports* 9.1 (2019), p. 3529 (cit. on p. 46).

[104] Baptiste Auguié and William L Barnes. „Diffractive coupling in gold nanoparticle arrays and the effect of disorder“. In: *Optics letters* 34.4 (2009), pp. 401–403 (cit. on p. 46).

[105] VG Kravets, F Schedin, Giampaolo Pisano, et al. „Nanoparticle arrays: From magnetic response to coupled plasmon resonances“. In: *Physical Review B* 90.12 (2014), p. 125445 (cit. on p. 46).

[106] Anton D Utyushev, Vadim I Zakomirnyi, and Ilia L Rasskazov. „Collective lattice resonances: Plasmonics and beyond“. In: *Reviews in Physics* 6 (2021), p. 100051 (cit. on p. 46).

[107] Lauren Zundel and Alejandro Manjavacas. „Finite-size effects on periodic arrays of nanostructures“. In: *Journal of Physics: Photonics* 1.1 (2018), p. 015004 (cit. on pp. 46, 47).

[108] SRK Rodriguez, MC Schaafsma, A Berrier, and J Gómez Rivas. „Collective resonances in plasmonic crystals: Size matters“. In: *Physica B: Condensed Matter* 407.20 (2012), pp. 4081–4085 (cit. on p. 46).

[109]Lauren Zundel, Juan R Deop-Ruano, Rosario Martinez-Herrero, and Alejandro Manjavacas. „Lattice resonances excited by finite-width light beams“. In: *ACS omega* 7.35 (2022), pp. 31431–31441 (cit. on p. 46).

[110]M Saad Bin-Alam, Orad Reshef, Yaryna Mamchur, et al. „Ultra-high-Q resonances in plasmonic metasurfaces“. In: *Nature communications* 12.1 (2021), p. 974 (cit. on pp. 46, 47).

[111]Baptiste Auguié, Xesús M Bendana, William L Barnes, and F Javier García de Abajo. „Diffractive arrays of gold nanoparticles near an interface: Critical role of the substrate“. In: *Physical Review B—Condensed Matter and Materials Physics* 82.15 (2010), p. 155447 (cit. on pp. 46, 47).

[112]Andrey G Nikitin, Tuyen Nguyen, and Hervé Dallaporta. „Narrow plasmon resonances in diffractive arrays of gold nanoparticles in asymmetric environment: Experimental studies“. In: *Applied Physics Letters* 102.22 (2013) (cit. on p. 46).

[113]Baptiste Auguié, Xesús M Bendana, William L Barnes, and F Javier García de Abajo. „Diffractive arrays of gold nanoparticles near an interface: Critical role of the substrate“. In: *Physical Review B—Condensed Matter and Materials Physics* 82.15 (2010), p. 155447 (cit. on p. 47).

[114]Wei Zhou, Yi Hua, Mark D Huntington, and Teri W Odom. „Delocalized lattice plasmon resonances show dispersive quality factors“. In: *The journal of physical chemistry letters* 3.10 (2012), pp. 1381–1385 (cit. on p. 48).

[115]Wei Zhou and Teri W Odom. „Tunable subradiant lattice plasmons by out-of-plane dipolar interactions“. In: *Nature nanotechnology* 6.7 (2011), pp. 423–427 (cit. on p. 48).

[116]Ivan Fernandez-Corbaton, Xavier Zambrana-Puyalto, and Gabriel Molina-Terriza. „Helicity and angular momentum: A symmetry-based framework for the study of light-matter interactions“. In: *Physical Review A—Atomic, Molecular, and Optical Physics* 86.4 (2012), p. 042103 (cit. on p. 48).

[117]Y.P. Svirko and N.I. Zheludev. *Polarization of Light in Nonlinear Optics*. Wiley, 1998 (cit. on p. 49).

[118]Baptiste Auguié, José Lorenzo Alonso-Gómez, Andrés Guerrero-Martínez, and Luis M Liz-Marzán. „Fingers crossed: Optical activity of a chiral dimer of plasmonic nanorods“. In: *The Journal of Physical Chemistry Letters* 2.8 (2011), pp. 846–851 (cit. on p. 55).

[119]M Decker, R Zhao, CM Soukoulis, Stefan Linden, and M Wegener. „Twisted split-ring-resonator photonic metamaterial with huge optical activity“. In: *Optics letters* 35.10 (2010), pp. 1593–1595 (cit. on p. 55).

[120]Martin Schäferling, Xinghui Yin, and Harald Giessen. „Formation of chiral fields in a symmetric environment“. In: *Optics Express* 20.24 (2012), pp. 26326–26336 (cit. on p. 55).

[121] Bruce T Draine and Piotr J Flatau. „Discrete-dipole approximation for scattering calculations“. In: *Josa a* 11.4 (1994), pp. 1491–1499 (cit. on p. 57).

[122] Maxim A Yurkin and Alfons G Hoekstra. „The discrete dipole approximation: an overview and recent developments“. In: *Journal of Quantitative Spectroscopy and Radiative Transfer* 106.1-3 (2007), pp. 558–589 (cit. on p. 57).

[123] Jian-Ming Jin. *The finite element method in electromagnetics*. John Wiley & Sons, 2015 (cit. on p. 57).

[124] FJ García De Abajo and A Howie. „Relativistic electron energy loss and electron-induced photon emission in inhomogeneous dielectrics“. In: *Physical review letters* 80.23 (1998), p. 5180 (cit. on p. 57).

[125] S. C. Hagness A. Taflove and B. I. London. *Computational electrodynamics: the Finite-Difference Time-Domain method*. Artech House, 2005 (cit. on pp. 57, 63).

[126] Kane S. Yee. „Numerical Solution of Initial Boundary Value Problems Involving Marxwell's Equations in Isotropic Media“. In: *IEEE Transactions on Antennas and Propagation* 14.3 (1966), pp. 302–307 (cit. on pp. 57, 58).

[127] *Ansys Lumerical* (cit. on pp. 58, 60, 65).

[128] Richard Courant, Kurt Friedrichs, and Hans Lewy. „Über die partiellen Differenzengleichungen der mathematischen Physik“. In: *Mathematische annalen* 100.1 (1928), pp. 32–74 (cit. on p. 60).

[129] J. Berenger. „A perfectly matched layer for the absorption of electromagnetic waves“. In: *Journal of Computational Physics* 114.2 (1994), pp. 185–200 (cit. on p. 63).

[130] Stephen D. Gedney and Bo Zhao. „An Auxiliary Differential Equation Formulation for the Complex-Frequency Shifted PML“. In: *IEEE Transactions on Antennas and Propagation* 58.3 (2010), pp. 838–847 (cit. on p. 64).

[131] Stephan Link and Mostafa A El-Sayed. „Spectral properties and relaxation dynamics of surface plasmon electronic oscillations in gold and silver nanodots and nanorods“. In: *The Journal of Physical Chemistry B* 103.40 (1999), pp. 8410–8426 (cit. on p. 70).

[132] Yadong Yin, Zhi-Yuan Li, Ziyi Zhong, et al. „Synthesis and characterization of stable aqueous dispersions of silver nanoparticles through the Tollens process“. In: *Journal of Materials Chemistry* 12.3 (2002), pp. 522–527 (cit. on p. 70).

[133] S.A. Campbell. *Fabrication Engineering at the Micro and Nanoscale*. The Oxford Series in Electrical and Computer Engineering. OUP USA, 2008 (cit. on p. 70).

[134] Larry F Thompson. „An introduction to lithography“. In: ACS Publications, 1983 (cit. on p. 70).

[135]Rudolf Karl Luneburg. *Mathematical theory of optics*. Univ of California Press, 1966 (cit. on p. 71).

[136]Ivan H Deutsch and John C Garrison. „Paraxial quantum propagation“. In: *Physical Review A* 43.5 (1991), p. 2498 (cit. on p. 71).

[137]Mark J Beran and George B Parrent. „Theory of partial coherence“. In: Society of Photo-optical Instrumentation Engineers. 1974 (cit. on p. 71).

[138]Nan Fu, Yanxiang Liu, Xiaolong Ma, and Zanfeng Chen. „EUV lithography: state-of-the-art review“. In: *J. Microelectron. Manuf* 2.2 (2019), pp. 1–6 (cit. on p. 71).

[139]Yifang Chen. „Nanofabrication by electron beam lithography and its applications: A review“. In: *Microelectronic Engineering* 135 (2015), pp. 57–72 (cit. on p. 71).

[140]José Danglad-Flores, Stephan Eickelmann, and Hans Riegler. „Deposition of polymer films by spin casting: A quantitative analysis“. In: *Chemical Engineering Science* 179 (2018), pp. 257–264 (cit. on p. 71).

[141]Christophe Vieu, F Carcenac, A Pepin, et al. „Electron beam lithography: resolution limits and applications“. In: *Applied surface science* 164.1-4 (2000), pp. 111–117 (cit. on p. 72).

[142]AN Broers, JME Harper, and WW Molzen. „250-Å linewidths with PMMA electron resist“. In: *Applied Physics Letters* 33.5 (1978), pp. 392–394 (cit. on p. 72).

[143]Joan Vila-Comamala, Sergey Gorelick, Vitaliy A Guzenko, et al. „Dense high aspect ratio hydrogen silsesquioxane nanostructures by 100 keV electron beam lithography“. In: *Nanotechnology* 21.28 (2010), p. 285305 (cit. on pp. 72, 75).

[144]Michal Urbánek, Vladimír KOLAŘÍK, Stanislav Krátkỳ, et al. „Monte carlo simulation of proximity effect in e-beam lithography“. In: *Proceedings of the 5th International conference NANOCON 2013*. 2013, pp. 723–726 (cit. on p. 74).

[145]*Monte Carlo Simulation of Electron Trajectory in Solids (CASINO)* (cit. on p. 74).

[146]Babak Ziaie, Antonio Baldi, and Massood Z Atashbar. „Introduction to micro-/nanofabrication“. In: *Springer handbook of nanotechnology* (2010), pp. 231–269 (cit. on p. 75).

[147]Xiaojin Jiao, Jeremy Goeckeritz, Steve Blair, and Mark Oldham. „Localization of near-field resonances in bowtie antennae: influence of adhesion layers“. In: *Plasmonics* 4 (2009), pp. 37–50 (cit. on p. 75).

[148]Hamish R Colenso, Eden Z Rafealov, Mohsen Maddah, et al. „Comparison of seed layers for smooth, low loss silver films used in ultraviolet-visible plasmonic imaging devices“. In: *Thin Solid Films* 656 (2018), pp. 68–74 (cit. on p. 75).

[149] VJ Logeeswaran, Nobuhiko P Kobayashi, M Saif Islam, et al. „Ultrasmooth silver thin films deposited with a germanium nucleation layer“. In: *Nano letters* 9.1 (2009), pp. 178–182 (cit. on p. 75).

[150] Thomas Mortelmans, Dimitrios Kazazis, Vitaliy A Guzenko, et al. „Grayscale e-beam lithography: Effects of a delayed development for well-controlled 3D patterning“. In: *Microelectronic Engineering* 225 (2020), p. 111272 (cit. on p. 75).

[151] Adriaan J Taal, Jake Rabinowitz, and Kenneth L Shepard. „mr-EBL: ultra-high sensitivity negative-tone electron beam resist for highly selective silicon etching and large-scale direct patterning of permanent structures“. In: *Nanotechnology* 32.24 (2021), p. 245302 (cit. on p. 75).

[152] Ampere A Tseng. „Recent developments in nanofabrication using focused ion beams“. In: *Small* 1.10 (2005), pp. 924–939 (cit. on pp. 75, 76).

[153] Jon Orloff. „High-resolution focused ion beams“. In: *Review of Scientific Instruments* 64.5 (1993), pp. 1105–1130 (cit. on p. 76).

[154] Federica Catania, Elia Scattolo, Damiano Giubertoni, et al. „Channel Nanoscaling of InGaZnO TFTs and Circuits via Focused Ion Beam“. In: *ACS Applied Electronic Materials* 6.3 (2024), pp. 1841–1847 (cit. on p. 76).

[155] Elia Scattolo, Alessandro Cian, Damiano Giubertoni, et al. „Optimization of focused ion beam patterning parameters for direct integration of plasmonic nanostructures on silicon photodiodes“. In: *Engineering Proceedings* 10.1 (2021), p. 2 (cit. on p. 76).

[156] Nan Yao. *Focused ion beam systems: basics and applications*. Cambridge University Press, 2007 (cit. on p. 76).

[157] Megan Canavan, Dermot Daly, Andreas Rummel, et al. „Novel in-situ lamella fabrication technique for in-situ TEM“. In: *Ultramicroscopy* 190 (2018), pp. 21–29 (cit. on p. 77).

[158] Katerina Mouralova, Radim Zahradnicek, Libor Benes, et al. „Study of micro structural material changes after WEDM based on TEM lamella analysis“. In: *Metals* 10.7 (2020), p. 949 (cit. on p. 77).

[159] Konstantinos Pantzas and Gilles Patriarche. „Experimental quantification of atomically-resolved HAADF-STEM images using EDX“. In: *Ultramicroscopy* 220 (2021), p. 113152 (cit. on p. 77).

[160] Albert Abraham Michelson. *Light waves and their uses*. Vol. 2. University of Chicago Press, 1903 (cit. on p. 78).

[161] Francisco Javier García de Abajo. „Optical excitations in electron microscopy“. In: *Reviews of modern physics* 82.1 (2010), pp. 209–275 (cit. on pp. 80, 82).

[162] Albert Polman, Mathieu Kociak, and F Javier García de Abajo. „Electron-beam spectroscopy for nanophotonics“. In: *Nature materials* 18.11 (2019), pp. 1158–1171 (cit. on p. 80).

[163] Satoshi Kawata, Yasushi Inouye, and Prabhat Verma. „Plasmonics for near-field nano-imaging and superlensing“. In: *Nature photonics* 3.7 (2009), pp. 388–394 (cit. on p. 80).

[164] Zhibo Dang, Yuxiang Chen, and Zheyu Fang. „Cathodoluminescence nanoscopy: state of the art and beyond“. In: *ACS nano* 17.24 (2023), pp. 24431–24448 (cit. on p. 80).

[165] Mathieu Kociak and Odile Stéphan. „Mapping plasmons at the nanometer scale in an electron microscope“. In: *Chem. Soc. Rev.* 43 (11 2014), pp. 3865–3883 (cit. on p. 81).

[166] Claire A West, Agust Olafsson, Grace Pakeltis, et al. „Plasmon hybridization in nanorhombus assemblies“. In: *The Journal of Physical Chemistry C* 124.49 (2020), pp. 27009–27016 (cit. on p. 82).

[167] Francisco Javier García de Abajo and M Kociak. „Probing the photonic local density of states with electron energy loss spectroscopy“. In: *Physical Review Letters* 100.10 (2008), p. 106804 (cit. on p. 82).